MODEL BASED FAULT AND SYSTEM PARAMETER IDENTIFICATION IN ROTOR-AMB SYSTEMS WITH BREATHING CRACK

A Thesis Submitted in Partial Fulfillment of the Requirements for the Degree of

DOCTOR OF PHILOSOPHY

by

SANDEEP SINGH

(Roll No. 126103035)

DEPARTMENT OF MECHANICAL ENGINEERING

INDIAN INSTITUTE OF TECHNOLOGY GUWAHATI

GUWAHATI 781 039, INDIA

OCTOBER 2015

Department of Mechanical Engineering
Indian Institute of Technology Guwahati
Guwahati- 781 039, INDIA.

CERTIFICATE

It is certified that the work contained in this Thesis titled "**Model Based Fault and System Parameter Identification in Rotor-AMB Systems with Breathing Crack"** submitted by **Mr. Sandeep Singh** (Roll no. 126103035) to the Indian Institute of Technology Guwahati for the award of the degree of Doctor of Philosophy has been carried out under my supervision in the Department of Mechanical Engineering, Indian Institute of Technology Guwahati. This work has not been submitted elsewhere for the award of any other degree or diploma.

October 2015

Dr. Rajiv Tiwari
Professor
Department of Mechanical Engineering
Indian Institute of Technology Guwahati
Guwahati – 781 039, INDIA

Acknowledgements

No undertaking involved in carrying out PhD work can be accomplished without the help of expert individuals. First, I would like to express my sincerest regards and gratitude to Professor Rajiv Tiwari for serving as my thesis supervisor. His expert guidance, unbound cooperation and generous support are much appreciated. It would be my privilege to correspond and learn from him in future as well. I would also like to express my deep sense of respect and thanks to Professors U. S. Dixit, S. K. Kakoty and A. Chakraborty for serving on my committee and valuable suggestions.

My stay in IIT Guwahai was made pleasant by many friends and seniors of the research fraternity. Dr. D. J. Bordoloi of Vibration and Acoustics lab has been one such person. I specially mention Dr. Mohit Lal, Dr. C. Sharavankumar, Purushottam Gangsar and Ansul Garg for being constant source of encouragement and help as friends.

The pain my wife and children have taken to keep me free from the daily routine of being the master of the house and to keep me engaged in my thesis work cannot be expressed in words. I am obliged for all the sacrifices they made for this endeavour. My parents and my parent-in-laws had been a constant source of inspiration and motivation, all these years. I am ever grateful to them.

I thank almighty for having blessed me with all the happiness these three years to keep me motivated towards the goal.

October 2015

IIT Guwahati (Sandeep Singh)

ABSTRACT

Active Magnetic Bearings (AMBs) are a recent mechatronic adaptation to the field of rotor dynamics. It offers an unparalleled benefit of excellent journal positioning with clean and frictionless operation due to absence of any mechanical load bearing components. This work focuses on two main facets of rotor–AMB systems, namely, the analysis of the system (i.e., the direct problem) and the fault parameter identification (i.e., the inverse problem).

The fault identification and diagnostic is not a straight forward in the case of AMB integrated rotors, since the AMB action has the overall effect of attenuating the rotor vibrations. This renders the pure vibration based methods susceptible to errors in analysing such systems. Apart from the rotor vibration history, some more observables must be sought for the analysis and the identification in AMB integrated rotors.

Frequent faults that appear in rotating machinery are residual unbalances, the shaft bow/bent, the shaft misalignment, bearing faults, gear faults, rotor cracks and motor faults. Of them all, the residual unbalance and the rotor crack are the most critical because of the presence of residual unbalance is almost a certain event, and the appearance of and growth crack is a catastrophic event in rotors. In this work, the emphasis rests on the identification of these two rotor fault parameters in particular, in AMB integrated rotors.

First, a cracked Jeffcott rotor with AMB support at the disc location is analysed, with intent of obtaining a clear understanding of issues and difficulties associated with the identification in such systems. The equations of motion (EOM) developed indicate the need for observing the AMB current history along with the rotor vibration history for the correct representation of rotor–AMB

systems. For the identification of transverse rotor crack a single crack parameter of crack stiffness, Δk_{22}, is used and the residual unbalance is identified with the parameters, e and β, i.e. the eccentricity and the phase, respectively. Frequency domain equations are developed to formulate an identification problem based on the least–squares regression method. The requirement of positive and negative harmonics of the rotor vibration displacement and AMB currents in identification equations is fulfilled by the full spectrum analysis, with Fast Fourier Transform (FFT). For the correction of phase ambiguity in these harmonics due to random instants of picking time domain signals, a phase compensation algorithm is developed and implemented. The identification algorithm is used to estimate the crack, unbalance, viscous damping and AMB stiffness parameters, and the procedure is standardised for use in complex models.

Gyroscopic effects and angular deflections arising in rotor–AMB systems are analysed in the next analytical model. It is observed that the accurate measurement of angular deflections has practical limitations. A dynamic reduction scheme based on available literature is developed to do away with the need for measurement of rotational degrees of freedom (DOFs). The identification algorithm developed on the basis of the reduced EOM is used to estimate the crack, unbalance, viscous damping and AMB stiffness parameters. The dynamic reduction scheme is extended in the subsequent models based on Finite Elements Method (FEM) where reduction of a large number of DOFs is required including some translatory and all rotational DOFs.

Subsequent models are based on the FEM, with the analytical concepts developed in the last two models used for the generation of more accurate synthetic responses. The first FEM model assumes the support bearings as rigid. This is in line with the assumptions made in the previous numerical models. The procedure of phase correction at various harmonics developed in the first

analytical model and the procedure of dynamic reduction of rotational DOFs developed in the second analytical model are used in this model to for the phase compensation and the dynamic reduction, respectively. This model is used for the identification of transverse crack and disc unbalance parameters along with AMB stiffness constants.

The second FEM model is representation of the most generic case that may be experienced in field. This modelling and analysis is based on consideration of the multiple discs, AMBs and support bearings. Support bearings are assumed flexible in this model, in contrast to all the previous models, where they were assumed rigid. A numerical experiment is performed to ascertain the applicability and robustness of the developed identification algorithm on the basis of two discs cracked rotor with flexible supports and an AMB support. The transverse crack and disc unbalance parameters, AMB stiffness constants and support dynamic parameters are identified and the algorithm found to be robust against the moderate signal noise and modelling errors.

The work reported in this dissertation concentrates principally on the analysis and fault parameter identification aspect of rotors with AMB support as opposed to the analysis where AMB is used as an external exciter to magnify the symptoms of the fault. The faults addressed in the present work are – the unbalance and a transverse crack. The analysis and identification plans reported has scope in the design stage of smart machine development and of applicability in field as well as.

TABLE OF CONTENTS

LIST OF FIGURES

LIST OF TABLES

LIST OF SYMBOLS

$\mathbf{A}$	Regression matrix
$\mathbf{b}$	Regressand or known vector
c	Viscous damping
$\mathbf{C}$	Damping matrix
$\mathbf{D}_{1,2}$	Sub-matrices
e	Disc eccentricity
E	Young's modulus of elasticity
$\mathbf{f}$	Force vector
$\mathbf{G}$	Gyroscopic matrix
h_{ij}	Intact shaft flexibilities
Δh_{ij}	Additional flexibility in the i^{th} direction due to forcing in the j^{th} direction
$\Delta\mathbf{H}$	Local flexibility matrix at the crack section
i	Current
$i=-n,..,0,1,..+n$	Integer showing number of the harmonic component
I	Area moment of inertia
I_i	i^{th} harmonic of complex current
$\mathbf{I}$	Identity matrix
Im	Imaginary part of
$\mathrm{j} = \sqrt{-1}$	Imaginary number
k_{ij}	Direct and coupled shaft stiffness terms
k_s	AMB force-displacement constant
k_I	AMB force-current constant
K_P, K_I, K_D	PID controller proportional, integral and derivative gains

m	Disc mass
$\mathbf{M}$	Mass matrix
n	Real number
$\mathbf{q}$	Displacement vector
R_i	i^{th} harmonic of complex displacement
$\mathbf{T}$	Overall rotational transformation matrix
s	Periodic, time-varying crack switching function
t	Time
Δt	Sampling time
$\mathbf{u}$	Vibration displacement vector
x	Response direction perpendicular to the crack front
$\mathbf{x}$	Intercept or unknown vector
y	Response direction along the crack front
oxyz	Inertial frame of reference for the system
$Cxyz$	Inertial frame at the disc position
$\dot{}$	First order time derivative
$\ddot{}$	Second order time derivative
$\times$	Order of the frequency
∞	Infinity

Subscripts

0	Corresponding to intact shaft
AMB	Due to AMB
central	Central frequency of the spin-speed range
cr	Due to crack

cu	Due to current only
d	Diametric
i	i^{th} co-efficient of the force or displacement
m	Master DOFs
rot	Rotating frame
s	Slave DOFs
st	Due to the static deflection
unb	Due to the unbalance
x	Along the x -coordinate axis
y	Along the y -coordinate axis
z	Along the z -co-ordinate axis
ξ	Along the ξ -co-ordinate axisg
η	Along the η -co-ordinate axis
ξz	Plane of the moment
ηz	Plane of the moment

Superscripts

d	Dynamically reduced system matrices
int	intact shaft
T	Transpose
x	Along the x -coordinate axis
y	Along the y -coordinate axis

Greek

α	Angle of the tilt
β	Phase angle between the crack front direction and the unbalance
δ_x	Static deflection
φ	Transverse rotational displacement
Φ	Complex rotational displacement
ω	Spin-speed of the rotor
θ	Phase of displacement harmonic output by FFT
ϕ	Phase of current harmonic output by FFT
Ψ	Phase of reference signal used for phase correction

Abbreviations

AMB	Active Magnetic Bearing
FFT	Fast Fourier Transform
Im	Imaginary part of
Re	Real part of
SIF	Stress Intensity Factor
SCEF	Switching Crack Excitation Function

CHAPTER 1

Introduction and Literature Survey

1.1 Importance of Study

Rotating machineries are important components of the industrial world, since every manufacturing, transport and power generation facility greatly relies on them. Rotating machinery, like all other machines, have finite life spans. They degrade due to the fatigue, overloads, wear, corrosion and erosion. The degradation continues until they are no longer fit for their intended use or their operation involves hazardous situation. Of all the parts that form the ensemble of rotating machinery, the shaft is the most critical component as it transmits power. Apart from degradation to the rotating machine as a whole, rotor shafts endure multiple faults, such as, the unbalance, cracks, misalignment, looseness, rub or bow during its operation. The machine failure because of any of these faults would result in a compromise with the safety, increase of downtime and mounting maintenance costs.

Fatigue cracks account for the most common form of loss of structural integrity of rotating shafts. However small the crack be, once appeared, high stress intensity factor (SIF) at the crack tip leads to its rapid growth and ultimately the failure of the shaft. Fatigue cracks may go undetected in initial phase of its propagation and lead to catastrophic damages. Hence, a continuous assessment of health of the rotor for the crack formation and propagation is necessary for its safe and economically profitable operation.

For the continuous health monitoring of industrial appliances, many techniques are applied. Some of them are (Randall, 2011; ASTM D6595-00, 2011; Robichaud, 2003; Nowicki, 2004)

- Vibration condition monitoring and diagnostics
- Lubricant and oil analysis
- Acoustic and ultrasound emission
- Infrared thermography
- Motor current signature analysis
- Characterization techniques including the visual inspection, die penetration test, scanning electron microscopy, atomic force microscopy and wear debris analysis

.

For greater reliability and better performance of rotating machinery, apart from health monitoring of rotors, quest continues for the best combination of speed, power, compactness and service life. Active Magnetic Bearings (AMBs) are the recent mechatronics import to the field of rotating machinery, promising greater speeds, life and durability. AMBs support the rotor without any physical contact, the load is borne by the continuously varying magnetic field. Thus, AMBs are seen as an attractive replacement for conventional bearings due to their unique feature of active vibration control. Since AMBs can be used as a source of non-contact external excitation, their application in health monitoring of rotors is an active area of research (Schweitzer and Maslen, 2009).

The objective of this dissertation is to present a framework for the identification of a crack in rotors supported with an AMB as an auxiliary bearing (in additional to conventional bearings). A wealth of literature exists on the identification of cracks in structures, rotors in particular. However, very few papers are available on the crack identification with the active control of rotors,

in particular rotor integrated with AMBs. In following sections, a literature review is presented; it is organized in five parts as: review on the condition monitoring, crack modelling, crack identification, experimental studies on crack identification and crack identification in AMB integrated rotors.

1.2 Condition Monitoring of Rotating Machinery

Condition monitoring is a continuous study of various machine parameters related to the operational and structural conditions of the machinery. It helps to judge whether the machine is in satisfactory or deteriorating mechanical conditions, which could prevent otherwise unforeseen damage. Condition monitoring is a strong tool to assist the maintenance crew to shift from the schedule based maintenance to the Condition-Based Maintenance (CBM strategy), where the machine condition is continuously monitored to predict the breakdown and an optimum maintenance is carried out (Randall, 2011). Since, the schedule based maintenance may overlook some of deficiencies in the machine condition and overemphasize some less critical components due to its very intrinsic nature of being schedule based; such a maintenance strategy is neither cost effective nor scientific. Exact financial incentives of the CBM is very machine and service specific, nevertheless a translucent idea of stakes involved can be had from some of the published reports (Bayoumi et al., 2008).

Condition monitoring being a vast field of research has attracted researchers in different disciplines and contexts. Many different faults and fault identification methods have been studied and documented. Common rotordynamic fault signatures include the self-excited vibration due to system instability, vibration due to externally applied loads; such as the cracked and bent shafts, and mass unbalances. Early studies on the vibration-based condition monitoring in rotating systems has been carried out by Stewart (1976) along with ways to process the measured data for

the fault identification. Downham (1976) compiled case-studies for faults such as the turbine blade failure, and the gear and bearing wear. Iwatsubo (1976) considered possible errors occurring in vibration analysis, and their implications on calculation of critical speeds, instabilities, and unbalances. He concluded that errors in bearing dynamic coefficients have a much larger effect on the variance of system instability than do errors in the mass and stiffness terms. Smith (1980) discussed the basics of fault recognition from their vibration characteristics. Thomas (1984) outlined a vibration monitoring strategy for large turbo generators. Bearing defects were studied by McFidden and Smith (1984), giving insight into the vibration spectra.

Hill and Baines (1988) discussed the design of an expert system for the analysis of measured data, which consists of computer algorithms simulating a human expert. It was concluded that an expert system approach to the vibration monitoring may be advantageous provided detailed design of the system is taken care of. He et al. (1990) presented a method for identifying the shaft rub. Principal components and autoregressive spectra technique (PCAT) was used to identify coloured noise due to the shaft rub in large machinery. Works of Taylor (1995) supplement the work of previous researchers. Childs and Jordan (1997) concluded that a clearance at the location of rub improves the system stability. Lee and Joh (1994) developed directional frequency response functions (dFRFs) to identify the support anisotropy and the shaft asymmetry.

For a systematic damage identification procedure, Rytter (1993) envisioned four steps of damage identification, as follows

- Step 1: Identification - Determination that damage is present in the structure
- Step 2: Localization - Determination of the geometric location of the damage

- Step 3: Sizing - Quantification of the severity of the damage
- Step 4: Prognosis - Prediction of the remaining service life of the structure

Step 4 of the above procedure relies heavily on fracture mechanics, fatigue life analyses, or structural design assessments and, as such, not addressed in the structural vibration or modal analysis literature. Steps 1 through 3 are most often directly related to the modeling and structural dynamics testing, and could be achieved with model based inverse methods.

Standardization of procedures and terminology used in any field of practice helps that particular field, by facilitating flow of information and ideas by making possible the cross laboratory reproduction and verification of new ideas and results. Isermann and Balle (1997) presented a short overview of the historical development of model-based fault detection, as well as suggestions for standardizing the fault-detection terminology. Basic terminology was provided in contributions to IFIP (International Federation for Information Processing, 1983), in the RAM (Reliability, Availability and Maintainability) dictionary (1988), and in German standards such as DIN standards and VDI/VDE-Richtlinien. Glossary of terms used in the RAM practice is also available in some NASA standards like NASA-STD-8729.1 (1998).

The key idea in the paper by Isermann and Balle (1997) was the classification of detection methods. Based on process parameters, model-based methods were classified as: (i) the state and output observers (or estimators), (ii) parity equations, and (iii) the parameter estimation. Based on the measurement of output response signals, the classification was as: (i) band–pass filters, (ii) spectral analysis, and (iii) maximum–entropy estimation. If features from the fault detection show a stochastic behavior, the classification is as: (i) mean and variance estimation, (ii) likelihood-ratio

test, and (iii) run-sum test or two-probe *t*-test. Classification methods were used when several symptoms change differently for certain faults. Classification methods are: (i) geometrical distance and probabilistic methods, (ii) artificial neural networks, and fuzzy clustering. If more information about relation between symptoms and faults was available, reasoning methods were used such as: (i) probabilistic reasoning, (ii) probabilistic reasoning with fuzzy logic, and (iii) reasoning with artificial neural networks. It was concluded that the parameter estimation and observer based methods was the most frequently applied methods for the fault detection. In most applications, the fault detection was supported by the simple hypothesis testing and the fault isolation was carried out using neural networks.

As reported in Doebling and Farrar (1996, 1998), it could be inferred, as of 1996, all the damage identification methods available were largely visual or localized methods, which required a prior knowledge and accessibility of the damage location. The need for global damage identification methods that could be applied to complex structures led to the development of methods that examined the vibration characteristics of the structure. Steps of the damage identification were defined in line with Rytter (1993). Frequency shifts were the earliest and widely studied methods for the damage detection, studied and used by many researchers. An exhaustive listing of references is presented in a survey article by Salawu (1997). Due to the nature of its operation, non-local techniques are important for rotating machinery. Edwards et al. (1998) provides a broad review of the state of the art in fault diagnosis techniques of rotating structures. They concluded from several past works that model-based methods were the heart of fault diagnosis. Among model-based methods, the observer based fault detection methods were widely used. Vibration based model−dependent techniques are also discussed by Zou et al. (2000) from the perspective of composite structures.

Robustness is one of the key traits desired in any fault identification process; to minimize extra losses on account of false alarms as well as on account of underestimation of damages. Patton (1997) discussed the robustness issues in the model-based fault detection and isolation. In this context, the robustness is defined as capability of the identification process to provide a rapid and reliable detection and isolation of system faults when the plant (or process) under control is disturbed, and when the mathematical model upon which the diagnosis is based cannot fully reproduce the dynamics. The quantitative model based fault detection uses a dynamic model of the system to generate estimates of the measured and unmeasured variables of the system. The estimates are compared with actual measurements thereby generating error signals known as residuals. Quantitative models used for the fault detection are generally linear, using either time or frequency domains. However, known non-linear equations of a physical system were also used. The most common model-based methods use state-space observers or Kalman filters. The residual generation and decision making are its main steps.

As mentioned by Tarantola (2005), the scientific study and analysis of any physical system essentially involves the following three steps

- Parameterization: defining the smallest set of model parameters whose values will completely characterize the system
- Forward modeling: formulation of relations based on physical laws, to make predictions on results of measurements on some observable parameters, for given values of model parameters
- Inverse modeling: use of results of some measurements of observable parameters to infer actual values of model parameters

A review of inverse methods used in the damage identification was made by Friswell (2007). Generally, inverse methods are based on an initial model of the structure and measured data are used to refine (or update) the model. Model updating techniques have been broadly classified as sensitivity methods and direct methods. Sensitivity methods allow a wide choice of physically meaningful fault parameters. It aims at minimizing, the error between measurements and model predictions, generally termed as a penalty function. One of the problems identified with the sensitivity method is that changes in measurements between the damaged and healthy structures/machines may be much smaller than those observed between the modelled and healthy structures/machines. To overcome this lacuna, the model updating with the measured data could be done. As the model gets consistently enhanced over time, the understanding of the system is expected to get better and the model can, thus, address more complicated issues. On the contrary, direct methods reproduce the measured data by updating the whole mass or stiffness matrices.

The modelling error is a common problem in the damage identification; it requires suitable parameters to be included for undamaged model errors. The use of finite element model updating as suggested in Friswell and Mottershead (1995) or the use of difference of responses between the damaged and undamaged models as reported in Parloo et al. (2003) reduce modelling errors. The environmental and non-stationary effects, nonlinearity, and the operating frequency range also present problems in the damage identification. Since inverse approaches rely on a model of the damage, the accuracy of the estimation depends on the accuracy with which the model replicates the true physical phenomena.

Literature indicates that quantitative model-based methods are preferred in comparison to sensitivity based methods, which minimize the error function between the computed and measured

modal data; or classifier methods such as the probabilistic, neural network or fuzzy logic. Estimating damage parameters using the model-based identification has advantages of using the model further for the quantification as well as for the prognosis. For a good expert system, a detailed design of the system is to be taken care of. Available literature also emphasizes the need for addressing modeling errors for a successful model based condition monitoring scheme.

1.3 Crack Modeling

Fatigue cracks may arise in rotors due to asymmetry in the geometry, stress concentration (such as keyways, threads and notches), mechanical faults, and thermal stresses as in the steam and gas turbines. Different types of cracks such as the transverse, slant, and helical cracks have been reported. Bachschmid et al. (2010) have listed some of the occurrences since 1953.

Of a variety of methods in practice, according to a review by Sabnavis et al. (2004), methods for the crack identification can be broadly divided into three groups as: the model and signal based methods, modal testing methods and non-traditional methods. In signal-based methods, the vibration signature of the machine is compared with that of a reference signature, taken when there was no crack in the shaft. The signal based condition monitoring can be further improved by the spectral analysis (fast Fourier transformation (FFT), frequency response function (FRF), full-spectrum analysis, and time-frequency analysis) to obtain more information and features. While most of spectral tools are mathematical manipulation processes to visualise hidden features in signals, the full-spectrum analysis provides a glimpse of physical behaviour of the rotor motion characterized by the forward and backward whirls. Need of authentic and accurate machinery condition data from the past, is a prerequisite and thus a bottle neck in this monitoring strategy. On the other hand, model-based methods are based on the analytical or numerical models. They simulate the behaviour of cracked shafts during the operation and attempt to correlate the observed vibration signature with the

presence of a crack at discrete locations on the shaft. Model based methods have added advantage of being suitable for the simultaneous identification (i.e., the detection and quantification) of many other faults. The spectral analysis enhances the applicability of this method. In the modal-testing, changes in system modal characteristics such as changes in mode shapes and system natural frequencies are used for the identification of cracks. Genetic algorithms, neural networks, fuzzy logic along with signal-processing techniques such as the wavelet or Hilbert transforms outline non-traditional methods for the crack identification.

For the model based identification in rotors, an accurate mathematical modeling of faults to closely represent the dynamics of the system in the presence or absence of the said fault is of the primary importance. When the crack identification is the goal, the principal focus should be to model the crack to represent its true dynamics. Cracks present in rotating heavy shafts with the horizontal axis has two peculiarities in comparison to cracks in stationary structures

- The crack related vibration is naturally excited (due to inherent gravity and unbalances) by the rotation of shaft, the external forcing is required in stationary structures to excite vibrations.
- The crack opens and closes periodically during the revolution of the shaft, independent of vibration. This phenomenon is termed as the breathing of the crack. In stationary structures the opening and closure of the crack is a function of the applied force.

The geometry and orientation of cracks greatly influences the dynamics of the cracked rotor. Based on the geometry and breathing mechanism cracks are categorized as (Sabnavis et al., 2004)

- *Transverse cracks*: These are cracks perpendicular to the shaft axis. These are the most probable (thus common) and serious as they reduce the cross-section and thereby weaken the rotor.
- *Longitudinal cracks*: Cracks parallel to the shaft axis are known as longitudinal cracks.
- *Slant cracks*: Cracks that are at an angle to the shaft axis are known as slant cracks.
- *Open cracks*: Cracks that always remain open are known as gaping or open cracks. They are more correctly called notches. Open cracks are easy to reproduce in a laboratory environment and hence many experimental work reported in literature is focused on this particular crack type.
- *Breathing cracks*: Cracks that open when the affected part of the material is subjected to tensile stresses and close when the stress is reversed; are known as breathing cracks. The breathing of crack results in the non-linearity in the vibrational behavior of the rotor. Due to their direct practical relevance, the most theoretical research efforts are concentrated on "transverse breathing" cracks.
- *Switching cracks*: A subset of the group of breathing cracks that are either completely open or completely closed at any given time are called switching cracks.

The breathing is typical to cracked rotating shafts, the rotation of shaft governing the transition from the open to closed states of the crack. The full shaft stiffness is available in the closed crack situation and the reduced stiffness in the open crack situation. The mathematical modeling of a crack involves three main factors: the stiffness, damping and nonlinearity. The stiffness and non-linearity have been addressed by many researchers. Few papers discuss accommodation of other factors such as: thermal effects (Bachschmid, 2004) and damping (Wauer, 1990a) in the crack modeling. A crack, particularly breathing and switching cracks, can produce complicated

dynamics. However, the nonlinearity introduced by the crack is generally weak (Friswell, 2002) thus can be safely ignored without compromising the exactness of the model.

Among the initial literature dealing with the crack modeling, bending vibrations were only studied, by utilizing the fracture mechanics approach to calculate the loss of stiffness due to the crack. Simple models were used for the breathing mechanism. The main idea of most of these papers was to model the crack with a 6×6 (or less) flexibility matrix (Wauer, 1990b).

The direct stiffness reduction formulation is mainly used to model the crack where the stiffness of a complete element is reduced to simulate a small crack. This approach has problems in matching the damage severity to the crack depth. In an attempt to find the closed form solution, some researchers tried to formulate the stiffness along the rotor axis by an exponential function. For instance, the work of Christides and Barr (1984) is based on this concept, wherein the exponent is to be determined experimentally. This theory is an important step for the generation of a rigorous closed form solution of dynamics of cracked beam. However, in analyses based on the FEM, such a formulation would prove numerically expensive simply because the stiffness needs to be calculated for each element. Sinha et al. (2002) simplified the formulation by a triangular reduction in the stiffness. They assumed the stiffness reduction to be zero everywhere except around the crack, where the stiffness would reduce linearly to a value and then increase linearly back to its normal value thus forming a triangle. Also, the need for determination of the exponent of the stress field experimentally, limited the applicability of method adopted by Christides and Barr (1984) to general structures.

Nelson and Nataraj (1986) modeled a shaft with the breathing crack using finite element methods. A periodic switching function represented by a Fourier series was incorporated into the model to account for the actual opening and closing of the crack. The function had a value of one for open and zero for closed condition of the crack. They noted that the sign of minor axis for each harmonic was dependent on the shaft speed. This means that as the shaft speed varies, the harmonics experience reversals in the direction of whirl.

Jun et al. (1992) developed a crack model based on the traditional fracture mechanics theory. This model used only direct stiffness terms, which meant- the crack could only be fully open or fully closed. However, it's intuitive that, there must exist a period of time (however small) when the crack is only partially open. The cross-coupled stiffness matrix therefore more adequately represents a breathing crack. Fracture mechanics allows the development of a continuous cracked beam theory without need for the stress field. A continuous cracked rectangular beam theory was developed by Chondros and Dimarogonas (1998) for an open crack and later for a breathing crack . In these works, fracture mechanics methods were used to model the crack as a continuous flexibility in the vicinity of the crack region by utilizing the displacement field.

The crack modelling based on the discrete spring (hinge model) approach envisions dividing a structure into two parts that are pinned at the crack location and the crack is simulated by the rotational and torsional springs. Gasch (1993, 2008) analysed dynamics and stability of a Laval rotor using a simple hinge model. The system equations of motion were derived and linearized using the assumption of weight dominance, which was valid even in the unstable ranges of rotation. His approach introduced only one fault parameter, namely, the additive stiffness due to crack. Since weight dominance was assumed, only the static deflection of the rotor system

determined the crack opening/closing and not the vibration displacement. The ratio of cross crack flexibility to main crack flexibility (in the direction perpendicular to the crack front) as a function of the crack depth was presented, on the basis of which the cross−flexibility was neglected. Square wave was used as a switching function and the crack stiffness matrix was obtained as a transformation of the crack flexibility matrix defined in a rotating co-ordinate system. The stability using the Floquet analysis was studied. Forced vibration responses due to the crack and unbalance forces was studied. Complex responses in time and frequency domains were discussed. The author suggested the spectral analysis (or trend analysis) over long periods where regularly increasing amplitudes of 1×, 2×, and 3× frequency components could be monitored as possibilities for the crack identification.

Friswell and Penny (2002) compared various crack modeling approaches for the structural health monitoring. Common methods of the crack model were broadly classified as the local stiffness reduction, discrete spring models, complex FEM models, and the bilinear breathing crack model. Mathematical models are particularly required for the identification of the crack depth and the location using inverse methods. They considered finite element models based on these approaches for an open crack and a breathing crack. For the open crack, two FEM models one with beam elements and other with plate elements were compared. Also, the crack element was modeled both as a reduction in stiffness elements and as a rotational spring at which a node was placed. The reduced stiffness was obtained using the Christides and Barr's (1984) continuous system approach for a cracked beam. Also, the flexibility matrix based on fracture mechanics approach suggested by Lee and Chung (2001) was used. The percentage change in natural frequencies for a damaged beam was observed using different methods. Experimental natural frequencies were also compared based on Rizos et al. (1990). The paper demonstrated that for the structural health monitoring

using the low frequency vibration, simple models of crack flexibility based on beam elements were adequate. Similarly, a bilinear stiffness model for a breathing crack was studied and the method was observed to estimate the crack location.

Apart from transverse cracks in simple loading conditions, other crack forms and more complex loadings conditions have been studied; for instance - Darpe et al. (2004) studied the coupled bending, longitudinal, and torsion vibrations of a cracked rotor. The stiffness matrix of a Timoshenko beam was modified to account for a crack with all six degrees of freedom (DOFs). The coupling of longitudinal and torsional vibrations was studied in this work. The model incorporated coupling between all three modes of vibration. The additional stiffness matrix due to crack was derived based on the strain energy associated with the crack. The concept of crack closure line (CCL) was introduced, to correlate the crack flexibility variation with the amount of crack opening. The variation of crack flexibility coefficients was obtained as a function of CCL.

Darpe (2007) presented a finite element model of a rotor with a slant crack. Influence of orientation of the slant crack on stiffness values was investigated and the flexibility matrix was derived by taking into account the orientation. It was shown that, in comparison with transverse cracks, slant crack stiffness matrices had additional cross-coupled stiffness terms. Also, cross-coupled stiffness values were larger for the slant crack, which led to a stronger cross-coupling in bending-torsional-longitudinal vibrations compared to the pure transverse crack.

Multiple cracks appearing on a single shaft has also been investigated. Singh and Tiwari (2010) studied the multi-crack identification in the shaft system using transverse response functions. The Timoshenko beam theory was applied to model the beam with multiple cracks using finite element

methods. Two cracks were modeled as flexibility matrices based on the fracture mechanics approach. An external force excitation was considered in the vertical direction. Assembled system equations of motion were obtained in frequency domain. An algorithm was formulated for identifying location of cracks based on change in the elastic shaft curvature. The difficulty of this method was the effect of noise on the curvature measurement, which was reduced by measurements at several frequencies. A number of axial measurement locations were chosen. Deflections at three consecutive axial positions were selected to find out coefficients of the quadratic polynomial between them, which was proportional to the curvature of the shaft. Polynomial coefficients from the cracked shaft were normalized with coefficients from that of the intact shaft. Coefficients were further compressed to a range between 0 and 1. A Crack Probability Function (CPF) was defined as absolute distance of these coefficients from their mean. Numerical simulations were conducted to identify the initial number and location of cracks, by plotting the variation of coefficients against measurement locations. Cracks were located by high values of the CPF. In order to identify the actual location and size, an optimization algorithm was designed. It was concluded that the algorithm using the normalized polynomial coefficients had advantages over other algorithms in cancelling the effect of stepped shafts.

A realistic modeling of crack necessitates an accurate representation of the breathing mechanism. Bachschmid et al. (2008) introduced an approach for calculating the accurate breathing mechanism of the crack in a cracked rotor. In their approach a linear stress/strain distribution was assumed at the crack location to approximate the actual breathing of the crack that was found via three-dimensional nonlinear finite element calculations. An excellent agreement was found between the simplified linear model and the nonlinear finite element model for determining the accurate breathing mechanism of the crack. Even though the approach was highly accurate, no

mathematical formulas of the breathing mechanism were introduced. To be of practical importance, it is necessary to introduce breathing functions that closely approximate the actual breathing mechanism of the crack where the time-varying stiffness matrix can be formulated and incorporated to the linear time-periodic equations of motion of the cracked rotor system.

Al-Shudeifat and Butcher (2011) proposed breathing functions for the transverse breathing crack of the cracked rotor system. A linear stress/strain relation was assumed in the crack location to formulate the actual crack breathing. As the shaft rotates, locations of the centroid and the neutral axis of the cracked element change with rotation. The breathing was formulated by using the constant area moment of inertia of the cracked element and the time varying area moment of inertia of the crack. For each time step, after the crack starts to close, new values of the area and the area moment of inertia are calculated based on which the centroid location is updated. Based on this, a finite element stiffness matrix was derived. The finite element system equations of motion were solved using the harmonic balance method. A shift in the critical and subcritical speeds was observed. The exact critical and subcritical speeds, and their shift due to increase in the crack depth were obtained from the waterfall plots. There was also appearance of orbits with two and three outer loops, during passage through the first subcritical forward and backward whirls, respectively. These orbits were observed within the static deflection range for a relatively high unbalance force. Theoretical results were in agreement to experimental results performed on a rotor kit.

Ebrahimi et al. (2014) developed a continuous model for the flexural vibration analysis of a rotor with an open edged crack. Models developed by Behzad (2008) were modified for obtaining the displacement and stress fields in two directions. The Hamilton principle was used to obtain the

system equations of motion as a partial differential equation. The solutions for an open edged crack were obtained using Galerkin methods and then compared with finite element model results.

In fields other than rotor dynamics, differing approaches to model cracks may be used, to suit the application and analysis. For instance, Fu (2015) modeled switching cracks appearing in beam bridges, by means of a crack disturbance function designed to represent the variation of the response or the stiffness around the crack region. Its parameters could be estimated by experimentation or by use of fracture mechanics methods.

From literature, it is apparent that the most commonly the crack is modeled with the flexibility matrix based on the fracture mechanics approach. This approach has the benefit of ease of defining the form of flexibility matrix, the coefficients of which can be theoretically evaluated from the stress intensity factor. Various models have been used, such as, the local stiffness reduction, spring models, FEM models, bilinear switching functions, continuous cracked beam models, equivalent loads and the reduction of second moment of area. Crack models are mostly based on the increase in the flexibility at the cross-section due to occurrence of the crack. Coupling effects due to the crack have also been studied. Use of an accurate breathing mechanism of the crack is crucial for the realistic representation of dynamics of the cracked rotor; literature suggests use of a square waveform for the crack breathing suffices for the analysis of rotors with shallow cracks. In the next section, a review on crack identification methods is presented.

1.4 Crack Identification in Rotors

There has been a wealth of analytical, numerical and experimental investigations on cracked rotors. Many techniques have been proposed, of which, some have been applied on industrial

systems. Most of these techniques are based on Non Destructive Evaluation (NDE). A reliable NDE method is always preferred to DE due to it involves, at least, disassembling of structures which is very undesirable due to associated down time and lost production costs and sometimes not feasible (for example, a propeller shaft of a ship in the high sea).

NDE techniques can be broadly classified as: the local and global methods. Local methods pose the requirement of knowledge of the vicinity of the potential damage and give no indication of the rotor health at a system level. These shortcomings indicate a requirement of damage inspection techniques that can give global information on the structure. For global techniques, the measurement and identification of the system's health is not necessarily correlated with the physical location of damage. The most popular global techniques are Vibration-Based (VB) analysis, further classified into three approaches, viz. the signal and model based, modal properties based and other advanced machine learning methods (Basseville, 1999; Mevel et al., 1999), commonly referred as non traditional methods.

1.4.1 Signal Based Approaches

In signal-based methods, steady-state and/or transient vibration data are measured and analysed for known indicators of damages. These methods are heuristic in nature since the basic approach of these methods is to develop feature vectors from the acquired data (or signal) using signal processing techniques. They are not based on any specific physical or analytical treatment of the system. For the shaft crack detection, many authors like - Bently and Muszynska (1986a), Sanderson (1992), Lazzeri et al. (1992), Werner (1993), Ishida et al. (1995), Saavedra and Cuitino (2002) and many others have tried to interpret 1×, 2× (and so on) components of the signal in frequency domain. There is much debate about which component gives better indication of the

crack. A fair compilation and comparison of these methods was presented by Sabnavis et al. (2004). Zhang et al. (1999) came out with another signal-based method of computation of transmittance functions. Transmittance functions can be computed from different measured responses using broadband excitations. This method is unique in the sense that no system model is used and the excitation is not measured either.

Recent research considered more advanced tools such as wavelet transform, neural networks, Wigner-ville distributions, fuzzy logic and genetic algorithm. Among these, the wavelet transform is the most popular one. In an experimental study, Adewusi et al. (2001) used the discrete wavelet transform (Db6 mother wavelet) for an overhang rotor with a propagating transverse crack. They concluded that the crack reduces the critical speed of the rotor system and the vibration amplitude of frequency scale level corresponding to 1× may increase or decrease depending on the location of crack and the side load. However, the amplitude of frequency scale level corresponding to 2× increases continuously as the crack propagates.

Although signal-based methods are easy to implement, the implementation lacks a sound theoretical basis. As a result, a choice of feature that works well for one system may not work well for another. The quantification of damage may also suffer.

1.4.2 Model Based Approaches

Model-based methods are based on the analytical treatment that deals with the modelling of system. In principle, these methods are very general in the perspective that changes of any number of system parameters can be detected. Also, as the model gets consistently enhanced over the time,

understanding of the system gets better; so, the model can be used to address more complicated issues.

By now, it is well established that the crack in a structure introduces local flexibility, which causes a change in dynamics of the structure. This makes possible the formulation of an inverse problem based on changes in modal parameters and the free and forced responses of the structure. In dealing with cracked rotors (as opposed to structures in general) a more accurate model is needed which considers: the coupling between different motions such as the bending, longitudinal, and torsional vibrations, the splitting of natural frequencies due to the presence of a crack, the nonlinearity in stiffness due to the breathing, and the friction between cracked surfaces. These phenomena are key features for the crack identification and explored by several researchers for the purpose. Also, a rotor crack opens and closes with the shaft spin. When the crack is fully closed, its local stiffness is maximum, and when the crack is fully open, its local stiffness is minimum. At other positions, the crack is partially open. This opening/closing mechanism generally distinguishes a rotor crack from other structural cracks, hence a pivotal feature of modelling a rotor crack.

Dimentberg (1961) studied the rotation motion of an asymmetric shaft center. The motion was the sum of two vectors, one that turned at the angular velocity of the shaft and the other that turned at twice that angular velocity. Result was an elliptical orbit characterized by relative lengths of two vectors. This was because the shaft crossed two limiting stiffness twice during one revolution. The shaft would rest at a higher position when the stiffness was more and vice a versa. This oscillation caused the 2× component in the frequency spectrum. Since a crack introduces a loss of stiffness in a direction perpendicular to the crack front, analogically, 2× component in the frequency spectrum

was considered a strong indication of presence of a crack in the shaft. Now it is known that the bearing misalignment could also result in the 2× and 3× components in the spectrum.

Dimarogonas and Papodopoulos (1983) presented an identification method for an open crack. It was shown that due to coupling of lateral and longitudinal vibration, a surface crack on a rotating shaft can display a variety of unstable regions of operation. This coupling could be attributed only to the existence of cracks and hence used for crack identification. It can also supplement the utilization of twice the speed of rotation and half the critical speed signals in the process of crack identification.

Gounaris and Dimarogonas (1988) derived a model of a cracked prismatic beam based on the finite element for structural analysis. The crack was modeled using a crack flexibility matrix based on principles of fracture mechanics. The crack stiffness matrix was obtained as an inverse of the flexibility matrix. However, for small cracks, the entries in crack flexibility matrices are very small and consequently entries in stiffness matrices are larger. Solutions based on such matrices are not reliable as they lead to numerical ambiguities during the solution generation such as singular matrices. To overcome this, authors developed the stiffness matrix for a cracked beam element, based on transfer matrices and shape functions. Numerical results showed discontinuity in the slope of beam at the location of crack.

Many later researchers like Liang et al. (1992), Capecchi and Vestroni (1999) and Hasan (1995) have utilised the local flexibility based analysis for the identification of cracks in rotors and other structures. Based on the principle of local flexibility, Sehkar et al. (1994, 1997 and 1999) used FEA for the identification of transverse, slant crack and multiple cracks, respectively.

The size of the damage is one of the important considerations in the crack identification exercise. Pandey et al. (1991) used the finite element analysis to obtain relationships between the changes in eigen-parameters, the damage location and the damage size. A parameter, namely the curvature mode shape was investigated as a possible candidate for identifying and locating damages in the structure. Absolute changes in curvature mode shapes were observed to be localized in the region of the damage and hence used to detect damage in the structure. The change in the parameter increased with the increase in the size of damage. Gasch (1993) introduced a perturbation method into his analysis of a linearized crack model with direct stiffness terms. He provided suggestions for the detection of cracks, such as the long-term monitoring of the mean additional static deflection and the trend analysis over long periods. It was suggested that 1×, 2×, and 3× response amplitudes would all increase in the direct proportion to the crack size, thus providing a way to estimate the crack size.

Dharmaraju et al. (2004) used an inverse engineering approach based on the model updating for identifying a crack in a beam. The system equation of motion in frequency domain was reduced to a regression form, containing unknown crack flexibility coefficients in a vector. The problem of excessive number of measurements required for the estimation was overcome by the static (Guyan) reduction scheme to obliterate the need for measurements that are not feasible. An error function was defined in terms of the theoretical and estimated flexibility coefficients, and it was used to determine the crack depth with the help of least-squares technique in conjunction with the bisection root−searching method. The identification algorithm was found robust against a moderate level of measurement noise.

Sekhar (2004a, 2004b) used a crack model based on equivalent loads to identify its depth and location on the shaft. The nature and symptoms of the fault were ascertained using the harmonic analysis implemented with the FFT. It was found that the estimation of crack depth, to a good extent, was dependent on the number of measurement locations. In yet another paper, Sekhar (2004c) used the model-based continuous wavelet transform (CWT) approach to extract sub-harmonics from the coast-down time domain vibration signal from journal locations of cracked rotors supported on fluid–film bearings. The analysis of dissipation through the journal film and evaluation of the deceleration for each speed were the main factors of the coast-down phenomenon studied. The CWT of a time-varying function was defined as the sum over all time of the signal multiplied by the scale shifted versions of the wavelet function. The sub-critical response peaks found in the CWT is useful for detecting cracks even for low crack depths as compared to time response.

The fact that crack introduces coupling between orthogonal flexibilities has been used by some researchers as an indicator of presence of crack in the rotor. Darpe *et al.* (2004) identified the crack from the coupling effect it introduces in the crack flexibility matrix. The intact rotor showed absence of higher harmonic frequencies in the response (indicating presence of unbalance as the only flaw), even under torsional excitation of the intact shaft, no coupling effect was seen in the response of other modes. The response due to the cracked rotor contained 1×, 2× and 3× frequency components in its lateral vibration spectrum; the longitudinal and torsional spectrum showed 1× and 2×, while the torsional spectrum showed addition 4× component. This indicated a prominent coupling mechanism due to the crack. Next, with the crack, an additional harmonic torsional excitation was given, at a frequency closer to the bending natural frequency. An interaction of the torsional and bending frequencies showed the appearance of sum and difference frequencies

around the bending natural frequency. Similar results established the coupling between the torsion and bending vibrations as well as the bending and longitudinal vibrations.

El Arem and Maitournam (2008) developed a cracked beam finite element formulation for studying rotor dynamics in presence of a crack and performing stability analyses. According to them, the bilinear stiffness model of the crack was a simplistic approach that led to some uncertainties about the accuracy of quantitative results stemming from its exploitation. On the other hand, three dimensional crack models were relatively free from the simplifying hypothesis and approximations. The crack stiffness variation was deduced from finite element computations accounting for the unilateral contact between crack lips. They preferred using 3-D (3-Dimensional) FEM models, also as there were hardly any SIF formulas for cracks on cylindrical shafts till that time. The shaft was only considered as an assembly of elemental rectangular strips, which was similar to the FEM software approach. Crack models based on FEM models and beam models were obtained and compared.

Various crack identification methods have been conceptualized, implemented and reported in literature are discussed in this section. The presence of 2× frequency component of the spin speed in the frequency spectrum of the rotor response is considered a strong indicator of the crack. This also causes a sub-harmonic critical speed at half of the system natural frequency. Cracks are also identified from changes in modal parameters such as natural frequencies and mode shapes. Because of the complexity in the crack identification, the trend analysis for increase in 1×, 2× and 3× vibration response amplitudes is suggested. Model-based methods are also used which identify crack parameters such as the crack stiffness, location, and its depth based on an inverse problem approach. 3-D finite element models have also been used for the identification.

A physical system and its model differ on account of DOFs considered in the analysis. Theoretically, physical systems have infinite DOFs. The model can have large but limited DOFs; greater the DOFs considered for the analysis, closer are the model to the physical system. For large size models, DOFs required to correctly describe the system may be computationally intensive on account of the storage and resource exploitation. Model reduction (or condensation) is an efficient technique to reduce DOFs needed to describe the model behaviour. This reduces the computational time and cost drastically, since the number of equations to be solved is reduced with the reduction of DOFs. In many models, DOFs considered for development of the model may not be physically measurable, for instance rotational displacements, due to gyroscopic effects in an offset rotor. In such situations also, model reduction is required such that the model considers only those DOFs that are physically measurable and hence meaningful in the physical system. The condensation scheme is an important aspect of the whole modelling process; a brief review of condensation techniques is presented in the next section.

1.4.3 Condensation Schemes

Model reduction methods remove some DOFs (slave DOFs) of the original model and represent discarded DOFs with retained DOFs (master DOFs). Afterwards, equations of motion of the reduced model are solved for the response of the original structure. The condensation technique in undamped systems was first proposed by Guyan (1965) and Irons (1965). Guyan (1965) reduction scheme is probably the most popular reduction scheme, due to its low computational complexities (Genta, 2005). For applications of this reduction scheme, the deflection and force vectors **q** and **f**, and the mass and stiffness matrices, **M** and **K**, are reordered such as to partition them into separate sub-matrices and sub-vectors related to master DOFs (retained) and slave DOFs (reduced or discarded). Under the assumption of negligible damping, the equations of motion becomes

$$\begin{bmatrix} \mathbf{M}_{mm} & \mathbf{M}_{ms} \\ \mathbf{M}_{sm} & \mathbf{M}_{ss} \end{bmatrix} \begin{Bmatrix} \ddot{\mathbf{q}}_m \\ \ddot{\mathbf{q}}_s \end{Bmatrix} + \begin{bmatrix} \mathbf{K}_{mm} & \mathbf{K}_{ms} \\ \mathbf{K}_{sm} & \mathbf{K}_{ss} \end{bmatrix} \begin{Bmatrix} \mathbf{q}_m \\ \mathbf{q}_s \end{Bmatrix} = \begin{Bmatrix} \mathbf{f}_m \\ \mathbf{0} \end{Bmatrix} \tag{1.1}$$

The subscripts “m” and “s” represent the master and slave coordinates, respectively. Neglecting the inertia term, slave DOFs may be eliminated as follows

$$\begin{Bmatrix} \mathbf{q}_m \\ \mathbf{q}_s \end{Bmatrix} = \begin{bmatrix} \mathbf{I} \\ -\mathbf{K}_{ss}^{-1}\mathbf{K}_{sm} \end{bmatrix} \{\mathbf{q}_m\} = \mathbf{T}_s \mathbf{q}_m \tag{1.2}$$

Though, the Guyan reduction method cannot produce accurate eigen solutions because the effect of mass related to the slave DOFs is not rationally considered when constructing the reduced system matrices (Jeong et al., 2012), the errors introduced is usually very small (Genta, 2005). Any response generated by reduced matrices following Guyan (1965) reduction scheme is exact only at zero frequency; this reduction scheme is also named as the *static reduction*. With increase of the excitation frequency, the inertia term neglected in the reduction process becomes more significant. In very large models, DOFs may be so large that the identification of slave and master DOFs may not be intuitive. Henshell and Ong (1975) suggested an iterative procedure to automate the selection of master or slave DOFs in the static reduction, on the basis of the magnitude of the ratio of elastic to inertia terms. The procedure eliminates one DOF at each iteration.

Leung (1978) developed a method to construct the dynamic reduction matrix more exactly but the dynamic reduction developed by Paz (1984) is regarded a better alternative to the static reduction, in which the frequency at which the reduction is exact, may be chosen arbitrarily. In rotordynamic application, this freedom to choose the frequency of reduction is an advantage – since the reduction may be performed at the frequency of external forcing which in turn is a multiple/factor

of the shaft spin frequency. To perform the reduction to be exact at a frequency ω_0, the reduction transformation is given as

$$\begin{Bmatrix} \mathbf{q}_m \\ \mathbf{q}_s \end{Bmatrix} = \begin{bmatrix} \mathbf{I} \\ -\left[\mathbf{K}_{ss}^{-1} - \omega_0^2 \mathbf{M}_{ss}\right]^{-1} \left[\mathbf{K}_{sm} - \omega_0^2 \mathbf{M}_{sm}\right] \end{bmatrix} \mathbf{q}_m = \mathbf{T}_d \mathbf{q}_m \tag{1.3}$$

O'Callahan et al. (1989) and Gordis (1992) improved the static reduction method through the improved reduced systems (IRS) method, which is approximated up to the first order of a binomial series expansion in the transformation of slave DOFs. Suarez (1992) introduced an iterative scheme for the reduction of system matrices. Friswell et al. (1995, 1998) proposed the iterated IRS (IIRS) method in order to obtain more accurate reduction. The IIRS method repeatedly updates a transformation matrix between the master and slave DOFs through iteration procedures. Furthermore, Xia and Lin (2004) developed an iterative order reduction (IOR) method to improve the computational efficiency. Depending upon the requirements in the numerical analysis and experimental model updating, new condensation schemes are developed, for instance – High frequency reduction scheme for elimination of transverse rotational degrees of freedom in identification of beam crack parameters has been reported in literature (Dharmaraju et al., 2005).

Apart from structural dynamics, the model reduction finds wide applications in the field of numerical mathematics, and systems and control. By and large, developments in the model reduction in one field does not percolate to the other field quickly, rather developments are mostly independent. A review article by Besselink et al. (2013) presents a detailed bibliography of research in area of model reduction in the above three fields and compares the popular methods of three fields against a common benchmark for the accuracy and the ease of implementation.

Modeling yields the maximum gain to the practitioner, if it could be experimentally verified. The experimental verification provides opportunity for the model updating and improvement. While experimental works abound faults like the unbalance and misalignment in rotors, it is less frequent for rotor cracks. Multiple factors contribute to this fact, the most important being, the creation of cracks for performing experimentation on cracked rotors is a complicated task. A review on experimental studies on rotor cracks is presented in the following section.

1.5 Experimental Studies on Rotor Cracks

Fatigue cracks lead structures to catastrophic failures, since in early stage they are difficult to detect and in later stage the growth is too rapid to allow any correction measures to be taken. A spinning rotor under the weight–dominance is a typical candidate for appearance of a fatigue crack. The vibration based detection of fatigue cracks has been a current challenge in the condition–based maintenance. Literature is rich on numerical studies involving the model-based identification of rotor fatigue cracks but few experimental studies have been published. Most of the experimental studies reported in literature involved the study of cracks in form of discontinuities created on the rotor shaft with a hacksaw or EDM cut or welded shaft crack. However, cracks induced by these methods hardly ape the characteristics of a fatigue crack, particularly the breathing behavior. Nevertheless, some recent works in the field are based on fatigue cracks initiated on a three–point bending machine, which are more representative of cracks that a practitioner may come across in the field work.

Gudmundson (1983) reported studies on cross-sectional cracks in beams. Modelling and experimentation was based on a cantilever beam of a rectangular cross section. Two different modeling methods were considered: the flexibility matrix based on static stress intensity factors

and finite element equations. Experiments were conducted with saw-cut edge-cracked cantilever beams, for varying crack lengths and the width of 0.4 mm to simulate a crack in a preloaded beam. In the absence of a preload, the crack would have a closure effect as well. In order to investigate the effect of crack closure on vibrations of a cracked beam, a fatigue crack was introduced in the beam. A signal generator, in conjunction with the ensemble of power amplifiers and a frequency analyzer, was used to induce a continuous sine-sweep in a narrow frequency band around the eigen-frequency. The lowest bending eigen-frequencies in two orthogonal directions were obtained. Eigen frequencies were presented as a function of the crack length. During the crack growth, frequencies were observed to be constant up to a crack-length to width ratio of 0.5 and then they slowly decreased. Measured frequencies deviated from frequencies obtained for an open crack. These observations were attributed to the crack closure effect, where the crack remains closed for small vibration amplitudes due to residual stresses. Theoretical results were observed to be in agreement with experimental results.

The vibration behaviour of a more realistic situation, i.e. a multi-shaft, multi-bearing system in presence of a propagating transverse crack; has a greater relevance to actual machines. A study on this aspect was reported by Mayes and Davies (1984). The crack was modeled as a reduced second moment of inertia of the shaft section. The expression for dynamic bending moment causing the crack opening was considered along with damping forces. The test rig consisted of two solidly coupled rotors mounted on four journal bearings, each mounted on a flexible support. A section of the rotor shaft was machined to have a step with a reduced diameter of 25 mm and notch in its centre. A crack propagated from the notch at a running speed of 2000 rpm. A crack of 6.5 mm was studied. The rig was initially balanced and crack initiated from a transverse slot generated by spark erosion into the center of the reduced section. The crack depth was monitored using the potential-

drop method. Coast-down measurements were considered with the bearing pedestal and shaft-to-bearing vibrations. In order to obtain dynamic stresses at the crack, the shaft was strain gauged on the opposite side of the crack. From the frequency analysis, the crack opening/closing was observed to follow a profile of $(1+\cos\omega t)$ with 1× stiffness variation; where ω the spin speed of the rotor and t is is the time. It was concluded that the dynamic bending moment must be taken into account for fracture mechanics calculations of the crack growth rates when the crack was larger than 1/3rd of the shaft diameter.

Darpe et al. (2003) experimentally investigated coupled vibration responses of a cracked rotor to the periodic axial excitation. From experimental observations, the coupling of longitudinal and bending vibrations was established by the presence of axial excitation frequencies in the spectrum of lateral vibrations. It was also observed that the bending natural frequency could be excited by matching any one of harmonics of the axial excitation frequency, or by matching any of the sum and difference combination frequencies. Findings were suggested for the rotor crack detection utilizing the response of rotor to the axial excitation, particularly during slow roll conditions.

Experimental studies on the nonlinear dynamic behavior of a cracked rotor were reported by Zhou et al. (2005). An artificial transverse crack was seeded in the shaft with a right angled notch and propagated by means of the three-point bending fatigue method. Four shaft specimens were tested, one with no crack, two with fatigue cracks, and one with an open slot. From results, the orbit of the cracked rotor had a clear two-circle topological shape. A correlation was drawn between the speed range in which this character existed, and the crack depth. This phenomenon was absent for an intact shaft. Among frequency components, the second-order was the leading frequency component. When the depth of crack increased, amplitudes of 2× and 3× critical speed components

increased. For the case of disc eccentricity, it was observed that vibration amplitudes may increase or decrease depending on directions of the crack and unbalance vectors. These inherent features of the crack were observed even in presence of disturbances such as the oil film, rub impact and noise. Generally, the energy of higher order components was low; however, in the case of deep cracks, these were predominant and the first-order frequency component was dominant only near the critical speed.

Pennacchi et al. (2006) performed a model-based identification of transverse fatigue cracks in rotors, with methods suitable to applying for industrial machines. A linear cracked rotor model was considered, and the crack breathing was modeled using Fourier series of harmonic components. The FEM was considered and bending moments on nodes of the crack element were calculated. Three different cases of cracks were studied: a slot made by electro-erosion which was representative of an open crack, a fatigue crack initiated from the notch having depth of 14% of the shaft diameter, and a fatigue crack with a depth of 47% of the shaft diameter. The 1×, 2×, and 3× revolution components were primarily observed. The 1× component had additional effects of the shaft bow and the unbalance. For the case of slot, the breathing was absent and only 2× component due to asymmetry in the stiffness was observed. It was used in identifying moments and crack parameters. For the case of fatigue cracks, the position of crack and the relative depth was identified, from 2× revolution component. 1× and 3× components were considered for the identification, only in the case of 47% of the crack depth. In order to obtain the bow induced vibrations, first unbalances on discs were identified, and then the dynamical behaviour due to unbalances only were subtracted from the measured data.

Newer data processing and analysis tools have been applied to identify cracks from the experimental data. Sinha (2007) introduced higher−order spectra (HOS) tools, namely the bi-spectrum and the tri-spectrum, for the identification of crack and misalignment faults in a rotor system. Conventionally, HOS tools were used to detect the non-linear behavior in responses such as for the coupling of harmonic components. The bi-spectrum is the double Fourier transformation of the third-order moment of a time signal. Similarly, the tri-spectrum is the triple Fourier transformation of the fourth−order moment of a time signal. HOS tools classified the crack and misalignment faults, which were important as the characteristic response of both faults. The crack was developed by welding two pieces, which could create the breathing effect. The crack depth was half of the shaft diameter. A change in the orbit behaviour, which is obtained at a speed near half of the critical speed of a cracked rotor, indicated the change in phase and amplitude of 2× component. Then, the misalignment of around 0.5 mm was introduced between two bearing pedestals. From results, a total of four peaks appeared in the bi-spectrum for the crack fault; where as a total of five peaks appeared in the case of misalignment fault. Similar results were obtained using the tri-spectrum, which could classify the crack and misalignment faults.

Karthikeyan and Tiwari (2010) conducted an experimental investigation on the detection, location, and sizing of a structural flaw in a beam, using forced response measurements. A circular beam with an open flaw, supported on ball bearings was used for the set up. The test beam was excited by a harmonic sine-sweep forcing of known amplitude, and the force and displacement responses were measured. The Timoshenko beam theory was considered for system modelling, the open flaw modeled as a 4×4 flexibility matrix. The flexibility matrix for the element with flaw was considered as the sum of flexibility matrices for the intact shaft and the crack. Two algorithms were designed: a crack location algorithm, and a flaw sizing algorithm. For the crack location, the

fundamental natural frequency was calculated as a function of flaw locations, for an initial guess of the flaw depth ratio. Their variation was plotted against assumed flaw locations, and intersections were obtained as flaw locations. In a flaw sizing algorithm, one of the obtained flaw locations was selected to find out flaw flexibility coefficients and the flaw depth ratio. The flaw depth ratio was updated in the flaw location algorithm iteratively, for the convergence of crack location and crack depth ratio. Experimental measurements were correlated with numerically simulated measurements and used to update the theoretical model accordingly. Estimated flaw parameters were found to be in good agreement with the measured data.

Cai (2011) studied vibration based crack detection in shafts. Three different types of transverse cracks were studied, namely, the fatigue crack, the welded crack and the wire-cut crack. Based on experimental results, it was concluded that the fatigue induced crack (by the three-point bending) was the most accurate for representing the breathing of true cracks. The variation of bending stiffness as a function of angle of rotation was studied and indicated that existing switching and harmonic models cannot accurately describe the periodic stiffness of a transverse crack.

Chasalevris and Papadopoulos (2013) used coupled bending vibrations introduced due to the crack for its early detection. The external excitation was provided by means of an AMB. Vibration signals of the vertical response of intact system were subtracted from responses of the shaft with a crack. The Continuous Wavelet Transforms (CWTs) of resulting signals was obtained. For the chosen scale corresponding to the excitation the envelope of coefficients was obtained using the Hilbert transform. Further, the FFT was obtained, which showed a coupled response with a high sensitivity in the 2× frequency component.

Singh and Tiwari (2014) experimentally identified the crack based on algorithms detecting the slope discontinuity. Transverse deflections were measured at regular axial locations of the shaft using a laser vibrometer. External sine-sweep excitation was provided between 1 Hz to 60 Hz. Frequency response functions measurements were obtained, which were used as an input for identification algorithms. For the localization of cracks, crack probability functions (CPF_{vi}) were derived, that gave the probability of presence of crack between the $(i\text{-}1)^{th}$ and $(i\text{+}1)^{th}$ measurement locations along the shaft length.

Shravankumar and Tiwari (2014) estimated crack breathing forces, experimentally. A fatigue crack was experimentally introduced by three-point bending in a mild steel shaft and spun at 44 rad/s to 88 rad/s on the laboratory setup. Force coefficients and displacement coefficients were obtained using the full-spectrum tool. They also developed an identification algorithm to estimate other unknown system parameters, viz. viscous damping and the unbalance.

In this section, literature elaborating experimental works on studies of rotor cracks with particular emphasis on the fatigue crack have been presented. The works of Zhou et al. (2005), Pennacchi et al. (2006), Cai (2011) and Shravankumar and Tiwari (2014) contains information about the rotors with the fatigue crack seeded by 3–point bending procedure and hence more representative of field problems. In the next section, a brief introduction of the Active Magnetic Bearing is presented followed by literature on its application in the rotor crack detection.

1.6 AMB and their Applications in Rotor Crack Detection

AMB is a mechatronic product capable of imparting a stable levitation to a spinning rotor by continuously manipulating the magnetic field between the stationary magnetic poles and the spinning rotor. A schematic construction of an AMB is presented in Figure 1-1.

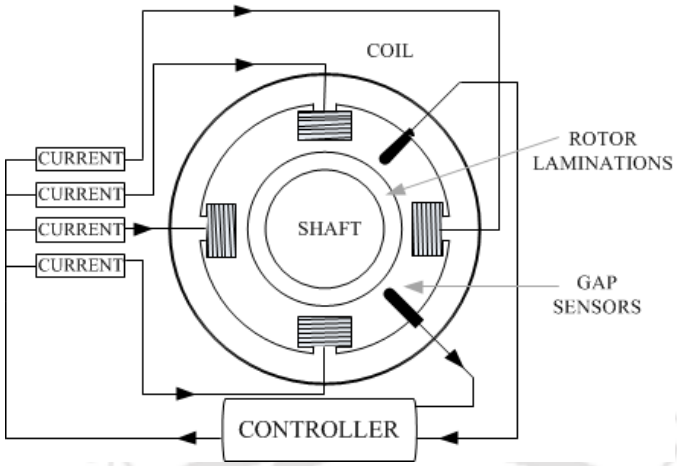

Figure 1-1 Schematic construction of active magnetic bearing

Gap (or displacement) sensors read the instantaneous position of the rotor shaft and pass on the signal to the controller. Based on the control strategy, the controller generates the control signal, which is amplified through a power amplifier to alter the current flowing through magnetic coils. The event occurs in real time, limited by the sampling frequency of the gap sensor thus keeping the rotor at a reference position, any deviation read and corrected, instantaneously.

Need for the lubrication or any surface engineering is completely redundant in the AMB technology. For these reasons AMBs are indispensable in applications like turbo-molecular pumps and vacuum ambience devices, where lubrication is prohibitive and high speeds are the basic requirement. Apart from these two, AMBs find application on wide variety of rotating machinery. Magnetic bearings use advanced control algorithms to monitor the motion of shaft and therefore have the inherent capability to precisely control the position of shaft within microns and to virtually eliminate vibrations. Kasarda (2000) demonstrated the mid–span use of an AMB as an auxiliary bearing or magnetic damper, for the reduction of up to three modes of the rotor synchronous vibration. Additional work by Mendoza (2000) also demonstrated the reduction of

sub-synchronous vibrations such as those resulting from the aerodynamic rotor instability using the magnetic bearing approach. In addition to using actuators as rotor dynamic design tools, they can also be used for the active vibration cancellation.

Hope (1998) demonstrated the use of a feed−forward approach for reducing unbalance forces in a commercial centrifugal compressor supported on AMBs. These can also be used in conjunction with conventional bearings for the weight reduction. In jet engines, the addition of one or two AMBs as additional bearings may add enough stiffness to the system to allow for the reduction of shaft diameters resulting in weight reduction and lower surface speeds for rolling-element support bearings, resulting in longer bearing life (Mendoza, 2000). AMBs can operate in extreme (in terms of temperature, corrosion or pressure) conditions. The magnetic bearing system is capable of operating through an extremely wide temperature range. There are some AMB applications that operate at as low as −256 ^{o}C and as high as 220 ^{o}C, thus allowing operation where traditional bearings will hard to function (Kasarda, 2000).

Active Magnetic bearings (AMBs) are increasingly being used for a large variety of applications like high−speed operations or where oil contamination must be prevented, with limitations imposed by principally valid physical constraints and by the actual state of the art of the control unit. Nevertheless, their unique features (like being contactless, clean, high speed and more efficient control) make them attractive for solving classical rotor−bearing problems in a new way and allow a novel design approache for the rotating machinery. AMB has been used for the external excitation to interrogate rotors which otherwise would not manifest sizeable signals for the fault identification. In such applications, the AMB is used as an actuator, where the bearing

force is modulated for a deliberate excitation of vibrations. The excitation force is applied to the rotor without contact. In addition, it can be precisely measured.

Iwatsubo et al. (1992) proposed that an external force could be used to detect cracks in the shaft of a machine. It was later demonstrated by Ishida and Inoue (2001) that if the applied force is periodic, then the presence of the crack generates responses containing frequencies at combinations of the rotor spin speed and applied forcing frequency. Later, works of Mani et al. (2005) and Sawicki et al. (2009) relied heavily on this concept. Although other methods such as piezoelectric actuation applied through auxiliary bearings could be used (Tuma et al., 2010); in both the works, AMB was used as the source of contactless external excitation. The excitation by the unbalance and AMB forces produce combinational frequencies between critical speeds of the shaft, the rotor spin speed and the frequency of the AMB excitation. The key was to determine the correct excitation frequency to induce a combinational frequency that could be used to identify the magnitude of the time−dependent stiffness arising from the breathing mode of the rotor crack.

From the rotor condition monitoring standpoint, AMBs can be used in two ways

- As a purely additional component to the whole system to act as a damage detection tool, or
- As support to the rotor with additional function of acting as a damage detection tool

Though the second choice seems more desirable than the first one, the associated difficulties overweigh the apparent benefits as demonstrated by Zhu et al. (2003). They showed that adaptive control with AMBs (that support rotors) may hide the fault characteristics of the cracked rotor, rather than helping to diagnose a crack, depending on the controller strategy used. In such a

scenario, it would be difficult to detect a crack in the rotor with an AMB support system when the vibration of the rotor system would be fully controlled.

Nevertheless, few researchers have worked on finding health monitoring strategies that utilizes supporting AMBs' potential ability to work as exciter and/or damper. Humphris (1992) utilized AMBs that supported a rotor as a source for applying various perturbations to the shaft to collect faulty/healthy response of the rotor. Aenis et al. (2002) introduced a model based diagnosis using AMBs in a centrifugal pump where the pump impeller was levitated by two AMBs.

Nordmann and Aenis (2004) used a built-in software for the fault identification together with AMBs to measure the force and the frequency response of the centrifugal pump, and to diagnose faults. Mani et al. (2005, 2006) and Quinn et al. (2005) demonstrated a technique of the health monitoring of rotor systems with a breathing crack using the AMB as a force actuator. In their work, the rotor was supported on conventional ball bearings with the AMB situated at the mid−span of the rotor. The AMB was used to introduce a sinusoidal excitation force. They used a multiple scale analysis in order to identify combinational resonances, which occur due to the crack. Also, it was shown that the cracked rotor under an excitation force at the combinational frequency experiences an increase in the response amplitude at the fundamental frequency as the depth of the crack increases.

Sawicki et al. (2008) presented the modeling, simulations and experimental results obtained using the cracked rotor supported on ball bearings under the external excitation generated with the AMB positioned at the mid span of the spinning rotor. It was shown that when a cracked rotor undergoes

a specially designed harmonic excitation, the combinational frequencies are induced, which can be used as an indicator of presence of the crack.

An external excitation induced with AMBs for the identification of rotor flaws has been used in many work (Sawicki et al., 2010; Sawicki et al., 2011). Other than the work of Zhu et al. (2003) none have attempted to investigate the dynamics of the cracked rotor, when it is supported on the AMB itself or when the AMB is used in an additional auxiliary configuration.

A rich amount of literatures exists on the design (Polajzer, 2010; Schweitzer and Maslen, 2009) and the control of AMB (for instance - Kim and Lee, 2006; Chen et al., 2013), but they have not been included in this section, for the sake of brevity. From the literature, it is evident that the use of AMB as support to the rotor with additional function of acting as a damage detection tool has been conceptualized but not addressed.

The next section summarizes the outcome of the literature review of previous sections.

1.7 Outcome of the Literature Review

The first part of the literature review focuses on the condition monitoring of structures with special emphasis to transverse cracks in rotor systems. The classification of condition monitoring methods and their application to various rotor faults has been discussed. In subsequent parts, crack models such as a spring, reduced stiffness, flexibility matrix based on the SIF, finite element models, and continuous beam models have been reviewed. A review on the state of the art of the experimental study of cracks in rotor systems and their identification has been included. In the crack modelling as well as the identification, the application of AMB appeared in many published works. Literature

on the application of AMBs in the crack identification has been reviewed in the last section. From the literature reviewed in previous sections, following general observations have been made

- Quantitative model-based methods have been widely preferred in condition monitoring activity. They have the main advantage of quantifying the fault, along with possible location and prognosis. Modeling errors and determination of the damage mechanism are the areas that have a scope for study in model-based condition monitoring.
- Need exists for early fault detection as well as for the robustness of monitoring methods. Also, dependence of the monitoring methods on the external force excitation makes the method impractical for industrial applications due to need for additional attachments and measurements.
- Online condition-monitoring and simultaneous monitoring of multiple faults is still a challenge. Identification of simultaneous faults, like the crack, rub, and misalignment still require a comprehensive research.
- A variety of crack models is discussed in the literature. Modeling based on fracture mechanics is widely used, though approximations are used for obtaining the SIF. Similarly, modeling cracks using the theory of shafts with dissimilar moments of inertia has disadvantage that multiple rotor faults exhibit similar behavior.
- 2-D and 3-D FE models of cracks are complicated and computationally intensive to analyze even a simple beam like structure with cracks. Modeling errors associated with such models lower the merits of estimation.
- Scope exists for studies on effects of coupled vibrations and nonlinearity in crack models. Study on the stability behavior of crack models is also required.

- The switching mechanism incorporated in cracks modeled for rotor systems is one of the key features that determine the accuracy of the final model. The switching behaviour has been modeled in literature by using a hinge model. It has also been modeled by defining a crack closure line. It is also represented as a harmonic series of a trigonometric function. The experimental verification of the true switching mechanism has been attempted by few researchers. Scope exists for more accurate modeling of breathing functions and its validation with the experimental work.
- Crack identification algorithms perform better using frequency responses. Traditional frequency spectrums as well as novel signal-processing methods such as the full-spectrum are discussed. The full-spectrum has been chiefly discussed for the signal-based identification of the crack and other faults. Since, the full-spectrum signal processing is highly suitable for crack problems; it can be exploited for the model-based crack identification.
- The location of placement of the controlled external excitation (AMB) for the best possible extraction for the rotor flaw information extraction has not been dealt in the literature. Scope exists for the optimization of placement location of the excitation source.
- In most of the literature, contrary to its name, AMB has been used as a replacement for the mechanical external exciter. Availability of AMB in the support system diminishes the vibration signals (Kasarda, 2000). Response analysis of cracked rotors supported in AMB particularly from the rotor condition monitoring view point is missing. Scope exists for developing methods to identify transverse cracks in such rotors.
- The literature on experimental study of cracks mainly involves saw-cut or wire-cut EDM or welded shafts, for studying a rotor crack. But, they do not simulate the

breathing behavior of a transverse fatigue crack. Very few works on fatigue cracks have been found. Hence, more investigation on the artificial generation and study of a fatigue crack becomes necessary.

Almost all the literature associated with AMB in rotor condition monitoring has considered it for the single purpose – as an external excitation. Some researchers, like Zhu et al. (2003), have studied the dynamics of a cracked rotor supported in the AMB, but the focus of their work has mostly been on the instability and the controller design. This paper discusses in detail the reasons behind difference in modelling a traditional cracked rotor system and those with AMB support. Need for change in control strategy in case of appearance of crack is also discussed. With the progressive development of controllers and magnetic components, and with ever increasing stringency in performance expectation from rotating machines, AMBs are to find more applications and deployment. In such applications, the identification of rotor flaws would be a challenge; due to the flaw itself and due to the fact that the AMB may suppress vibration signals, which are used for the flaw detection, otherwise. The model based identification of rotor flaws, the transverse crack is particular, in AMB supported rotor is an open field for the investigation.

1.8 Objectives and Scope of the Present Study

The broader objective of the present work is to study the dynamics of cracked rotor supported in an AMB. The identification of transverse cracks in such rotors with the help of vibration and the AMB control current time history is the key purpose. Following steps are envisioned towards this objective:

- To develop mathematical models of cracked rotor system supported on AMB based on existing literature available. The crack itself will be modelled and linearized as a switching crack. The AMB control strategy and design will be based on information available in literature. The developed rotor-AMB model will be used to obtain numerical system responses and to develop model-based identification algorithms to estimate the fault and unknown system parameters. Mathematical models will be developed for the following cases: (a) the cracked rotor with disc and AMB in Jeffcott configuration, with only consideration of two translational displacements (b) the cracked rotor with disc and AMB offset from the central plane (c) FEM based cracked flexible rotor supported on rigid bearings, and disc and AMB offset from the central plane, with 4–DOFs at each node and (d) FEM based cracked flexible rotor end supported on flexible bearings, with multiple disk and multiple AMB, with 4–DOFs at each node. In the last three cases, the disc moment of inertia and gyroscopic effects will be considered in the models.
- Model-based identification algorithms will be developed for identifying fault parameters, namely, the additive stiffness due to crack and disc eccentricity (in magnitude and orientation with respect to the crack front), along with the rotor-AMB system parameters, viz. the viscous damping, AMB force-displacement constant and AMB force-current constant.
- A full-spectrum signal processing method will be used to obtain coefficients of harmonics of AMB controller current and displacement, of the forward and reverse whirling frequency components of the current and response signals, respectively. These coefficients can be directly used as an input, instead of estimating them from time domain data, for proposed identification algorithms.

- Developed identification algorithms will be numerically tested. Different ranges of measurement spin speeds will be chosen for the testing. Also, effect on the estimates for different levels of measurement noise in responses will be tested. There may remain some factors that could not be conceptualized a priori and could not be modeled with sufficient accuracy. To account for such shortcomings in the modeling, the effect of modeling error (or bias error) on the estimates will be quantified.
- Due to the inherent property of the AMB action, the rotor is likely to exhibit very small vibration signals. This poses a practical difficulty in accurate measurement of rotational displacements. For the crack model containing rotational co-ordinates, a dynamic reduction scheme will be used to eliminate rotational displacements from equations of motion.

1.9 Organization of the Thesis

The thesis is organized into six chapters. The introduction and literature review are presented in Chapter 1. The mathematical modeling, its numerical simulations and development of identification algorithm for a Jeffcott rotor with a transverse crack and AMB support is presented in Chapter 2. The transverse crack is identified with single parameter of additive crack stiffness (Δk_{22}). Other parameters like the unbalance magnitude and phase, system viscous damping and AMB stiffness constants (k_s and k_I) are also identified. In Chapter 3, the mathematical model, its simulation and development of identification algorithm is extended to an offset rotor with a crack and an AMB support. The crack and other system parameters are identified. Chapter 4 discusses the development of mathematical model and identification algorithm for a cracked flexible shaft with AMB support. The analysis is based on a single disc and rigid supports. Finally, in Chapter 5, the analysis with FEM based model of the cracked rotor is generalized to the complete extent by

consideration of multiple discs, multiple AMB supports and flexible support bearings. In this chapter, apart from the crack and AMB stiffness, the support bearing dynamic parameters are also identified. Conclusions, limitations and applicability, and future scopes from the present work are presented in Chapter 6.

CHAPTER 2

Identification in Cracked Jeffcott Rotor with AMB Support

2.1 Introduction

This chapter presents development of a mathematical model of an AMB assisted Jeffcott rotor with a transverse fatigue crack. A Jeffcott rotor with a crack close to the disc position is considered. An eight-pole AMB is used as an additional active supporting device to the cracked rotor. At particular spin speeds, the crack and the unbalance give rise to unique response of vibration displacements and AMB control currents. The dynamic equations of motion of the rotor with due consideration to the crack, unbalance and AMB action is developed, and the vibration displacement and AMB currents are simulated with the developed equations of motion. The nature and behaviour of the vibration displacement and the AMB current for this system configuration is reported.

The simple rotor model considered in this chapter has translational displacements (2-Degrees of Freedom (DOF) system) only. Modelling of the fatigue crack is based on a crack flexibility matrix, based on the works of Gasch (2008). The crack model in rotational co-ordinate system is converted to crack model in the inertial co-ordinate system with help of a transformation matrix. The AMB incorporated in the model in auxiliary bearing configuration is accounted for in the Equations of Motion (EOM) in form of a negative magnetic force acting on the rotor such that this force has overall impact of keeping the rotor as close as possible to its reference position. The control strategy used for the AMB controller, linearization of the crack model and the overall system EOMs is discussed in the following sections.

Forces acting on the system consist of force vectors due to the crack, unbalance and AMB support: acting in tandem. The combination of unbalance, crack and AMB forcing acting together provide excitations of multiple harmonics of the rotor spin frequency. In the process, the overall forcing contains harmonics which excite the rotor either in the same direction of spin (forward whirl) or in the reverse direction of spin (backward or reverse whirl). The steady-state response of the system to these excitations can be studied essentially by means of time-histories and frequency responses. The present chapter discusses the mathematical formulation of the problem and solution procedures for the time and frequency response analyses. Numerical illustrations are also provided with a simple rotor configuration data.

2.2 Model of a 2-DOF Cracked Rotor with AMB Support

The mathematical model to simulate dynamics of a cracked rotor with an AMB support is presented. A Jeffcott rotor, which is a simply supported elastic shaft with a centrally located disc, is considered. A transverse crack on the rotor, close to the disc and an AMB support in auxiliary bearing configuration is considered. It is a lumped parameter model with the shaft assumed as mass-less. This section considers a 2-DOF model with the transverse translational motion in two orthogonal directions. However, for this section, it ignores gyroscopic couple and elastic coupling due to the disc. Figure 2-1 schematically shows such a rotor with a fatigue crack near the disc. As detailed in Schweitzer and Maslen (2009), for a successful implementation of AMB, the part of the rotor inside the AMB must be suitably laminated to minimize the electromagnetic resistance to rotation due to eddy currents. This lamination core acts as the rigid disc considred in this work; thus the AMB and the disc are collocated.

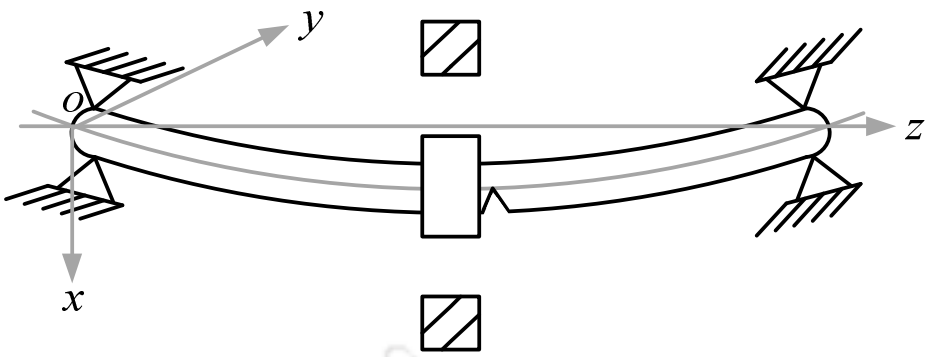

Figure 2-1 A cracked Jeffcott rotor system with an AMB

2.2.1 Equations of Motion of Cracked Jeffcott Rotor

It is known that the crack introduces a local flexibility in the shaft and alters the system natural frequency (Sabnavis et al., 2004). In true rotor cracks, it is most likely to observe opening and closing of the crack as a function of time or the rotor swept angle. In heavy horizontal rotors, the static deflection (δx) is large compared to the additional vibration due to dynamics of rotation. In such cases, opening and closing of the crack depends on its instantaneous position with respect to the neutral axis of the deflected shaft (Gasch, 2008). The crack remains open when it is in the tensile zone and closed when in the compressive zone. If the transition from open to close and close to open is not gradual but sudden, the crack will have only two possible positions; either completely close or completely open, with no intermediate position. Such cracks are known as switching cracks. They are visually approximated by a hinge model. A switching crack and the basic definition of coordinate system are given in Figure 2-2. Coordinate system ξ-O-η is the rotating coordinate system fixed with the rotor and coordinates x-O-y is the inertial coordinate system. The direction ξ is defined as perpendicular to the crack front, thus direction η is parallel to the crack front. At the instant of initiation of time count the rotating axes ξ and η are aligned to the inertial axes x and y, respectively.

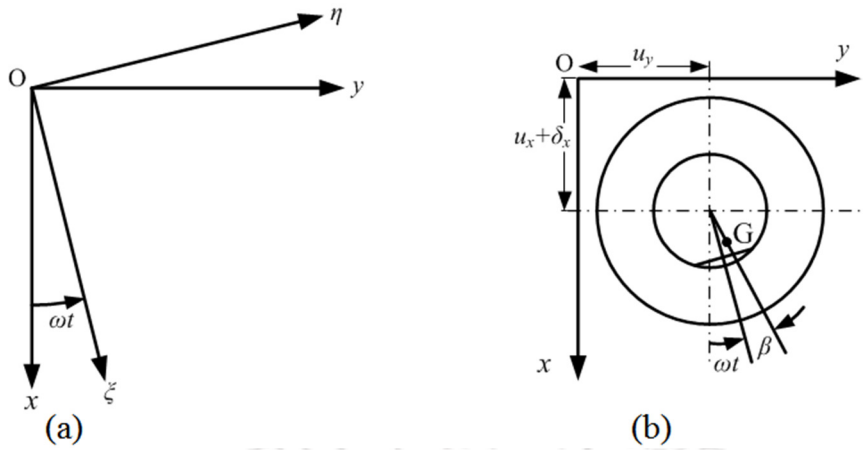

Figure 2-2 (a) Inertial and rotating coordinate references (b) Relative position of crack and unbalance

EOMs of a rotor system with intact shaft has been reported by many authors, for instance Mayes and Davies (1984), Lalanne and Ferraris (1998) and Yamamoto and Ishida (2001). For this case the EOM are given as

$$\mathbf{M}\ddot{\mathbf{q}} + \mathbf{C}\dot{\mathbf{q}} + \mathbf{K}\mathbf{q} = \mathbf{f}_{st} + \mathbf{f}_{unb} \tag{2.1}$$

For the model with two degrees of freedom, following system matrices and vectors are defined in the inertial coordinate system

$$\mathbf{q} = \mathbf{u} + \mathbf{u_0} = \begin{Bmatrix} u_x \\ u_y \end{Bmatrix} + \begin{Bmatrix} \delta_x \\ 0 \end{Bmatrix}; \quad \mathbf{M} = \begin{bmatrix} m & 0 \\ 0 & m \end{bmatrix}; \quad \mathbf{C} = \begin{bmatrix} c & 0 \\ 0 & c \end{bmatrix};$$

$$\mathbf{K} = \begin{bmatrix} k & 0 \\ 0 & k \end{bmatrix}; \quad \mathbf{f}_{st} = \begin{Bmatrix} mg \\ 0 \end{Bmatrix}; \quad \mathbf{f}_{unb} = me\omega^2 \begin{Bmatrix} \cos(\omega t + \beta) \\ \sin(\omega t + \beta) \end{Bmatrix} \tag{2.2}$$

Here, **M**, **C** and **K** are the mass, damping and stiffness matrices of the rotor system, $\mathbf{f}_{st}$ is the weight vector , $\mathbf{f}_{unb}$ is the force vector due to the disc unbalance, **q** is the displacement vector in the inertial co-ordinate system that could be factored into the vibration displacement (**u** , displacement due to out of balance force) and a permanent set ($\mathbf{u}_0$, static deflection), m is the disc mass, c is the viscous damping in the rotor system, k is the stiffness of the shaft, u_x and u_y are vibration displacements at the centre of shaft in the plane of the disc, ω is the rotor spin speed, e is the eccentricity of the disc (i.e., the distance between the centre of gravity and the shaft centre at the disc), and β is the angle between unbalance and crack front direction as shown in Figure 2-2 (b). Matrices have been represented with bold upper case letters and vectors with bold lower case letters. Nomenclature section may be referred to, for details.

The presence of crack in the shaft alters the stiffness of the rotor system. The crack section introduces a local stiffness matrix leading to effective change in the stiffness matrix, say $\Delta\mathbf{K}$ - into EOMs (Eqn.(2.1)). It is established from the literature (Grabowski, 1980) that a rotor crack opens and closes due to variation of stresses with the shaft rotation, presenting different stiffness at the crack section depending upon the fact whether the crack is open or closed. This *crack stiffness* parameter varies due to the periodical shaft rotation ($\theta = \omega t$) as well as the rotor vibration displacement, **u**. Thus, the local stiffness matrix shows a *non-linear* behaviour (i.e. $\Delta\mathbf{K}(u,t)$). The non-linear EOM of the cracked Jeffcott rotor can be, hence, written as follows

$$\mathbf{M}\ddot{\mathbf{q}}(t) + \mathbf{C}\dot{\mathbf{q}}(t) + \left(\mathbf{K} + \Delta\mathbf{K}(u,t)\right)\mathbf{q}(t) = \mathbf{f}_{st} + \mathbf{f}_{unb} \tag{2.3}$$

It is seen from literature (Grabowski, 1980; Gasch, 1993) that the mean static deflection in heavy rotor systems is an order more than unbalance responses. For instance, Penny and Friswell (2003)

indicated a static deflection of the order of 1 mm against a running speed vibration amplitude of 50 µm, for a typical turbine rotor. Even at the critical speed the vibration amplitude is not expected to exceed 250 µm. Hence, it is justified not to consider nonlinear models of the cracked rotor below or near the critical speed range. The linearization of the cracked rotor EOMs is elaborated in the following paragraph.

2.2.2 Linearization of System Equations of Motion

As since the present work studies linear rotor models, the crack flexibility matrix in EOMs (Eqn.(2.3)) needs to be linearized. It is linearized by the assumption of weight-dominance for elastic deflections (Gasch, 1993). Under the assumption of weight-dominance, the static deflection ($\mathbf{u}_0$) is much greater than the response due to the unbalance or rotating asymmetry ($\mathbf{u}(t)$, the vibrational displacement), thus $|\mathbf{u}_0| \gg |\mathbf{u}(t)|$. In such rotors, the crack opening/closing depends only on the shaft rotation under the effect of gravity of the rotor system and hence the instantaneous stiffness presented by the rotor is only time dependent (i.e. $\Delta\mathbf{K}(u,t) \to \Delta\mathbf{K}(t)$). This assumption of linearization has practical validity in the case of heavy rotors as enunciated in Penny and Friswell (2003) and Gasch (2008). The total response of the rotor includes the static deflection, $\mathbf{u}_0$, and the vibrational displacement vector, $\mathbf{u}(t)$. Thus, the EOM (Eqn. (2.3)) can be re-written as

$$\mathbf{M}\ddot{\mathbf{u}}(t) + \mathbf{C}\dot{\mathbf{u}}(t) + \left(\mathbf{K} + \Delta\mathbf{K}(t)\right)\left(\mathbf{u}_0 + \mathbf{u}(t)\right) = \mathbf{f}_{st} + \mathbf{f}_{unb} \tag{2.4}$$

or

$$\mathbf{M}\ddot{\mathbf{u}}(t) + \mathbf{C}\dot{\mathbf{u}}(t) + \mathbf{K}\mathbf{u}_0 + \Delta\mathbf{K}(t)\mathbf{u}_0 + \mathbf{K}\mathbf{u}(t) + \Delta\mathbf{K}(t)\mathbf{u}(t) = \mathbf{f}_{st} + \mathbf{f}_{unb} \tag{2.5}$$

Since, $|\mathbf{K}| \gg |\Delta\mathbf{K}(t)|$ and $|\mathbf{u}_0| \gg |\mathbf{u}(t)|$ the term $\Delta\mathbf{K}(t)\mathbf{u}(t) \approx 0$ and could be safely ignored in further analysis. Also, $\mathbf{K}\mathbf{u}_0 = \mathbf{f}_{st}$. With these underlying simplifications, Eqn. (2.5) could be rewritten as

$$\mathbf{M}\ddot{\mathbf{u}} + \mathbf{C}\dot{\mathbf{u}} + \mathbf{K}\mathbf{u} = -\Delta\mathbf{K}\mathbf{u}_0 + \mathbf{f}_{unb} \tag{2.6}$$

Force vectors on the RHS of the above EOMs are due to the crack and the unbalance, respectively. Presence of any other forcing term can be accounted for, by adding it to the RHS of Eqn. (2.6).

2.2.3 Modeling of the Crack

A schematic representation of a transverse crack and the associated loads along coordinate directions is shown in Figure 2-3.

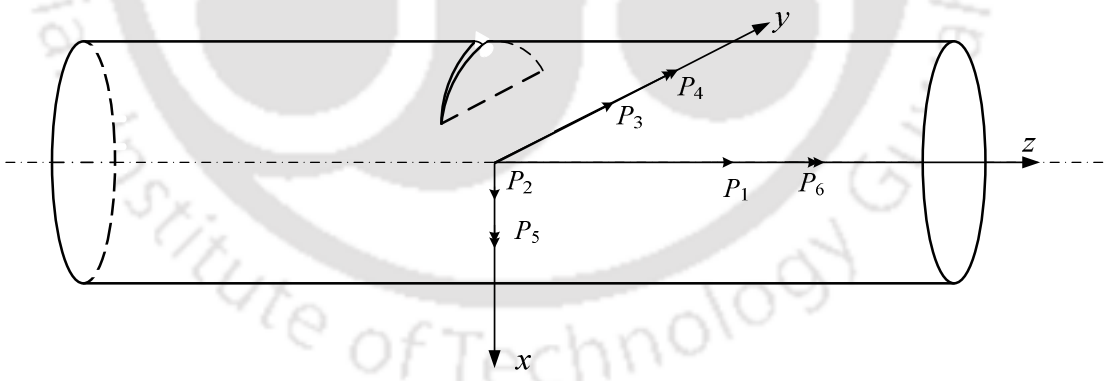

Figure 2-3 A rotor element showing various loads at the crack section

It is known from Dimarogonas (1995) that the form of *crack flexibility matrix* based on the fracture mechanics approach is widely used as the crack model. Elements of the flexibility matrix, in general, includes the coupling of lateral, longitudinal, and torsional vibration effects. As

enunciated in Papadopoulos and Dimarogonas (1988) and Darpe (2007), the crack flexibility matrix for a transverse crack is defined as follows

$$\mathbf{\Delta H}_{\text{FULL}} = \begin{bmatrix} \Delta h_{11} & 0 & 0 & \Delta h_{14} & \Delta h_{15} & 0 \\ 0 & \Delta h_{22} & 0 & 0 & 0 & \Delta h_{26} \\ 0 & 0 & \Delta h_{33} & 0 & 0 & \Delta h_{36} \\ \Delta h_{41} & 0 & 0 & \Delta h_{44} & \Delta h_{45} & 0 \\ \Delta h_{51} & 0 & 0 & \Delta h_{54} & \Delta h_{55} & 0 \\ 0 & \Delta h_{62} & \Delta h_{63} & 0 & 0 & \Delta h_{66} \end{bmatrix} \tag{2.7}$$

In the case of slant crack, the flexibility matrix is more populated (Darpe, 2007). In Eqn. (2.7), Δh terms denote the change in flexibility (or compliance) due to the crack effect. Flexibility is defined as the deflection in i^{th} direction due to the force in j^{th} direction. As depicted in (2.7), subscript 1 corresponds to the axial force (z-axis direction), subscripts 2 and 3 correspond to shearing forces, subscripts 4 and 5 correspond to the bending moment about two lateral directions, and subscript 6 corresponds to the torque. A combination of subscripts corresponds to cross-coupled terms.

The crack flexibility matrix in Eqn. (2.7) corresponds to a 6-DOF rotor system. In the case of a 4-DOF model, crack flexibilities and loads in the axial direction are not considered thus the flexibility matrix is obtained considering the deflections and loads in the two lateral directions alone. The crack flexibility matrix for a 4-DOF model thus can be obtained by reducing terms in 1st and 6th rows and respective columns in Eqn. (2.7). The crack flexibility matrix so obtained for 4-DOF analysis is

$$\mathbf{\Delta H}_{\text{4-DOF}} = \begin{bmatrix} \Delta h_{22} & 0 & 0 & 0 \\ 0 & \Delta h_{33} & 0 & 0 \\ 0 & 0 & \Delta h_{44} & \Delta h_{45} \\ 0 & 0 & \Delta h_{54} & \Delta h_{55} \end{bmatrix} \tag{2.8}$$

The crack flexibility matrix for a 2 DOF analysis based on linear response in two directions is similarly obtained by retaining the rows and columns corresponding to shearing forces along two orthogonal directions. The 3rd and 4th rows and columns of the matrix in Eqn. (2.8) thus get eliminated to give the flexibility matrix for the 2-DOF analysis, as

$$\mathbf{\Delta H}_{\text{2-DOF}} = \begin{bmatrix} \Delta h_{22} & 0 \\ 0 & \Delta h_{33} \end{bmatrix} \tag{2.9}$$

Except under the situation of slow roll or very deep cracks, the cross flexibility, Δh_{33}, introduced by the presence of a crack are many times smaller than the main flexibility, Δh_{22}. So, for the sake of simplicity this has been neglected in the further derivations of this chapter. Deflection at the position of the disc with an open crack adjacent to it, in the rotating coordinate system ξ– η, as given by Gasch (2008) is

$$\begin{Bmatrix} u_\xi \\ u_\eta \end{Bmatrix} = \begin{bmatrix} h_0 + \Delta h_{22} & 0 \\ 0 & h_0 + 0 \end{bmatrix} \begin{Bmatrix} f_\xi \\ f_\eta \end{Bmatrix} \tag{2.10}$$

where h_0 is the flexibility of the round intact shaft, Δh_{22}, is the additional flexibility due to the crack, and f_ξ and f_η are excitation forces along the ξ and η coordinate axis directions, respectively. With rotation of the shaft, as the crack enters the compressive zone, the crack will close and Δh_{22} becomes zero. Now the shaft behaves as if the crack is not present. Since h_0 is

constant and Δh_{22} has a periodicity of 2π, the flexibility matrix in equation (2.10) can be factored into matrices containing h_0 and Δh_{22}. The behaviour of the crack opening and closure in the period of 2π rad is controlled by many factors, the most prominent being the depth of the crack.

The crack opening and closing is generally modelled by a suitable crack excitation function (CEF). Irrespective of the type of crack excitation function made use of, a value of 1 of this function represents an open crack and a value of 0 represents the closure of the crack. The rotor cracks in early stage of propagation are likely to have a sudden opening/closing as compared to the advance stage of crack propagation when the opening and closing may be smoother. A hinge model simulates the opening/closing profile of a rotor crack in early stage of propagation and is given by a bi-linear square-wave function as follows (Gasch, 1993)

$s(t) = 1$ when the crack is in the tensile portion of the shaft, i.e. the crack is open

$s(t) = 0$ when the crack is in the compressed portion of the shaft, i.e. the crack is closed

Pictorial representation of this crack excitation function is presented in Figure 2-4.

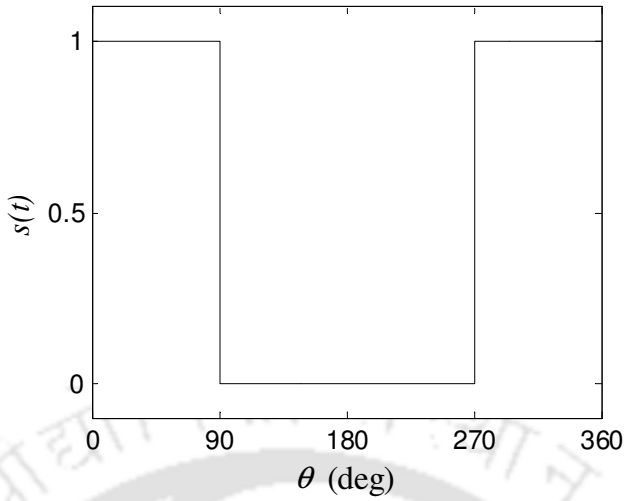

Figure 2-4 Variation of a switching crack excitation function over a shaft rotation

It may be seen in the figure that the crack suddenly closes at 90° and opens at 270°. Such cracks are also called as switching cracks (Mayes and Davies, 1984; Gasch, 1993) and the crack excitation function accordingly named as switching crack excitation function (SCEF). This bi-linear square wave SCEF may be approximated as a Fourier series as

$$s(t) = \frac{1}{2} + \frac{2}{\pi}\cos\omega t - \frac{2}{3\pi}\cos(3\omega t) + \frac{2}{5\pi}\cos(5\omega t) - \frac{2}{7\pi}\cos(7\omega t) + \frac{2}{9\pi}\cos(9\omega t) - \cdots \qquad (2.11)$$

In contrast to the switching crack, a breathing crack has more gradual opening and closing profile. Any suitable non-linear function such as Mayes' modified function (Gasch, 1993) simulates its opening/closing profile. Mayes' function for the breathing crack is given as

$$s(t) = \tfrac{1}{2}(1 + \cos\omega t) \qquad (2.12)$$

In the present work, the switching crack function represented by Eqn. (2.11) is used for numerical simulations. Thus, a crack switching/breathing function $s(t)$ accounts for time variation into the crack flexibility matrix and it is defined as,

$$\begin{Bmatrix} u_\xi \\ u_\eta \end{Bmatrix} = \left(\begin{bmatrix} h_0 & 0 \\ 0 & h_0 \end{bmatrix} + s(t) \begin{bmatrix} \Delta h_{22} & 0 \\ 0 & 0 \end{bmatrix} \right) \begin{Bmatrix} f_\xi \\ f_\eta \end{Bmatrix} \tag{2.13}$$

After the introduction of the steering function $s(t)$, the restoring force vector in the rotating coordinate system may be obtained by inverting the flexibility matrix as

$$\begin{Bmatrix} f_\xi \\ f_\eta \end{Bmatrix} = \left(\begin{bmatrix} k_{22} & 0 \\ 0 & k_{22} \end{bmatrix} - s(t) \begin{bmatrix} \Delta k_{22} & 0 \\ 0 & 0 \end{bmatrix} \right) \begin{Bmatrix} u_\xi \\ u_\eta \end{Bmatrix} \tag{2.14}$$

Here, $(1/h_0) = k_{22}$ and $1/(h_0 + \Delta h_{22}) = k_{22} - \Delta k_{22}$ and k_{22} is the stiffness of the intact shaft and Δk_{22} is the loss in stiffness due to opening of the crack. Eqn. (2.14) can be written in terms of the intact shaft stiffness and the additive stiffness due to crack as

$$\begin{Bmatrix} f_\xi \\ f_\eta \end{Bmatrix} = \left(\mathbf{K}_{rot} + s(t) \mathbf{\Delta K}_{rot} \right) \begin{Bmatrix} u_\xi \\ u_\eta \end{Bmatrix} \tag{2.15}$$

with

$$\mathbf{K}_{rot} = \begin{bmatrix} k_{22} & 0 \\ 0 & k_{22} \end{bmatrix} \quad \text{and} \quad \mathbf{\Delta K}_{rot} = -\begin{bmatrix} \Delta k_{22} & 0 \\ 0 & 0 \end{bmatrix} \tag{2.16}$$

Eqn. (2.15) represents a mathematical model of a crack in 2 DOF. Here subscript *rot* denotes matrices defined in the rotating coordinate system. The negative sign of the additive crack stiffness implies reduction in the stiffness due to appearance of the crack.

2.2.4 Transformation Matrix and Equations of Motion in Inertial Coordinates

It is observable in Eqn. (2.15) that the intact shaft stiffness and the crack stiffness have been defined in rotating coordinates. For use of the crack model in the EOM of the shaft, i.e. Eqn. (2.6), matrices in Eqn. (2.15) must shall be transformed into the inertial coordinates. The transformation of co-ordinates from the rotating to inertial co-ordinate systems is made with help of a transformation matrix as

$$\begin{Bmatrix} u_\xi \\ u_\eta \end{Bmatrix} = \mathbf{T} \begin{Bmatrix} u_x \\ u_y \end{Bmatrix} \qquad \text{with } \mathbf{T} = \begin{bmatrix} \cos\omega t & \sin\omega t \\ -\sin\omega t & \cos\omega t \end{bmatrix} \tag{2.17}$$

The transformation of crack stiffness matrix to *x*-o-*y* co-ordinate system is as follows,

$$\begin{Bmatrix} f_x \\ f_y \end{Bmatrix} = \mathbf{T}^T \left(\mathbf{K}_{rot} - s(t)\Delta\mathbf{K}_{rot} \right) \mathbf{T} \begin{Bmatrix} u_x \\ u_y \end{Bmatrix} \tag{2.18}$$

The above transformation results into the following equations

$$\begin{Bmatrix} f_x \\ f_y \end{Bmatrix} = \left(\mathbf{K} + \Delta\mathbf{K}(t) \right) \begin{Bmatrix} u_x \\ u_y \end{Bmatrix} \tag{2.19}$$

with

$$\mathbf{K} = \begin{bmatrix} k_{22} & 0 \\ 0 & k_{22} \end{bmatrix} \quad \text{and} \quad \mathbf{\Delta K}(t) = -\tfrac{1}{2} s(t) \Delta k_{22} \begin{bmatrix} 1+\cos 2\omega t & \sin 2\omega t \\ \sin 2\omega t & 1-\cos 2\omega t \end{bmatrix} \tag{2.20}$$

Substituting expressions given by Eqn. (2.20) for the intact shaft stiffness and the additive crack stiffness into Eqn. (2.6) the system EOMs of a cracked rotor in the inertial co-ordinate system is obtained as follows,

$$\mathbf{M\ddot{u}} + \mathbf{C\dot{u}} + \mathbf{Ku} = \mathbf{f}_{cr}(t) + \mathbf{f}_{unb} \tag{2.21}$$

with the crack force defined as

$$\mathbf{f}_{cr}(t) = -\mathbf{\Delta K u}_0 = \tfrac{1}{2} s(t) \Delta k_{22} \begin{bmatrix} 1+\cos 2\omega t & \sin 2\omega t \\ \sin 2\omega t & 1-\cos 2\omega t \end{bmatrix} \begin{Bmatrix} \delta_x \\ 0 \end{Bmatrix} \tag{2.22}$$

where δ_x is the static deflection of the shaft in x direction, as indicated in Figure 2-2. The RHS of Eqn. (2.21) contains the forcing due to crack and unbalance. Presence of AMB restitution forces in the system can be included in the analysis by adding them on the RHS.

2.2.5 Restitution due to AMB Support

The AMB force in a particular direction depends on two variables; the coil current i_x or i_y, and the air gap between the magnet pole face and the rotor u_x or u_y depending upon the direction. The term air gap used in context of magneto-mechanical systems refers to the distance between the magnet pole and the object being supported. In AMB applications this term is synonymous to the distance of separation between the magnet pole and the journal, i.e. the vibration displacement with respect

to the mean journal position. Near the operating point the force–current and force–displacement (air gap) relationship is linear, and hence the AMB force in terms of the force-displacement factor k_u and force-current factor k_I can be written as

$$\mathbf{f}_{\text{AMB}} = \begin{Bmatrix} -k_{ux}u_x + k_{Ix}i_x \\ -k_{uy}u_y + k_{Iy}i_y \end{Bmatrix} \tag{2.23}$$

Since the AMB is intrinsically unstable, a feedback control loop is used to determine i_x and i_y based on the instantaneous value of u_x and u_y to ensure stability of the system. In control design for AMB implementation, digital PID control and other advanced algorithms like Kalman filter, H_∞ and $\mu_{\text{- synthesis}}$ have been reported in literature, for instance Schweitzer and Maslen (2009). Since the aim of the present work is to utilize the behaviour of control current and the vibtration displacement response of a cracked roror with AMB support, the simplest of all the control strategies has been considered.

A PD controller is the minimum requirement; in the present work a PID controller has been used. The integrator component of the controller corrects the long term positioning of the journal about its reference position. This controller outputs the current i sent to the magnetic coils as a function of the measured air gap. The expression for the current output of a PID controller in coils for force in a particular direction is given as

$$i(t) = K_{\text{P}}u(t) + K_{\text{I}}\int u(t)dt + K_{\text{D}}\frac{du(t)}{dt} \tag{2.24}$$

where K_P is the proportional gain, K_I is the integral gain, K_D is the derivative gain factors of the controller and u is the displacement. The AMB with eight poles could be treated as an isotropic, thus factors k_{ux} and k_{uy} in equation (2.23) can be replaced by a single factor k_s and the similar for k_I. With this simplification, equation (2.23) is modified as

$$\mathbf{f}_{\text{AMB}} = -\begin{bmatrix} k_s & 0 \\ 0 & k_s \end{bmatrix}\begin{Bmatrix} u_x \\ u_y \end{Bmatrix} + \begin{bmatrix} k_I & 0 \\ 0 & k_I \end{bmatrix}\begin{Bmatrix} i_x \\ i_y \end{Bmatrix} \tag{2.25}$$

When the AMB is incorporated in the support system of the rotor with a crack, the AMB force can be put in the RHS of Eqn. (2.21) with appropriate sign. If the AMB is used as an external non-contact exciter, as reported in multitude of crack related literature, (for instance – Aenis et al., 2002; Nordmann and Aenis, 2004; Quinn et al., 2005; Litak et al., 2009; Friswell et al., 2010; Sawicki et al., 2009) the AMB forcing appears in the RHS of Eqn. (2.21) with a positive sign. Since, in this work the AMB is used as an additional support, its nature and purpose is to minimize the vibration displacement; the AMB forcing appears in RHS of Eqn. (2.21) with a negative sign. With addition of AMB forcing, Eqn. (2.21) modifies to

$$\mathbf{M}\ddot{\mathbf{u}} + \mathbf{C}\dot{\mathbf{u}} + \mathbf{K}\mathbf{u} = \mathbf{f}_{cr}(t) + \mathbf{f}_{un} - \mathbf{f}_{AMB} \tag{2.26}$$

The crack, unbalance and AMB excitation forces are available on the RHS and treated as external forces. The crack, unbalance and AMB forces act in tandem, with the AMB forcing attempting to nullify the effects of crack and unbalance.

2.3 Analyses of Forced Responses

Equations of motion (Eqn.(2.26)) are non-homogeneous and represent forced vibration of the cracked rotor system. For ease of handling equations and computational benefit, displacements u_x and u_y can be combined as a complex vector r with real x-axis, i.e. $r = u_x + \mathrm{j}u_y$ with $\mathrm{j} = \sqrt{-1}$. And so for currents i_x and i_y, as $i_c = i_x + \mathrm{j}i_y$. Multiplying the second of the system of equations of motion (2.26) by j and adding to first, the complex form is obtained

$$m\ddot{r} + c\dot{r} + kr = f_{cr}^{c} + f_{un}^{c} - f_{AMB}^{c} \tag{2.27}$$

with

$$f_{cr}^{c} = \tfrac{1}{2} s(t) \Delta k_{22} \delta_x (1 + \mathrm{e}^{2\,\mathrm{j}\omega t}) \; ; \quad f_{un}^{c} = me\omega^2 \mathrm{e}^{\mathrm{j}(\omega t + \beta)} \; ; \quad f_{AMB}^{c} = -k_s r + k_I i_c \tag{2.28}$$

A switching crack can be well approximated by a rectangular waveform (Gasch, 1993; Gasch, 2008) and can be expressed as a Fourier series as Eqn. (2.11). With the SCEF expressed as Eqn. (2.11), using the Euler formula, the crack excitation force, can be expressed in a series of various harmonics as

$$\begin{aligned} f_{cr}^{c} = \Delta k_{22} \delta_x \{ \cdots + 0.009\mathrm{e}^{-\mathrm{j}5\omega t} - 0.021\mathrm{e}^{-\mathrm{j}3\omega t} + 0.106\mathrm{e}^{-\mathrm{j}\omega t} + 0.25 + 0.319\mathrm{e}^{\mathrm{j}\omega t} \\ + 0.25\mathrm{e}^{\mathrm{j}2\omega t} + 0.106\mathrm{e}^{\mathrm{j}3\omega t} - 0.021\mathrm{e}^{\mathrm{j}5\omega t} + 0.009\mathrm{e}^{\mathrm{j}7\omega t} + \cdots \} \end{aligned} \tag{2.29}$$

The above equation can be written in notational form as

$$f_{cr}^{c} = \Delta k_{22} \delta_x \sum_{i=-n}^{+n} p_i \mathrm{e}^{\mathrm{j}i\omega t} \tag{2.30}$$

Here p_i is the coefficient of the i^{th} harmonic of the crack force excitation. For early stages of the crack propagation, these coefficients are independent of the crack depth. As stated earlier, this is the domain of crack growth for which the hinge model is valid.

In active systems, the delay between the appearance of the error signal and generation of the control signal depends upon the sampling frequency. For a properly tuned controller, the control action delay may be longer than one sampling period but shorter than two sampling periods (Larsonneur, 2009). Thus, at high sampling rates (sampling rate of the proximity probe of the AMB) and a descent hardware setup, the rotor response and the AMB control current (error and control signal respectively, for the controller) will have the same nature and similar time history. Thus, all the harmonics present in the shaft response should be present in the complex current of Eqn. (2.27). With incorporation of this assumption, Eqn. (2.27) can be modified as

$$m\ddot{r} + c\dot{r} + (k_0 - k_s)r = f_{cr}^{c} + f_{un}^{c} - f_{cu}^{c} \tag{2.31}$$

with

$$f_{cu}^{c} = k_I \sum_{i=-n}^{+n} I_i \mathrm{e}^{\mathrm{j}i\omega t} \tag{2.32}$$

where I_i is the i^{th} harmonic of complex current and f_{cu}^{c} is the magnetic force due to the current only. From Eqns. (2.30) and (2.32), it is seen that equations of motion of the rotor system with the transverse crack contains forcing components of multiple harmonics. The assumed solution $R_i(t)$ for a particular harmonic of the crack force excitation is $R_i(\omega)\mathrm{e}^{\mathrm{j}i\omega t}$. Because the equation of motion is linear, using the principle of superposition, assumed solutions for each harmonic are

added up. Thus, at any time instant the complex displacement signal is related to its individual complex harmonics as

$$r(t) = \cdots + R_{-3}\mathrm{e}^{-3\,\mathrm{j}\omega t} + R_{-1}\mathrm{e}^{-1\,\mathrm{j}\omega t} + R_0\mathrm{e}^{-0\,\mathrm{j}\omega t} + R_1\mathrm{e}^{1\,\mathrm{j}\omega t} + R_2\mathrm{e}^{2\,\mathrm{j}\omega t} + R_3\mathrm{e}^{3\mathrm{j}\omega t} + R_5\mathrm{e}^{5\,\mathrm{j}\omega t} + \cdots \tag{2.33}$$

Equation (2.33) forms the basic structure of solution expected in the case of rotor with a transverse crack and represents the time history of nature of variation of air gap for the cracked rotor. Current harmonics should have the same frequency components as displacement harmonics, as an output of the real time PID control. At any time instant the complex current signal is related to its individual complex harmonics as

$$i_c(t) = \cdots I_{-3}\mathrm{e}^{-3\,\mathrm{j}\omega t} + I_{-1}\mathrm{e}^{-1\,\mathrm{j}\omega t} + I_0\mathrm{e}^{-0\,\mathrm{j}\omega t} + I_1\mathrm{e}^{1\,\mathrm{j}\omega t} + I_2\mathrm{e}^{2\,\mathrm{j}\omega t} + I_3\mathrm{e}^{3\mathrm{j}\omega t} + \cdots \tag{2.34}$$

Progressively differentiating the assumed solution, $R_i(t)$, yields $\dot{R}_i(t) = \mathrm{j}i\omega R_i(\omega)e^{\mathrm{j}i\omega t}$ and $\ddot{R}_i(t) = -i^2\omega^2 R_i(\omega)e^{\mathrm{j}i\omega t}$. By placement of these derivatives in LHS of Eqn. (2.31)and cancellation of exponential term $\mathrm{e}^{\mathrm{j}i\omega t}$ present on RHS by virtue of Eqns.(2.30) and (2.32), equation can be transformed to frequency domain as

$$R_i\left\{(-i^2\omega^2 m) + (\mathrm{j}i\omega c) + (k_0 - k_s)\right\} = \Delta k_{22}\delta_x p_i - k_I I_i \qquad \text{for } i \neq 1 \tag{2.35}$$

and

$$R_1\{(-\omega^2 m) + (\mathrm{j}\omega \mathrm{c}) + (k_0 - k_s)\} = \Delta k_{22}\delta_x p_1 + me\omega^2\mathrm{e}^{\mathrm{j}\beta} - k_I I_1 \quad \text{for } i = 1 \tag{2.36}$$

While, Eqn.(2.33) and (2.34) can be used in estimation of complex harmonics of vibration displacements and AMB currents; Eqns. (2.35) and (2.36) can be used in formulation of identification equations in frequency domain for estimating system parameters.

2.3.1 Estimation of Displacement and Current Harmonics in Time Domain

For estimation of R_i and I_i (complex harmonic amplitude of displacement and current) in time domain, the linear regression can be used. Governing equations are written in regression form as $\mathbf{Ax = b}$, where **A** is the regression matrix or the regressor, **b** is the vector of known quantities and **x** is the intercept, i.e. the vector containing the unknowns to be determined. For betterment of estimation, the complete time domain information may be utilized; Eqns. (2.33) and (2.34) are written for n time instants and converted to regression form as

$$\mathbf{A}_{\mathbf{1}n\times i}\mathbf{x}_{\mathbf{R}i\times 1} = \mathbf{b}_{\mathbf{r}n\times 1} \qquad \text{for displacements} \tag{2.37}$$

and

$$\mathbf{A}_{\mathbf{1}n\times i}\mathbf{x}_{\mathbf{I}i\times 1} = \mathbf{b}_{\mathbf{i_c}n\times 1} \qquad \text{for currents} \tag{2.38}$$

with

$$\mathbf{A}_{\mathbf{1}n\times i} = \begin{bmatrix} 1 & e^{j\omega t_1} & e^{j(2\omega)t_1} & e^{j(3\omega)t_1} & e^{j(5\omega)t_1} & e^{j(7\omega)t_1} & .. & .. & e^{j(-\omega)t_1} & e^{j(-3\omega)t_1} & e^{j(-5\omega)t_1} & .. & .. \\ 1 & e^{j\omega t_2} & e^{j(2\omega)t_2} & e^{j(3\omega)t_2} & e^{j(5\omega)t_2} & e^{j(7\omega)t_2} & .. & .. & e^{j(-\omega)t_2} & e^{j(-3\omega)t_2} & e^{j(-5\omega)t_2} & .. & .. \\ .. & .. & .. & .. & .. & .. & .. & .. & .. & .. & .. & .. & .. \\ .. & .. & .. & .. & .. & .. & .. & .. & .. & .. & .. & .. & .. \\ 1 & e^{j\omega t_n} & e^{j(2\omega)t_n} & e^{j(3\omega)t_n} & e^{j(5\omega)t_n} & e^{j(7\omega)t_n} & .. & .. & e^{j(-\omega)t_n} & e^{j(-3\omega)t_n} & e^{j(-5\omega)t_n} & .. & .. \end{bmatrix} \tag{2.39}$$

$$\mathbf{x}_{\mathbf{R}i\times 1} = \begin{bmatrix} R_0(\omega) & R_1(\omega) & R_2(\omega) & R_3(\omega) & .. & R_{-1}(\omega) & R_{-3}(\omega) & R_{-5}(\omega) & .. \end{bmatrix}^T \tag{2.40}$$

$$\mathbf{b}_{\mathbf{r}n\times 1} = \begin{bmatrix} r_c(t_1) & r_c(t_2) & r_c(t_3) & .. & .. & .. & .. & .. & r_c(t_n) \end{bmatrix}^T \tag{2.41}$$

$$\mathbf{x}_{\mathbf{I}i\times 1} = \lfloor I_0(\omega) \quad I_1(\omega) \quad I_2(\omega) \quad I_3(\omega) \quad I_5(\omega) \quad .. \quad I_{-1}(\omega) \quad I_{-3}(\omega) \quad .. \rfloor^T \tag{2.42}$$

$$\mathbf{b}_{\mathbf{i}_c n\times 1} = \lfloor i_c(t_1) \quad i_c(t_2) \quad i_c(t_3) \quad .. \quad .. \quad .. \quad .. \quad .. \quad i_c(t_n) \rfloor^T \tag{2.43}$$

Herein the matrix $\mathbf{A}_{\mathbf{1}n\times i}$ contains i exponentials for n time instants, vectors $\mathbf{x}_{\mathbf{R}i\times 1}$ and $\mathbf{x}_{\mathbf{I}i\times 1}$ contain the i harmonics of displacement and current, respectively; and the vectors $\mathbf{b}_{\mathbf{r}n\times 1}$ and $\mathbf{b}_{\mathbf{i}_c n\times 1}$ contain the complex displacement and current, respectively, as available in LHS of Eqns. (2.33) and (2.34). Since the regressor is same in both equations (i.e. Eqns. (2.33) and (2.34)), they can be combined to form a single matrix equation

$$\mathbf{A}_2 \begin{Bmatrix} \mathbf{x}_\mathbf{R} \\ \mathbf{x}_\mathbf{I} \end{Bmatrix} = \begin{Bmatrix} \mathbf{b}_\mathbf{R} \\ \mathbf{b}_{\mathbf{Ic}} \end{Bmatrix} \qquad \text{with } \mathbf{A}_2 = \begin{bmatrix} \mathbf{A}_1 & \mathbf{0} \\ \mathbf{0} & \mathbf{A}_1 \end{bmatrix} \tag{2.44}$$

Eqn. (2.44) can be solved to obtain the complex harmonics as

$$\begin{Bmatrix} \mathbf{x}_\mathbf{R} \\ \mathbf{x}_\mathbf{I} \end{Bmatrix} = \left(\mathbf{A}_2{}^\mathbf{T}\mathbf{A}_2\right)^{-1} \mathbf{A}_2{}^\mathbf{T} \begin{Bmatrix} \mathbf{b}_\mathbf{R} \\ \mathbf{b}_{\mathbf{Ic}} \end{Bmatrix} \tag{2.45}$$

For factoring the complex displacement and current signals into complex harmonics in time domain, Eqn. (2.45) can be used. Determination of complex harmonics can be performed in frequency domain with the full spectrum FFT. Detailed procedure of which is presented in the following section.

2.3.2 Estimation of Displacement and Current Harmonics from Full Spectrum

A close examination of Eqns. (2.33) and (2.34) reveals an important aspect of this estimation process: the harmonics can be extracted (in place of estimation in time domain) by using FFT also, which is much faster for all practical purposes. Since the harmonics have negative frequencies also as seen in above equations; full spectrum of the FFT is required. The full spectrum plot is a powerful tool for processing quadrature signals in complex form (Tuma and Bilos, 2004). The full spectrum plot determines whether the rotor orbit frequency components are forward or backward in relation to the direction of the rotor spin; hence, beneficial in presenting a bird eye view of the actual rotor behaviour that is characterized by the forward and backward whirls. Some other methods for obtaining the full spectrum (mainly the amplitude) are discussed in Goldman and Muszynska (1999), Patel and Darpe (2008) and Zhao et al. (2012).

The standard FFT implementation works on the concept of factoring time domain signal into the cosine and sine harmonics of integral frequencies with amplitude and phase such that the addition of these harmonics with due consideration of amplitude and phase is able to reconstruct the original time domain signal. The cosine and sine functions have a phase difference of $\pi/2$ radians, thus representation of the individual FFT harmonics in complex form is possible with cosine terms taken as real and sine terms as imaginary. The output of an FFT process is thus a complex number, representing the cosine and sine terms as discussed. The modulus and angle of this complex number is the amplitude and phase of the particular harmonic. While the amplitude of the harmonic carries information of the size (magnitude) of the time domain signal, information of the shape of the time domain signal is carried in the phase.

The FFT is a linear process but not shift invariant (Smith, 1998), i.e. with shift of time domain signal, the amplitude of the harmonics remains same but the phase changes. This necessitates passing the time domain signal to the FFT algorithm, starting at time instants when the inertial and rotating coordinates shown in Figure 2-2 (a) are aligned to each other, i.e. instants such that $\omega t = 0, 2\pi, 4\pi, \cdots\cdots$. This is necessary for maintaining the consistency between equations of motion and the assumed system configuration. For all practical purposes, it is not possible to capture signal in the aforesaid manner. More details and a numerical example to enunciate the need for phase compensation in full spectrum FFT is available in Appendix-D.

The shortcomings in the phase of harmonics due to random selection of instants of picking time domain signal can be made up for, by making suitable correction in the phase to compensate for the discrepancy. A multi harmonic quadrature reference signal in unison with the spinning rotor has been envisioned and implemented for this purpose. Implementation of the quadrature reference signal and procedure of making phase correction to remove the discrepancy arising due to random instants of picking the time domain signal is presented in the next section.

2.3.3 Multi-Harmonic Quadrature Reference Signal and Phase Compensation Algorithm

For time domain signal starting at different instants, the phase compensation can be made with the help of a reference signal to match the rotor system configuration assumed in this work. A multi harmonic quadrature reference signal is conceptualized and implemented for this purpose. Along with the time domain displacement and current signals, this multi harmonic quadrature reference signal is also passed through the FFT algorithm. All the signals are picked starting at the same time instant. For the displacement and current signals the amplitude and the phase are both important for the present analysis, for the reference signal it's only the phase shift that is useful. The phase

shift suffered by individual harmonic of the reference quadrature is subtracted from the phase of the corresponding displacement and current quadrature harmonics, retaining the amplitude unaltered. The phase compensation of displacement and current quadrature harmonics brings forth consistency with the assumed system configuration.

The output of an FFT process is an array of complex numbers as described in Section 2.3.2. In polar form, this complex array can be written in terms of the magnitude and angle of individual entries. The FFT converts time domain complex displacement signal, r, and complex current signal, i_c, to frequency domain in the following form

$$r(\mathrm{t}) \xrightarrow{\text{FFT}} |R_i| \angle \theta_i(\omega) \ , \quad -\infty \le i \le \infty \ , \qquad i \text{ limited by Nyquist criteria} \tag{2.46}$$

and

$$i_c(\mathrm{t}) \xrightarrow{\text{FFT}} |I_i| \angle \psi_i(\omega) \ , \quad -\infty \le i \le \infty \ , \qquad i \text{ limited by Nyquist criteria} \tag{2.47}$$

wherein $|R_i|$ and $|I_i|$ are the magnitude and θ_i and ψ_i are the phase of the i^{th} harmonic of the displacement and current, respectively. The multi-harmonic complex reference signal has the form

$$s_c(t) = \cos(i\omega t) + \mathrm{j}\sin(i\omega t), \quad i = -n, -(n-1), \ldots -1, 0, 1, \ldots, n \tag{2.48}$$

For all practical purposes, the harmonics that are of importance in Eqns. (2.35) and (2.36) only needs to be present in the reference signal. The FFT process converts the time domain quadrature reference signal to frequency domain as

$$s_c(\mathrm{t}) \xrightarrow{FFT} |s_i| \angle \phi_i(\omega), \qquad i = -n, -(n-1), \ldots -1, 0, 1, \ldots, n \tag{2.49}$$

Here, $|s_i|$ is the magnitude and ϕ_i is the phase of i^{th} harmonic of the complex reference signal upon FFT. With the definition of the reference signal given by Eqn. (2.48), it is evident that $|s_i| = 1$. In terms of the assumed system configuration, angle ϕ_i corresponds to the angle by which i^{th} harmonic of the displacement and current signals passed on to the FFT algorithm is shifted from the assumed system configuration. Subtracting this angle from the phase of i^{th} harmonic of the displacement and current signals, viz. θ_i and ψ_i compensates for the phase shift in the displacement and current harmonics obtained from full spectrum FFT. The displacement and current harmonics duly compensated for the phase shift take the form

$$R_i = |R_i| \angle (\theta_i - \phi_i) \tag{2.50}$$

and

$$I_i = |I_i| \angle (\psi_i - \phi_i) \tag{2.51}$$

The displacement and current harmonics obtained from Eqns. (2.50) and (2.51) are true representation of the time domain signal consistent with the assumed system configuration and can be used in the identification algorithm developed subsequently, without ambiguity.

Since, the availability of the displacement and current harmonics is a prerequisite for the development of identification schemes in frequency domain, both the methods, viz. the regression based and the full spectrum using FFT will be tried and logically compared for the correctness, accuracy and speed.

2.4 Generation of Simulated Responses

A SIMULINK^{TM} model based on Eqn. (2.31) is developed for the generation of simulated displacement and current responses. The SCEF, $s(t)$ is formulated based on Eqn. (2.11). A provision for generating quadrature reference signal of form $\cos(i\omega t) + j\sin(i\omega t)$ with values of i limited to the harmonics of interest, is added in the model. Generation and use of the quadrature reference signal of this form is useful in the phase correction of the quadrature signal used in the identification. The SIMULINK^{TM} block used for the response generation is presented in Figure 2-5.

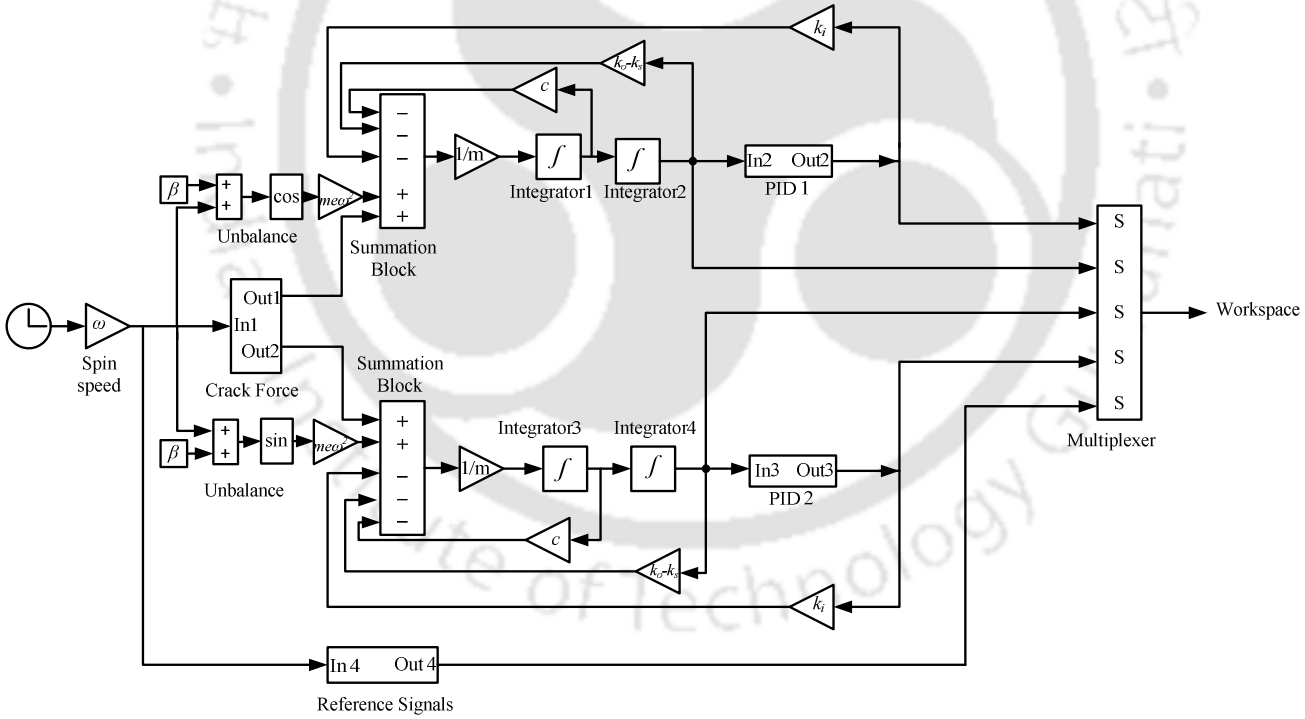

Figure 2-5 SIMULINK^{TM} model used for the response generation

The simulation time is maintained by the SIMULINK™ block 'Clock'. The triangular blocks contain numbers and parameters progressively multiplied. Operating parameters like the spin speed (ω), mass (m) and viscous damping (c) are placed in such blocks. Trigonometric function blocks 'cos' and 'sin' perform the assigned trigonometric function on the incoming signal. Unbalance phase 'β' is placed in constants block. Summation blocks perform algebraic operations over the input signals in the sequence in which the + and – sign appears inside the block. Integrator and differentiator blocks perform the calculus operation over the input signal. Dynamics of main blocks of the above model are

Unbalance Force: For x direction the trigonometric block 'cos' has input $\omega t+\beta$. Multiplied with $me\omega^2$, the output is $me\omega^2 \cos(\omega t+\beta)$. For y direction the output is $me\omega^2 \sin(\omega t+\beta)$.

Crack Force: Input to this sub-block is ωt. Sub-block outputs $\frac{1}{2}s(t)\Delta k_{22}(1+\cos 2\omega t)\delta_x$ and $\frac{1}{2}s(t)\Delta k_{22}(\sin 2\omega t)\delta_x$, in the x and y directions respectively, as provided for in Eqn. (2.22).

Summation Block: This block performs algebraic summation of all force signals in accordance to Eqn. (2.26). The block accumulation amounts to $m\ddot{x}$ and $m\ddot{y}$, respectively, for the x and y directions.

Integration Blocks: These blocks perform numerical integration over the input signal. The sum total of the summation block is the force term. Before the integration block, multiplication by 1/m is performed to obtain the acceleration term. The progressive integration blocks output velocity and displacement, respectively, for both the orthogonal directions.

PID Blocks: The displacement output from the integration block is the input to the PID block. This block executes the simulation for the PID controller in accordance to Eqn.(2.24) and outputs the control current.

Reference Signals Block: This block implements a complex reference signal of the form $\cos(i\omega t)+\mathrm{j}\sin(i\omega t)$. The input to the block is ωt and the individual harmonic sub-block has multiplier i (the harmonic) before passing on the signal to trigonometric blocks. A representative SIMULINKTM block implementing i^{th} complex reference signal is presented in Figure 2-6.

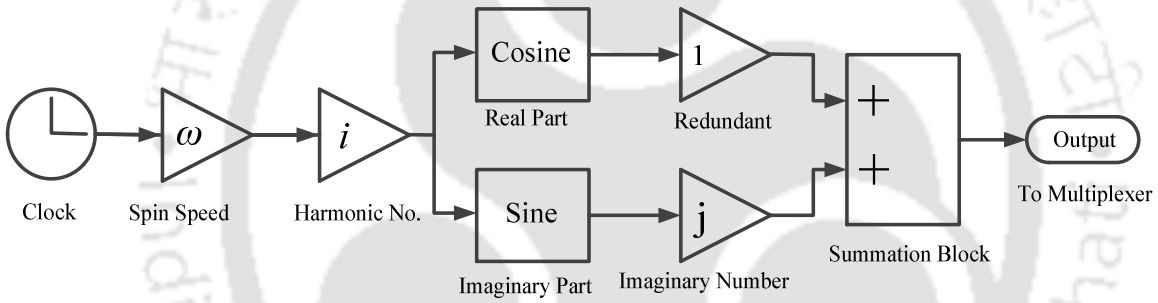

Figure 2-6 One harmonic of multi-harmonic complex reference signal

Bus Creator: Bus creator stacks the multiple incoming signals as a single signal line, with individual signals stacked as individual vectors in the Bus output.

The model offers wide choice for simulation conditions particularly, with or without any of three conditions, viz. the crack, unbalance and AMB, simply by disconnecting the signal flow across the individual component. The effect of relative positioning of crack and unbalance can also be

simulated by varying the angle β in the input. The simulation data used for the response generation is summarized in Table 2-1.

Table 2-1 The rotor and AMB system data for the numerical simulation

Parameters	**Values**		**Parameters**	**Values**	
Disc mass, m	2	kg	*Actuator Factors*		
Intact shaft stiffness, k_0	7.6×10^5	Nm^{-1}	Force – current factor, k_i	42.1	N/A
Additive crack stiffness, Δk_{22}	3×10^5	Nm^{-1}	Force – displacement factor, k_s	105210	N/m
Viscous damping, c	76	Nsm^{-1}	*Controller Gains*		
Phase of unbalance, β	30°	deg.	Proportional, K_P	12200	A/m
Shaft deflection, δx	2.6×10^{-5}	m	Derivative, K_D	3	$A\text{-}s\text{-}m^{-1}$
Disc eccentricity, e	24	μm	Integral, K_I	2000	A/(m-s)

Numerical values of the intact shaft stiffness – k_0 and the shaft static deflection – δx, are based on mild steel shaft material of length 500 mm and 16 mm diameter carrying a disc mass of 2 kg and reported in Shravankumar and Tiwari (2014). Gains of the PID controller used in the simulation are based on the performance optimization study on gain parameters by Bordoloi and Tiwari (2013). The response is generated with a fourth-order Runga-Kutta integration solver. A typical response of the vibration displacement and the AMB control current obtained at the shaft spin speed of 1500 rpm (25 Hz) is presented in Figure 2-7.

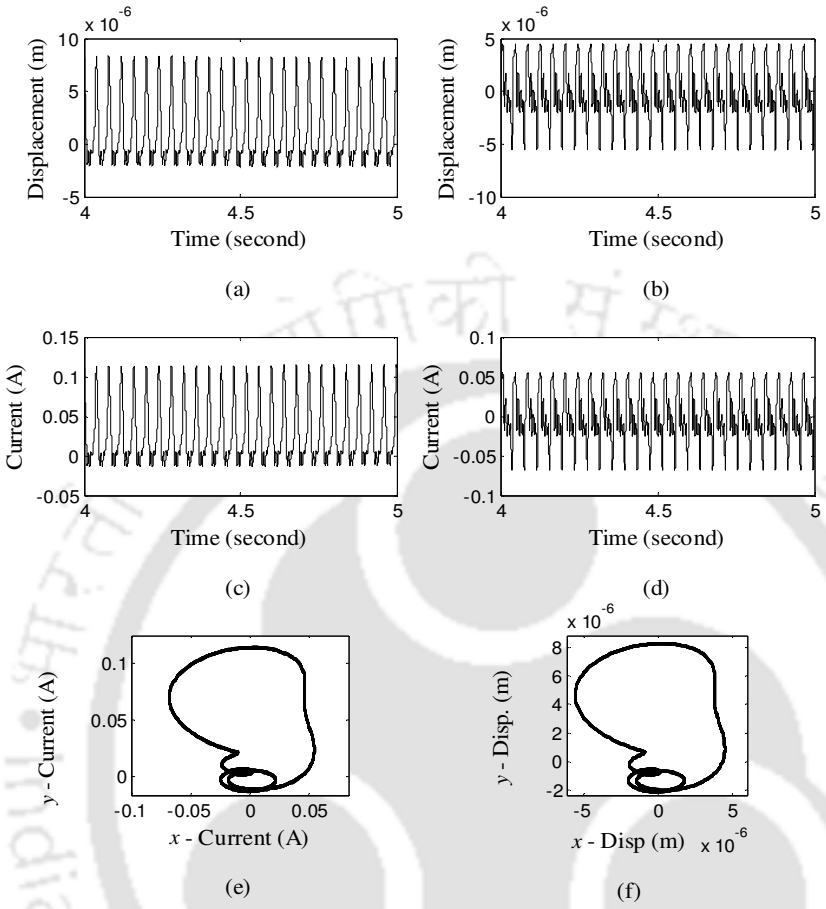

Figure 2-7 Generated response (a) *x*-displacement (b) *y*-displacement (c) *x*-current (d) *y*-current (e) current orbit (f) shaft centreline orbit

The effect of presence of AMB on the rotor behaviour can be studied by comparison of the response of the rotor with and without AMB support. The response of vibration displacements at 1500 rpm in two directions and the shaft centreline orbit are generated with rotor properties as detailed in Table 2-1, in absence of AMB in the support system. The response of the rotor with and without AMB in the support system is presented in Figure 2-8 and it may be seen that the presence

of AMB reduces the magnitude of the vibration displacement. The centreline orbit also gets diminished.

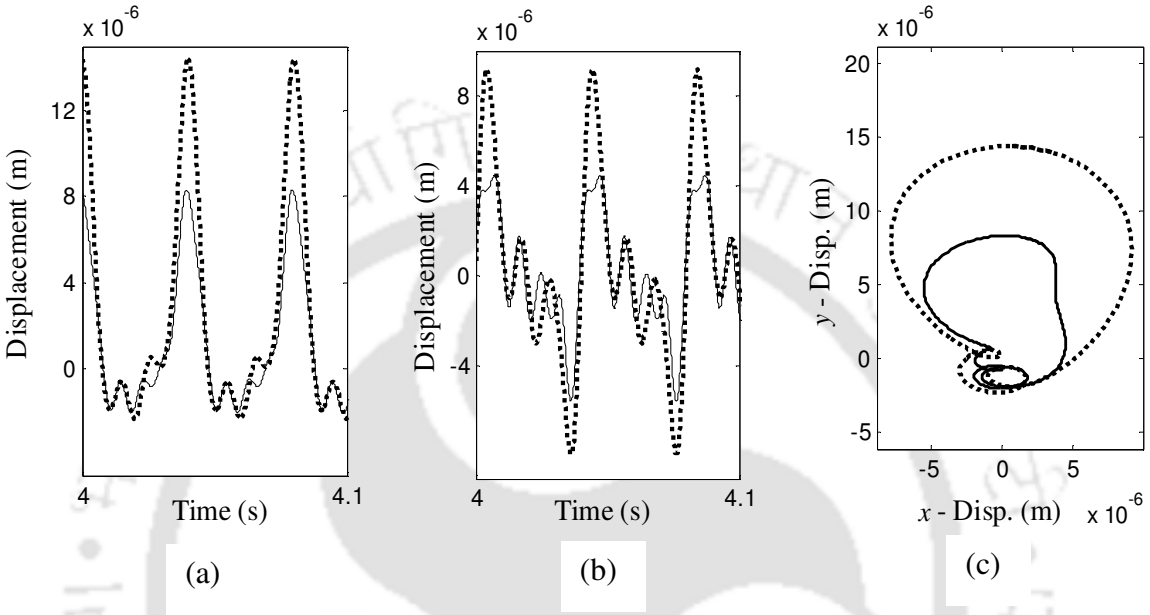

Figure 2-8 Rotor response without AMB (- - -) and with AMB (──): (a) *x*-displacement (b) *y*-displacement (c) shaft centreline orbit

Since the unbalance force increases with the square of angular velocity of the shaft, at higher spin speeds, the response due to the crack is overshadowed by response due to the unbalance, in time domain signal. In such cases, the shaft centerline orbit will not exhibit the characteristic double loop discussed in literature, for instance – Sinou and Lees (2005) and Shravankumar and Tiwari (2013). At lower speeds the crack effect is visible in time domain also, as seen in displacement response at a spin speed of 900 rpm (15 Hz) in Figure 2-9.

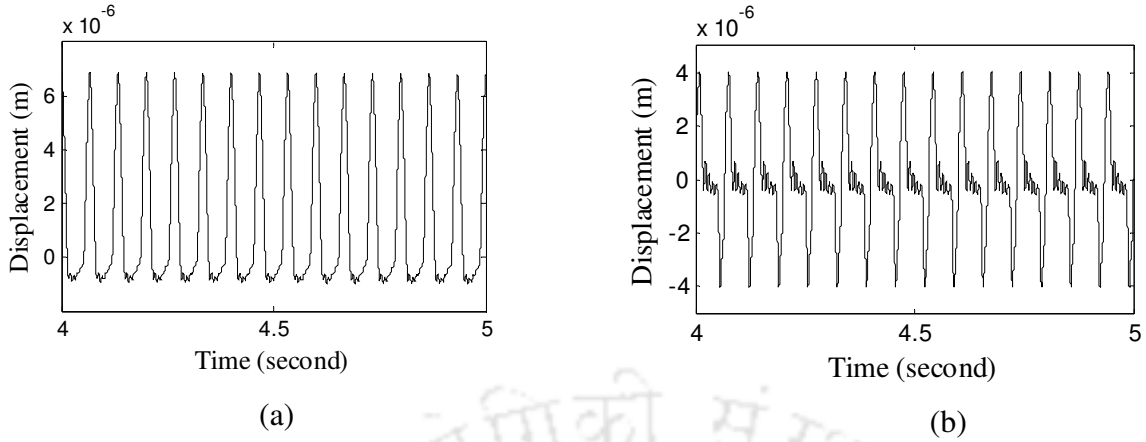

Figure 2-9 Response generated at 900 rpm (a) *x*-displacement (b) *y*-displacement

In general, the shape of the orbit plot is indicative of the type of rotor defects and the size of the orbit plot indicates the severity of defects, for example – a circular orbit plot indicates a dominant unbalance in the rotor, the magnitude of which is directly proportional to the radius of the orbit. Since, for the rotor health monitoring, the motion of the rotor is characterized by the forward and backward whirls; more information about the rotor condition could be obtained by analyzing the participation of individual harmonics that constitutes the response signal. The analysis of participating harmonics could be performed by the regression analysis as detailed in Section 2.3.1 or by full spectrum of the frequency transformed response as detailed in Section 2.3.2. A comparison of the speed, the accuracy and adequacy of both methods is presented in the next section.

2.5 Harmonic Analysis of Generated Responses

The analysis is performed for the segregation of displacement and current harmonics, R_i and I_i, respectively. Segregation of R_i and I_i can be performed in time domain as described in Section 2.3.1 or frequency domain as described in Section 2.3.2. The frequency domain approach for the

segregation of these harmonics involves the phase compensation to account for the discrepancy in signal processing via full spectrum and the assumed system configuration. The segregation in both domains has been attempted and a critical comparison made of their ability to reproduce the original signal from R_i and I_i. The time domain segregation of R_i and I_i is made using Eqn. (2.45). For the simulated response at 157 rad/s, complex harmonics of displacement and current obtained are presented in Table 2-2.

Table 2-2 Displacement and current harmonics obtained in time domain

Harmonic (i)	Displacement (R_i)		Current (I_i)	
	Amplitude (m)	Phase (deg.)	Amplitude (A)	Phase (deg.)
0	1.2×10^{-6}	-0.05	2.75×10^{-2}	0.04
1	3.17×10^{-6}	7.97	3.88×10^{-2}	10.15
2	2×10^{-6}	-3.73	2.45×10^{-2}	-0.66
3	1.13×10^{-6}	-7.48	1.39×10^{-2}	-0.89
5	9.68×10^{-7}	68.44	1.21×10^{-3}	79.27
7	5.61×10^{-8}	-169.8	7.18×10^{-4}	-155.08
-1	7.39×10^{-7}	1.64	9.02×10^{-3}	-0.6
-3	2.26×10^{-7}	-172.57	2.78×10^{-3}	-179.04
-5	4.15×10^{-7}	111.55	5.2×10^{-3}	100.73

For verification of the accuracy of this segregation to individual harmonics, the displacement and current signals were reconstructed using these harmonic components and compared to original signals, from which they were factored. At this stage only those harmonics that would be used in the identification purpose (i.e., i = -5, -3, -1, 0, 1, 2, 3, 5, and 7) in subsequent work, are considered, and the displacement and current signals regenerated by the time integration of Eqns. (2.33) and (2.34). When plotted on the same time scale, the reconstructed signal completely covers the original signal. For easy interpretation, the reconstructed signal is subtracted from the original signal and the root mean square value of the difference obtained and compared with the

root-mean-square (RMS) value of the original signal. The RMS values of the difference are 3.45×10^{-3}, 3.24×10^{-3}, 4×10^{-3} and 3.47×10^{-3} % of the original signal RMS values for the *x*-displacement, *y*-displacement, *x*-current and *y*-current, respectively.

Greater accuracy and speed is expected in determination of R_i and I_i from the full spectrum with the help of FFT. The procedure and application of FFT to deal with quadrature signals is well established. For a correct and meaningful application of the full spectrum certain cautions are to be observed. The frequency bin created in the FFT process must be integral multiple of frequencies of interest to minimize the leakage error. This can be achieved by correctly deciding the sampling length, as a ratio of sampling frequency that yields frequencies of interest in discrete bins. Since, in a field application it may not be possible to consider an integral number of response waveform, for passing on to the FFT algorithm: the phase correction of complex harmonics needs to be done to tackle this deficiency. The algorithm developed for this purpose has been presented in Section 2.3.3. The implementation of a quadrature reference signal of multiple frequencies as depicted in Figure 2-6, helps in this correction.

The simulation was run for 5 s and the response for the duration 4s-5s (1 s time length) was considered for the analysis. The initial 4 s response was discarded to let transients disappear. Since the PID controller is one of components in the simulation, greater settling time is required due to integrator action of the controller. The step size of simulation for response generation was 0.0001 s, thus the response has a sampling rate of 10 kHz. The signal considered for the analysis also has 10000 data points in each vector, these 10000 data points out of 50000 points of the SIMULINK^{M} output were used to define the displacement and current quadrature. For spin speeds

considered for this numerical experiment, a frequency bin is ensured for integral multiples of every spin speed by this choice of number of data points; any chance of the leakage error was eliminated. The standard FFT function of MATLAB^{TM}, based on Cooley and Tukey (1965) algorithm was used to obtain the full spectrum. Since, the input to the FFT function here was quadrature and not real valued signal, the symmetry of the FFT does not exist, therefore all negative frequencies were retained for the analysis and plot. This procedure of retaining the negative part of the frequency spectrum along with the positive spectrum gives rise to *full spectrum* analysis. Full spectrum plots of the displacement and current are presented in Figure 2-10.

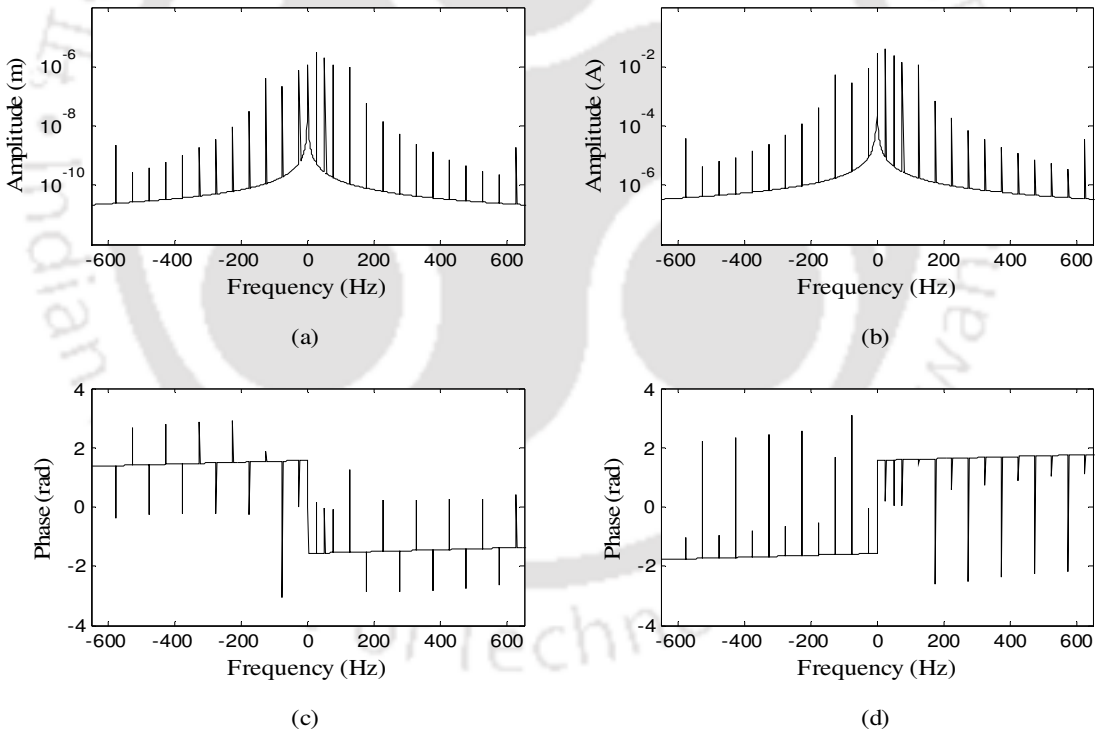

Figure 2-10 Full spectrum plots (a) amplitude of quadrature displacement(b) amplitude of quadrature current (c) phase of quadrature displacement (d) phase of quadrature current

The full spectrum plots of the displacement and AMB current signals can be used to pick the participating harmonics, utilizing the standard *peak detection* algorithm of MATLAB™. When the sampling frequency and the number of data points in the sample array are known, the harmonics can also be picked by using the index of the array elements. In the present work, array indexing has been utilized to pick the harmonics. As is visible in Figure 2-10, the magnitude of the harmonics beyond 7th harmonic are quite insignificant – the harmonics picked are i = -5, -3, -1, 0, 1, 2, 3, 5, and 7. As compared to the regression based method, where in the harmonics to be identified are pre-defined in the algorithm, FFT based full spectrum method identifies all the harmonics allowed under the Nyquist criteria. The R_i and I_i obtained from the full spectrum using FFT analysis are summarized in Table 2-3.

Table 2-3 The phase corrected displacement and current harmonics obtained from the full spectrum

Harmonic	Reference signal	Displacement (R_i)		Current (I_i)	
(i)	Phase (deg.)	Amplitude	Phase (deg.)	Amplitude (A)	Phase(deg.)
0	0	1.2×10^{-6}	-0.05	2.75×10^{-2}	0.04
1	0.9	3.17×10^{-6}	7.97	3.88×10^{-2}	10.15
2	1.8	2×10^{-6}	-3.73	2.45×10^{-2}	-0.66
3	2.7	1.13×10^{-6}	-7.48	1.39×10^{-2}	-0.89
5	4.5	9.68×10^{-7}	68.44	1.21×10^{-3}	79.27
7	6.3	5.61×10^{-8}	-169.8	7.18×10^{-4}	-155.08
-1	-0.9	7.39×10^{-7}	1.64	9.02×10^{-3}	-0.6
-3	-2.7	2.26×10^{-7}	-172.57	2.78×10^{-3}	-179.04
-5	-4.5	4.15×10^{-7}	111.55	5.2×10^{-3}	100.73

For full spectrum based method, values of the RMS difference for *x*-displacement, *y*-displacement, *x*-current and *y*-current are 1.13×10^{-3}, 3.69×10^{-4}, 1.43×10^{-3} and 3.99×10^{-4} %, respectively, of original signal values.

The phase shift of the harmonics of reference signal as presented in Table 2-3, indicates the amount of phase correction required for correct representation of the displacement and current harmonics. After the phase correction, comparison of R_i and I_i in Table 2-2 and Table 2-3 indicates them to be identical. Since the R_i and I_i obtained from both the methods are identical, both are able to reconstruct the original signal in time domain. Since the error in reconstruction of the original signal is very small in both methods for the simulation generated response, both the methods appear equally efficient in factoring R_i and I_i. Nevertheless, the FFT based full spectrum method registers significantly lower values of error RMS. For the limited performance comparison test of the two methods (based on the existing work only) on the MATLAB^{TM} platform, the full spectrum based factoring completed in 5.138×10^{-3} s as compared to the regression based time domain factoring which completed in 2.0785 s; the full spectrum based method was nearly 400 times faster.

This section compares two methods used for extracting the participating displacement and current harmonics from time domain signals. The FFT based full spectrum extraction method has been found fast and more accurate compared to the regression based method.

2.6 Development of Identification Algorithm

The identification of crack is accomplished with a single parameter of additive crack stiffness, Δk_{22}. The identification algorithm is developed to simultaneously identify the viscous damping – c, unbalance magnitude – e and phase – β, AMB force-displacement constant k_s and AMB force-current constant k_i. The frequency domain equations of motion Eqns.(2.35) and (2.36) are rearranged to have all the identifiable parameters on the LHS and the known quantities on the RHS. This is prerequisite for formulation of regression equations. The real and imaginary parts of the complex equation are separated. The number of equations available for the identification is double of the number of harmonics identified in the full spectrum, because the real and imaginary parts of Eqns. (2.35) and (2.36) are separated.

The complex displacement and current harmonics are split in the real and imaginary parts as

$$R_i = R_{i,\mathrm{Re}} + \mathrm{j}R_{i,\mathrm{Im}} \ , \quad I_i = I_{i,\mathrm{Re}} + \mathrm{j}I_{i,\mathrm{Im}} \tag{2.52}$$

The complex unbalance is split as

$$me\omega^2 \mathrm{e}^{\mathrm{j}\beta} = m\omega^2(e\cos\beta + \mathrm{j}e\sin\beta) = m\omega^2(e_{real} + \mathrm{j}e_{imag}) \tag{2.53}$$

Eqns. (2.35) and (2.36) are accordingly modified as

$$(R_{i,\mathrm{Re}} + \mathrm{j}R_{i,\mathrm{Im}})\{(-i^2\omega^2 m) + (\mathrm{j}i\,\omega c) + (k_0 - k_s)\} = \Delta k_{22}\delta_{st} p_i - k_I(I_{i,\mathrm{Re}} + \mathrm{j}I_{i,\mathrm{Im}}) \tag{2.54}$$

and

$$\begin{aligned}(R_{1,\mathrm{Re}} + \mathrm{j}R_{1,\mathrm{Im}})\{(-\omega^2 m) + (\mathrm{j}\omega c) + (k_0 - k_s)\} &= \Delta k_{22}\delta_{st} p_1 \\ &+ m\omega^2(e_{\mathrm{Re}} + \mathrm{j}e_{\mathrm{Im}}) - k_I(I_{1,\mathrm{Re}} + \mathrm{j}I_{1,\mathrm{Im}})\end{aligned} \tag{2.55}$$

Equating the real and imaginary parts of LHS and RHS of above equations

$$-i^2\omega^2 mR_{i,\mathrm{Re}} - \mathrm{i}\,\omega cR_{i,\mathrm{Im}} + k_0 R_{i,\mathrm{Re}} - k_s R_{i,\mathrm{Re}} = \Delta k_{22}\delta_{st} p_i - k_I I_{i,\mathrm{Re}} \tag{2.56}$$

$$-i^2\omega^2 mR_{i,\mathrm{Im}} + \mathrm{i}\,\omega cR_{i,\mathrm{Re}} + k_0 R_{i,\mathrm{Im}} - k_s R_{i,\mathrm{Im}} = -k_I I_{i,\mathrm{Im}} \tag{2.57}$$

$$-\omega^2 mR_{1,\mathrm{Re}} - \omega cR_{1,\mathrm{Im}} + k_0 R_{1,\mathrm{Re}} - k_s R_{1,\mathrm{Re}} = \Delta k_{22}\delta_{st} p_1 + m\omega^2 e_{\mathrm{Re}} - k_I I_{1,\mathrm{Re}} \tag{2.58}$$

$$-\omega^2 mR_{1,\mathrm{Im}} + \omega cR_{1,\mathrm{Re}} + k_0 R_{1,\mathrm{Im}} - k_s R_{1,\mathrm{Im}} = m\omega^2 e_{\mathrm{Im}} - k_I I_{1,\mathrm{Im}} \tag{2.59}$$

Rearranging above equations for regression equations and placing redundant zeros for quantities appearing in first harmonic only

$$-i\omega cR_{i,\mathrm{Im}} - \Delta k_\xi \delta_{st} p_i - 0 - 0 - k_s R_{i,\mathrm{Re}} + k_I I_{i,\mathrm{Re}} = (i^2\omega^2 m - k_0) R_{i,\mathrm{Im}} \tag{2.60}$$

$$-i\omega cR_{i,\mathrm{Re}} - 0 - 0 - 0 - k_s R_{i,\mathrm{Im}} + k_I I_{i,\mathrm{Im}} = (i^2\omega^2 m - k_0) R_{i,\mathrm{Im}} \tag{2.61}$$

$$-\omega cR_{1,\mathrm{Re}} - \Delta k_{22}\delta_{st} p_1 - m\omega^2 e_{\mathrm{Re}} - 0 - k_s R_{1,\mathrm{Re}} + k_I I_{1,\mathrm{Re}} = (\omega^2 m - k_0) R_{1,\mathrm{Re}} \tag{2.62}$$

$$-\omega cR_{1,\mathrm{Im}} - 0 - 0 - m\omega^2 e_{\mathrm{Im}} - k_s R_{1,\mathrm{Im}} + k_I I_{1,\mathrm{Im}} = (\omega^2 m - k_0) R_{1,\mathrm{Im}} \tag{2.63}$$

In above equations all identifiable parameters, viz. c, Δk_{22}, e_{Re}, e_{Im}, k_s and k_I (viscous damping, additive crack stiffness, unbalance magnitude, unbalance phase, AMB force-displacement constant and AMB force-current constant, respectively) are available in terms in the LHS, and the RHS contains terms with known parameter. For performing the linear regression, Eqns. (2.60) through (2.63) can be written in matrix form as

$$\begin{bmatrix} -\omega R_{1,\mathrm{Im}} & -\delta_x p_1 & -m\omega^2 & 0 & -R_{1,\mathrm{Re}} & I_{1,\mathrm{Re}} \\ 0 & -\delta_x p_0 & 0 & 0 & -R_{0,\mathrm{Re}} & I_{0,\mathrm{Re}} \\ -2\omega R_{2,\mathrm{Im}} & -\delta_x p_2 & 0 & 0 & -R_{2,\mathrm{Re}} & I_{2,\mathrm{Re}} \\ -3\omega R_{3,\mathrm{Im}} & -\delta_x p_3 & 0 & 0 & -R_{3,\mathrm{Re}} & I_{3,\mathrm{Re}} \\ -5\omega R_{5,\mathrm{Im}} & -\delta_x p_5 & 0 & 0 & -R_{5,\mathrm{Re}} & I_{5,\mathrm{Re}} \\ \vdots & \vdots & \vdots & \vdots & \vdots & \vdots \\ \omega R_{-1,\mathrm{Im}} & -\delta_x p_{-1} & 0 & 0 & -R_{-1,\mathrm{Re}} & I_{-1,\mathrm{Re}} \\ 3\omega R_{-3,\mathrm{Im}} & -\delta_x p_{-3} & 0 & 0 & -R_{-3,\mathrm{Re}} & I_{-3,\mathrm{Re}} \\ \vdots & \vdots & \vdots & \vdots & \vdots & \vdots \\ \omega R_{1,\mathrm{Re}} & 0 & 0 & -m\omega^2 & -R_{1,\mathrm{Im}} & I_{1,\mathrm{Im}} \\ 0 & 0 & 0 & 0 & -R_{0,\mathrm{Im}} & I_{0,\mathrm{Im}} \\ 2\omega R_{2,\mathrm{Re}} & 0 & 0 & 0 & -R_{2,\mathrm{Im}} & I_{2,\mathrm{Im}} \\ 3\omega R_{3,\mathrm{Re}} & 0 & 0 & 0 & -R_{3,\mathrm{Im}} & I_{3,\mathrm{Im}} \\ 5\omega R_{5,\mathrm{Re}} & 0 & 0 & 0 & -R_{5,\mathrm{Im}} & I_{5,\mathrm{Im}} \\ \vdots & \vdots & \vdots & \vdots & \vdots & \vdots \\ -\omega R_{-1,\mathrm{Re}} & 0 & 0 & 0 & -R_{-1,\mathrm{Im}} & I_{-1,\mathrm{Im}} \\ -3\omega R_{-3,\mathrm{Re}} & 0 & 0 & 0 & -R_{-3,\mathrm{Im}} & I_{-3,\mathrm{Im}} \\ \vdots & \vdots & \vdots & \vdots & \vdots & \vdots \end{bmatrix} \begin{Bmatrix} c \\ \Delta k_\xi \\ e_{\mathrm{Re}} \\ e_{\mathrm{Im}} \\ k_s \\ k_I \end{Bmatrix} = \begin{Bmatrix} (\omega^2 m - k_0) R_{1,\mathrm{Re}} \\ -k_0 R_{0,\mathrm{Re}} \\ (4\omega^2 m - k_0) R_{2,\mathrm{Re}} \\ (9\omega^2 m - k_0) R_{3,\mathrm{Re}} \\ (25\omega^2 m - k_0) R_{5,\mathrm{Re}} \\ \vdots \\ (\omega^2 m - k_0) R_{-1,\mathrm{Re}} \\ (9\omega^2 m - k_0) R_{-3,\mathrm{Re}} \\ \vdots \\ (\omega^2 m - k_0) R_{1,\mathrm{Im}} \\ -k_0 R_{0,\mathrm{Im}} \\ (4\omega^2 m - k_0) R_{2,\mathrm{Im}} \\ (9\omega^2 m - k_0) R_{3,\mathrm{Im}} \\ (25\omega^2 m - k_0) R_{5,\mathrm{Im}} \\ \vdots \\ (\omega^2 m - k_0) R_{-1,\mathrm{Im}} \\ (9\omega^2 m - k_0) R_{-3,\mathrm{Im}} \\ \vdots \end{Bmatrix} \tag{2.64}$$

which is a standard matrix formulation $\mathbf{Ax = b}$, with individual vector and matrices as available in Eqn. (2.64). This matrix equation has sufficient constituent equations to enable a solution by least-squares regression and can be solved as

$$\mathbf{x} = (\mathbf{A}^{\mathrm{T}}\mathbf{A})^{-1}\mathbf{A}^{\mathrm{T}}\mathbf{b} \tag{2.65}$$

To study the effect of a range of rotor spin speeds on performance of the estimation procedure, it may be essential to accommodate information from more spin speeds. In such cases, with *n* spin speeds considered in the range of interest, the regression matrices will take the form, as

$$\begin{bmatrix} \mathbf{A}(\omega_1) \\ \mathbf{A}(\omega_2) \\ \vdots \\ \mathbf{A}(\omega_n) \end{bmatrix} \mathbf{x} = \begin{Bmatrix} \mathbf{b}(\omega_1) \\ \mathbf{b}(\omega_2) \\ \vdots \\ \mathbf{b}(\omega_n) \end{Bmatrix} \tag{2.66}$$

and can be solved as Eqn. (2.65). The results obtained on the estimation of parameters covered in the identification algorithm are presented in the next section.

2.7 Results and Discussions

To ascertain the range of spin speeds to test the identification algorithm, a numerical ramp up of the cracked rotor model is performed and the Hilbert envelope of the displacement response is obtained. Hilbert envelope of the displacement response presents a clear view of the critical speed and magnitude of peak displacements at critical speeds. Use of Hilbert transform to obtain the envelope of analytic signals and many other applications has been discussed by Feldman (2011). A 20 s numerical ramp up was simulated with constant angular acceleration of 50 rad/s^2. The displacement history and the envelope of displacement response along x direction, obtained by Hilbert transform is presented in Figure 2-11.

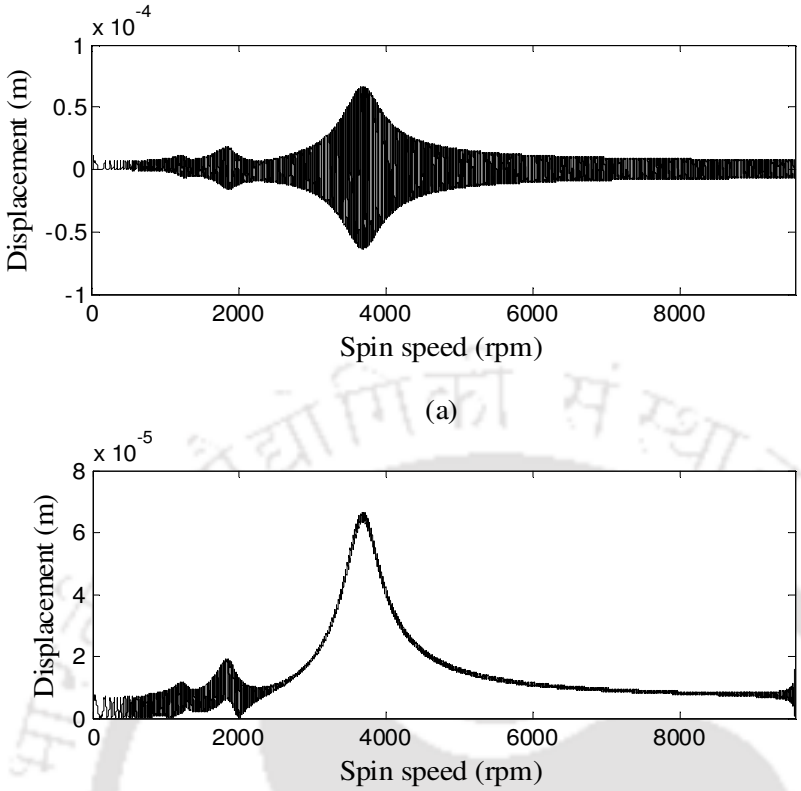

Figure 2-11 (a) *x*-displacement response during ramp up (b) Envelope of *x*-displacement response during ramp up

The 1× resonance is observed at 3684 rpm with peak displacement of 8.723×10^{-5} m. The $\frac{1}{2}\times$ and $\frac{1}{3}\times$ resonances are observed at 1841 rpm and 1222 rpm respectively, with corresponding peak displacements of 2.289×10^{-5} m and 1.283×10^{-5} m, respectively. Vibration displacements at 5527 rpm is observed at 1.275×10^{-5} m and higher spin speeds (limited up to 10000 rpm) register vibration displacements lower than it. For testing the algorithm, two speed ranges are selected – the lower speed range below 1617 rpm (vibration displacement below 1.194×10^{-5} m) and the higher speed range above 5527 rpm (vibration displacement below 1.008×10^{-5} m). Spin speeds used for identification are presented in Table 2-4.

Table 2-4 Spin speeds used for identification

Speed range	Spin speeds (rpm)
Lower	1140, 1200, 1260, 1320, 1380, 1440, 1500, 1560, 1620 (19 -27 Hz)
Upper	5520, 5580, 5640, 5700, 5760, 5820, 5880, 5940, 6000 (92 -100 Hz)

To simulate real measurement conditions and to ascertain robustness of the identification procedure against instrument and measurement errors, random noise of 1%, 2%, and 5% are added serially to the generated response. Here, the Gaussian white noise is used for the simulation. It is defined as a statistical noise that has its probability density function equal to that of the normal distribution. It is a random signal with a flat power spectral density, uncorrelated and normally distributed with a mean zero and unit variance. The noising response signal could be obtained as

$$r_{noise}(t) = r(t) + \left\{ r(t) \frac{(R_{and} - 0.5) N_p}{100} \right\} \tag{2.67}$$

Here, $r(t)$ is the vibration displacement signal as in Eqn. (2.27), R_{and} is a random scalar value with mean 0 and standard deviation 1 and N_p is the noise %. Noisy response for AMB current is obtained similarly.

The random noise is generated with 4 different seeds and channeled to the 4 responses, viz. the x and y direction displacements and the x and y direction currents. Results of the estimation based on two speed ranges noted in Table 2-4, with clean and noise corrupted response signal are summarized in Table 2-5 and Table 2-6. It may be noted here that harmonics of vibration

displacements and AMB control currents for this estimation has been obtained from the FFT based full spectrum method.

Table 2-5 Noise sensitivity of parameters estimated in lower speed range

Parameter	Assumed value	Estimated value at various noise			
		0%	1%	2%	5%
c	76 (Ns m-1)	75.3	75.32	74.72	74.69
	% error	-0.92	-0.88	-1.67	-1.71
Δk_{22}	3×10^5 (N/m)	299490	299190	299770	299010
	% error	-0.16	-0.26	-0.8	-0.33
e	24 (μm)	23.95	23.92	23.97	24.27
	% error	-0.21	-0.32	-0.14	1.13
β	30º (deg.)	30.002	30.007	30.002	30.001
	% error	0.008	0.023	0.006	0.002
k_s	105210 (N/m)	106410	106510	106520	106960
	% error	1.14	1.24	1.25	1.66
k_I	42.1 (N/A)	42.12	42.12	42.13	42.11
	% error	0.04	0.04	0.05	0.03

It is noticeable from Table 2-5 that the estimation in lower speed range is quite robust against instrument errors. With up to 5% noise, the error introduced by noise is not severe for any of the parameters but the AMB constants k_s and within limits acceptable for the identification purpose. It may be seen that k_s shows the maximum estimation error with clean signal also. Estimates of additive crack stiffness (Δk_{22}) and unbalance (e and β) are particularly less affected by noise. The results of identification in higher speed range is presented in Table 2-6.

Table 2-6 Noise sensitivity of parameters estimated in higher speed range

Parameter	Assumed value	Estimated value at various noise			
		0%	1%	2%	5%
c	76 (Ns m-1)	75.86	75.71	75.57	78.52
	% error	-0.18	-0.37	-0.56	3.31
Δk_{22}	3×10^5 (N/m)	299820	299930	299050	300210
	% error	-0.06	-0.02	-0.32	0.07
e	24 (μm)	23.95	23.96	23.94	24.14
	% error	-0.28	-0.16	-0.24	0.59
β	30º (deg.)	30.04	30.04	29.83	30.06
	% error	0.13	0.13	-0.57	0.2
k_s	105210 (N/m)	107490	108470	102660	100960
	% error	2.17	3.09	-2.42	-4.03
k_I	42.1 (N/A)	42.157	42.253	41.77	41.9
	% error	0.14	0.36	-0.77	-0.45

Comparison of results in Table 2-4(a) and Table 2-4(b) indicates more error of estimation of k_s (AMB force-displacement factor) in higher speed range. With clean response signal, the error in estimation of k_s is 2.17% in higher speed range as compared to 1.14% in lower speed range. Other parameters are estimated with similar accuracy in both the speed ranges. It is notable that the noise corruption of response signals has greater effects in higher speed range as compared to the lower speed range, which is particularly pronounced in estimation of k_s and c (viscous damping).

Due to multiple operational constraints, measurement of model parameters (known parameters in the grey box modelling) may contain errors which in turn would introduce error in the estimation process. Such errors are commonly known as the modelling error or bias. To simulate the modelling error and its impact on the identification algorithm, random errors (in form of noise) in range of 1%, 2% and 5% of the correct values are introduced in numerical model parameters, viz. mass (m), intact shaft stiffness (k_0) and shaft static deflection (δ_x). The response is generated in

accordance to Eqn. (2.31) with correct model parameters and then the error is added in model parameters in Eqn. (2.66) used for estimation in identification algorithm. Thus, correct response is used in a model containing error and the estimates obtained are compared with the assumed values to quantify estimation error due to bias error. Effect of bias error magnitude on results of estimation in lower speed range is summarized in Table 2-7. The effect of bias error is similar in higher speed range also and thus not included here.

Table 2-7 Sensitivity of estimated parameters to the modelling error

Parameter	Assumed value	Estimated value at various bias error level			
		0%	1%	2%	5%
c	76 (Ns m^{-1})	75.3	76.43	76.92	79.01
	% error	-0.92	0.56	1.21	3.96
Δk_{22}	3×10^5 (N/m)	299490	299820	299180	308120
	% error	-0.16	-0.06	-0.27	2.7
e	24 (μm)	23.95	23.96	23.96	23.96
	% error	-0.21	-0.13	-0.13	-0.13
β	30º (deg)	30.002	30.002	30.002	30.002
	% error	0.008	0.008	0.008	0.008
k_s	105210	106410	108020	112780	114720
	% error	1.14	2.67	7.23	9.51
k_I	42.1(N/Amp)	42.12	42.14	42.34	44.07
	% error	0.04	0.09	0.57	4.68

The developed identification algorithm found to be robust against bias errors. From Table 2-7, it is observed that rotor parameters are the least affected by bias errors with the additive crack stiffness (Δk_{22}) deviating a maximum by 2.7% and viscous damping (c) by 3.96% at 5% bias error. AMB constants k_s and k_I are most vulnerable with 9.51% and 3.61% deviation, respectively, at 5% bias error.

2.8 Concluding Remarks

In this chapter, system EOMs for a 2 DOF model for the cracked rotor with AMB support has been obtained. Numerical illustrations are performed on a sample rotor –AMB data, and the time and frequency responses are studied. The methods for obtaining the forward and reverse components of the spectrum of the rotor displacement and AMB current have been compared and FFT based full spectrum method found better suited as compared to the regression based method. In quest of correcting the phase ambiguity introduced in the FFT process, a multi harmonic reference signal has been conceptualized and implemented, giving rise to the phase correction algorithm developed in this chapter. Now on, for the subsequent chapters, the harmonics of rotor displacement and AMB current signals would be obtained with the phase corrected FFT based full spectrum.

The development and testing of an identification algorithm for identification of transverse crack (identified by parameter - Δk_{22}, the additive crack stiffness) and the rotor –AMB system parameters along with the viscous damping and rotor unbalance has been performed using the frequency domain equations developed in this chapter. The developed algorithm has been found robust against moderate level of instrument and modeling errors. Also, the possibility of crack and other system parameter identification, with incorporation of AMB current as one of the observables could be demonstrated for a simplified 2-DOF model.

The present chapter develops a frame work for the crack and other system parameter identification in case of cracked rotors with the AMB support. The framework developed could be applied to a more realistic model, where the requirement of placement of the disc at the central plane of the rotor is eased out. Since the static deflection curve of the rotor, on the placement of disc away from

the central plane, is not symmetric on both the sides of the disc – the disc experiences wobbling when the rotor spins. In such cases the rotor will experience gyroscopic effects in addition to other effects considered in the present chapter, thus necessitating use of a 4-DOF model for the analysis. Apart from the quantification of linear vibration displacements, quantification and measurements of angular displacements of the disc also becomes necessary. But, in practical cases due to very small magnitudes of the angular displacements, its accurate measurement may not be plausible. Thus the identification algorithm developed for such rotors must take into account the requirement of removal of unmeasurable DOFs from the algorithm.

Analysis of a cracked rotor with disc offset from the central plane is presented in the next chapter. It contains a dynamic analysis of the system with intent of development of an identification algorithm and reduction of the unmeasurable DOFs of the model.

CHAPTER 3

Crack Identification in Rotor–AMB Systems Carrying an Offset Disc

3.1 Introduction

The governing equations of motion of a cracked Jeffcott rotor with the AMB support were developed in the previous chapter, which were solved to obtain the vibration displacement and AMB current responses. Two methods to transform the time domain responses to frequency domain, i.e. to obtain the full spectrum of the displacement and current signals were explored, and FFT based method of extracting the full spectrum of the time domain signal was found more suitable for our work. The present chapter explores the possibility of application of methods developed in chapter 2, to rotors with offset disc. This rotor configuration necessitates use of analysis based on 4-DOF model with gyroscopic effects, which introduces additional complexity in the present approach in the form of skew-symmetry in the gyroscopic matrix. The Identification algorithm has been developed in frequency domain with the harmonics of vibration displacement and AMB current obtained by methods described in Chapter 2. Identification algorithm is developed based on an inverse problem approach, and the estimates are obtained using the least-squares estimation method.

In the present chapter, a 4-DOF cracked rotor is modelled considering the gyroscopic effect due to the offset disc and a switching crack excitation function to introduce the breathing of crack. The dynamic reduction is applied to eliminate rotational displacements, which would pose practical difficulty in its accurate measurement, from the system equations of motion to develop an identification algorithm. An algorithm developed with the purpose of crack identification in form

of additive crack stiffness estimates the viscous damping, disc unbalance and active magnetic bearing constants as well. The algorithm has been tested for the measurement noise (in the displacement and the current) and bias errors in system parameters. Findings are reported at the end of the chapter.

3.2 System Configurations

For the present analysis, a cracked rotor with disc placed offset from the mid-span is considered. The shaft mass is neglected. To maintain the radial position of the rotor an AMB with a PID control strategy is placed at the disc location. A transverse crack is considered on the shaft, which affects effective stiffness of the shaft. A schematic arrangement of various constituents of the system is shown in Figure 3-1.

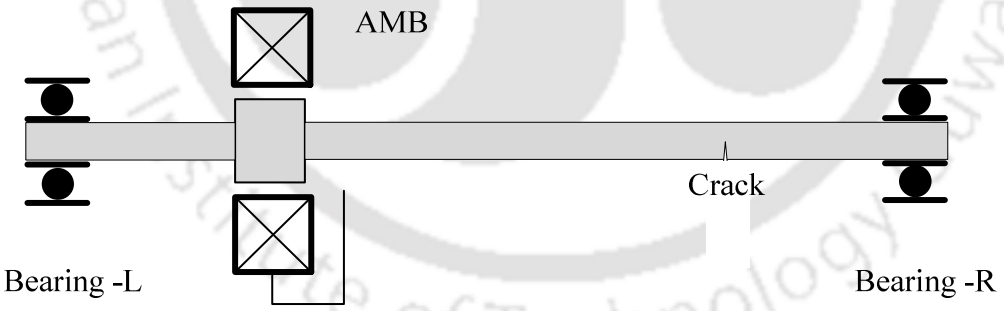

Figure 3-1 A cracked rotor with an offset disc and an AMB

The crack front is perpendicular to the rotating ξ-axis and remains so at all instants of time. The rotating ξ-η-z and inertial x-y-z frame of references are defined to be aligned at the instant of starting the time count. The relationship between the two frames of reference and other configuration parameters are shown in Figure 2-2.

3.3 System Equations of Motion

Referring to Figure 2-2, O is the origin of co-ordinate system O*xyz* and is defined on the bearing axis, C is the centre of rotation of the disc, G is the centre of gravity of the disc, and CG = *e* is the disc eccentricity. The angular position of the unbalance with respect to the normal to the crack front is quantified by a constant angle, β. For the horizontal shaft, the static deflection is present along the vertical direction and marked as δ_x. An initial tilt of the disc responsible for the external couple unbalance is negligible and thus not considered in the present model. Transverse translational displacements (u_x and u_y) and transverse rotational displacements (φ_y and φ_x) are considered. A transverse crack is considered on the shaft, the crack axial location parameter is not considered in the model. Transverse rotational displacements in two orthogonal planes are coupled because of gyroscopic effects. Also, shaft elastic couplings are considered between the translational and rotational displacements in the same plane on motion.

In the inertial frame of reference, the general system EOM of the intact rotor with consideration of gyroscopic effects, however, *without crack* have been reported by many authors (for instance, Lalanne and Ferraris (1998) or Yamamoto and Ishida (2001)) and given as

$$\mathbf{M}'\ddot{\mathbf{q}}(t) + (\mathbf{C}' - \omega\mathbf{G}')\dot{\mathbf{q}}(t) + \mathbf{K}'\mathbf{q}(t) = \mathbf{f}'_{st} + \mathbf{f}'_{unb}(t) \tag{3.1}$$

Matrices $\mathbf{M}'$, $\mathbf{C}'$, $\mathbf{G}'$ and $\mathbf{K}'$ are the mass, damping, gyroscopic and stiffness matrices of the rotor system, respectively; vectors $\mathbf{f}'_{st}$ and $\mathbf{f}'_{un}$ are force vectors due to the static deflection and the unbalance, respectively; $\mathbf{q}$ is the displacement vector, $\mathbf{q}_0$ corresponds to static transverse displacements, m is the disc mass, I_d is the diametral mass moment of inertia of the disc, I_p is the

polar mass moment of inertia of the disc, c_{ij} are the viscous damping in the rotor system, k_{ij} are the shaft stiffness, e is the disc eccentricity, β is the phase of the unbalance force with respect to the crack front and ω is the spin speed of the rotor. Subscripts i and j represent coordinate directions z, x and y with values 1, 2 and 3, respectively. For the 4-DOF system considered in the present chapter, various matrices and vectors are defined as

$$\mathbf{M}' = \begin{bmatrix} m & 0 & 0 & 0 \\ 0 & m & 0 & 0 \\ 0 & 0 & I_d & 0 \\ 0 & 0 & 0 & I_d \end{bmatrix} ; \quad \mathbf{C}' = \begin{bmatrix} c_{22} & 0 & c_{23} & 0 \\ 0 & c_{22} & 0 & c_{23} \\ c_{32} & 0 & c_{33} & 0 \\ 0 & c_{32} & 0 & c_{33} \end{bmatrix} ; \quad \mathbf{K}' = \begin{bmatrix} k_{22} & 0 & k_{23} & 0 \\ 0 & k_{22} & 0 & k_{23} \\ k_{32} & 0 & k_{33} & 0 \\ 0 & k_{32} & 0 & k_{33} \end{bmatrix}$$

$$\mathbf{G}' = \begin{bmatrix} 0 & 0 & 0 & 0 \\ 0 & 0 & 0 & 0 \\ 0 & 0 & 0 & I_p \\ 0 & 0 & -I_p & 0 \end{bmatrix} ; \quad \mathbf{q} = \mathbf{q}_v + \mathbf{q}_0 = \begin{Bmatrix} u_x \\ u_y \\ \varphi_y \\ \varphi_x \end{Bmatrix} + \begin{Bmatrix} \delta_x \\ \delta_y \\ \delta_{\varphi_y} \\ \delta_{\varphi_x} \end{Bmatrix} ; \quad \mathbf{f}'_{unb} = \begin{Bmatrix} me\omega^2 \cos(\omega t + \beta) \\ me\omega^2 \sin(\omega t + \beta) \\ 0 \\ 0 \end{Bmatrix}$$

$$\mathbf{f}'_{st} = \begin{Bmatrix} k_{22}\delta_x \\ k_{22}\delta_y \\ k_{33}\delta_{\varphi_y} \\ k_{33}\delta_{\varphi_x} \end{Bmatrix} \tag{3.2}$$

The total displacement $\mathbf{q}$ is a sum of two displacements, viz. the vibration displacement due to dynamics of the rotor, $\mathbf{q}_v$, and the static displacement due to disc weight, $\mathbf{q}_0$. Thus, the displacement vector $\mathbf{q}$ can be factored as

$$\mathbf{q}(t) = \mathbf{q}_v(t) + \mathbf{q}_0 \tag{3.3}$$

The crack alters (lowers) the stiffness of the shaft, which can be accounted for by the placement of crack stiffness matrix, $\mathbf{\Delta K}'(u,t)$, into Eqn. (3.1). The EOM accounting for the presence of crack can be written as

$$\mathbf{M}'\ddot{\mathbf{q}}_{\mathrm{v}} + (\mathbf{C}' - \omega\mathbf{G}')\dot{\mathbf{q}}_{\mathrm{v}} + (\mathbf{K}' - \mathbf{\Delta K}'(u,t))(\mathbf{q}_{\mathrm{v}} + \mathbf{q}_0) = \mathbf{f}'_{st} + \mathbf{f}'_{unb} \tag{3.4}$$

The above equation is nonlinear due to the presence of crack stiffness term. Under the consideration of weight dominance, which is a true representation of phenomenon associated in heavy rotors; the crack stiffness matrix becomes a function of time alone. Under this assumption, Eqn. (3.4) can be linearized as enunciated in Gasch (1993) and written as

$$\mathbf{M}'\ddot{\mathbf{q}}_{\mathrm{v}} + (\mathbf{C}' - \omega\mathbf{G}')\dot{\mathbf{q}}_{\mathrm{v}} + \mathbf{K}'\mathbf{q}_{\mathrm{v}} = \mathbf{\Delta K}'(t)\mathbf{q}_0 + \mathbf{f}'_{unb} \tag{3.5}$$

Here, $\mathbf{\Delta K}'(t)$ is the additional flexibility matrix due to occurrence of the crack and $\mathbf{\Delta K}'(t)\mathbf{q}_0 = \mathbf{f}_{\mathrm{cr}}$ is the crack force, as discussed in Chapter 2. Rotor cracks have been modelled in a number of ways (for instance – Grabowski, 1984; Mayes and Davies, 1984; Sinou and Lees, 2005; Sinou, 2009; Darpe et al., 2004; etc.), in this work it has been modelled by means of a crack flexibility matrix. Modelling of the crack effect for a 4-DOF model of the rotor is presented in the following section.

3.3.1 Crack Model

Starting from the most generalized case of 6-DOF system, the adaptation for a 4-DOF analysis has been made in Chapter 2 at Eqn. (2.8) as

$$\mathbf{\Delta H}_{\text{4-DOF}} = \begin{bmatrix} \Delta h_{22} & 0 & 0 & 0 \\ 0 & \Delta h_{33} & 0 & 0 \\ 0 & 0 & \Delta h_{44} & \Delta h_{45} \\ 0 & 0 & \Delta h_{54} & \Delta h_{55} \end{bmatrix} \tag{3.6}$$

Wherein, subscripts 2 and 3 correspond to shearing forces, and subscripts 4 and 5 correspond to the bending moment about two lateral directions. Subscripts 1 and 6 correspond to the axial force (z-axis direction) and torque, respectively, which are not present in the 4-DOF model. A combination of subscripts corresponds to cross-coupled terms.

During the whirling, an elastic shaft at the disc location undergoes transverse deflections, the translational and the rotational both. Linear reaction forces and moments onto the shaft can be expressed in terms the rotational and translational displacements of the shaft at the disc location, with help of influence coefficients. From basic mechanics of solids (Timoshenko and Young, 1962), for a simply supported shaft of span $l=a+b$, a being the distance of disc from the left support; following relationships hold in the rotating coordinate system ξ-O-η (Figure 2- 2), for the case of an intact shaft (superscript 'int')

$$\begin{Bmatrix} u_{\xi}^{\text{int}} \\ u_{\eta}^{\text{int}} \\ \varphi_{\eta}^{\text{int}} \\ \varphi_{\xi}^{\text{int}} \end{Bmatrix} = \begin{bmatrix} h_{22} & 0 & h_{23} & 0 \\ 0 & h_{22} & 0 & h_{23} \\ h_{32} & 0 & h_{33} & 0 \\ 0 & h_{32} & 0 & h_{33} \end{bmatrix} \begin{Bmatrix} f_{\xi}^{\text{int}} \\ f_{\eta}^{\text{int}} \\ M_{\eta}^{\text{int}} \\ M_{\xi}^{\text{int}} \end{Bmatrix} \tag{3.7}$$

with

$$h_{22} = \frac{a^2 b^2}{3EIl}; \quad h_{23} = -\frac{3a^2 l - 2a^3 - al^2}{3EIl}; \quad h_{32} = \frac{ab(b-a)}{3EIl}; \quad h_{33} = -\frac{3al - 3a^2 - l^2}{3EIl} \tag{3.8}$$

Here, E is the Young's modulus of elasticity, I is the area moment of inertia of the shaft cross section, $\left(u_{\xi}^{\text{int}},\ u_{\eta}^{\text{int}}\right)$ are transverse translational displacements, $\left(\varphi_{\eta}^{\text{int}},\ \varphi_{\xi}^{\text{int}}\right)$ are transverse rotational displacements, $\left(f_{\xi}^{\text{int}},\ f_{\eta}^{\text{int}}\right)$ are forces and $\left(M_{\xi z}^{\text{int}},\ M_{\eta z}^{\text{int}}\right)$ are moments for the case of an intact shaft. The relationship of the reactions and deflections due to the crack (superscript 'cr') is similarly obtained, using the crack flexibility matrix given by Eqn. (3.6), as

$$\begin{Bmatrix} u_{\xi}^{cr} \\ u_{\eta}^{cr} \\ \varphi_{\eta}^{cr} \\ \varphi_{\xi}^{cr} \end{Bmatrix} = \begin{bmatrix} \Delta h_{22} & 0 & 0 & 0 \\ 0 & \Delta h_{33} & 0 & 0 \\ 0 & 0 & \Delta h_{44} & \Delta h_{45} \\ 0 & 0 & \Delta h_{54} & \Delta h_{55} \end{bmatrix} \begin{Bmatrix} f_{\xi}^{cr} \\ f_{\eta}^{cr} \\ M_{\eta}^{cr} \\ M_{\xi}^{cr} \end{Bmatrix} \tag{3.9}$$

Here, $\left(u_{\xi}^{cr}, u_{\eta}^{cr}\right)$ are transverse translational displacements, $\left(\varphi_{\eta}^{cr}, \varphi_{\xi}^{cr}\right)$ are transverse rotational displacements, $\left(f_{\xi}^{cr}, f_{\eta}^{cr}\right)$ are forces and $\left(M_{\xi z}^{cr}, M_{\eta z}^{cr}\right)$ are moments due to the crack. Flexibilities, which do not lie in the direction normal to the crack front (i.e. along rotating axis, ξ), are negligible; hence, Δh_{33} and Δh_{55} are assumed to be zero (Sinou and Lees, 2005). In addition, as the coupling of transverse rotational displacements in two orthogonal planes due to the crack is negligibly small, cross-coupled terms Δh_{45} and Δh_{54} can be neglected. With incorporation of these simplifying assumptions, Eqn. (3.9) reduces to

$$\begin{Bmatrix} u_{\xi}^{cr} \\ u_{\eta}^{cr} \\ \varphi_{\eta}^{cr} \\ \varphi_{\xi}^{cr} \end{Bmatrix} = \begin{bmatrix} \Delta h_{22} & 0 & 0 & 0 \\ 0 & 0 & 0 & 0 \\ 0 & 0 & \Delta h_{44} & 0 \\ 0 & 0 & 0 & 0 \end{bmatrix} \begin{Bmatrix} f_{\xi}^{cr} \\ f_{\eta}^{cr} \\ M_{\eta}^{cr} \\ M_{\xi}^{cr} \end{Bmatrix} \tag{3.10}$$

Eqn. (3.9) and Eqn. (3.10) can be combined to obtain the flexibility of a cracked rotor. The equation is

$$\begin{Bmatrix} u_\xi \\ u_\eta \\ \varphi_\eta \\ \varphi_\xi \end{Bmatrix} = \left(\begin{bmatrix} h_{22} & 0 & h_{23} & 0 \\ 0 & h_{22} & 0 & h_{23} \\ h_{32} & 0 & h_{33} & 0 \\ 0 & h_{32} & 0 & h_{33} \end{bmatrix} + \begin{bmatrix} \Delta h_{22} & 0 & 0 & 0 \\ 0 & 0 & 0 & 0 \\ 0 & 0 & \Delta h_{44} & 0 \\ 0 & 0 & 0 & 0 \end{bmatrix} \right) \begin{Bmatrix} f_\xi \\ f_\eta \\ M_{\xi z} \\ M_{\eta z} \end{Bmatrix} \tag{3.11}$$

Here, $\lfloor u_\xi \quad u_\eta \quad \varphi_\eta \quad \varphi_\xi \rfloor^{\mathrm{T}}$ represents the displacement vector and $\lfloor f_\xi \quad f_\eta \quad M_{\xi z} \quad M_{\eta z} \rfloor^{\mathrm{T}}$ is the force vector corresponding to the combined flexibility matrix (i.e., of the intact shaft as well as of the crack section) in the rotating frame of reference. Stiffness matrices can be obtained by the matrix inversion of Eqn. (3.11), in the rotating co-ordinate system, ξ-O-η. The direct inversion of the sum of flexibility matrices poses a problem of the intact shaft stiffness getting expressed in terms of crack flexibilities, which interferes with the purpose of this inversion. The inversion can be performed using Woodbury (1950) matrix identity based on lemma suggested by Miller (1981). The lemma and its application to this inversion is provided in Appendix-A. The final form of the stiffness formulation is as under

$$\mathbf{K}_{rot} = \mathbf{K}'_{rot} - \mathbf{\Delta K}'_{rot} = \begin{bmatrix} k_{22} & 0 & k_{23} & 0 \\ 0 & k_{22} & 0 & k_{23} \\ k_{32} & 0 & k_{33} & 0 \\ 0 & k_{32} & 0 & k_{33} \end{bmatrix} - \begin{bmatrix} \Delta k_{22} & 0 & 0 & 0 \\ 0 & 0 & 0 & 0 \\ 0 & 0 & \Delta k_{44} & 0 \\ 0 & 0 & 0 & 0 \end{bmatrix} \tag{3.12}$$

The individual stiffness entries of two stiffness matrices are defined as

$$\Delta k_{22} = \frac{\Delta h_{22} h^2{}_{33} + \Delta h_{44} h^2{}_{23}}{H^2}, \quad \Delta k_{44} = \frac{\Delta h_{44} h^2{}_{22} + \Delta h_{22} h^2{}_{23}}{H^2}$$

$$k_{22} = \frac{h_{33}}{H}, \quad k_{33} = \frac{h_{22}}{H}, \quad k_{23} = k_{32} = -\frac{h_{23}}{H}, \quad \text{with } H = h_{22}h_{33} - h_{23}^2 \tag{3.13}$$

Stiffness matrices in Eqn. (3.12) are relative to rotating axes. For their placement in the system equation of motion in Eqn. (3.5) they need to be transformed to inertial coordinates.

3.3.2 Transformation of Stiffness Matrices

With reference to Figure 2-2, rotation φ_z defines the angle swept due to shaft rotation, hence, for a rotor spinning at angular velocity ω, the swept angle $\varphi_z = \omega t$. Under assumptions of small displacements, the axis of shaft rotation (z) remains the same in rotating and inertial frames. Transformation between rotating frame of reference O$\xi\eta$z to inertial frame of reference Oxyz, has been dealt in detail in Genta (2005) and Friswell et al. (2010). The transformation matrix connecting displacements relative to two frames has been defined as

$$\begin{Bmatrix} u_x \\ u_y \\ \varphi_y \\ \varphi_x \end{Bmatrix} = \mathbf{T} \begin{Bmatrix} u_\xi \\ u_\eta \\ \varphi_\eta \\ \varphi_\xi \end{Bmatrix} \quad \text{with} \quad \mathbf{T} = \begin{bmatrix} \cos\varphi_z & \sin\varphi_z & 0 & 0 \\ -\sin\varphi_z & \cos\varphi_z & 0 & 0 \\ 0 & 0 & \cos\varphi_z & \sin\varphi_z \\ 0 & 0 & -\sin\varphi_z & \cos\varphi_z \end{bmatrix} \tag{3.14}$$

Stiffness matrices in Eqn. (3.12) now can be transformed to inertial coordinates with help of transformation matrix **T** with substitution of $\varphi_z = \omega t$. The transformation yields

$$\mathbf{K}' = \mathbf{T}^T \mathbf{K}'_{rot} \mathbf{T} = \begin{bmatrix} k_{22} & 0 & k_{23} & 0 \\ 0 & k_{22} & 0 & k_{23} \\ k_{32} & 0 & k_{33} & 0 \\ 0 & k_{32} & 0 & k_{33} \end{bmatrix} \tag{3.15}$$

and similarly

$$\Delta\mathbf{K}'(t) = \frac{1}{2}\begin{bmatrix} \Delta k_{22}(1+\cos 2\omega t) & \Delta k_{22}\sin 2\omega t & 0 & 0 \\ \Delta k_{22}\sin 2\omega t & \Delta k_{22}(1-\cos 2\omega t) & 0 & 0 \\ 0 & 0 & \Delta k_{44}(1+\cos 2\omega t) & \Delta k_{44}\sin 2\omega t \\ 0 & 0 & \Delta k_{44}\sin 2\omega t & \Delta k_{44}(1-\cos 2\omega t) \end{bmatrix} \tag{3.16}$$

Certain observations could be made regarding the behaviour of stiffness matrices in two coordinate references. The intact shaft stiffness remains unaltered during transformation from one coordinate to the other as it is expected due to the shaft symmetry. The additive crack stiffness represented in rotating coordinates is independent of time, which becomes time dependent in inertial coordinates. The periodic opening/closing of the crack is modelled by introduction of a suitable crack excitation function, $s(t)$. Introducing $s(t)$, the crack stiffness gets represented as

$$\Delta\mathbf{K}(t) = s(t)\Delta\mathbf{K}'(t) \tag{3.17}$$

For a generalized case of the static deflection due to self-weight of the rotor, ($\delta_y = 0$ and $\delta_{\varphi_x} = 0$) the crack force vector $\mathbf{f_{cr}}$, defined in Eqn. (3.5) , is obtained as

$$\mathbf{f}_{\mathbf{cr}} = \Delta\mathbf{K}(t)\,\mathbf{q}_0 = \tfrac{1}{2}s(t)\begin{Bmatrix} \Delta k_{22}(1+\cos 2\omega t)\delta_x \\ \Delta k_{22}(\sin 2\omega t)\delta_x \\ \Delta k_{44}(1+\cos 2\omega t)\delta_{\varphi_y} \\ \Delta k_{44}(\sin 2\omega t)\delta_{\varphi_y} \end{Bmatrix} \tag{3.18}$$

On substitution of crack forces as given by Eqn. (3.18) with $\delta_{\varphi_y} = 0$ into equations of motion, Eqn. (3.5) takes the final form as

$$\begin{bmatrix} m & 0 & 0 & 0 \\ 0 & m & 0 & 0 \\ 0 & 0 & I_d & 0 \\ 0 & 0 & 0 & I_d \end{bmatrix}\begin{Bmatrix} \ddot{u}_x \\ \ddot{u}_y \\ \ddot{\varphi}_y \\ \ddot{\varphi}_x \end{Bmatrix} + \left(\begin{bmatrix} c_{11} & 0 & c_{12} & 0 \\ 0 & c_{11} & 0 & c_{12} \\ c_{12} & 0 & c_{22} & 0 \\ 0 & c_{12} & 0 & c_{22} \end{bmatrix} - \omega \begin{bmatrix} 0 & 0 & 0 & 0 \\ 0 & 0 & 0 & 0 \\ 0 & 0 & 0 & I_p \\ 0 & 0 & -I_p & 0 \end{bmatrix} \right)\begin{Bmatrix} \dot{u}_x \\ \dot{u}_y \\ \dot{\varphi}_y \\ \dot{\varphi}_x \end{Bmatrix}$$

$$+ \begin{bmatrix} k_{22} & 0 & k_{23} & 0 \\ 0 & k_{22} & 0 & k_{23} \\ k_{23} & 0 & k_{33} & 0 \\ 0 & k_{23} & 0 & k_{33} \end{bmatrix}\begin{Bmatrix} u_x \\ u_y \\ \varphi_y \\ \varphi_x \end{Bmatrix} = \tfrac{1}{2}s(t)\begin{Bmatrix} \Delta k_{22}(1+\cos 2\omega t)\delta_x \\ \Delta k_{22}(\sin 2\omega t)\delta_x \\ 0 \\ 0 \end{Bmatrix} + \begin{Bmatrix} me\omega^2 \cos(\omega t + \beta) \\ me\omega^2 \sin(\omega t + \beta) \\ 0 \\ 0 \end{Bmatrix} \tag{3.19}$$

The LHS of equation of motion (3.19) contains all the rotor specific quantities while RHS contains forcing terms. Presence of other forcing (i.e. from the AMB) terms may be accommodated in the above equation of motion by placing the additional forcing terms in the RHS.

3.3.3 Equations of Motion in the Presence of AMB Support

The nature of AMB forcing and its variation with the position of the shaft with PID control strategy has been described in Chapter 2 under Section 2.2.5. With isotropic AMB, the same idea and concept adapted for a 4-DOF model yields the AMB force vector as

$$\mathbf{f}_{AMB} = -\begin{bmatrix} k_s & 0 \\ 0 & k_s \\ 0 & 0 \\ 0 & 0 \end{bmatrix} \begin{Bmatrix} u_x \\ u_y \end{Bmatrix} + \begin{bmatrix} k_I & 0 \\ 0 & k_I \\ 0 & 0 \\ 0 & 0 \end{bmatrix} \begin{Bmatrix} i_x \\ i_y \end{Bmatrix} \tag{3.20}$$

In the above expression, quantities k_s and k_I are the AMB specific force–current and force–displacement constants. Since the AMB is incorporated in the support (not as an external excitation) of the rotor with a crack, the AMB force can be put in the RHS of Eqn. (3.19) with a negative sign. With addition of the AMB forcing, Eqn. (3.19) modifies to

$$\mathbf{M}\ddot{\mathbf{q}}_{\mathbf{v}} + (\mathbf{C} - \mathrm{j}\omega\mathbf{G})\dot{\mathbf{q}}_{\mathbf{v}} + \mathbf{K}_0\mathbf{q}_{\mathbf{v}} = \mathbf{f}_{cr}(t) + \mathbf{f}_{un}(t) - \mathbf{f}_{AMB}(t) \tag{3.21}$$

As seen from the RHS of Eqn. (3.21) the crack, unbalance and AMB forces act in tandem, with the AMB forcing attempting to nullify the effects of crack and unbalance. The response of the system under these forcing can be better studied in complex formulation, presented in the next section.

3.4 Time and frequency responses

For ease of further analysis, a set of complex coordinates is defined that allows writing Eqn. (3.21) in a complex form. Complex displacement variables r and ϕ, and complex current i_c are defined as, $r = u_x + \mathrm{j}\, u_y$, $\phi = \varphi_y + \mathrm{j}\, \varphi_x$ and $i_c = i_x + \mathrm{j}i_y$. While combining equations in Eqn. (3.21) in the complex form, gyroscopic terms combine as, $\left(-I_p\omega\dot{\varphi}_x\right) + \mathrm{j}\left(I_p\omega\dot{\varphi}_y\right) = \mathrm{j}\, I_p\omega\dot{\phi}$. The complex system EOM of a cracked rotor with gyroscopic effects in the inertial co-ordinates is given as follows

$$\bar{\mathbf{M}}\ddot{\mathbf{v}} + \left(\bar{\mathbf{C}} - \mathrm{j}\omega\bar{\mathbf{G}}\right)\dot{\mathbf{v}} + \bar{\mathbf{K}}\mathbf{v} = \frac{1}{2}\Delta k_{22}s(t)(1 + e^{2\mathrm{j}\omega t})\mathbf{v}_0 + \bar{\mathbf{f}}_{un} - \bar{\mathbf{f}}_{AMB} \tag{3.22}$$

$$\bar{\mathbf{M}}=\begin{bmatrix} m & 0 \\ 0 & I_d \end{bmatrix}; \qquad \bar{\mathbf{C}}=\begin{bmatrix} c_{11} & c_{12} \\ c_{21} & c_{22} \end{bmatrix}; \qquad \bar{\mathbf{G}}=\begin{bmatrix} 0 & 0 \\ 0 & -I_p \end{bmatrix}; \qquad \bar{\mathbf{K}}=\begin{bmatrix} k_{22} & k_{23} \\ k_{32} & k_{33} \end{bmatrix};$$

Here,

$$\mathbf{v}=\begin{Bmatrix} r \\ \phi \end{Bmatrix}; \qquad \mathbf{v}_0=\begin{Bmatrix} \delta_x \\ 0 \end{Bmatrix}; \qquad \bar{\mathbf{f}}_{un}=\begin{Bmatrix} me\omega^2 \mathrm{e}^{\mathrm{j}(\omega t+\beta)} \\ 0 \end{Bmatrix}; \; \bar{\mathbf{f}}_{\mathbf{AMB}}=-k_s\begin{Bmatrix} r \\ 0 \end{Bmatrix}+k_I\begin{Bmatrix} i_c \\ 0 \end{Bmatrix}$$

The AMB forcing has two components; first $k_s \lfloor r \quad 0 \rfloor^T$ due to linear displacements and the second $k_I \lfloor i_c \quad 0 \rfloor^T$ due to control currents. While the first component can be combined with the stiffness term on the LHS, the second component represents the AMB forcing due to the control current alone. With this rearrangement made, Eqn. (3.22) is written as

$$\bar{\mathbf{M}}\ddot{\mathbf{v}}+\left(\bar{\mathbf{C}}-\mathrm{j}\omega\bar{\mathbf{G}}\right)\dot{\mathbf{v}}+\tilde{\mathbf{K}}\mathbf{v}=\tfrac{1}{2}\Delta k_{22}s(t)(1+e^{j i\omega t})\mathbf{v}_0+\bar{\mathbf{f}}_{un}-\bar{\mathbf{f}}_{cu} \tag{3.23}$$

with

$$\tilde{\mathbf{K}}=\begin{bmatrix} k_{22}-k_s & k_{23} \\ k_{32} & k_{33} \end{bmatrix} \quad \text{and} \quad \bar{\mathbf{f}}_{cu}=k_I\begin{Bmatrix} i_c \\ 0 \end{Bmatrix} \tag{3.24}$$

The crack with a depth lower than half of the shaft radius, exhibit a switching behaviour well represented by a rectangular Switching Crack Excitation Function (SCEF) as reported in (Gasch, 1993; Gasch, 2008) and can be expressed as a Fourier series as shown in Eqn. (2.11). With the SCEF expressed by Eqn. (2.11), using the Euler formula, the crack excitation force, can be expressed in a sum of various harmonics as

$$\bar{\mathbf{f}}_{cr}=\begin{Bmatrix} \Delta k_{22}\delta_x \sum_{i=-n}^{+n} p_i \mathrm{e}^{\mathrm{j}i\omega t} \\ 0 \end{Bmatrix} \tag{3.25}$$

Here p_i is participation factor of the i^{th} harmonic of the crack force excitation. These coefficients are independent of the crack depth for the whole range of $t/R_a < 0.5$, where t is the crack depth and R_a is the shaft radius. This is the range of t/R_a for which the rectangular SCEF, expressed as in Eqn. (2.11) is a valid approximation (Gasch, 2008).

Since, the complex current indicated in Eqn. (3.23) should contain the harmonics as in the vibration displacement; the AMB force component due to the current only, $\overline{\mathbf{f}}_{cu}$, in Eqn. (3.23) is expressed as

$$\overline{\mathbf{f}}_{cu} = \begin{Bmatrix} k_I \sum_{i=-n}^{+n} I_i e^{ji\omega t} \\ 0 \end{Bmatrix} \tag{3.26}$$

With incorporation of Eqn. (3.25) and Eqn. (3.26) into Eqn. (3.23), the complex equation of motion can be now expressed in terms of harmonics of forcing terms as

$$\overline{\mathbf{M}}\ddot{\mathbf{v}} + \left(\overline{\mathbf{C}} - j\omega\overline{\mathbf{G}}\right)\dot{\mathbf{v}} + \tilde{\mathbf{K}}\mathbf{v} = \begin{Bmatrix} \Delta k_{22}\delta_x \sum_{i=-n}^{+n} p_i \\ 0 \end{Bmatrix} e^{ji\omega t} + \begin{Bmatrix} me\omega^2 e^{j\beta} \\ 0 \end{Bmatrix} e^{j\omega t} - \begin{Bmatrix} k_I \sum_{i=-n}^{+n} I_i \\ 0 \end{Bmatrix} e^{ji\omega t} \tag{3.27}$$

The assumed solution to Eqn. (3.27) will also contain the same harmonics as forcing terms. Thus, the assumed solution will have the form

$$\mathbf{v}(t) = \sum_{i=-\infty}^{i=\infty} \overline{\mathbf{v}}_i \, e^{ji\omega t} \tag{3.28}$$

Substituting the assumed solution into Eqn. (3.27) and rearranging, it gives the frequency domain equation for particular harmonics, for $i = 1$ and $i \neq 1$, respectively, as

$$\left[\left(-(i\omega)^2\,\bar{\mathbf{M}}\right)+\mathrm{j}(i\omega)\left(\bar{\mathbf{C}}-\mathrm{j}\omega\bar{\mathbf{G}}\right)+\tilde{\mathbf{K}}\right]\bar{\mathbf{v}}_1=\begin{Bmatrix}\Delta k_{22}\delta_x p_1\\0\end{Bmatrix}+\begin{Bmatrix}me\omega^2\mathrm{e}^{\mathrm{j}\beta}\\0\end{Bmatrix}-\begin{Bmatrix}k_I I_1\\0\end{Bmatrix} \tag{3.29}$$

and

$$\left[\left(-(i\omega)^2\,\bar{\mathbf{M}}\right)+\mathrm{j}(i\omega)\left(\bar{\mathbf{C}}-\mathrm{j}\omega\bar{\mathbf{G}}\right)+\tilde{\mathbf{K}}\right]\bar{\mathbf{v}}_i=\begin{Bmatrix}\Delta k_{22}u_{x0}p_i\\0\end{Bmatrix}-\begin{Bmatrix}k_I I_i\\0\end{Bmatrix} \tag{3.30}$$

The system response in time domain, $\mathbf{v}(t)$, can be obtained by the time integration of Eqn. (3.27) and the frequency domain response, $\bar{\mathbf{v}}_i$, can be obtained from the full spectrum of $\mathbf{v}(t)$. Details of the full spectrum extraction and implementation are available in Chapter 2 under Sections 2.3.2 and 2.3.3. The AMB current i_c and its harmonic components I_i will be also obtained as a result of the time integration and the full spectrum analysis, respectively. The displacement and current harmonics, $\bar{\mathbf{v}}_i$ and I_i, respectively, will be used for development of identification algorithm for the crack and rotor–AMB system parameters. The development of the identification is presented next.

3.5 Crack Identification Algorithm

In the present scheme, some of system parameters, like the disc mass and the shaft stiffness are assumed to be known, and parameters like – the crack parameter Δk_{22}, the unbalance parameter e and β, are to be identified. The inverse engineering problem is converted to a mathematical form by writing the system equations of motion in a linear regression form. A general form of Eqn. (3.29) and (3.30) is used for the development of regression equations. These contain rotational DOFs which can cause practical difficulties as they cannot be measured accurately. Hence, a

dynamic reduction scheme (Paz, 1984) is used to first obtain the reduced EOMs in frequency domain, which are then used for the parameter identification. Time domain EOMs are not reduced since these will be used to generate simulated responses.

3.5.1 Application of the Dynamic Reduction Scheme

The dynamic reduction eliminates some or most of the unwanted DOFs from the equations of motion such that, otherwise difficult to measure DOFs could be done away with in the identification process. DOFs are classified as masters and slaves, depending upon whether they are retained or eliminated respectively, in the analysis. Eliminated coordinates (slaves) correspond to points in the model, which are non-critical, or of secondary interest such as rotational DOFs and intermediate locations on the shaft. In the present analysis, rotational DOFs are eliminated. The state vector (displacement vector), force vectors, the mass matrix, and the stiffness matrix are partitioned into sub-vectors and sub-matrices relating to masters DOFs that are to be retained, and slave DOFs, which are to be eliminated. When no forces or moments are applied at slave DOFs (here it is assumed that initial tilt of the disc is negligibly small to produce appreciable moments), frequency domain equation Eqn. (3.29) can be partitioned as follows, where subscript *m* and *s* represent masters and slaves, respectively.

$$\left(-(i\omega)^2\begin{bmatrix}\mathbf{M}_{mm} & 0\\ 0 & \mathbf{M}_{ss}\end{bmatrix}+\mathrm{j}(i\omega)\left(\begin{bmatrix}\mathbf{C}_{mm} & \mathbf{C}_{ms}\\ \mathbf{C}_{sm} & \mathbf{C}_{ss}\end{bmatrix}-\omega\begin{bmatrix}0 & 0\\ 0 & \mathbf{G}_{ss}\end{bmatrix}\right)+\begin{bmatrix}\mathbf{K}_{mm} & \mathbf{K}_{ms}\\ \mathbf{K}_{sm} & \mathbf{K}_{ss}\end{bmatrix}\right)\begin{Bmatrix}\mathbf{Q}_m\\ \mathbf{Q}_s\end{Bmatrix}_i=\begin{Bmatrix}\mathbf{f}_i\\ 0\end{Bmatrix} \tag{3.31}$$

with

$$\mathbf{M}_{mm}=\begin{bmatrix}m & 0\\ 0 & m\end{bmatrix};\quad \mathbf{M}_{ss}=\begin{bmatrix}I_d & 0\\ 0 & I_d\end{bmatrix};\quad \mathbf{G}_{ss}=\begin{bmatrix}0 & I_p\\ -I_p & 0\end{bmatrix};\quad \mathbf{C}_{mm}=\begin{bmatrix}c_{11} & 0\\ 0 & c_{11}\end{bmatrix};\quad \mathbf{C}_{ss}=\begin{bmatrix}c_{22} & 0\\ 0 & c_{22}\end{bmatrix}$$

$$\mathbf{K}_{ss}=\begin{bmatrix}k_{33} & 0\\ 0 & k_{33}\end{bmatrix};\quad \mathbf{C}_{ms}=\mathbf{C}_{sm}=\begin{bmatrix}c_{12} & 0\\ 0 & c_{12}\end{bmatrix};\quad \mathbf{K}_{mm}=\begin{bmatrix}k_{22}-k_s & 0\\ 0 & k_{22}-k_s\end{bmatrix};\quad \mathbf{K}_{ms}=\mathbf{K}_{sm}=\begin{bmatrix}k_{23} & 0\\ 0 & k_{23}\end{bmatrix}$$

$$\mathbf{f}_i=\begin{Bmatrix}\Delta k_{22}u_{x_0}p_i\\ \Delta k_{22}u_{x_0}p_i\end{Bmatrix}+\begin{Bmatrix}me\omega^2\cos\beta\\ me\omega^2\sin\beta\end{Bmatrix}-k_I\begin{Bmatrix}I_{i,\mathrm{Re}}\\ I_{i,\mathrm{Im}}\end{Bmatrix};\qquad \mathbf{Q}_m=\begin{Bmatrix}R_{i,\mathrm{Re}}\\ R_{i,\mathrm{Im}}\end{Bmatrix};\qquad \mathbf{Q}_s=\begin{Bmatrix}\Phi_{i,\mathrm{Re}}\\ \Phi_{i,\mathrm{Im}}\end{Bmatrix}$$

The transformation matrix $\mathbf{T}^d$ for the dynamic condensation that eliminates rotational co-ordinates φ_y and φ_x holds the following property

$$\begin{Bmatrix}\mathbf{Q}_m\\ \mathbf{Q}_s\end{Bmatrix}=\mathbf{T}^d\mathbf{Q}_m \tag{3.32}$$

A general method for derivation of $\mathbf{T}^d$ from Eqn. (3.31) is available in literature, for instance - Friswell and Mottershead (1995), and given as

$$\mathbf{T}^d=\begin{bmatrix}1 & 0\\ 0 & 1\\ \dfrac{k_{23}}{(i\omega)^2 I_d-k_{33}} & 0\\ 0 & \dfrac{k_{23}}{(i\omega)^2 I_d-k_{33}}\end{bmatrix}=\begin{bmatrix}1 & 0\\ 0 & 1\\ t^d & 0\\ 0 & t^d\end{bmatrix}\quad\text{with}\quad t^d=\frac{k_{23}}{(i\omega)^2 I_d-k_{33}} \tag{3.33}$$

In the above transformation, apart from the mass and stiffness terms, frequency ω also appears. For the transformation matrix, it is chosen as $\omega=\omega_{central}$. Here, $\omega_{central}$ is called as the central

frequency, and is chosen as the mean of the measurement spin speeds of interest. Substituting this transformation into Eqn. (3.31), we get

$$\left(\mathbf{T}^d\right)^T\left(-(i\omega)^2\begin{bmatrix}\mathbf{M}_{mm} & 0\\ 0 & \mathbf{M}_{ss}\end{bmatrix}\mathbf{T}^d + \mathrm{j}i\omega\left(\begin{bmatrix}\mathbf{C}_{mm} & \mathbf{C}_{ms}\\ \mathbf{C}_{sm} & \mathbf{C}_{ss}\end{bmatrix} - \omega\begin{bmatrix}0 & 0\\ 0 & \mathbf{G}_{ss}\end{bmatrix}\right)\mathbf{T}^d + \begin{bmatrix}\mathbf{K}_{mm} & \mathbf{K}_{ms}\\ \mathbf{K}_{sm} & \mathbf{K}_{ss}\end{bmatrix}\mathbf{T}^d\right)\begin{Bmatrix}\mathbf{Q_m}\\ \mathbf{Q_s}\end{Bmatrix} = \left(\mathbf{T}^d\right)^T\mathbf{f}_i \tag{3.34}$$

Here,

$$\begin{Bmatrix}\mathbf{Q}_m\\ \mathbf{Q}_s\end{Bmatrix} = \begin{Bmatrix}U_i^x\\ U_i^y\\ \varphi_i^y\\ \varphi_i^x\end{Bmatrix} \quad \text{and} \quad \mathbf{f}_i = \begin{Bmatrix}\Delta k_{22}\delta_x p_i\\ \Delta k_{22}\delta_x p_i\\ 0\\ 0\end{Bmatrix} + \begin{Bmatrix}me\omega^2\cos\beta\\ me\omega^2\sin\beta\\ 0\\ 0\end{Bmatrix} - k_I\begin{Bmatrix}I_i^x\\ I_i^y\\ 0\\ 0\end{Bmatrix} \tag{3.35}$$

Reduced matrices with slave DOFs eliminated are

$$\mathbf{M}^d = \left(\mathbf{T}^d\right)^T\begin{bmatrix}\mathbf{M}_{mm} & 0\\ 0 & \mathbf{M}_{ss}\end{bmatrix}\mathbf{T}^d = \begin{bmatrix}m+\left(t^d\right)^2 I_d & 0\\ 0 & m+\left(t^d\right)^2 I_d\end{bmatrix} \tag{3.36}$$

$$\mathbf{K}^d = \left(\mathbf{T}^d\right)^T\begin{bmatrix}\mathbf{K}_{mm} & \mathbf{K}_{ms}\\ \mathbf{K}_{sm} & \mathbf{K}_{ss}\end{bmatrix}\mathbf{T}^d = \begin{bmatrix}(k_{22}-k_s)+2(t^d)k_{23}+\left(t^d\right)^2 k_{33} & 0\\ 0 & (k_{22}-k_s)+2(t^d)k_{23}+\left(t^d\right)^2 k_{33}\end{bmatrix} \tag{3.37}$$

$$\mathbf{C}^d = \left(\mathbf{T}^d\right)^T\begin{bmatrix}\mathbf{C}_{mm} & \mathbf{C}_{ms}\\ \mathbf{C}_{sm} & \mathbf{C}_{ss}\end{bmatrix}\mathbf{T}^d = \begin{bmatrix}c_{11}+2(t^d)c_{12}+\left(t^d\right)^2 c_{22} & 0\\ 0 & c_{11}+2(t^d)c_{12}+\left(t^d\right)^2 c_{22}\end{bmatrix} \tag{3.38}$$

$$\mathbf{G}^d = \left(\mathbf{T}^d\right)^T \omega \begin{bmatrix} 0 & 0 \\ 0 & \mathbf{G}_{ss} \end{bmatrix} \mathbf{T}^d = \begin{bmatrix} 0 & \left(t^d\right)^2 I_p \\ -\left(t^d\right)^2 I_p & 0 \end{bmatrix} \tag{3.39}$$

$$\mathbf{f}^d = (\mathbf{T}^d)^T \mathbf{f}_c = \begin{Bmatrix} \Delta k_{22} \delta_x p_i \\ \Delta k_{22} \delta_x p_i \end{Bmatrix} + \begin{Bmatrix} me\omega^2 \cos\beta \\ me\omega^2 \sin\beta \end{Bmatrix} - k_I \begin{Bmatrix} I_{i,\mathrm{Re}} \\ I_{i,\mathrm{Im}} \end{Bmatrix} \tag{3.40}$$

The placement of reduced sub-matrices in Eqn. (3.34) yields reduced equations of motion expressed in terms of master DOFs as

$$\left(-(i\omega)^2 \mathbf{M}^d + \mathrm{j}(i\omega)\left(\mathbf{C}^d - \omega \mathbf{G}^d\right) + \mathbf{K}^d\right)\mathbf{Q}_m = \mathbf{f}^d \tag{3.41}$$

EOMs in Eqn. (3.34) are combined together as a single equation in a complex form, as

$$\left[-(i\omega)^2 \left\{m + \left(t^d\right)^2 I_d\right\} + \mathrm{j}(i\omega)\left\{c_{11} + 2t^d c_{12} + \left(t^d\right)^2 c_{22} + \mathrm{j}\, I_p \omega \left(t^d\right)^2\right\} + \left\{(k_{22} - k_s) + 2t^d k_{23} + \left(t^d\right)^2 k_{33}\right\}\right] R_i$$

$$= \Delta k_{22} \delta_x p_i + me\omega^2 \mathrm{e}^{\mathrm{j}\beta} + k_I I_i \tag{3.42}$$

Here, R_i is the complex frequency response and I_i is the complex AMB control current for the i^{th} harmonic. Now, all the variables in Eqn. (3.42) are associated with master DOFs. This equation will be used further to develop regression equations for the identification of crack parameters.

3.5.2 Estimation of the Rotor and AMB Parameters

For the parameter identification, the frequency domain Eqn. (3.42) is split into known and unknown parts, and re-arranged such that the unknown rotor and AMB parameters are grouped in a vector. Here, the additive crack stiffness Δk_{22}, viscous damping c_{22}, the unbalance magnitude e

and phase β, and AMB stiffness constants k_s and k_I , are assumed unknown hence identifiable. Eqn. (3.42) is rearranged as

$$\begin{aligned} &\mathrm{j}(i\omega)c_{22}R_i - \Delta k_{22}\delta_x p_i - me\omega^2 \mathrm{e}^{\mathrm{j}\beta} - k_s R_i + k_I I_i \\ &= \left[(i\omega)^2 \left\{ m + \left(t^d\right)^2 I_d \right\} - \mathrm{j}(i\omega)\left\{ 2t^d c_{23} + \left(t^d\right)^2 c_{33} \right\} + i\omega^2 \left(t^d\right)^2 I_p - \left\{ k_{22} + 2t^d k_{23} + \left(t^d\right)^2 k_{33} \right\} \right] R_i \end{aligned} \tag{3.43}$$

For further rearrangement, following quantities are defined

$$m' = m + \left(t^d\right)^2 I_d; \qquad c' = 2t^d c_{23} + \left(t^d\right)^2 c_{33}; \qquad k' = k_{22} + 2t^d k_{23} + \left(t^d\right)^2 k_{33} \tag{3.44}$$

With the above defined quantities, Eqn. (3.43) is written as

$$\mathrm{j}(i\omega)c_{11}R_i - \Delta k_{22}\delta_x p_i - me\omega^2 \mathrm{e}^{\mathrm{j}\beta} - k_s R_i + k_I I_i = \left((i\omega)^2 m' - \mathrm{j}(i\omega)c' + i\omega^2 \left(t^d\right)^2 I_p - k' \right) R_i \tag{3.45}$$

The response R_i and AMB current I_i can be factored into their real and imaginary components as $R_i = R_{i,\mathrm{Re}} + \mathrm{j}R_{i,\mathrm{Im}}$ and $I_i = I_{i,\mathrm{Re}} + \mathrm{j}I_{i,\mathrm{Im}}$. Segregating the real and imaginary components splits Eqn. (3.45) into two equations in all real quantities as

$$\begin{aligned} &-(i\omega)c_{11}R_{i,\mathrm{Im}} + \Delta k_{22}\delta_x p_i - m\omega^2 e_{\mathrm{Re}} - k_s R_{i,\mathrm{Re}} + k_I I_{i,\mathrm{Re}} = \left\{ (i\omega)^2 m' + i\omega^2 \left(t^d\right)^2 I_p - k' \right\} R_{i,\mathrm{Re}} + (i\omega)c' R_{i,\mathrm{Im}} \\ &(i\omega)c_{11}R_{i,\mathrm{Re}} \quad + \quad 0 \quad - m\omega^2 e_{\mathrm{Im}} - k_s R_{i,\mathrm{Im}} + k_I I_{i,\mathrm{Im}} = \left\{ (i\omega)^2 m' + i\omega^2 \left(t^d\right)^2 I_p - k' \right\} R_{i,\mathrm{Im}} - (i\omega)c' R_{i,\mathrm{Re}} \end{aligned} \tag{3.46}$$

Consideration of m harmonics of the response, i.e. $i = m$ provides m equations of the form as in Eqn. (3.45) or $2m$ equations of the form as in Eqn. (3.46). Stack of equations of various harmonics

as in Eqn. (3.46) is rearranged to place all identifiable parameters in a column vector such that the system of equations is reshaped as $\mathbf{Ax = b}$, yielding

$$\begin{bmatrix}
-\omega R_{1,\mathrm{Im}} & -x_0 p_1 & -m\omega^2 & 0 & -R_{1,\mathrm{Re}} & I_{1,\mathrm{Re}} \\
0 & -x_0 p_0 & 0 & 0 & -R_{0,\mathrm{Re}} & I_{0,\mathrm{Re}} \\
-2\omega R_{2,\mathrm{Im}} & -x_0 p_2 & 0 & 0 & -R_{2,\mathrm{Re}} & I_{2,\mathrm{Re}} \\
-3\omega R_{3,\mathrm{Im}} & -x_0 p_3 & 0 & 0 & -R_{3,\mathrm{Re}} & I_{3,\mathrm{Re}} \\
-5\omega R_{5,\mathrm{Im}} & -x_0 p_5 & 0 & 0 & -R_{5,\mathrm{Re}} & I_{5,\mathrm{Re}} \\
\vdots & \vdots & \vdots & \vdots & \vdots & \vdots \\
\omega R_{-1,\mathrm{Im}} & -x_0 p_{-1} & 0 & 0 & -R_{-1,\mathrm{Re}} & I_{-1,\mathrm{Re}} \\
3\omega R_{-3,\mathrm{Im}} & -x_0 p_{-3} & 0 & 0 & -R_{-3,\mathrm{Re}} & I_{-3,\mathrm{Re}} \\
\vdots & \vdots & \vdots & \vdots & \vdots & \vdots \\
\omega R_{1,\mathrm{Re}} & 0 & 0 & -m\omega^2 & -R_{1,\mathrm{Im}} & I_{1,\mathrm{Im}} \\
0 & 0 & 0 & 0 & -R_{0,\mathrm{Im}} & I_{0,\mathrm{Im}} \\
2\omega R_{2,\mathrm{Re}} & 0 & 0 & 0 & -R_{2,\mathrm{Im}} & I_{2,\mathrm{Im}} \\
3\omega R_{3,\mathrm{Re}} & 0 & 0 & 0 & -R_{3,\mathrm{Im}} & I_{3,\mathrm{Im}} \\
5\omega R_{5,\mathrm{Re}} & 0 & 0 & 0 & -R_{5,\mathrm{Im}} & I_{5,\mathrm{Im}} \\
\vdots & \vdots & \vdots & \vdots & \vdots & \vdots \\
-\omega R_{-1,\mathrm{Re}} & 0 & 0 & 0 & -R_{-1,\mathrm{Im}} & I_{-1,\mathrm{Im}} \\
-3\omega R_{-3,\mathrm{Re}} & 0 & 0 & 0 & -R_{-3,\mathrm{Im}} & I_{-3,\mathrm{Im}} \\
\vdots & \vdots & \vdots & \vdots & \vdots & \vdots
\end{bmatrix}
\begin{Bmatrix} c_{11} \\ \Delta k_{22} \\ e_{\mathrm{Re}} \\ e_{\mathrm{Im}} \\ k_s \\ k_I \end{Bmatrix} =
\begin{Bmatrix}
(\omega^2 m' - k' + \omega^2 \left(t^d\right)^2 I_p) R_{1,\mathrm{Re}} + \omega c' R_{1,\mathrm{Im}} \\
-k' R_{0,\mathrm{Re}} \\
(4\omega^2 m' - k' + 2\omega^2 \left(t^d\right)^2 I_p) R_{2,\mathrm{Re}} + 2\omega c' R_{2,\mathrm{Im}} \\
(9\omega^2 m' - k' + 3\omega^2 \left(t^d\right)^2 I_p) R_{3,\mathrm{Re}} + 3\omega c' R_{3,\mathrm{Im}} \\
(25\omega^2 m' - k' + 5\omega^2 \left(t^d\right)^2 I_p) R_{1,\mathrm{Re}} + 5\omega c' R_{1,\mathrm{Im}} \\
\vdots \\
(\omega^2 m' - k' - \omega^2 \left(t^d\right)^2 I_p) R_{1,\mathrm{Re}} - \omega c' R_{1,\mathrm{Im}} \\
(9\omega^2 m' - k' - 3\omega^2 \left(t^d\right)^2 I_p) R_{3,\mathrm{Re}} - 3\omega c' R_{3,\mathrm{Im}} \\
\vdots \\
(\omega^2 m' - k' + \omega^2 \left(t^d\right)^2 I_p) R_{1,\mathrm{Re}} - \omega c' R_{1,\mathrm{Im}} \\
-k' R_{0,\mathrm{Re}} \\
(4\omega^2 m' - k' + 2\omega^2 \left(t^d\right)^2 I_p) R_{2,\mathrm{Im}} - 2\omega c' R_{2,\mathrm{Re}} \\
(9\omega^2 m' - k' + 3\omega^2 \left(t^d\right)^2 I_p) R_{3,\mathrm{Im}} - 3\omega c' R_{3,\mathrm{Re}} \\
(25\omega^2 m' - k' + 5\omega^2 \left(t^d\right)^2 I_p) R_{1,\mathrm{Im}} - 5\omega c' R_{1,\mathrm{Re}} \\
\vdots \\
(\omega^2 m' - k' - \omega^2 \left(t^d\right)^2 I_p) R_{-1,\mathrm{Im}} + \omega c' R_{-1,\mathrm{Re}} \\
(9\omega^2 m' - k' - 3\omega^2 \left(t^d\right)^2 I_p) R_{-3,\mathrm{Im}} + 3\omega c' R_{1,\mathrm{Re}} \\
\vdots
\end{Bmatrix} \tag{3.47}$$

Eqn. (3.47) which is in the standard matrix formulation, $\mathbf{Ax = b}$ can be solved by least-squares regression and the vector of identifiable is evaluated as: $\mathbf{x} = \left(\mathbf{A}^{\mathrm{T}}\mathbf{A}\right)^{-1}\mathbf{A}^{\mathrm{T}}\mathbf{b}$. Availability of response data at various spin speeds in a speed range can be utilised in the identification process by row addition of equations available at multiple speeds, in the matrix formulation, Eqn. (3.47). Details

have been discussed in Section 2.6. The harmonics of vibration and current responses, as required in Eqn. (3.47) will be obtained from FFT based full spectrum extraction duly compensated for the phase ambiguity. The method developed in Chapter 2 for the aforesaid purpose will be used.

3.6 Generation of Simulated Responses

A Simulink model to generate displacement responses and AMB control currents, by execution of time domain EOM, as in Eqn. (3.27), is developed. A schematic representation of this model is presented in Figure 3-2. The simulation time is maintained by the Simulink™ block *Clock*. A provision for the multi harmonic reference signal generator in accordance to Eqn. (2.48) is placed in the model, which helps in removal of phase ambiguity during data processing with FFT in frequency domain. The harmonics generated in the reference signal is limited to harmonics of displacement and current signal used in Eqn. (3.47).

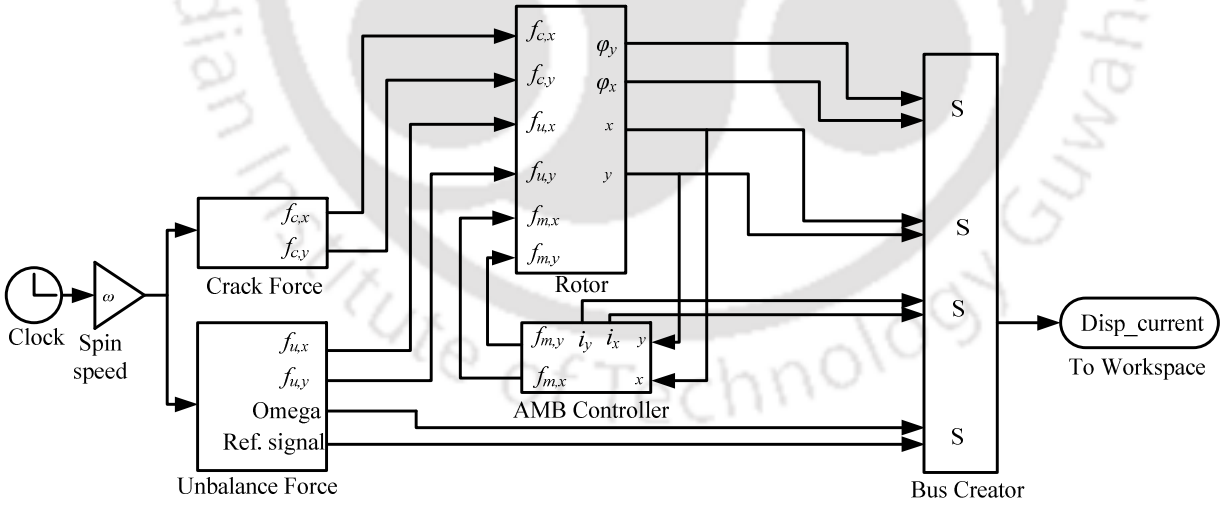

Figure 3-2 The Simulink™ model used for the response generation

Other subsystems used in the above model are as under:

Crack Force: This subsystem executes the effect of a transverse crack in the rotor according to Eqn. (3.18). The rotor spin speed and the simulation time are inputs and forces along the coordinate directions are the output of this subsystem block.

Unbalance Force: This subsystem executes the effect of unbalance in the rotor. The mathematical expression representing this subsystem block is $\bar{\mathbf{f}}_{un}$ as in Eqn. (3.21). The multi-harmonic complex reference generator is also placed inside the same subsystem. The unbalance force and reference signals are the output of this subsystem.

AMB Controller: Displacement signals are the input to this subsystem. It executes the PID function in accordance to expression for $\bar{\mathbf{f}}_{cu}$ in Eqn. (3.26) , and outputs the AMB currents and forces due to the current. While AMB currents are channelled to the bus creator, forces are fed to the rotor block.

Rotor: The rotor subsystem stores the generalized mass, stiffness, gyroscopic and damping matrices. All forces from the previous subsystems are added up and the time integration performed to obtain the velocity and displacement signals. The velocity information is processed to generate the damping and gyroscopic effects. The displacement information is used internally to generate the stiffness effects and externally output to the AMB controller subsystem to generate the control current.

Bus Creator: The bus creator block creates the signal bus of displacement, current and reference signals, which is the output to the workspace for processing and analysis.

The simulation data used for the response generation is summarized in Table 3-1. The response is generated with a fourth-order Runga-Kutta integration solver with a fixed step size of 0.0001 s. A higher order Runga-Kutta solver based on method of Dormand and Prince (1980) was tried, but did not show any particular computational benefit in this particular simulation.

Table 3-1 The rotor and AMB system data for the numerical simulation

Parameters		**Values**		**Parameters**		**Values**	
				Rotor			
Disc mass	m	2	kg	Disc eccentricity	e	24	μm
	I_p	0.0048	kg-m^2	Phase of unbalance	β	30°	deg
Shaft stiffness	k_{22}	7.6×10^5	Nm^{-1}	Viscous damping,	c_{22}	76	Ns m^{-1}
	k_{23}	8900	Nm^{-1}		c_{23}	11	Ns m^{-1}
	k_{33}	2350	Nm^{-1}		c_{33}	6	Ns m^{-1}
crack stiffness	Δk_{22}	3×10^5	Nm^{-1}	Shaft deflection	δ_x	26	μm
	Δk_{44}	1175	Nm^{-1}		$\delta_{\varphi 0}$	0	rad
				AMB			
Controller gains				*Actuator factors*			
Proportional, K_P		12200	A/m				
Derivative, K_D		3	A-s-m^{-1}	Force – current factor, k_i		42.1	N/A
Integral, K_I		2000	A/(m-s)	Force – disp. factor, k_s		105210	N/m

A typical response of the vibration displacement and the AMB control current in x- direction, obtained at the shaft spin speed of 1620 rpm (27 Hz) is presented in Figure 3-3.

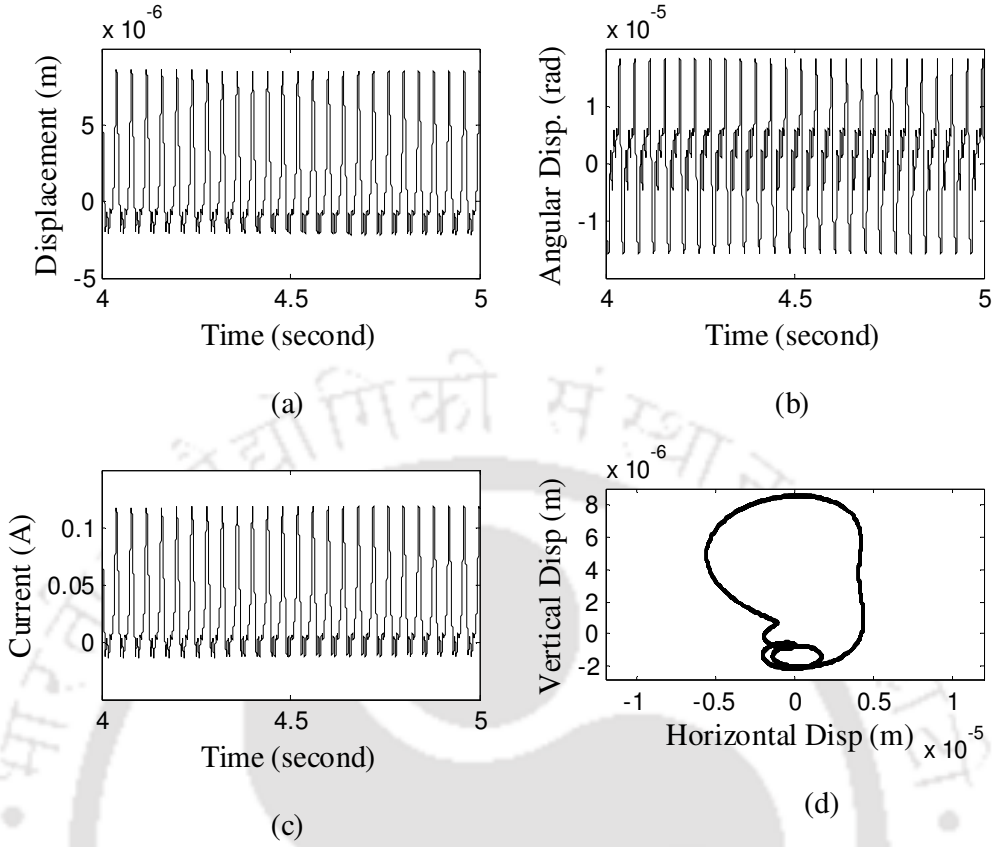

Figure 3-3 Generated response (a) *x*-displacement (b) angular displacement about *x*- axis (c) *x*-current (d) shaft centreline orbit

The vibration behaviour along the *y*–direction is similar. Certain observations could be made from the appearance of response plots. The shaft centreline orbit is not symmetric about axes, indicating the presence of crack. At higher spin speeds, the unbalance response overshadows the crack response and the centreline orbit becomes symmetric. The angular displacement peaks are close to 1.82×10^{-5} rad (0.00104°), which is generally difficult to measure accurately within the limits of practical instrumentation. This explains the need for dynamic reduction postulated in the identification algorithm.

The significance and amount of participation of the gyroscopic matrix *G* in dynamics of the rotor could be estimated by comparison of responses with and without inclusion of the *G* matrix in the ramp up test. Presence of gyroscopic matrix in the equations of motion has an effect on the critical speeds of the rotor configuration chosen, which may be readily seen in the ramp up response of the rotor, generated with and without inclusion of gyroscopic matrix, as shown in Figure 3-4. While the critical speed with inclusion of the gyroscopic matrix is observed as 3596 rpm, in its absence the critical speed has been observed as 3579 rpm.

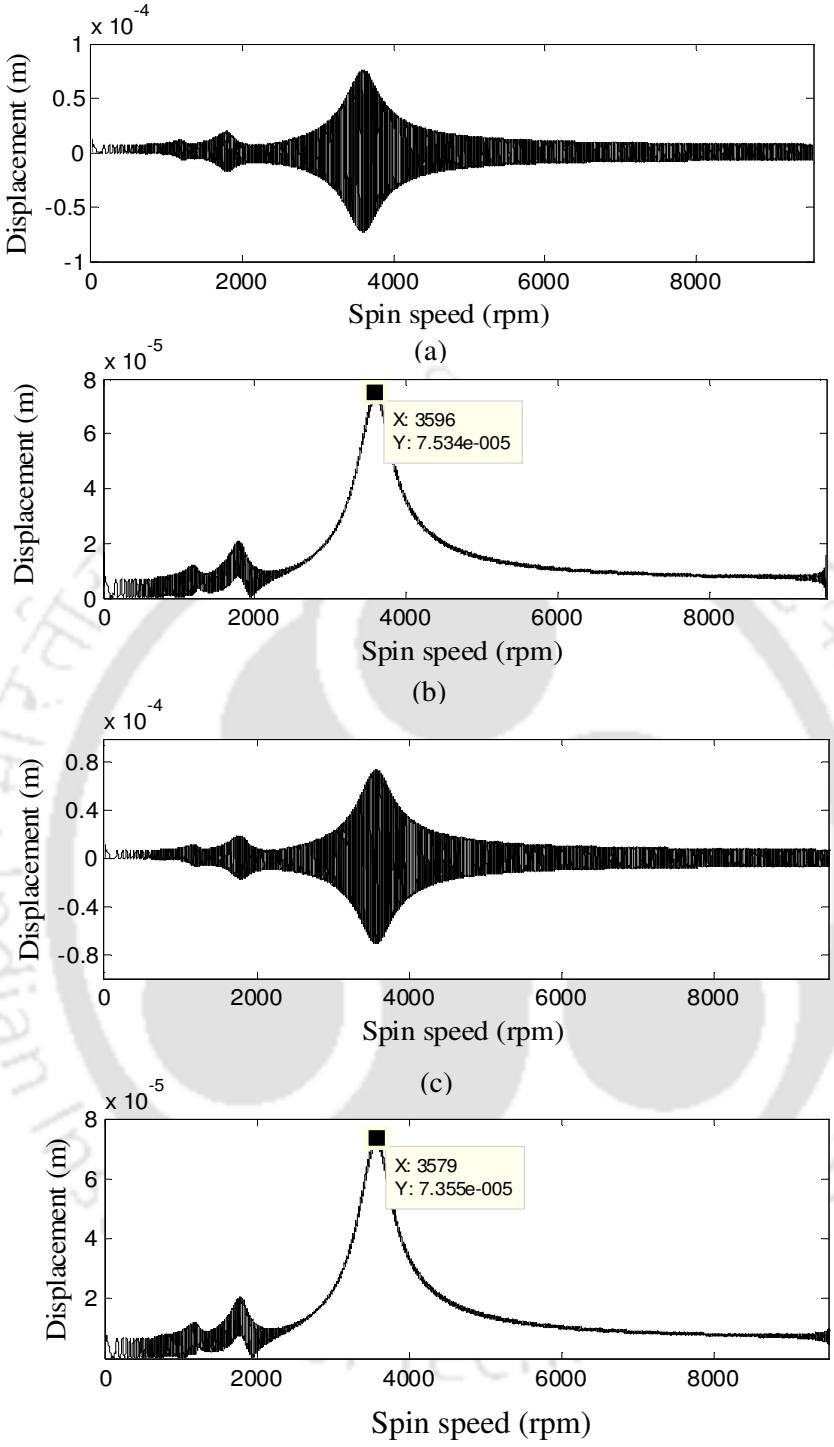

Figure 3-4 (a) *x*-displacement response during ramp up with G (b) Envelope of *x*-displacement response during ramp up with G (c) *x*-displacement response during ramp up without G (d) Envelope of *x*-displacement response during ramp up without G

3.7 Results and Discussions

The rotor-AMB system parameter estimation involves two steps, segregation of the displacement and current harmonics, R_i and I_i respectively, followed by the estimation of unknown rotor-AMB parameters. Segregation of R_i and I_i in frequency domain involves the full spectrum generation followed by the phase compensation to account for the discrepancy in phase with respect to the assumed system configuration. The step size of simulation for the response generation was 0.0001 s. The simulation was run for 5 s and response for the duration 4 s to 5 s (1 s time length) was considered for the analysis. The initial 4 s response was discarded to let transients due to integrator action of the controller disappear. The standard FFT function of MATLAB™ was used to obtain the full spectrum. Full spectrum plots of the displacement and current generated at spin speed of 1620 rpm (27 Hz) are presented in Figure 3-5.

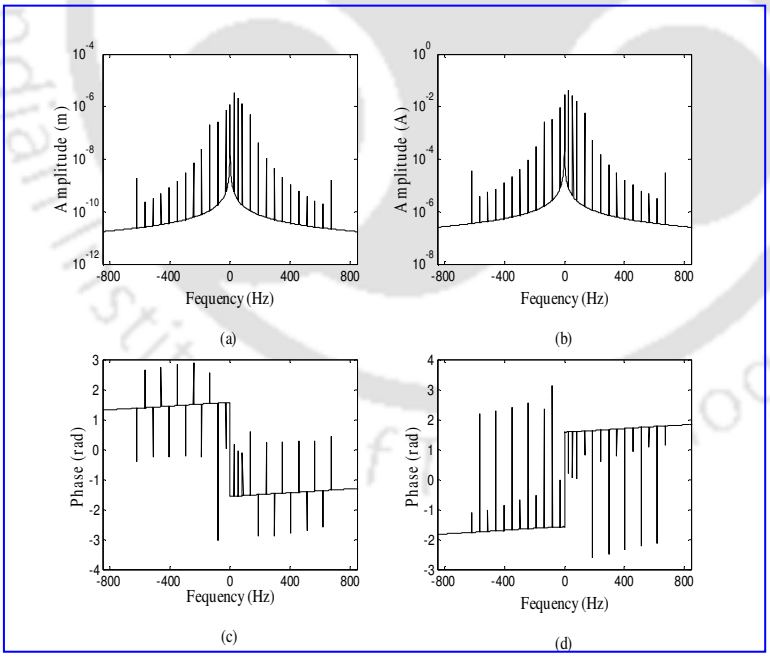

Figure 3-5 Full spectrum plots (a) amplitude of quadrature linear displacement (b) amplitude of quadrature current (c) phase of quadrature displacement (d) phase of quadrature current

To decide the range of spin speeds at which the analysis could be performed, a 20 s numerical ramp up was simulated with constant angular acceleration of 50 rad/s^2. The Hilbert envelope of the displacement response presents a clear view of the critical speed and magnitude of peak displacements at critical speeds. Use of Hilbert transform to obtain the envelope of analytic signals and many other applications has been discussed by Feldman (2011). The displacement history and the envelope of displacement response along x direction, obtained by the Hilbert transform is presented in Figure 3-4 (a) and (b).

The 1× resonance is observed at 3596 rpm with corresponding peak displacement of 7.54×10^{-5} m. Other subcritical resonances are also seen. The $\frac{1}{2}\times$ and $\frac{1}{3}\times$ resonance are observed at 1793 rpm and 1186 rpm with peak displacements of 2.085×10^{-5} m and 1.227×10^{-5} m, respectively. In the spin speed range of 1954 rpm and 2696 rpm vibration displacements are below 1.177×10^{-5} m. Vibration displacements at spin speed below 1580 rpm are lower than 1.27×10^{-5} m and at spin speed speeds above 5592 rpm is below 1.243×10^{-5} m. Spin speeds used for testing the identification algorithm are based on these observations and ranges. For further analysis, two speed ranges are selected – the lower speed range below 1580 rpm (vibration displacement below 1.27×10^{-5} m) and the higher speed range above 5592 rpm (vibration displacement below 1.24×10^{-5} m). The spin speeds used for identification are presented in Table 3-2. The central frequency used for dynamic reduction in the lower and the higher speed ranges are 1140 and 5820 rpm (19 and 97 Hz), respectively.

Table 3-2 Spin speeds used for identification

Speed range	Spin speeds (rpm)
Lower	900, 960, 1020, 1080, 1140, 1200, 1260, 1320, 1380 (15 -23 Hz)
Upper	5580, 5640, 5700, 5760, 5820, 5880, 5940, 6000,6060 (93 -101 Hz)

To simulate real measurement conditions, random noise of 1%, 2% and 5% were added to the response. These random noise were generated with 4 different seeds and channelled to 4 responses pertaining to master DOFs, viz. the *x* and *y* direction linear displacements, and the *x* and *y* direction currents. Results of the estimation in the spin speed range of 900 rpm to 1380 rpm (15-23 Hz) is presented in Table 3-3.

Table 3-3 Noise sensitivity of identification in speed range of 900 rpm to 1380 rpm

Parameter	Assumed value	Estimated value at various noise			
		0%	1%	2%	5%
c_{22}	76 (Ns m^{-1})	74.82	70.69	70.74	71.27
	% error	-1.55	-6.97	-6.92	-6.22
Δk_{22}	3×10^5 (N/m)	304830	306410	307930	312400
	% error	1.61	2.13	2.64	4.13
e	24 (μm)	24.26	24.38	24.5	24.86
	% error	1.08	1.6	2.1	3.59
β	30º (deg.)	30.05	30.06	30.06	30.04
	% error	0.17	0.2	0.2	0.14
k_s	105210 (N/m)	98602	98540	98561	98740
	% error	-6.28	-6.34	-6.32	-6.15
k_I	42.1 (N/A)	42.74	42.75	42.75	42.73
	% error	1.52	1.54	1.54	1.5

From Table 3-3 certain observations could be made regarding the influence of signal noise on performance of the identification procedure developed. In relative terms, noise has altered the estimations of c_{11} and Δk_{22} the maximum, though the absolute error introduced are lower. Similarly, the AMB force-displacement factor, k_s, has the highest absolute error in the estimation but it is quite inert to the signal noise. For instance, the variation in estimates of k_s at 5% noise corruption in signal compared to the estimates with the clean signal is only 0.13%.

Results of the estimation in the spin speed range of 5580 rpm to 6060 rpm (93-101 Hz) is presented in Table 3-4.

Table 3-4 Noise sensitivity of identification in speed range of 5580 rpm to 6060 rpm

Parameter	Assumed value	Estimated value at various noise			
		0%	1%	2%	5%
c_{22}	76 (Ns m^{-1})	73.14	73.08	73.63	74.5
	% error	-3.76	-3.84	-3.12	-1.96
Δk_{22}	3×10^5 (N/m)	308880	312560	313660	308950
	% error	2.96	4.18	4.55	2.98
e	24 (μm)	24.52	24.64	24.77	25.36
	% error	2.18	2.68	3.21	5.68
β	30º (deg.)	30.18	30.18	30.16	28.9
	% error	0.61	0.6	0.53	-3.66
k_s	105210 (N/m)	102370	102420	100850	97130
	% error	-2.7	-2.65	-4.14	-7.68
k_I	42.1 (N/A)	43.2	43.19	43.43	40.23
	% error	2.61	2.58	3.17	-4.43

The measurement of rotor properties like its mass, disc moment of inertia and intact shaft stiffness may contain errors. Certain simplifying assumptions used in development of the mathematical model of the rotor-AMB system like rigid end support bearings may also introduce some errors in estimation equations. All such errors which may be present in the estimation process can be summed up as the *modelling error*. The robustness of the identification procedure developed was tested by introduction of random modelling errors of 1%, 2% and 5% to the most critical model parameters, viz. disc mass (m), intact shaft stiffness (k_{22}) and the shaft static deflection (δ_x). The response is generated using Eqn. (3.27) with correct model parameters and then the error is added in model parameters in Eqn. (3.47) used for the estimation in identification algorithm. Thus, correct response is used in an estimation model containing error. The estimates obtained are

compared with the assumed values. Effect of modelling error magnitude on results of estimation in lower speed range is summarized in Table 3-5.

Table 3-5 Sensitivity of estimated parameters to the modelling error

Parameter	Assumed value	Estimated value at various noise			
		0%	1%	2%	5%
c_{22}	76 (Ns m^{-1})	74.82	73.94	77.01	78.6
	% error	-1.55	-2.7	1.33	3.42
Δk_{22}	3×10^5 (N/m)	304830	306330	308100	306930
	% error	1.61	2.11	2.7	2.31
e	24 (μm)	24.26	24.25	24.39	24.51
	% error	1.08	1.06	1.66	2.13
β	30º (deg.)	30.05	30.05	30.05	30.11
	% error	0.17	0.17	0.17	0.37
k_s	105210 (N/m)	98602	100660	97267	96877
	% error	-6.28	-4.32	-7.55	-7.92
k_I	42.1 (N/A)	42.74	42.89	43.09	42.9
	% error	1.52	1.88	2.36	1.9

From Table 3-5, it is observed that the unbalance magnitude and phase has been faithfully identified under all levels of the modelling error. In general, rotor parameters are the least affected by modelling errors with the additive crack stiffness (Δk_{22}) deviating a maximum by 2.7 − 1.61 = 1.09% and the viscous damping (c_{22}) by 3.42 + 1.55 = 4.97% at 5% modelling error. AMB constants k_s is most vulnerable with -7.92% deviation at 5% modelling error. On the whole, the developed identification procedure is found robust against bias errors.

3.8 Concluding Remarks

In this chapter, system EOMs for a 4-DOF model for the cracked rotor with offset disc and AMB support has been obtained. Gyroscopic effects arising due to offset placement of the disc upon the

rotor could be taken into account, which is very peculiar to rotors as compared to structures. Numerical illustrations are performed on a sample rotor–AMB data, and the time and frequency responses are studied. The method for obtaining the full spectrum and removal of phase ambiguity of the displacement and AMB current responses was developed in the previous chapter. This method has been faithfully adopted in the present chapter to obtain the displacement and current harmonics used in the identification process.

Rotational displacements have been simulated in the present model, which pose practical difficulty of physical measurements. A suitable reduction scheme has been applied to do away with the need for this measurement and the identification plan developed based on the master (i.e. the retained) DOFs only. The development and testing of the identification algorithm for identification of transverse crack (identified by parameter - Δk_{22}, the additive crack stiffness) and the rotor–AMB system parameters along with the viscous damping and rotor unbalance has been performed using the frequency domain equations developed in this chapter. The developed algorithm has been found robust against moderate level of instrument and modelling errors. The dynamic reduction scheme used has been found adequate.

The present chapter develops a frame work for dynamic reduction and system parameter identification based on a 4-DOF lumped parameter model. The framework developed could be applied to a more realistic model based on finite element method. The next chapter presents the modelling and estimation of parameters in cracked rotor with AMB support, by finite element method.

CHAPTER 4

FEM based Modelling of Rotor–AMB System for Identification of Transverse Crack

4.1 Introduction

In Chapters 2 and 3, the principal emphasis had been on establishing methods for analysis of various aspects of the cracked rotor with AMB supports in the auxiliary bearing configuration. It was demonstrated that the loss of analytical information due to attenuation of vibrations by the AMB could be compensated for by considering the AMB control current signal as an additional information. Hence, fairly simple models of the rotor – AMB system were considered. To analyse situations close to real rotors, in this chapter a cracked rotor is modelled using finite elements with 4 degrees of freedom at each element node, considering the gyroscopic effect due to rigid discs and a switching crack excitation function to introduce the breathing behaviour of crack. Frequency domain of the time domain response is obtained with the full spectrum analysis. An algorithm developed with the purpose of identification of crack in the form of additive crack stiffness simultaneously estimates the disc unbalance and AMB stiffness constants.

4.2 System Configuration

A schematic illustration of the physical configuration of the rotor system considered for analysis is shown in Figure 4-1. It consists of a flexible shaft carrying *m* number of rigid discs. The rotor is end supported on conventional bearings with AMB support in the auxiliary bearing configuration. For successful implementation of AMB, the part of the rotor inside the AMB must be suitably laminated to minimize the electromagnetic resistance to rotation due to eddy currents (Traxler, 2009). Of the *m* discs on the shaft, this lamination core acts as one of the discs. The end support

bearings are assumed rigid in transverse directions. A transverse crack is considered on the shaft, which affects effective stiffness of the shaft.

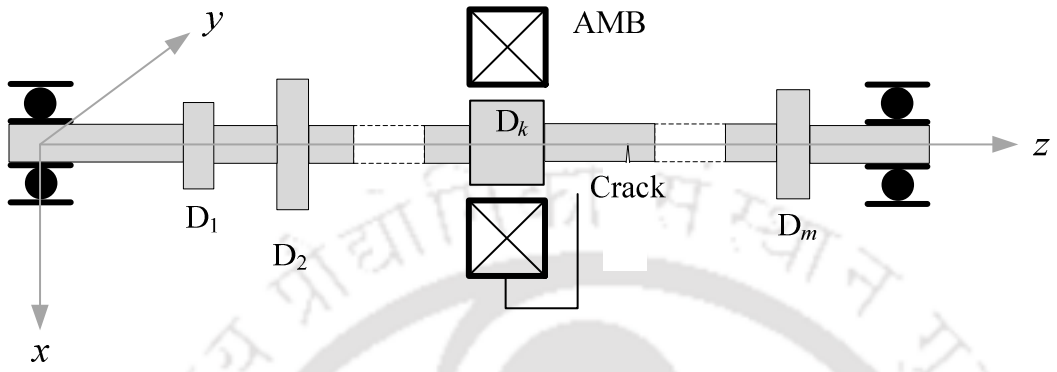

Figure 4-1 Physical configuration of cracked rotor with AMB support

The cracked rotor when spinning, will be excited by three forces, viz. the crack force, the force due to static unbalance and the AMB restitution force. Derivation of these forces in a fixed coordinate system has been made in previous chapter, under Section 3.3. For the description of coordinates and directions, Figure 2-2 in Chapter 2, may be referred.

The rotating coordinate directions ξ and η are defined such that ξ points perpendicular to the crack front and η points along the crack front. By this definition of rotating coordinates, the stiffness along these two directions are constant. O is the origin of co-ordinate system O*xyz* and is defined on the bearing axis. For a particular disc, C is the centre of rotation of the disc, and G is the centre of disc mass. CG = e is the disc eccentricity. For n number of discs on the rotor, e_1 through e_n is defined as the disc eccentricity for individual discs. Angular position of the unbalance in relation to perpendicular to the crack front is quantified by constant angles, β_1 through β_n, for each disc. The transverse translational displacements are u_x and u_y, and the corresponding transverse rotational displacements are φ_y and φ_x. For the horizontal shaft, the static linear deflection is present along

vertical direction and marked as δ_x and the static angular rotation is present about the *y* axis and marked as δ_{φ_y}. In general, the displacement vector $\mathbf{q}$ in terms of vibration displacements $\mathbf{q}_{\mathrm{v}}$ and static deflections $\mathbf{q}_{\mathbf{0}}$ is defined as

$$\mathbf{q} = \mathbf{q}_{\mathrm{v}} + \mathbf{q}_{\mathbf{0}} = \begin{Bmatrix} u_x \\ u_y \\ \varphi_y \\ \varphi_x \end{Bmatrix} + \begin{Bmatrix} \delta_x \\ \delta_y \\ \delta_{\varphi_y} \\ \delta_{\varphi_x} \end{Bmatrix} \tag{4.1}$$

Vibration displacements and static deflections, respectively, can be expressed in the complex form as

$$\mathbf{q}_{\mathrm{v}}^{c} = \begin{Bmatrix} u_x + \mathrm{j}u_y \\ \varphi_y + \mathrm{j}\varphi_x \end{Bmatrix} = \begin{Bmatrix} u_c \\ \varphi_c \end{Bmatrix} \tag{4.2}$$

and

$$\mathbf{q}_{0}^{c} = \begin{Bmatrix} \delta_x + \mathrm{j}\delta_y \\ \delta_{\varphi_y} + \mathrm{j}\delta_{\varphi_x} \end{Bmatrix} = \begin{Bmatrix} \delta_{u_c} \\ \delta_{\varphi_c} \end{Bmatrix} \tag{4.3}$$

The complex vibration displacement and static deflection will be used in defining the forcing terms due to the crack and AMB actions. The list of excitation forces acting in the assumed system configuration is derived in the next section.

4.3 Statement of Excitation Forces

Before discretising the rotor for further analysis with the finite element method, the forces acting on the rotor, viz. the unbalance force, crack force and AMB restitution force are expressed in the form suitable for inclusion in finite element equations. While the AMB restitution force and the force due to unbalance can be stated in fixed coordinate system from first principles, the derivation for crack force in fixed coordinates is derived with help of expressions in rotating coordinates, as derived in Section 3.3.1.

4.3.1 Crack Forces

In Chapter 3, the crack force in a weight dominated rotor was derived as

$$\mathbf{f}_{\mathbf{cr}} = \tfrac{1}{2} s(t) \begin{Bmatrix} \Delta k_{22}(1+\cos 2\omega t)\delta_x \\ \Delta k_{22}(\sin 2\omega t)\delta_x \\ \Delta k_{44}(1+\cos 2\omega t)\delta_{\varphi_y} \\ \Delta k_{44}(\sin 2\omega t)\delta_{\varphi_y} \end{Bmatrix} \tag{4.4}$$

Eqn. (4.4) can be written in complex form as

$$\mathbf{f}_{\mathrm{cr}}^{c} = \tfrac{1}{2} s(t) \begin{Bmatrix} \delta_x \Delta k_{22}(1+\mathrm{e}^{2\mathrm{j}\omega t}) \\ \delta_{\varphi_y} \Delta k_{44}(1+\mathrm{e}^{2\mathrm{j}\omega t}) \end{Bmatrix} \tag{4.5}$$

The expression of crack force in the above form helps in expansion of the crack force vector in Fourier series, for ease in the computational work.

4.3.2 Residual Unbalance Forces

For each rigid disc, D_1 through D_n, the force due to residual unbalance is defined in terms of the magnitude and orientation of the unbalance, e_n and β_n, respectively. For the n^{th} disc, the force due to disc unbalance is given as

$$\mathbf{f}^{c}_{\text{un},n} = \begin{Bmatrix} m e_n \omega^2 \mathrm{e}^{\mathrm{j}(\omega t + \beta_n)} \\ 0 \end{Bmatrix} \tag{4.6}$$

The expression of the unbalance force in Eqn. (4.6) is consistent with Eqn. (2.2) and Eqn. (3.22) in previous chapters.

4.3.3 Restitution force due to AMB

Isotropic AMBs are characterized by two orthogonal direction independent stiffness constants, k_s, the force–displacement constant and, k_I, the force–current constant. For active magnetic devices both these constants could be considered as linear, close to the operating point. Since the magnetic attraction increases with the decrease in the distance of separation of the magnetic specimen, the force–displacement constant is negative. With the definition of two AMB stiffnesses, as detailed above, the AMB restitution force is given as

$$\mathbf{f}'_{\text{AMB-R}} = -\begin{Bmatrix} -k_s u_x + k_I i_x \\ -k_s u_y + k_I i_y \\ 0 \\ 0 \end{Bmatrix} = \begin{Bmatrix} k_s u_x - k_I i_x \\ k_s u_y - k_I i_y \\ 0 \\ 0 \end{Bmatrix} \tag{4.7}$$

Currents along two orthogonal directions can be converted to a complex current as $i_c = i_x + \mathrm{j}i_y$. Eqn. (4.7) can be written in terms of the complex vibration displacement vector $\mathbf{q}_{\mathrm{v}}^{c}$ and the complex current i_c as

$$\mathbf{f}_{\text{AMB-R}}^{c} = \begin{bmatrix} k_u & 0 \\ 0 & 0 \end{bmatrix} \mathbf{q}_{\mathrm{v}}^{c} - \begin{bmatrix} k_I & 0 \\ 0 & 0 \end{bmatrix} \begin{Bmatrix} i_c \\ 0 \end{Bmatrix} = k_u u_c - k_I i_c \tag{4.8}$$

The PID control law correlating the vibration displacement with AMB coil currents has been described under Section 2.2.5. Once excitation forces are available in terms of the vibration displacement vector, they can be placed in appropriate equations during the FE modelling.

4.4 Finite Element Modelling of the Rotor System

The finite element method involves subdivision of a whole problem domain into simpler parts, called discrete elements, i.e. the discretization of a continuous structure. The method has been successfully used in the design and analysis of practical rotors with the complex and irregular shapes (Friswell et al., 2010). The model considered in this work consists of a cracked flexible rotor end supported on rigid bearings, rigid discs and an AMB in the additional bearing configuration. The whole model is subdivided into smaller models for simplicity, viz. the shaft model, the disc model and the AMB model. Each sub–model is considered individually and equations of motion for that sub–model developed, with help of excitation forces derived in the previous section. All equations from each sub-model are then reassembled to get global equations of motion and the boundary or support conditions are applied. The shaft is discretised into finite elements with 4–DOFs (2 linear displacements and 2 angular displacements) at each node as depicted in Figure 4-2.

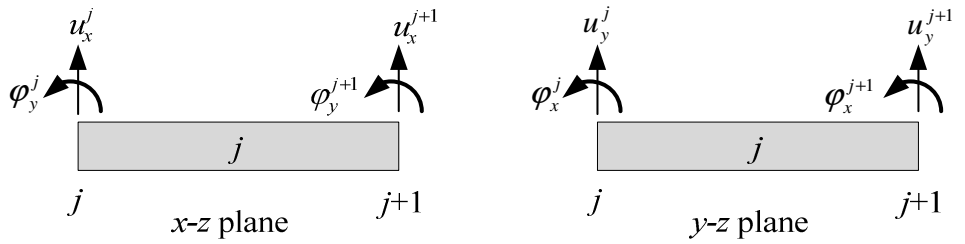

Figure 4-2 The j^{th} finite element with node points and DOFs

4.4.1 Sub-models

As stated earlier, the whole model is subdivided into smaller models for simplicity, each sub–model considered individually and equations of motion for that sub–model developed. All the sub-models of the present model are described in the following sections.

4.4.1.1 *Shaft sub-model*

The equation of motion for a shaft element is given as

$$\mathbf{M}^{(e)}\ddot{\boldsymbol{\eta}}^{(ne)} + \left(\mathbf{C}^{(e)} - \omega\mathbf{G}^{(e)}\right)\dot{\boldsymbol{\eta}}^{(ne)} + \mathbf{K}^{(e)}\boldsymbol{\eta}^{(ne)} = \mathbf{f}^{(ne)} \tag{4.9}$$

Here,

$$\boldsymbol{\eta}^{(ne)} = \begin{bmatrix} u_c^j & \varphi_c^j & u_c^{j+1} & \varphi_c^{j+1} \end{bmatrix}^{\mathrm{T}} \tag{4.10}$$

where $\boldsymbol{\eta}^{(ne)}$ and $\mathbf{f}^{(ne)}$ are the elemental nodal displacement and force vectors respectively, ω is the rotor angular speed (or the rotor spin frequency), u_c and φ_c are defined by Eqn. (4.2) at the numbered node. Matrices $\mathbf{M}^{(e)}$, $\mathbf{C}^{(e)}$, $\mathbf{G}^{(e)}$ and $\mathbf{K}^{(e)}$ are the elemental mass, damping, gyroscopic and stiffness matrices, respectively. Derivation and details of the above matrices is available in

Appendix B. The damping matrix is obtained, on assumption of Rayleigh damping enunciated in Appendix C.

4.4.1.2 *Crack sub-model*

The transverse crack is modelled as a switching force at the particular node, as derived in Section 3.3.1. Under practical assumption of very small static rotational displacement as compared to the static linear displacement, i.e. $\delta_{\varphi_y} \to 0$ the contribution of δ_{φ_y} in Eqn. (4.4) is insignificant. Thus, the crack force is obtained as

$$\mathbf{f}'_{\mathrm{cr}} = \tfrac{1}{2} s(t) \begin{Bmatrix} \Delta k_{22}(1+\cos 2\omega t)\delta_x \\ \Delta k_{22}(\sin 2\omega t)\delta_x \\ 0 \\ 0 \end{Bmatrix} \tag{4.11}$$

The expression in terms of nodal displacement vector is

$$\tfrac{1}{2} s(t) \Delta k_{22}(1+\mathrm{e}^{2\mathrm{j}\omega t})\boldsymbol{\eta}_{x0} = \mathbf{f}_{\mathrm{cr}} \tag{4.12}$$

Here vector $\boldsymbol{\eta}_{x0}$ contains linear static displacements in the x–z plane at the location of the crack, other elements of the vector are zero. Other underlying assumptions are described in Section 4.3.1.

4.4.1.3 *Disc sub-model*

Disc is assumed rigid and is modelled using the mass and mass moment of inertia terms at the node of its position in the configuration. The rigid disc equations of motion is expressed as

$$\mathbf{M}_d \ddot{\boldsymbol{\eta}}_d - \omega \mathbf{G}_d \dot{\boldsymbol{\eta}}_d = \mathbf{f}_d \tag{4.13}$$

Here, vectors $\boldsymbol{\eta}_d$ and $\mathbf{f}_d$ are the disc displacement and force vectors respectively, at the disc location; other elements of the vector are zero. Constituents of the vector $\mathbf{f}_d$ have been explained in Section 4.3.2. Matrices $\mathbf{M}_d$ and $\mathbf{G}_d$ are the disc mass and gyroscopic matrices, respectively, as detailed in Appendix B.

4.4.1.4 *AMB sub-model*

The AMB action has been described in Section 4.3.3. The AMB sub-model defines the restitution force exerted at the particular node on account of AMB action. The restitution force produced by the AMB at the shaft node is expressed as

$$\mathbf{f}_{\text{AMB-R}}(t) = k_u \boldsymbol{\eta}_{\text{AMB}}(t) - k_I \mathbf{i}_{\text{c}}(t) \tag{4.14}$$

Vectors $\boldsymbol{\eta}_{\text{AMB}}$ and $\mathbf{i}_{\text{c}}$ contain the displacement and current at the AMB location as described in Section 4.3.3; all other entries of the two vectors are zero. The control current could be expressed as

$$\mathbf{i}_{\mathbf{c}} = \begin{bmatrix} k_P & 0 & k_D & 0 & k_I & 0 \\ 0 & k_P & 0 & k_D & 0 & k_I \end{bmatrix} \begin{Bmatrix} u_x \\ u_y \\ \dot{u}_x \\ \dot{u}_y \\ \overline{u}_x \\ \overline{u}_y \end{Bmatrix} \tag{4.15}$$

The dot and bar on variables represent differentiation and integration. It may be noted that Eqns. (4.14) and (4.15) are convenient representation of Eqn. (4.8), rewritten for better suitability for the FEM formulation.

4.4.2 Assembled Equations of Motion of the Cracked-Rotor AMB System

Equations obtained for the individual subsystems viz. the shaft, disc, AMB and crack are combined together and boundary conditions applied to obtain the assembled equations of motion of the rotor. The assembled equation of motion is given as

$$\mathbf{M}\ddot{\boldsymbol{\eta}} + (\mathbf{C} - j\omega\mathbf{G})\dot{\boldsymbol{\eta}} + \mathbf{K}\boldsymbol{\eta} = \mathbf{f}_{unb} + \mathbf{f}_{cr} + \mathbf{f}_{AMB\text{-}R} \tag{4.16}$$

Here, **M**, **C**, **G** and **K** are the global mass, damping, gyroscopic and stiffness matrices and $\mathbf{f}_{unb}$, $\mathbf{f}_{cr}$ and $\mathbf{f}_{AMB\text{-}R}$ are vectors of the unbalance, crack and AMB control forces, respectively. A solution to Eqn. (4.16) will present the time history of displacements at all DOFs. The methods developed in Chapter 2 and Chapter 3 to convert the displacement histories to frequency domain can be utilised to obtain the harmonics of the linear and angular displacements. The nature of response in time and frequency domain is presented in the next section.

4.4.3 Time and Frequency Responses

Solution to Eqn. (4.16) yields the vector, $\boldsymbol{\eta}$, rotor responses at various nodes. To analyse the nature of response in time and frequency domain, Eqn. (4.16) is further simplified by defining the nature of breathing function $s(t)$ and splitting the AMB restitution force into component purely due to the vibration displacement and due to the control current. The crack with a depth much lower

than half of the shaft radius, exhibit a switching behaviour well represented by a rectangular breathing function, depicted in Figure 2-4, and reported in Gasch (2008). This breathing function is approximated by Fourier series as

$$s(t) = \tfrac{1}{2} + \tfrac{2}{\pi}\cos\omega t - \tfrac{2}{3\pi}\cos(3\omega t) + \tfrac{2}{5\pi}\cos(5\omega t) - \tfrac{2}{7\pi}\cos(7\omega t) + \tfrac{2}{9\pi}\cos(9\omega t) - \cdots \quad (4.17)$$

Using the Euler formula, the crack excitation force, Eqn. (4.12), can be expressed in a series of various harmonics as

$$\Delta k_{22}\{\cdots - 0.021\mathrm{e}^{-\mathrm{j}3\omega t} + 0.106\mathrm{e}^{-\mathrm{j}\omega t} + 0.25 + 0.319\mathrm{e}^{\mathrm{j}\omega t} + 0.25\mathrm{e}^{\mathrm{j}2\omega t} + \cdots\}\boldsymbol{\eta}_{x0} = \mathbf{f}_{\mathrm{cr}} \quad (4.18)$$

With introduction of *location flag vector*, described below, Eqn. (4.18) can be better written in notational form as

$$\mathbf{f}_{\mathrm{cr}} = \Delta k_{22}\delta_x \sum_{i=-n}^{+n} p_i \mathrm{e}^{\mathrm{j}i\alpha t}\boldsymbol{\lambda}_{\mathrm{cr}} \quad (4.19)$$

Here p_i is participation factor of the i^{th} harmonic of the crack force excitation.

Location flag vectors: The forcing terms on the RHS of assembled FEM equations should be column vectors of dimension consistent with the dimension on the LHS. For ease of ensuring this requirement to be fulfilled in the computational stage of the analysis, vector flags $\boldsymbol{\lambda}_{\mathrm{unb}}$, $\boldsymbol{\lambda}_{\mathrm{cr}}$ and $\boldsymbol{\lambda}_{\mathrm{AMB}}$ may be introduced. These vector flags have the same length as the global displacement vector. The elements of vector flags are 0 and 1, with the element at node position of forcing term

being 1 and all other elements 0. Hence, with multiplication of location flag vectors, the scalars can be converted to vectors consistent with dimensions of the matrix equation.

With a descent hardware setup, the rotor response at the node of AMB location and the AMB control current (error and control signal respectively, for the controller) will have the same nature. Thus, all the harmonics present in the shaft response should be present in the complex current of Eqn. (4.8). Incorporating this, the entry at AMB node in control current vector i_c can be written as

$$i_{c(\text{AMB node})} = \sum_{i=-n}^{+n} I_i e^{ji\omega t} \tag{4.20}$$

With help of Eqns. (4.19) and (4.20) , the EOM in Eqn. (4.16) can be suitably modified to

$$\begin{aligned} \mathbf{M}\ddot{\boldsymbol{\eta}} + (\mathbf{C} - j\omega\mathbf{G})\dot{\boldsymbol{\eta}} + \mathbf{K}\boldsymbol{\eta} = \Delta k_{22}\delta_x \sum_{i=-n}^{+n} p_i e^{ji\omega t}\boldsymbol{\lambda}_{\text{cr}} + \sum_{i=1}^{m}(me_i\omega^2 e^{j\beta_i})e^{j\omega t}\boldsymbol{\lambda}_{\text{unb}} \\ - k_I \sum_{i=-n}^{+n} I_i e^{ji\omega t}\boldsymbol{\lambda}_{\text{AMB}} + k_s\boldsymbol{\eta}\circ\boldsymbol{\lambda}_{\text{AMB}} \end{aligned} \tag{4.21}$$

Here, operator "○" in the last term of Eqn. (4.21) represents the Hadamard product or element wise multiplication. The assumed solution to Eqn. (4.21) will also contain the same harmonics as forcing terms. Thus, the assumed solution will have the form

$$\boldsymbol{\eta}(t) = \sum_{i=-\infty}^{i=\infty} \bar{\boldsymbol{\eta}}_i\, e^{ji\omega t} \tag{4.22}$$

Substituting the assumed solution into Eqn. (4.21) and rearranging gives the frequency domain equation for particular harmonics, for i =1 and ≠ 1, respectively, as

$$\left[\left(-\omega^2\mathbf{M}\right)+\mathrm{j}\omega\left(\mathbf{C}-\mathrm{j}\omega\mathbf{G}\right)+\mathbf{K}\right]\bar{\boldsymbol{\eta}}_1=\Delta k_{22}\delta_x p_1\boldsymbol{\lambda}_{\mathrm{cr}}+me\omega^2\mathrm{e}^{\mathrm{j}\beta}\boldsymbol{\lambda}_{\mathrm{unb}}-k_I I_1\boldsymbol{\lambda}_{\mathrm{AMB}}+k_s\bar{\boldsymbol{\eta}}_1\circ\boldsymbol{\lambda}_{\mathrm{AMB}} \tag{4.23}$$

$$\left[\left(-(i\omega)^2\mathbf{M}\right)+\mathrm{j}(i\omega)\left(\mathbf{C}-\mathrm{j}\omega\mathbf{G}\right)+\mathbf{K}\right]\bar{\boldsymbol{\eta}}_i=\Delta k_{22}\delta_x p_i\boldsymbol{\lambda}_{\mathrm{cr}}-k_I I_i\boldsymbol{\lambda}_{\mathrm{AMB}}+k_s\bar{\boldsymbol{\eta}}_i\circ\boldsymbol{\lambda}_{\mathrm{AMB}} \tag{4.24}$$

The system response in time domain, $\boldsymbol{\eta}(t)$, can be obtained by the time integration of Eqn. (4.21), and the frequency domain response, $\bar{\boldsymbol{\eta}}_i$, can be obtained from the full spectrum of $\boldsymbol{\eta}(t)$. The AMB current, i_c (t), and its harmonic components, I_i, will be also obtained as a result of the time integration and the full spectrum analysis, respectively.

4.4.4 Reduction of Unwanted DOFs

It may be seen from Eqn. (4.16) that, before application of boundary conditions, for a finite element discretization with j number of elements with k DOFs at all nodes, all matrices are sized $k(j+1)\times k(j+1)$ and all vectors as $k(j+1)\times 1$. Since, in real rotors the typical vibration is so small, the associated rotational displacements are smaller than measurement limits and pose difficulty in practical measurements. Also, with increase in the number of finite elements, number of linear DOFs to be measured may become difficult due to constraints like – availability of large number of sensors, access to mount the sensors, etc. The finite element equation can be suitably modified to reduce unwanted DOFs from the equation of motion, using the transformation defined as

$$\boldsymbol{\eta} = \begin{Bmatrix} \boldsymbol{\eta}_m \\ \boldsymbol{\eta}_s \end{Bmatrix} = \mathbf{T}^d \boldsymbol{\eta}_m \tag{4.25}$$

with

$$\mathbf{T}^d = \begin{bmatrix} \mathbf{I} \\ -\left[\mathbf{K}_{ss} - \omega_0^2 \mathbf{M}_{ss}\right]^{-1} & \left[\mathbf{K}_{sm} - \omega_0^2 \mathbf{M}_{sm}\right] \end{bmatrix} \tag{4.26}$$

here $\mathbf{T}^d$ is the transformation matrix for the dynamic reduction, subscripts *m* and *s* relate to the master (retained) and slave (reduced) DOFs, respectively. More details on reduction schemes are available in Section 1.4.3 and Section 3.5.1. The matrices on the LHS in Eqn. (4.16) are transformed as

$$\mathbf{M}^d = \left(\mathbf{T}^d\right)^T \mathbf{M}\mathbf{T}^d; \quad \mathbf{C}^d = \left(\mathbf{T}^d\right)^T \mathbf{C}\mathbf{T}^d; \quad \mathbf{G}^d = \left(\mathbf{T}^d\right)^T \mathbf{G}\mathbf{T}^d; \quad \mathbf{K}^d = \left(\mathbf{T}^d\right)^T \mathbf{K}\mathbf{T}^d \tag{4.27}$$

and the matrices on the RHS are transformed as

$$\mathbf{f}_{\text{unb}}^d = \left(\mathbf{T}^d\right)^T \mathbf{f}_{\text{unb}}; \quad \mathbf{f}_{\text{cr}}^d = \left(\mathbf{T}^d\right)^T \mathbf{f}_{\text{cr}}; \quad \mathbf{f}_{\text{AMB-R}}^d = \left(\mathbf{T}^d\right)^T \mathbf{f}_{\text{AMB-R}} \tag{4.28}$$

Eqn. (4.16) can be now expressed in terms of condensed matrices, with only master DOFs. The reduced equation is

$$\mathbf{M}^d \ddot{\boldsymbol{\eta}}_m + \left(\mathbf{C}^d - \mathrm{j}\omega\mathbf{G}^d\right)\dot{\boldsymbol{\eta}}_m + \mathbf{K}^d \boldsymbol{\eta}_m = \mathbf{f}_{\text{unb}}^d + \mathbf{f}_{\text{cr}}^d + \mathbf{f}_{\text{AMB-R}}^d \tag{4.29}$$

Eqn. (4.16) and Eqn. (4.29) are equivalent, with the former expressed in full DOFs of the model and the later in master DOFs only. The vector flags $\boldsymbol{\lambda}_{\text{unb}}$, $\boldsymbol{\lambda}_{\text{cr}}$ and $\boldsymbol{\lambda}_{\text{AMB}}$ are also reduced by removing the entries corresponding to the slave DOFs. Eqn. (4.16) and (4.21) will be used for the response generation and the identification algorithm will be developed with Eqn. (4.29).

4.5 Development of Identification Algorithm

For abridging the lengths of expressions used in the further derivations, following notation is used

$$\left(-(i\omega)^2\,\mathbf{M}^d\right)+\mathrm{j}(i\omega)\left(\mathbf{C}^d-\mathrm{j}\omega\mathbf{G}^d\right)+\mathbf{K}^d=\mathbf{D}_i \tag{4.30}$$

For the development of an identification algorithm, frequency domain equations, Eqns. (4.23) and (4.24) will be rewritten in terms of master DOFs, following the reduction of slave DOFs.

$$\Delta k_{22}\delta_x p_1\boldsymbol{\lambda}_{\text{cr}}+m\omega^2 e\mathrm{e}^{\mathrm{j}\beta}\boldsymbol{\lambda}_{\text{unb}}-k_I I_1\boldsymbol{\lambda}_{\text{AMB}}+k_s\overline{\boldsymbol{\eta}}_{1,m}\circ\boldsymbol{\lambda}_{\text{AMB}}=\mathbf{D}_1\overline{\boldsymbol{\eta}}_{1,m} \tag{4.31}$$

and

$$\Delta k_{22}\delta_x p_i\boldsymbol{\lambda}_{\text{cr}}-k_I I_i\boldsymbol{\lambda}_{\text{AMB}}+k_s\overline{\boldsymbol{\eta}}_{i,m}\circ\boldsymbol{\lambda}_{\text{AMB}}=\mathbf{D}_i\overline{\boldsymbol{\eta}}_{i,m} \tag{4.32}$$

The proposed identification algorithm seeks to detect presence of a crack in the rotor system as the first goal, and the unbalance magnitude and phase as the second. Presence of crack in the rotor can be ascertained by identification of the crack stiffness term, Δk_{22}. Additionally, the AMB stiffness k_I and k_s could also be identified. Considering n harmonics of the response to be used in the identification process, the above equations are written in a vector–matrix form, as

$$\begin{bmatrix} \vdots & \vdots & \vdots & \vdots \\ \delta_x p_3 \boldsymbol{\lambda}_{\text{cr}} & 0 & -I_3 \boldsymbol{\lambda}_{\text{AMB}} & \overline{\boldsymbol{\eta}}_{3,m} \circ \boldsymbol{\lambda}_{\text{AMB}} \\ \delta_x p_2 \boldsymbol{\lambda}_{\text{cr}} & 0 & -I_2 \boldsymbol{\lambda}_{\text{AMB}} & \overline{\boldsymbol{\eta}}_{2,m} \circ \boldsymbol{\lambda}_{\text{AMB}} \\ \delta_x p_1 \boldsymbol{\lambda}_{\text{cr}} & m\omega^2 \boldsymbol{\lambda}_{\text{unb}} & -I_1 \boldsymbol{\lambda}_{\text{AMB}} & \overline{\boldsymbol{\eta}}_{1,m} \circ \boldsymbol{\lambda}_{\text{AMB}} \\ \delta_x p_0 \boldsymbol{\lambda}_{\text{cr}} & 0 & -I_0 \boldsymbol{\lambda}_{\text{AMB}} & \overline{\boldsymbol{\eta}}_{0,m} \circ \boldsymbol{\lambda}_{\text{AMB}} \\ \delta_x p_{-1} \boldsymbol{\lambda}_{\text{cr}} & 0 & -I_{-1} \boldsymbol{\lambda}_{\text{AMB}} & \overline{\boldsymbol{\eta}}_{-1,m} \circ \boldsymbol{\lambda}_{\text{AMB}} \\ \delta_x p_{-3} \boldsymbol{\lambda}_{\text{cr}} & 0 & -I_{-3} \boldsymbol{\lambda}_{\text{AMB}} & \overline{\boldsymbol{\eta}}_{-3,m} \circ \boldsymbol{\lambda}_{\text{AMB}} \\ \vdots & \vdots & \vdots & \vdots \end{bmatrix} \begin{Bmatrix} \Delta k_{22} \\ e\mathrm{e}^{\mathrm{j}\beta} \\ k_I \\ k_s \end{Bmatrix} = \begin{Bmatrix} \vdots \\ \mathbf{D}_3 \overline{\boldsymbol{\eta}}_{3,m} \\ \mathbf{D}_2 \overline{\boldsymbol{\eta}}_{2,m} \\ \mathbf{D}_1 \overline{\boldsymbol{\eta}}_{1,m} \\ \mathbf{D}_0 \overline{\boldsymbol{\eta}}_{0,m} \\ \mathbf{D}_{-1} \overline{\boldsymbol{\eta}}_{-1,m} \\ \mathbf{D}_{-3} \overline{\boldsymbol{\eta}}_{-3,m} \\ \vdots \end{Bmatrix} \tag{4.33}$$

In general, elements of above vectors and the matrix are complex; the real and imaginary parts can be separated to develop the above matrix equation in terms of all real quantities. This modifies Eqn. (4.33) to

$$\begin{bmatrix} \vdots & \vdots & \vdots & \vdots & \vdots \\ \delta_x p_1 \boldsymbol{\lambda}_{\text{cr}} & m\omega^2 \boldsymbol{\lambda}_{\text{unb}} & 0 & -\text{Re}(I_1 \boldsymbol{\lambda}_{\text{AMB}}) & \text{Re}(\overline{\boldsymbol{\eta}}_{1,m} \circ \boldsymbol{\lambda}_{\text{AMB}}) \\ \delta_x p_0 \boldsymbol{\lambda}_{\text{cr}} & 0 & 0 & -\text{Re}(I_0 \boldsymbol{\lambda}_{\text{AMB}}) & \text{Re}(\overline{\boldsymbol{\eta}}_{0,m} \circ \boldsymbol{\lambda}_{\text{AMB}}) \\ \delta_x p_{-1} \boldsymbol{\lambda}_{\text{cr}} & 0 & 0 & -\text{Re}(I_{-1} \boldsymbol{\lambda}_{\text{AMB}}) & \text{Re}(\overline{\boldsymbol{\eta}}_{-1,m} \circ \boldsymbol{\lambda}_{\text{AMB}}) \\ \vdots & \vdots & \vdots & \vdots & \vdots \\ 0 & 0 & m\omega^2 \boldsymbol{\lambda}_{\text{unb}} & -\text{Im}(I_1 \boldsymbol{\lambda}_{\text{AMB}}) & \text{Im}(\overline{\boldsymbol{\eta}}_{1,m} \circ \boldsymbol{\lambda}_{\text{AMB}}) \\ 0 & 0 & 0 & -\text{Im}(I_0 \boldsymbol{\lambda}_{\text{AMB}}) & \text{Im}(\overline{\boldsymbol{\eta}}_{0,m} \circ \boldsymbol{\lambda}_{\text{AMB}}) \\ 0 & 0 & 0 & -\text{Im}(I_{-1} \boldsymbol{\lambda}_{\text{AMB}}) & \text{Im}(\overline{\boldsymbol{\eta}}_{-1,m} \circ \boldsymbol{\lambda}_{\text{AMB}}) \\ \vdots & \vdots & \vdots & \vdots & \vdots \end{bmatrix} \begin{Bmatrix} \Delta k_{22} \\ \text{Re}(e\mathrm{e}^{\mathrm{j}\beta}) \\ \text{Im}(e\mathrm{e}^{\mathrm{j}\beta}) \\ k_I \\ k_s \end{Bmatrix} = \begin{Bmatrix} \vdots \\ \text{Re}(\mathbf{D}_1 \overline{\boldsymbol{\eta}}_{1,m}) \\ \text{Re}(\mathbf{D}_0 \overline{\boldsymbol{\eta}}_{0,m}) \\ \text{Re}(\mathbf{D}_{-1} \overline{\boldsymbol{\eta}}_{-1,m}) \\ \vdots \\ \text{Im}(\mathbf{D}_1 \overline{\boldsymbol{\eta}}_{1,m}) \\ \text{Im}(\mathbf{D}_0 \overline{\boldsymbol{\eta}}_{0,m}) \\ \text{Im}(\mathbf{D}_{-1} \overline{\boldsymbol{\eta}}_{-1,m}) \\ \vdots \end{Bmatrix} \tag{4.34}$$

Eqns. (4.33) and (4.34), which is in the standard matrix formulation, $\mathbf{A}\mathbf{x} = \mathbf{b}$; can be solved by least-squares regression as enunciated in previous chapters, and the vector of identifiable is evaluated as

$$\mathbf{x} = \left(\mathbf{A}^{\mathrm{T}}\mathbf{A}\right)^{-1} \mathbf{A}^{\mathrm{T}}\mathbf{b} \tag{4.35}$$

Here vectors **x**, **b** and matrix **A** have standard meaning as available in Eqns. (4.33) and (4.34). The response and information of the rotor system available at multiple spin speeds can be accommodated in matrix equation as describesd in Section 2.6 in Chapter 2.

Since, the frequency domain matrix equation of motion and the subsequent identification equations utilize positive as well as negative frequency harmonics, $\bar{\boldsymbol{\eta}}_i$, of the time domain response, $\boldsymbol{\eta}(t)$; they can be obtained from the full spectrum FFT of the time domain response. To remove the phase ambiguity arising in the frequency domain, due to FFT process a suitable phase correction programme should be implemented. The extraction of full spectrum of the time domain signal and implementation of phase correction to this process has been dealt in detail under Sections 2.3.2 and 2.3.3 in Chapter 2 and the procedures developed therein are used in next sections.

4.6 Generation of Simulated Responses

The rotor – AMB system considered for numerical response generation is presented in Figure 4-3. The rotor is discretized into 5 finite elements of equal length, giving rise to 6 nodes. End supports are considered transversely rigid, thus linear displacements at nodes 1 and 6 are identically zero. The crack is assumed located at node 4, while the AMB and the disc are located at node 3. The crack location is assumed since main focus is to have identification of breathing behaviour, which involves the usage of full spectrum. The localisation of crack in rotor system has received substantial attention in literature as seen in the bibliographic references in Bachschmid et al. (2010) and Zhang et al. (2013).

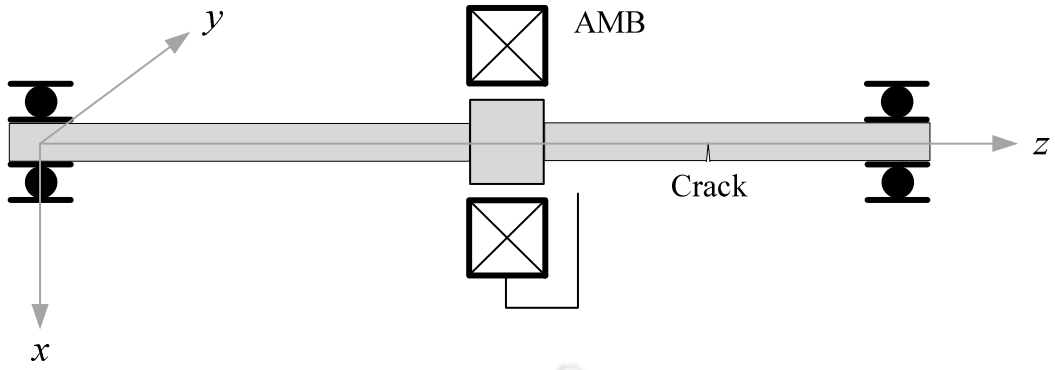

Figure 4-3 Rotor–AMB System configuration used for the numerical simulation

A Simulink model is implemented to generate the displacement response at all the nodes and also the AMB control current, by execution of time domain EOM in accordance to Eqn. (4.21). The model is presented in Figure 4-4.

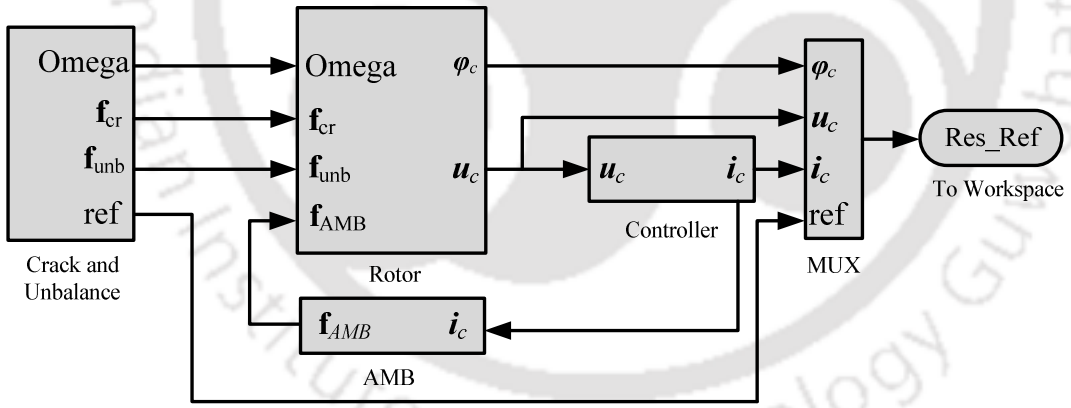

Figure 4-4 The Simulink^{TM} model used for response generation

The model is divided into two main blocks, viz. the *rotor* and the *controller*. The *rotor block* executes the dynamics of the cracked rotor as defined in the system configuration. The *controller block* executes the PID action. Based on the control current the *AMB block* inputs the AMB – restitution force on the rotor. The crack force, unbalance force and multi harmonic complex

reference signals are executed in the *crack and unbalance blocks*. The principal difference between the Simulink™ model used in previous chapters and the model depicted in Figure 4-4 is the dimension of the signal dealt by the model. In previous models, signals were 1 dimensional array, whereas in the present model, they are multidimensional arrays (of the dimension of the assembled response vector). The simulation data used for the response generation is summarized in Table 4-1.

Table 4-1 The rotor and AMB system data for the numerical simulation

Parameters		**Values**		**Parameters**		**Values**	
				Rotor			
Disc mass	m	2	kg	Disc eccentricity	e	24	μm
	I_p	45×10^{-4}	kg-m^2	Unbalance phase	β	30°	deg
	I_d	0.0024	kg-m^2	Shaft deflection	δ_x	26	μm
Shaft density	ρ	7850	kg-m^{-3}	crack stiffness	Δk_{22}	3×10^5	Nm^{-1}
Shaft length	l	0.5	m	Shaft diameter	d	0.016	m
				AMB			
Controller gains				*Actuator factors*			
Proportional,	K_P	12200	A/m				
Derivative,	K_D	3	A-s-m^{-1}	Force – current factor,	k_i	42.1	N/A
Integral,	K_I	2000	A/(m-s)	Force – disp. factor,	k_s	105210	N/m
Rayleigh's coefficients for the proportional damping:				$a_0 = 0.154$,		$a_1 = 0.00001$	

The response is generated with a fourth-order Runga-Kutta integration solver with a fixed step size of 0.00001 s. A typical response of AMB currents, obtained at the shaft spin speed of 1620 rpm (27 Hz) are shown in Figure 4-5. The vibration displacement in *x*-*z* plane, is presented in Figure 4-6. The vibration displacement response in the *y*-*z* plane is similar. The shaft centre-line orbit at node 4 is presented in Figure 4-7. The centreline orbit at other nodes are similar in appearance but

slightly different in span, which is infereable from Figure 4-6. The highest angular displacement of all the nodes is 2.004×10^{-5} rad (0.0011°), which is way smaller than the possible accurate physical measurement for rotors.

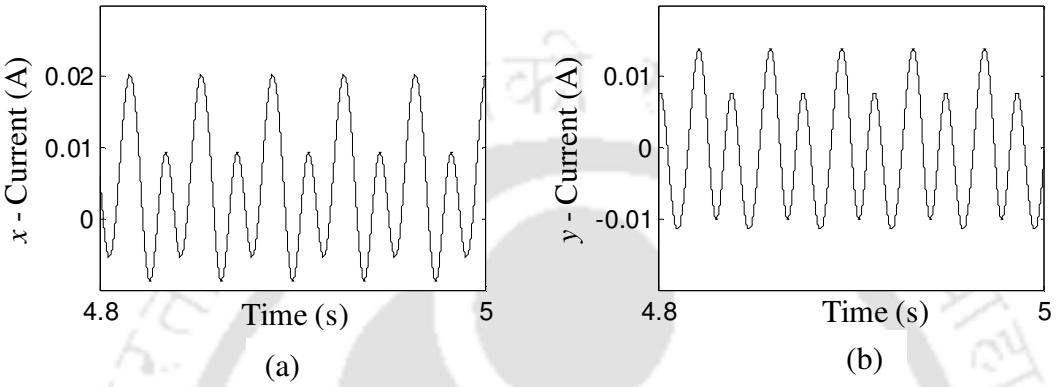

Figure 4-5 AMB control currents along x and y directions

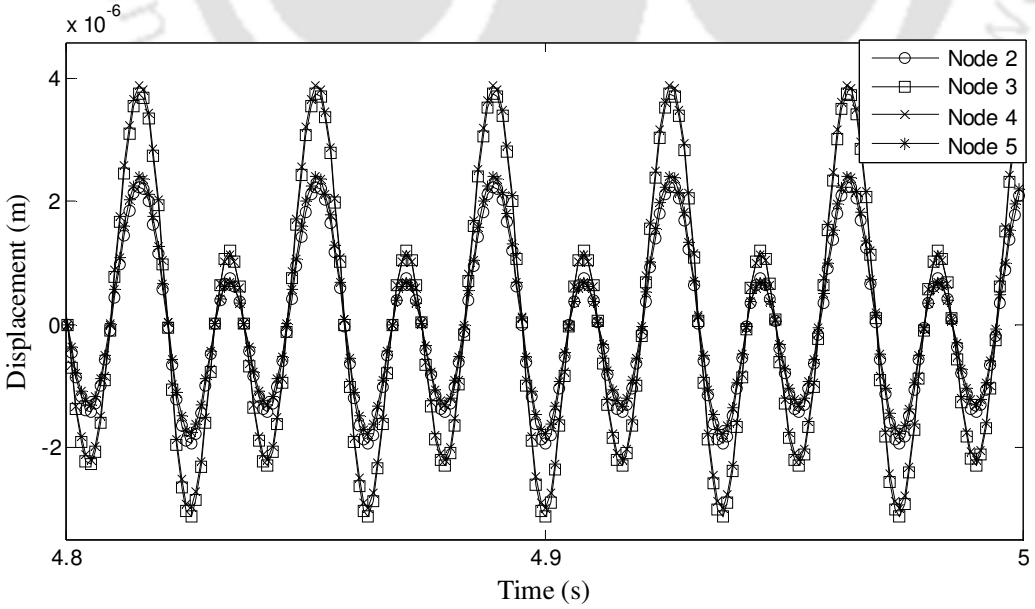

Figure 4-6 Displacement at various nodes in *x*–*z* plane

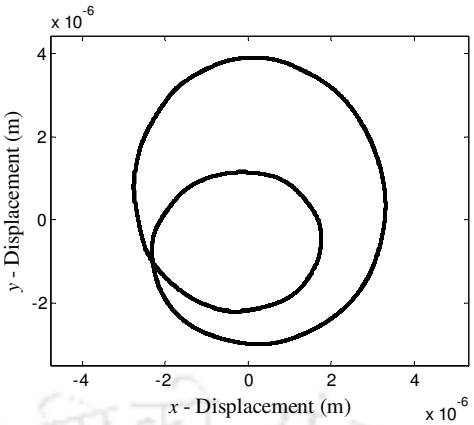

Figure 4-7 Shaft centre-line orbit at node 4

At lower speeds, the impact of unbalance forcing is minimal and shaft centre-line orbit is double looped, typically indicative of presence of crack in the rotor (Shravankumar and Tiwari, 2013), as seen in Figure 4-7. At higher speed the unbalance response overshawows the crack response and the double loop characteristic of the orbit is lost. As an illustration, the orbit plot of node 4 at 4500 rpm (75 Hz) is shown in Figure 4-8.

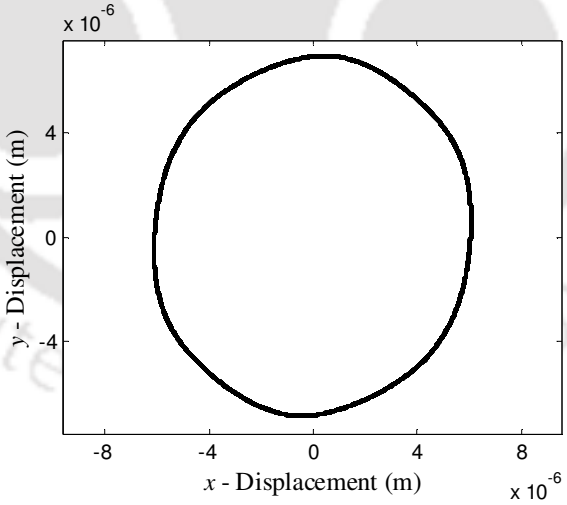

Figure 4-8 Typical orbit of cracked rotor at 4500 rpm spin speed

The examination and analysis of displacement and AMB current response in time domain presents a qualitative idea of the probable rotor faults. For ascertaining the appearance of a rotor crack,

identification of a suitable crack parameter (Δk_{22}, in this work) needs to be performed. Results of this identification based on methodology developed in Section 4.5 are presented in the next section.

4.7 Results and Discussions

A prerequisite for the assembling Eqn. (4.34) for the purpose of identification is availability of full spectrum of harmonics of linear displacements and control current. The FFT based full spectrum extraction is used with phase ambiguity removal to obtain them as established in Chapter 2. The full spectrum of the linear displacement at node 3 (representative) and the AMB control current are presented in Figure 4-9.

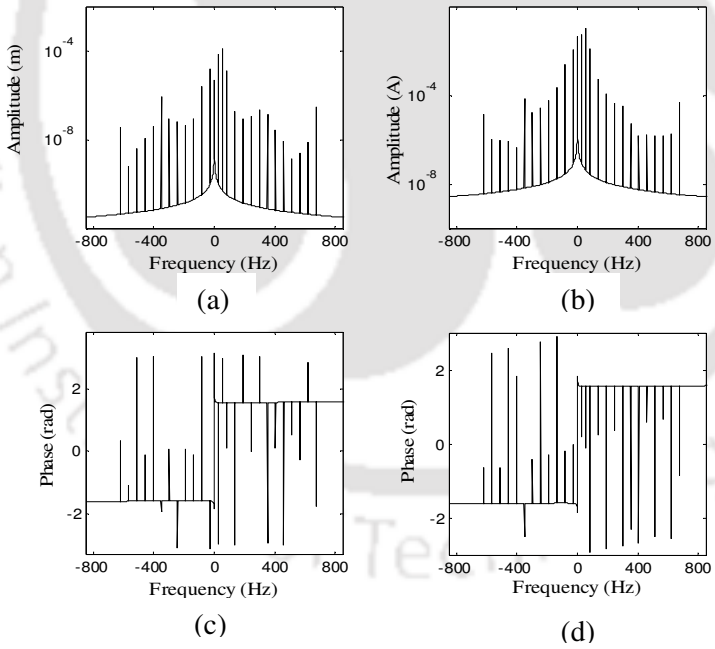

Figure 4-9 Full spectrum plots (a) amplitude of linear displacement (b) amplitude of AMB current (c) phase of displacement (d) phase of AMB current

The spin speed range for use in estimation is based on the critical speed of the rotor–AMB assembly. To ascertain critical speeds a ramp up of the rotor at the angular acceleration of 50 rad/s^2 are given and the linear response at all nodes are observed. The ramp up response at all nodes is similar in shape and envelope, but magnitudes vary. A representative ramp up response at node 3 and the Hilbert envelope (Feldman, 2011) of the displacement response is presented in Figure 4-10. In the present work, the Hilbert envelope of the displacement response has been used to obtain a clear view of the critical speed and magnitude of peak displacements at critical speeds.

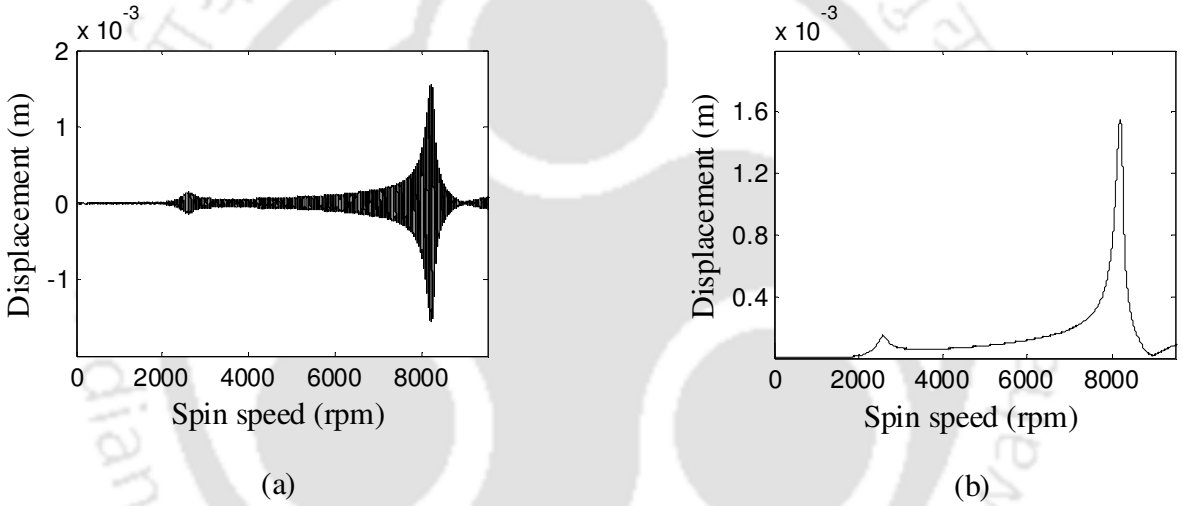

Figure 4-10 Ramp up response (a) Displacement in x-z plane (b) Hilbert envelope of displacement

The 1× and 2× resonances are observed at 2591 rpm (43.18 Hz) and 8208 rpm (136.8 Hz) with peak displacement of 14.48×10^{-5} m and 15.54×10^{-4} m, respectively. The displacement magnitude at spin speeds below 1958 rpm is lower than 1.232×10^{-5} m. The lowest displacement between the two critical speeds is observed at 3268 rpm. It is recorded as 5.74×10^{-5} m. The speed range to test the identification algorithm is kept below 1958 rpm so that the conditions of weight dominance used in derivation of EOMs are satisfied. Since, between the 1× and 2× resonance speeds, the vibration amplitude is on higher sides, this range is not utilised for identification. Nine spin speeds

of 900, 960, 1020, 1080, 1140, 1200, 1260, 1320, 1380 rpm (15 -23 Hz) with the mean speed of 1140 rpm as the $\omega_{central}$ is used for identification purpose.

For removal of slave DOFs from the estimation equations, the dynamic reduction is performed in accordance to Eqn. (3.44) for this range of spin speeds. The estimation of parameters was performed using Eqns. (4.35) inside the chosen speed range. To simulate real measurement conditions, random noise of 1%, 2% and 5% were added to the response, serially. These random noise were generated with 10 different seeds and channelled to 8 responses pertaining to master DOFs signals at 4 nodes and to 2 current responses along the *x* and *y* directions. Results of the estimation and the effect of signal noise on the quality of estimation is presented in Table 4-2.

Table 4-2 Estimation results and signal noise sensitivity in the speed range of 900 – 1380 rpm

Parameter	Assumed value	Estimated value at various noise			
		0%	1%	2%	5%
Δk_{22}	3×10^5 (N/m)	299880	297900	303990	308400
	% error	-0.04	-0.7	1.33	2.8
e	24 (μm)	23.68	23.67	23.64	23.92
	% error	-1.32	-1.37	-1.5	-0.32
β	30º(deg.)	29.52	29.52	29.52	29.18
	% error	-1.58	-1.6	-1.6	-2.73
k_s	105210 (N/m)	106020	107070	104810	111120
	% error	0.77	1.77	-0.38	5.62
k_I	42.1 (N/A)	42.12	40.61	42.75	43.62
	% error	0.058	1.21	1.55	3.61

Certain observations could be made from Table 4-2 regarding the influence of signal noise on performance of the identification procedure developed. The additive crack stiffness Δk_{22} is identifiable with minimum error with clean signal and error of estimation increses with increase in signal noise. The behavior of all the other parameters show same trend but they all have different

errors associated with clean signal, for instance the phase of the unbalance β, registers an estimation error of -1.58% with clean signal as well. Estimates of unbalance parameters are associated with relatively higher errors with clean signal, but they are not affected much with the signal noise. Though the AMB parameters are estimated well with the clean signal, they are more vulnerable to signal noise – particularly, k_s registers an estimation error of 5.62% at a signal noise of 5%.

The mathematical modeling of a system contains certain assumptions, which simplify the mathematical derivations; but may not be a true representation of the physical phenomenon being modeled. As an example, assumption of rigid end support bearings, may not be a physical reality. Also, due to multiple reasons, the measurement of rotor properties like the disc mass and moment of inertia, the material density of the shaft and the intact shaft stiffness may contain errors. These errors will be present in the estimation equations as a permanent set. All such errors which may be present in the estimation process can be summed up as the *modelling error*. The robustness of the identification procedure developed was tested by introduction of random modelling errors of 1%, 2% and 5% to the most critical model components, viz. the mass matrix (M), the stiffness matrix (K) and the shaft static deflection (δ_x). The effect of modelling error magnitude on results of estimation in the higher speed range is summarized in Table 4-3.

The response is generated using Eqn. (4.21) with correct model parameters and then the error is added in model parameters in Eqn. (4.34) used for the estimation in the identification algorithm. Thus, the correct response is used in an estimation model containing error (refer the procedural flow chart at the end of this section). The estimates obtained are compared with the assumed values.

Table 4-3 Sensitivity of estimated parameters to the modelling error

Parameter	Assumed value	Estimated value at various bias error level			
		0%	1%	2%	5%
Δk_{22}	3×10^5 (N/m)	299880	302400	304050	302160
	% error	-0.04	0.8	1.35	0.72
e	24 (μm)	23.68	23.61	23.75	23.72
	% error	-1.32	-1.62	-1.03	-1.18
β	30º(deg.)	29.52	29.63	29.45	29.61
	% error	-1.58	-1.22	-1.84	-1.31
k_s	105210 (N/m)	106020	105120	108180	109170
	% error	0.77	-0.09	2.82	3.76
k_I	42.1 (N/A)	42.12	42.41	42.69	42.84
	% error	0.058	0.74	1.42	1.75

It is observed from Table 4-3 that the estimates are not affected drastically due to modelling errors. All the identified parameters but the AMB force-displacement constant, k_s, have been estimated quite well in the range of modelling errors. The estimate of AMB force-displacement constant, k_s, has deviated by $3.76 - 0.77 = 2.99$ % at 5 % of the modelling error. Susceptibility of k_s to the bias error is in line with observations reported in previous chapters. Residual unbalance parameters, viz. e and β are the least effected and the deviation of estimates of crack stiffness (Δk_{22}) and AMB force-current constant (k_I) due modelling error is less than 2 %. On the whole, the developed identification procedure is found robust against bias errors.

Flowchart of the identification procedure followed is presented in Figure 4-11.

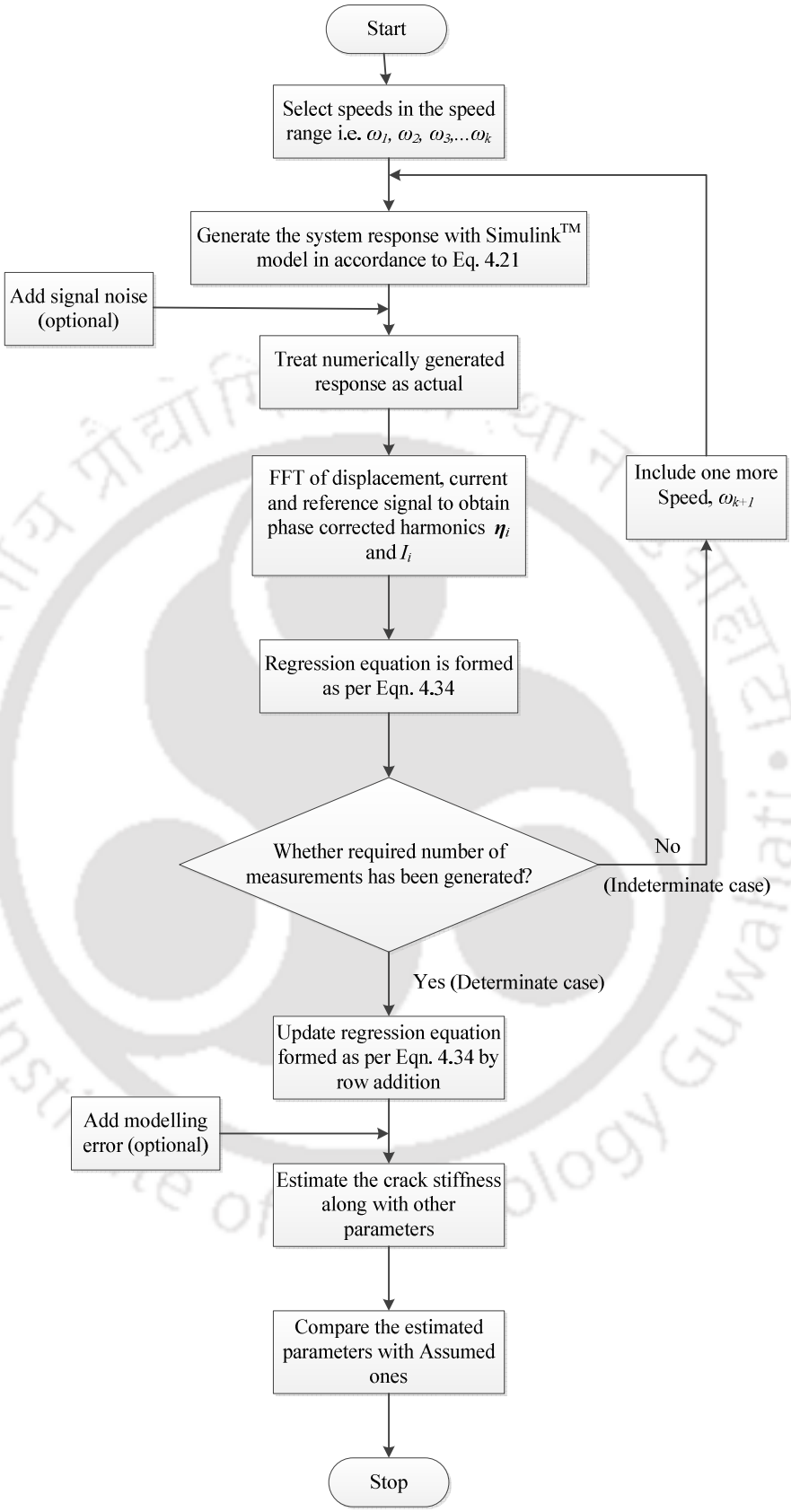

Figure 4-11 Flowchart showing steps of the identification procedure

4.8 Comparison with Numerical Models

Models used in Chapter 2 and Chapter 3 are based on lumped parameters and the rotor is a Jeffcott arrangement, initially with disc at the central plane and later with the disc offset from the central plane. The AMB configuration and control strategy are same in all the models. The rotor, end support, AMB gain and crack parameters are also same in all the models. This provides for an opportunity to compare the response and results from these three models. The key response is the shaft centreline orbit, which is a typical indicator of presence of a crack in the shaft. The typical double loop is present in the orbit plot of all the three models as may be seen in Figure 2-7 (f), Figure 3-3 (d) and Figure 4-7. This double loop converts to a single loop when the response due to residual unbalance overcomes the crack response. This is true in all the three models and has been presented in Figure 4-8, as an illustration.

The ramp up test used for estimation of critical speeds of the rotor – AMB model are also consistent with the assumed configuration. For the symmetrically placed disc, in Chapter 2, the first critical speed has been observed to be 3684 rpm, for the offset disc, in Chapter 3, it has been observed to be 3596 rpm. With offset placement of the disc, this change is expected. In FEM based model in the present chapter the 1st critical speed is found to be 3268 rpm. Since the mass of the shaft material does not contribute in the Jeffcott configuration, but it is accounted for in the FEM model hence a lowered value of the critical speed in the FEM based model is in line with the standard formulation of natural frequency.

The three models are able to estimate the parameters included in the identification algorithm with reasonable accuracy. While the model presented in Chapter 2 is able to identify the parameters with better accuracy in lower speed range, the same is true for the model in Chapter 3 as well. The

identification algorithm has not been tested in speeds above the first critical in case of the FEM based model, due to probable amplitudes of vibration displacements being greater than the static deflection but in the next chapter it has been used beyond critical speeds**.** All the three models identify the crack and unbalance parameters viz. k_{22}, e and β with better accuracy than the AMB constants k_s and k_i. The estimates of AMB constants are more vulnerable to signal noise as compared to the crack and unbalance parameters, with all the models - as can be seen in Table 2-5, Table 2-6, Table 3-3, Table 3-4 and Table 4-2.

On the whole, the three models and the identification algorithm developed on the basis of them return similar results. With the subsequent models, greater complexities could be addressed; FEM model being closer to a real rotor – AMB setup.

4.9 Concluding Remarks

In this chapter, the identification of crack in a flexible and distributed mass rotor has been performed with help of the vibration displacement and AMB current signals. The algorithm developed for the purpose was tested with simulated responses and found robust against the measurement noise and modelling errors. The FEM model developed for generation of simulated responses for use in the identification algorithm is based on simple beam theory with gyroscopic effects.

The principal focus of the present work is to establish a procedure for identification of crack force and other system parameters in rotors with AMB support, by utilizing the vibration displacement and AMB current signals. Dynamic reduction was performed to do away with the need for measurement of unwanted DOFs in the identification algorithm. For examining the applicability of

the identification algorithm developed, synthetic response from a FEM based model of the rotor–AMB system has been used and the algorithm found robust against moderate levels of measurement noise and modelling errors. However, in the present identification process, the crack location parameter is not included as identifiable, since it is a divergent field of research and rich literature is available on that aspect of rotor cracks.

The present chapter serves to establish a procedure for modelling the rotor–AMB systems with greater complexities; the shortcomings of the present model in form of simplifying assumptions will be addressed in the next chapter. In the present model, the support stiffness and damping was not taken into account. In the next chapter, the model has been extended to a very generic situation with multiple discs and multiple AMB support; and the support dynamics has also been taken into account.

CHAPTER 5

Crack Identification in Rotor on Flexible Support Carrying Multiple Discs and AMBs

5.1 Introduction

In the previous chapter, an FEM based model of a cracked rotor supported on rigid bearings and the AMB support at the disc location was analysed for the nature of time and frequency domain responses. A suitable identification algorithm was developed to estimate the crack and unbalance parameters along with AMB constants. The assumption of rigid supports simplifies the analysis to some extent but deviates from the reality of rotating machines. For modelling a rotor close to reality this condition must be relaxed. Also, the analysis based on a single disc and a single AMB may not represent a fairly generic rotor–AMB system. The rotor may be too long to necessitate the use of more than one AMB for maintaining alignment and reduction of vibration. The rotor may have different mass distribution at different sections along its length. Thus, for analysis multiple discs should be considered and these could act as balancing planes depending upon the requirement of modes to be balanced.

In this chapter, the analysis of the rotor–AMB system is generalised with consideration of a transverse crack, flexible support bearings, multiple discs and multiple AMB supports within the span of the rotor. The identification in frequency domain is attempted for the transverse crack, unbalance magnitude and phase at discs, AMB constants and anisotropic bearing dynamic parameters of supports. For validation of the identification algorithm, it is tested under the

influence of moderate level of signal noise and modelling errors for a representative numerical rotor model.

5.2 System Configuration

A schematic representation of the rotor configuration considered for the analysis is presented in Figure 5-1. The rotor supported on conventional bearings and AMBs, carries *p* number of discs. It consists of a flexible shaft with a single transverse crack and multiple rigid discs mounted on it. The rigid disc model in the analysis suits best for components, like flywheels, the turbine and fan impellers, the brake and clutch discs, and cranks, from the practical application. The rotor has support of *m* number of AMBs at different locations and is driven by a motor through a flexible coupling outside the end support bearing. Support bearings have been characterized by stiffness and damping along orthogonal transverse directions. Properties of bearings are considered different. The dynamics of the prime mover and the flexible coupling are not included in this analysis.

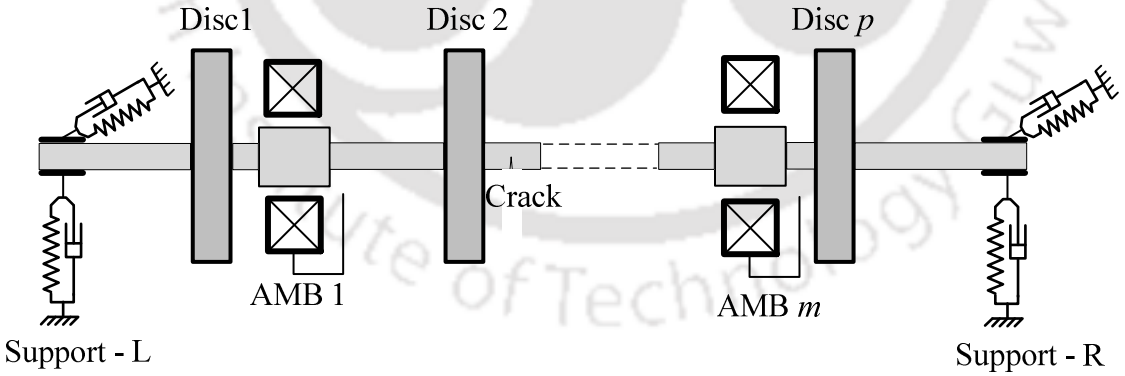

Figure 5-1 A schematic arrangement of the rotor-AMBs and flexible supports

All AMBs are assumed to be working close to the design operating point, thus, they possess the linearized current and displacement stiffnesses in two transverse directions. The proportional damping has been considered for the shaft. Unbalances in the rotor are assumed to be concentrated

to discrete discs in different magnitude and at different orientations. The orientation of the unbalance is quantified with respect to the direction perpendicular to the crack front. The controller used with the AMB is considered to work on the PID control strategy. Dynamics of sensors and amplifiers are not included in the present analysis.

In the generic configuration depicted in Figure 5-1, the spinning rotor will be excited by multiple forces at different locations along its length. These forces arise due to various accounts, categorised as – crack forces, forces due to unbalances at p discs, AMB restitution forces at m locations and support bearing forces. All these forces act in tandem with different effects on the rotor. While the crack and unbalance induced forces tend to make the shaft off centre, the AMB and the support bearing forces effectively try to centre the shaft. For the purpose of quantifying crack forces, definition of a rotating frame of reference eases the analysis while all the other force effects are quantifiable in a fixed coordinate. For arriving at the crack force in the fixed coordinates; a rotating coordinate, its relation with the fixed coordinate and the relative positioning of the unbalance on an arbitrary disc, with respect to the crack front is defined as shown in Figure 2-2 in Chapter 2.

For rotating coordinates, directions ξ and η are defined such that ξ points perpendicular to the crack front and η points along the crack front. The rotating and fixed coordinate systems are considered aligned at the instant of starting the time count. Thus, for a shaft spinning at angular velocity of ω, at time t the angular separation between ordinates of two coordinate references is ωt. O is the origin of co-ordinate system O-x-y-z and is defined on the bearing axis, C is the centre of rotation of the disc, and G_n is the centre of mass of the n^{th} disc. For that particular disc $CG_n = e_n$ is the disc eccentricity of the unbalance and the angular position of the unbalance with respect to axis ξ is quantified by a constant angle, β_n.

Transverse translational displacements are u_x and u_y, and the transverse rotational displacements are φ_y and φ_x. All other notations and definitions are same as in Chapter 4.

5.3 Derivation of the Excitation Forces

With the spin of the rotor, excitation forces will arise on account of the transverse crack, unbalances on multiple discs, the multiple AMB restitution and support bearings. Before discretising the rotor for further analysis with the finite element method, these forces acting on the rotor have to be derived which would be used later in the finite element formulation of the rotor-AMB problem. The crack force, residual unbalance force and the AMB restitution force has been alrady derived in previous chapters and available in the form suitable for FEM formulation, in Section 4.3 in Chapter 4. The new component added to the model is the flexible support bearing. These flexible support bearings can be modelled as forces at the support locations, as detailed in the next section.

5.3.1 Support Bearing Forces

Forces due to flexible bearings can be characterized in terms of the stiffness and damping in transverse directions and is given as

$$\mathbf{f}_{br} = \begin{Bmatrix} k_{bx}u_x + c_{bx}\dot{u}_x \\ k_{by}u_y + c_{by}\dot{u}_y \\ 0 \\ 0 \end{Bmatrix} = \begin{Bmatrix} k_{bx}u_x \\ k_{by}u_y \\ 0 \\ 0 \end{Bmatrix} + \begin{Bmatrix} c_{bx}\dot{u}_x \\ c_{by}\dot{u}_y \\ 0 \\ 0 \end{Bmatrix} \tag{5.1}$$

Here, k_{bx}, k_{by}, c_{bx} and c_{by} are the bearing stiffness and damping parameters along directions x and y, respectively. Defining the conjugate complex displacement as $u_c^* = u_x - \mathrm{j}u_y$, the complex

velocity as $\dot{u}_c = \dot{u}_x + \mathrm{j}\dot{u}_y$, conjugate complex velocity as $\dot{u}_c^* = \dot{u}_x - \mathrm{j}\dot{u}_y$, Eqn. (5.1) can be converted to complex form as

$$\mathbf{f}_{br}^{c} = \frac{1}{2}\begin{Bmatrix} k_{bx}(u_c + u_c^*) + k_{by}(u_c - u_c^*) \\ 0 \end{Bmatrix} + \frac{1}{2}\begin{Bmatrix} c_{bx}(\dot{u}_c + \dot{u}_c^*) + c_{by}(\dot{u}_c - \dot{u}_c^*) \\ 0 \end{Bmatrix} \tag{5.2}$$

Four force vectors defined above, along with force vectors on account of the crack, unbalance and AMB restitution will be used in finite element formulation of the rotor-AMB problem, detailed in next section.

5.4 Finite Element Modelling of the Rotor-AMB System

The rotor considered in this chapter is composed of a shaft with following effects: a transverse crack, *p* numbers of rigid discs, *m* numbers of AMB support and support bearings. The whole rotor model is subdivided into smaller models for simplicity, viz. the shaft model, the disc model, the AMB model and the bearing model. Each sub–model is considered individually and equations of motion for that sub–model are developed, with help of excitation forces derived in the previous section. All equations from each sub-model are then reassembled to get global equations of motion and the boundary/ support conditions are applied. The shaft is discretised into *n* finite elements with 4–DOFs (2 linear displacements and 2 angular displacements) at each node as defined in Section 4.4 and depicted in Figure 4-2.

5.4.1 Sub-models

The whole model is subdivided into smaller models for simplicity, each sub–model considered individually and equations of motion for that sub–model developed. All the sub-models of the present model other than the support bearing submodel has been developed in Chapter 4. The shaft sub-model, the crack sub-model, the disc sub-model and the AMB submodels have been described in section 4.4.1 in Chapter 4.

5.4.1.1 Support bearings sub-model

The mathematical model of support bearings is available in Section 5.3.1. The support bearing sub-model quantifies the forces exerted by supports to the shaft, at nodes of their placement. The bearing support force is given as

$$\tfrac{1}{2}\left(k_{bx}(\boldsymbol{\eta}_b+\boldsymbol{\eta}_b^*)+k_{by}(\boldsymbol{\eta}_b-\boldsymbol{\eta}_b^*)\right)+\tfrac{1}{2}\left(c_{bx}(\dot{\boldsymbol{\eta}}_b+\dot{\boldsymbol{\eta}}_b^*)+c_{by}(\dot{\boldsymbol{\eta}}_b-\dot{\boldsymbol{\eta}}_b^*)\right)=\mathbf{f}_{\text{br}} \tag{5.3}$$

In the above expression, the vector, $\boldsymbol{\eta}_b$, $\boldsymbol{\eta}_b^*$, $\dot{\boldsymbol{\eta}}_b$ and $\dot{\boldsymbol{\eta}}_b^*$, contain complex displacements and velocities and their conjugates, respectively.

With all sub-models defined, the sub-model equations can be combined to obtain the assembled equations of motion of the system, presented in the next section.

5.4.2 Assembled Equations of Motion of the Cracked-Rotor AMB System

Equations obtained for individual subsystems, viz. the shaft, crack, disc, AMB and support bearings are combined together and boundary conditions applied to obtain the assembled equations of motion of the rotor. The assembled equation of motion is given as

$$\mathbf{M}\ddot{\boldsymbol{\eta}} + (\mathbf{C} - \omega\mathbf{G})\dot{\boldsymbol{\eta}} + \mathbf{K}\boldsymbol{\eta} = \mathbf{f}_{\text{unb}} + \mathbf{f}_{\text{cr}} + \mathbf{f}_{\text{AMB}} - \mathbf{f}_{\text{br}} \tag{5.4}$$

Here, **M**, **C**, **G** and **K** are the global mass, damping, gyroscopic and stiffness matrices and $\mathbf{f}_{\text{unb}}$, $\mathbf{f}_{\text{cr}}$ $\mathbf{f}_{\text{AMB}}$ and $\mathbf{f}_{\text{br}}$ are vectors of the unbalance, crack and AMB restitution forces, respectively.

The assembled equation of motion can be solved for with a suitable numerical integration solver program to obtain the time history of the vibration displacement and the AMB current. Certain mathematical simplifications make this numerical integration simpler, as described in the next section.

5.4.3 Time and Frequency Responses

Solution to Eqn. (5.4) yields the vector, $\boldsymbol{\eta}$, rotor responses at various nodes. Since the nature of the forcing vector on the RHS of Eqn. (5.4) determines the nature of time and frequency domain response of the system, it is further simplified by defining the nature of breathing function, $s(t)$, and splitting the AMB restitution force into component purely due to the vibration displacement and due to the control current. With the $s(t)$ defined as in Section 4.4.3 and transformation of equation with the Euler identity, the crack force vector is obtained as

$$\Delta k_{22}\{\cdots + 0.106\mathrm{e}^{-\mathrm{j}\omega t} + 0.25 + 0.319\mathrm{e}^{\mathrm{j}\omega t} + 0.25\mathrm{e}^{\mathrm{j}2\omega t} + \cdots\}\boldsymbol{\eta}_{x0} = \mathbf{f}_{\text{cr}} \tag{5.5}$$

In Eqn. (5.5), vectors $\boldsymbol{\eta}_{x0}$ and $\mathbf{f}_{\text{cr}}$ contain the static deflection and crack force, respectively, at all nodes. Since, the rotor has only a single crack, only the entry at the node of the crack is significant, others should be zero. This could be effectively achieved by defining a crack *location flag vector* – $\boldsymbol{\lambda}_{\text{cr}}$; a zero vector with 0 entry replaced by 1 at the node of crack. For detailed discussion on

location flag vectors, Section 4.4.3 may be referred. With the static deflection corresponding to the crack node marked as δ_x, the crack force can be expressed in notational form as

$$\mathbf{f}_{\text{cr}} = \Delta k_{22} \delta_x \sum_{i=-\infty}^{+\infty} p_i \mathrm{e}^{\mathrm{j}i\omega t} \boldsymbol{\lambda}_{\text{cr}} \tag{5.6}$$

Here p_i is participation factor of the i^{th} harmonic of the crack force excitation. Over and above the crack force, the forcing due to unbalance is also present at the frequency of the shaft rotation. The AMB control current required to keep the rotor close to its predetermined position, is a close replica of the above two forcing and can be expressed as

$$\mathbf{i}_{\text{c}} = \sum_{i=-n}^{+n} I_i \mathrm{e}^{\mathrm{j}i\omega t} \boldsymbol{\lambda}_{\text{AMB}} \tag{5.7}$$

Here, vector $\boldsymbol{\lambda}_{AMB}$ is the AMB location flag vector; a zero vector with nodes where AMBs are present, replaced by 1. Similarly, the vector $\boldsymbol{\lambda}_{\text{unb}}$ is defined for locating the unbalance force due to multiple disc unbalances; and vector $\boldsymbol{\lambda}_{\text{br}}$ for bearing supports. As an illustration, for a model discretised into 5 elements, containing discs at 3 nodes (nodes 2, 3 and 4), AMBs at 2 nodes (nodes 3 and 5) and support bearings at 2 nodes (at node 1 and node 6), these flag vectors would be

$$\boldsymbol{\lambda}_{\text{unb}} = \begin{Bmatrix} 0\\0\\1\\0\\1\\0\\1\\0\\0\\0\\0\\0 \end{Bmatrix} = \begin{Bmatrix} 0\\0\\1\\0\\0\\0\\0\\0\\0\\0\\0\\0 \end{Bmatrix} + \begin{Bmatrix} 0\\0\\0\\0\\1\\0\\0\\0\\0\\0\\0\\0 \end{Bmatrix} + \begin{Bmatrix} 0\\0\\0\\0\\0\\0\\1\\0\\0\\0\\0\\0 \end{Bmatrix}; \quad \boldsymbol{\lambda}_{\text{AMB}} = \begin{Bmatrix} 0\\0\\0\\0\\1\\0\\0\\0\\0\\0\\0\\0 \end{Bmatrix} + \begin{Bmatrix} 0\\0\\0\\0\\0\\0\\0\\1\\0\\0\\0\\0 \end{Bmatrix}; \quad \boldsymbol{\lambda}_{\text{br}} = \begin{Bmatrix} 1\\0\\0\\0\\0\\0\\0\\0\\0\\0\\0\\0 \end{Bmatrix} + \begin{Bmatrix} 0\\0\\0\\0\\0\\0\\0\\0\\0\\0\\1\\0 \end{Bmatrix} \tag{5.8}$$

With all notations defined, equation of motion (5.4) can be written as

$$\begin{aligned} \mathbf{M}\ddot{\boldsymbol{\eta}} + (\mathbf{C} - \mathrm{j}\omega\mathbf{G})\dot{\boldsymbol{\eta}} + \mathbf{K}\boldsymbol{\eta} = \Delta k_{22}\delta_x \sum_{i=-\infty}^{+\infty} p_i \mathrm{e}^{\mathrm{j}i\omega t}\boldsymbol{\lambda}_{\text{cr}} + \sum_{n=1}^{p}(m_n e_n \omega^2 \mathrm{e}^{\mathrm{j}\beta_n})\mathrm{e}^{\mathrm{j}\omega t}\boldsymbol{\lambda}_{\text{unb}} \\ + \sum_{n=1}^{m}(-k_{I,n}\sum_{i=-\infty}^{+\infty} I_i \mathrm{e}^{\mathrm{j}i\omega t}\boldsymbol{\lambda}_{\text{AMB}} + k_{s,n}\boldsymbol{\eta}\circ\boldsymbol{\lambda}_{\text{AMB}}) - \sum_{n=1}^{b}(\mathbf{f}_{\text{br},n}^{c}\circ\boldsymbol{\lambda}_{\text{br}}) \end{aligned} \tag{5.9}$$

Here, the operator "$\circ$" represents element wise multiplication and $\mathbf{f}_{\text{br}}^{c}$ is as defined in Eqn. (5.3). The summation range running on i denotes the same quantity at the same node available at different multiples of the spin speed. For the number of discs, their contributions are summed over the range up to p and for the number of AMBs, their contributions are summed over the range up to m.

The assumed solution to Eqn. (5.9) will have the form

$$\boldsymbol{\eta}(t) = \sum_{i=-\infty}^{+\infty} \bar{\boldsymbol{\eta}}_{\mathbf{i}}\, \mathrm{e}^{\mathrm{j}i\omega t} \tag{5.10}$$

Placement of this value of the assumed solution in Eqn. (5.9) and substituting for $\mathbf{f}_{\text{br}}^{c}$ as per Eqn. (5.3) and cancelling out the common term of $\mathrm{e}^{\mathrm{j}i\omega t}$ from both the sides, yields the frequency domain of the equations of motion, for $i = 1$ and $i \neq 1$ respectively, given as

$$\left[\left(-\omega^2\mathbf{M}\right)+\mathrm{j}\omega\left(\mathbf{C}-\mathrm{j}\omega\mathbf{G}\right)+\mathbf{K}\right]\bar{\boldsymbol{\eta}}_1 = \Delta k_{22}u_{x0}p_1\boldsymbol{\lambda}_{\text{cr}}+\sum_{n=1}^{p}(m_n e_n\omega^2\mathrm{e}^{\mathrm{j}\beta_n})\mathrm{e}^{\mathrm{j}\omega t}\boldsymbol{\lambda}_{\text{unb}}$$

$$+\sum_{n=1}^{m}(-k_{I,n}I_1\boldsymbol{\lambda}_{\text{AMB}}+k_{s,n}\bar{\boldsymbol{\eta}}_1\circ\boldsymbol{\lambda}_{\text{AMB}})-\frac{1}{2}\sum_{n=1}^{b}\left(k_{bx}(\bar{\boldsymbol{\eta}}_1+\bar{\boldsymbol{\eta}}_1^{*})+k_{by}(\bar{\boldsymbol{\eta}}_1-\bar{\boldsymbol{\eta}}_1^{*})\right)\circ\boldsymbol{\lambda}_{\text{br}} \tag{5.11}$$

$$-\frac{1}{2}\sum_{n=1}^{b}\mathrm{j}\omega\left(c_{bx}(\bar{\boldsymbol{\eta}}_1+\bar{\boldsymbol{\eta}}_1^{*})+c_{by}(\bar{\boldsymbol{\eta}}_1-\bar{\boldsymbol{\eta}}_1^{*})\right)\circ\boldsymbol{\lambda}_{\text{br}}$$

and

$$\left[\left(-(i\omega)^2\mathbf{M}\right)+\mathrm{j}(i\omega)\left(\mathbf{C}-\mathrm{j}\omega\mathbf{G}\right)+\mathbf{K}\right]\bar{\boldsymbol{\eta}}_i = \Delta k_{22}u_{x0}p_i\boldsymbol{\lambda}_{\text{cr}}$$

$$+\sum_{n=1}^{m}(-k_{I,n}I_i\boldsymbol{\lambda}_{\text{AMB}}+k_{s,n}\bar{\boldsymbol{\eta}}_i\circ\boldsymbol{\lambda}_{\text{AMB}})-\frac{1}{2}\sum_{n=1}^{b}\left(k_{bx}(\bar{\boldsymbol{\eta}}_i+\bar{\boldsymbol{\eta}}_i^{*})+k_{by}(\bar{\boldsymbol{\eta}}_i-\bar{\boldsymbol{\eta}}_i^{*})\right)\circ\boldsymbol{\lambda}_{\text{br}} \tag{5.12}$$

$$-\frac{1}{2}\sum_{n=1}^{b}\mathrm{j}(i\omega)\left(c_{bx}(\bar{\boldsymbol{\eta}}_i+\bar{\boldsymbol{\eta}}_i^{*})+c_{by}(\bar{\boldsymbol{\eta}}_i-\bar{\boldsymbol{\eta}}_i^{*})\right)\circ\boldsymbol{\lambda}_{\text{br}}$$

The system response in time domain, $\boldsymbol{\eta}(t)$, and the AMB current, $\mathbf{i}_c(t)$, can be obtained by the time integration of Eqn. (5.9) and the frequency domain response, $\bar{\boldsymbol{\eta}}_i$, and harmonic components of the AMB current, $\mathbf{I}_i$, can be obtained from the full spectrum of $\boldsymbol{\eta}(t)$ and $\mathbf{i}_c(t)$, respectively. Practical difficulties associated with extraction of the harmonics based on full spectrum FFT include appearance of phase ambiguity in the harmonics, leakage error and aliasing. Practical methods to do away with these signal processing difficulties have been discussed and illustrated in Section 2.3.

The FEM based methods rely on discretising the physical system into a number of finite elements. Physical measurements of all the DOFs created due to large number of finite elements may not be practical to measure, so some of them must be eliminated from the equations of motion. The reduction scheme for such DOFs has been discussed in Section 3.5.1 and Section 4.4.4 in Chapter 3 and 4, respectively.

In terms of master DOFs, equations of motion can be written as

$$\mathbf{M}^d\ddot{\boldsymbol{\eta}}_m + \left(\mathbf{C}^d - \mathrm{j}\omega\mathbf{G}^d\right)\dot{\boldsymbol{\eta}}_m + \mathbf{K}^d\boldsymbol{\eta}_m = \mathbf{f}^d_{\text{unb}} + \mathbf{f}^d_{\text{cr}} + \mathbf{f}^d_{\text{AMB-R}} - \mathbf{f}^d_{\text{br}} \tag{5.13}$$

The vector flags $\boldsymbol{\lambda}_{\text{unb}}, \boldsymbol{\lambda}_{\text{cr}}, \boldsymbol{\lambda}_{\text{AMB}}$ and $\boldsymbol{\lambda}_{\text{br}}$ are also reduced by removing the entries corresponding to the slave DOFs. Eqn. (5.4) or (5.9) can be used for the response generation and the identification algorithm would be developed with Eqn. (5.13).

5.5 Development of Identification Equations

The identification problem would be formulated from Eqns. (5.11) and (5.12), reshaped as in Eqn.(5.13). To shorten the span of equations used for further derivation, the radical on the LHS of above equations could be written as

$$\left(-(i\omega)^2\mathbf{M}^d\right) + \mathrm{j}(i\omega)\left(\mathbf{C}^d - \mathrm{j}\omega\mathbf{G}^d\right) + \mathbf{K}^d = \mathbf{D}_i \tag{5.14}$$

Subsequent upon reduction of slave DOFs from Eqns. (5.11) and (5.12), these could be written as

$$\Delta k_{22} u_{x0} p_1 \boldsymbol{\lambda}_{\mathrm{cr}} + \sum_{n=1}^{p} (m_n e_n \omega^2 \mathrm{e}^{\mathrm{j}\beta_n}) \mathrm{e}^{\mathrm{j}\omega t} \boldsymbol{\lambda}_{\mathrm{unb}} + \sum_{n=1}^{m} (-k_{I,n} I_1 \boldsymbol{\lambda}_{\mathrm{AMB}} + k_{s,n} \overline{\boldsymbol{\eta}}_1 \circ \boldsymbol{\lambda}_{\mathrm{AMB}})$$

$$-\frac{1}{2}\sum_{n=1}^{b}\left(k_{bx}(\overline{\boldsymbol{\eta}}_1 + \overline{\boldsymbol{\eta}}_1^*) + k_{by}(\overline{\boldsymbol{\eta}}_1 - \overline{\boldsymbol{\eta}}_1^*)\right) \circ \boldsymbol{\lambda}_{\mathrm{br}} = \frac{1}{2}\sum_{n=1}^{b} \mathrm{j}\omega\left(c_{bx}(\overline{\boldsymbol{\eta}}_1 + \overline{\boldsymbol{\eta}}_1^*) + c_{by}(\overline{\boldsymbol{\eta}}_1 - \overline{\boldsymbol{\eta}}_1^*)\right) \circ \boldsymbol{\lambda}_{\mathrm{br}} + \mathbf{D}_1 \overline{\boldsymbol{\eta}}_1 \tag{5.15}$$

and

$$\Delta k_{22} u_{x0} p_i \boldsymbol{\lambda}_{\mathrm{cr}} + \sum_{n=1}^{m} (-k_{I,n} I_i \boldsymbol{\lambda}_{\mathrm{AMB}} + k_{s,n} \overline{\boldsymbol{\eta}}_i \circ \boldsymbol{\lambda}_{\mathrm{AMB}})$$

$$-\frac{1}{2}\sum_{n=1}^{b}\left(k_{bx}(\overline{\boldsymbol{\eta}}_i + \overline{\boldsymbol{\eta}}_i^*) + k_{by}(\overline{\boldsymbol{\eta}}_i - \overline{\boldsymbol{\eta}}_i^*)\right) \circ \boldsymbol{\lambda}_{\mathrm{br}} = \frac{1}{2}\sum_{n=1}^{b} \mathrm{j}\omega\left(c_{bx}(\overline{\boldsymbol{\eta}}_i + \overline{\boldsymbol{\eta}}_i^*) + c_{by}(\overline{\boldsymbol{\eta}}_i - \overline{\boldsymbol{\eta}}_i^*)\right) \circ \boldsymbol{\lambda}_{\mathrm{br}} + \mathbf{D}_i \overline{\boldsymbol{\eta}}_i \tag{5.16}$$

For sake of brevity, the following notation is introduced

$$\frac{1}{2}\sum_{n=1}^{b} \mathrm{j}(i\omega)\left(c_{bx}(\overline{\boldsymbol{\eta}}_i + \overline{\boldsymbol{\eta}}_i^*) + c_{by}(\overline{\boldsymbol{\eta}}_i - \overline{\boldsymbol{\eta}}_i^*)\right) \circ \boldsymbol{\lambda}_{\mathrm{br}} = \mathbf{B}_i \tag{5.17}$$

Eqns. (5.15) and (5.16) can be written in the matrix regression form as under

$$\begin{bmatrix}
\vdots & \vdots & \cdots & \vdots & \cdots & \vdots & \cdots & \vdots & \cdots \\
u_{x0} p_3 \boldsymbol{\lambda}_{\mathrm{cr}} & 0 & \cdots & -I_3 \boldsymbol{\lambda}_{\mathrm{AMB},1} & \cdots & \overline{\boldsymbol{\eta}}_{3,m} \circ \boldsymbol{\lambda}_{\mathrm{AMB},1} & \cdots & \overline{\boldsymbol{\eta}}_3 + \overline{\boldsymbol{\eta}}_3^* & \cdots \\
u_{x0} p_2 \boldsymbol{\lambda}_{\mathrm{cr}} & 0 & \cdots & -I_2 \boldsymbol{\lambda}_{\mathrm{AMB},1} & \cdots & \overline{\boldsymbol{\eta}}_{2,m} \circ \boldsymbol{\lambda}_{\mathrm{AMB},1} & \cdots & \overline{\boldsymbol{\eta}}_2 + \overline{\boldsymbol{\eta}}_2^* & \cdots \\
u_{x0} p_1 \boldsymbol{\lambda}_{\mathrm{cr}} & m_1 \omega^2 \boldsymbol{\lambda}_{\mathrm{unb},1} & \cdots & -I_1 \boldsymbol{\lambda}_{\mathrm{AMB},1} & \cdots & \overline{\boldsymbol{\eta}}_{1,m} \circ \boldsymbol{\lambda}_{\mathrm{AMB},1} & \cdots & \overline{\boldsymbol{\eta}}_1 + \overline{\boldsymbol{\eta}}_1^* & \cdots \\
u_{x0} p_0 \boldsymbol{\lambda}_{\mathrm{cr}} & 0 & \cdots & -I_0 \boldsymbol{\lambda}_{\mathrm{AMB},1} & \cdots & \overline{\boldsymbol{\eta}}_{0,m} \circ \boldsymbol{\lambda}_{\mathrm{AMB},1} & \cdots & \overline{\boldsymbol{\eta}}_0 + \overline{\boldsymbol{\eta}}_0^* & \cdots \\
u_{x0} p_{-1} \boldsymbol{\lambda}_{\mathrm{cr}} & 0 & \cdots & -I_{-1} \boldsymbol{\lambda}_{\mathrm{AMB},1} & \cdots & \overline{\boldsymbol{\eta}}_{-1,m} \circ \boldsymbol{\lambda}_{\mathrm{AMB},1} & \cdots & \overline{\boldsymbol{\eta}}_{-1} + \overline{\boldsymbol{\eta}}_{-1}^* & \cdots \\
u_{x0} p_{-3} \boldsymbol{\lambda}_{\mathrm{cr}} & 0 & \cdots & -I_{-3} \boldsymbol{\lambda}_{\mathrm{AMB},1} & \cdots & \overline{\boldsymbol{\eta}}_{-3,m} \circ \boldsymbol{\lambda}_{\mathrm{AMB},1} & \cdots & \overline{\boldsymbol{\eta}}_{-3} + \overline{\boldsymbol{\eta}}_{-3}^* & \cdots \\
\vdots & \vdots & \cdots & \vdots & \cdots & \vdots & \cdots & \vdots & \cdots
\end{bmatrix}
\begin{Bmatrix}
\Delta k_{22} \\
e_1 \mathrm{e}^{\mathrm{j}\beta_1} \\
\vdots \\
k_{I,1} \\
\vdots \\
k_{s,1} \\
\vdots \\
k_{bx,L} \\
\vdots
\end{Bmatrix}
=
\begin{Bmatrix}
\vdots \\
\mathbf{B}_3 + \mathbf{D}_3 \overline{\boldsymbol{\eta}}_{3,m} \\
\mathbf{B}_2 + \mathbf{D}_2 \overline{\boldsymbol{\eta}}_{2,m} \\
\mathbf{B}_1 + \mathbf{D}_1 \overline{\boldsymbol{\eta}}_{1,m} \\
\mathbf{B}_0 + \mathbf{D}_0 \overline{\boldsymbol{\eta}}_{0,m} \\
\mathbf{B}_{-1} + \mathbf{D}_{-1} \overline{\boldsymbol{\eta}}_{-1,m} \\
\mathbf{B}_{-3} + \mathbf{D}_{-3} \overline{\boldsymbol{\eta}}_{-3,m} \\
\vdots
\end{Bmatrix} \tag{5.18}$$

The matrix and the vector on the LHS of Eqn. (5.18) contain entries related to all the disc unbalances, all AMBs stiffness and all bearing dynamic parameters. For the sake of compactness,

only the entry related to the first disc, first AMB and left bearing stiffness along x axis has been explicitly mentioned. In general, entries of above vectors and matrix are complex. To develop the above matrix equation in terms of all real quantities, the real and imaginary parts can be separated, as detailed in Section 4.5.

Eqn. (5.18) is a standard matrix formulation, $\mathbf{A}\,\mathbf{x} = \mathbf{b}$ and can be solved by least-squares regression with the vector of identifiable evaluated as in Eqn. (2.65).Performance of the estimation procedure may improve with inclusion of information from more spin speeds of the rotor. In such cases, with multiple spin speeds considered in the range of interest, regression matrices will take the form as Eqn. (2.66).

The identification equation developed as Eqn. (5.18) utilize positive as well as negative frequency harmonics, $\bar{\boldsymbol{\eta}}_i$ and I_i ; they can be obtained from the full spectrum FFT of the time domain response and AMB current. A numerical experiment is performed in the next section to establish the procedures developed in this section.

5.6 Numerical Experiments

For the verification of accuracy of the procedure developed in previous sections, a numerical experiment has been performed. A flexible continuous shaft, supported on flexible bearings and carrying two discs, a transverse crack and an AMB support in auxiliary bearing configuration has been considered. The configuration considered for the numerical experiment is shown in Figure 5-2.

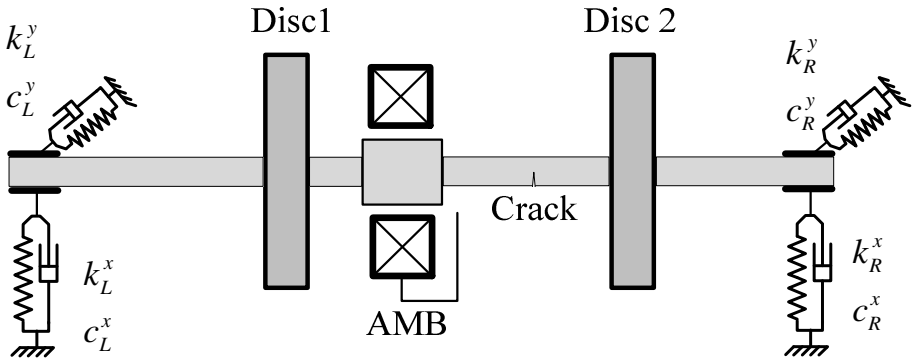

Figure 5-2 Rotor-bearing-AMB configuration used for the numerical experiment

The rotor shaft is discretised into 5 one dimensional finite elements (depending upon the accuracy required and complexity of the rotor it can be increased) of uniform lengths. At each node 4 DOFs, viz. the linear and angular displacements in both planes of *x*–*z* and *y*–*z*, are considered. Support flexible bearings characterised by anisotropic stiffness and damping parameters, as shown in Figure 5-2, are placed at node 1 and node 6, respectively. The first disc, the AMB and the second disc are placed at nodes 2, 3 and 5, respectively. A transverse crack in the shaft is located at the node 4.

5.6.1 Generation of Simulated Response

A Simulink model is implemented to generate displacement responses at all nodes and AMB control currents, by execution of time domain EOMs in accordance to Eqn. (5.9). A schematic diagram of the Simulink model is presented in Figure 5-3.

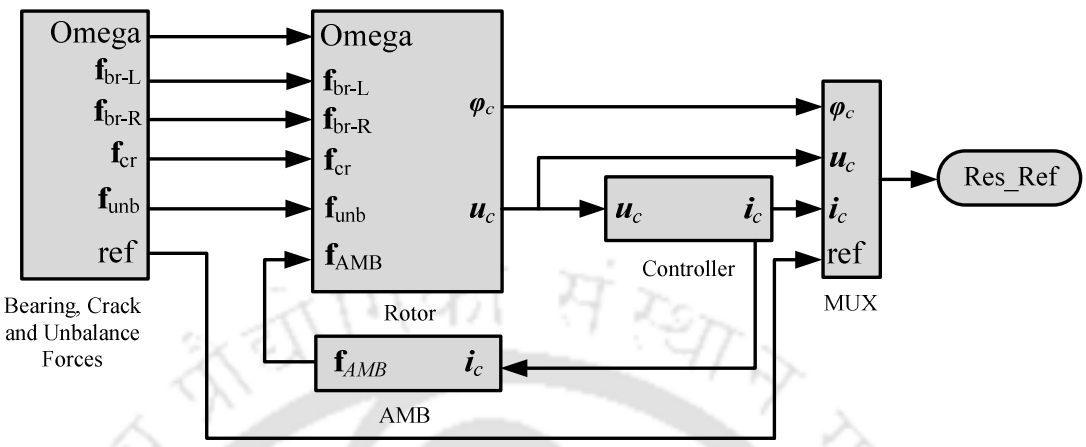

Figure 5-3 The Simulink^{TM} model used for the response generation

The model is divided into several subsystems, viz. the *rotor,* the *controller,* the *AMB* and the *forcing* subsystems. The *rotor* subsystem executes the dynamics of the cracked rotor as defined in the system configuration. The *controller* subsystem executes the PID action. Based on the control current the *AMB* subsystem inputs the AMB–restitution force on the rotor. The crack force, unbalance force, bearing forces and multi–harmonic complex reference signals are executed in the *bearing*, *crack* and *unbalance forces* subsystem. The *mux block* is a multi-input multi-output signal carrier for the complex displacement, current and reference signals, the signal is output to the *workspace* for further processing.

The response is generated with a fourth-order Runga-Kutta integration solver with a fixed step size of 0.00001 s. This step size for numerical simulation was arrived at based on the trials of simulation with various time steps. The response of simulation at this step size is comparable to response of simulation at other step sizes finer than 0.00001 s. The solution exhibits instability in

the case step size greater than 0.00001 s is used. Thus, as a trade-off between speed and accuracy, the step size used in this work has been arrived at. Use of 5th and higher order solver does not show any particular variation in the response. The simulation data used for the response generation is summarized in Table 5-1 and typical response of the system at 1620 rpm (27 Hz), i.e. the AMB current and the rotor displacement at node 4 is presented in Figure 5-4.

Table 5-1 The rotor-bearing-AMB system data used for the numerical simulation

Parameters	**Values**		**Parameters**	**Values**	
		Rotor			
Disc 1 mass m_1	2	kg	Disc 2 mass m_2	1.5	kg
eccentricity e_1	24	μm	eccentricity e_2	58	μm
Unbalance phase β_1	15°	deg	Unbalance phase β_2	45°	deg
Shaft density ρ	7850	kg-m^{-3}	Shaft deflection u_{x0}	3.1×10^{-5}	m
Shaft length l	0.5	m	Shaft diameter d	0.016	m
Left Bearing k_L^x	495.82	MN/m	Right Bearing k_R^x	355.82	MN/m
k_L^y	950.13	MN/m	k_R^x	805.82	MN/m
		AMB			
Controller gains			*Actuator factors*		
Proportional, K_P	12200	A/m			
Derivative, K_D	3	A-s-m^{-1}	Force-current factor, k_i	42.1	N/A
Integral, K_I	2000	A/(m-s)	Force-disp. factor, k_s	105210	N/m
Rayleigh's coefficients for the proportional damping:			$a_0 = 0.154$,	$a_1 = 0.00001$	

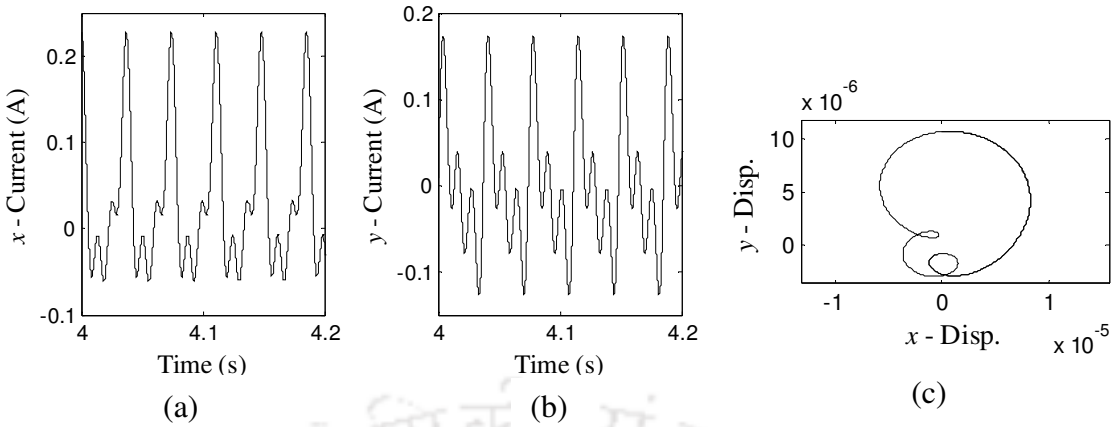

Figure 5-4 System response (a) AMB current in x – direction (b) AMB current in y – direction (c) Shaft centreline orbit at node 4

The variation of response with the spin speed at node 4 and its Hilbert envelope is presented in Figure 5-5. The Hilbert envelope of the response serves for the clear visualisation of critical speeds.

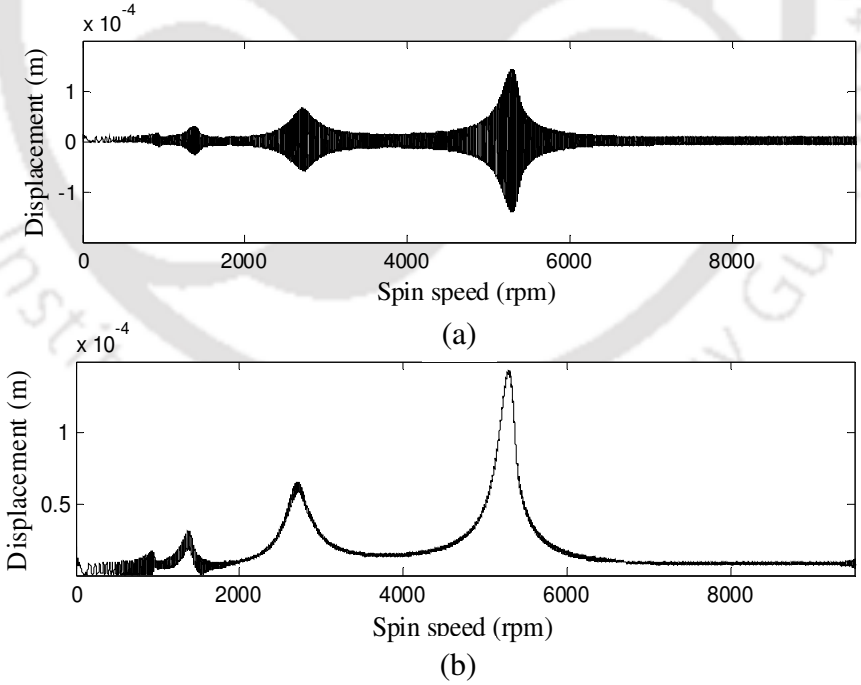

Figure 5-5 Ramp up response at node near the mid span of the rotor (a) Displacement in x-z plane (b) Hilbert envelope of displacement

The 1× resonance peak is seen at 2715 rpm, the 2× resonance peak is seen at 5284 rpm and a $\frac{1}{2}\times$ resonance is seen at 1378 rpm with peak displacements of 65.72 μm, 143.14 μm and 30.34 μm, respectively. Displacements in the speed range of 1563 rpm to 2060 rpm are below 11.34 μm and thus chosen for testing the identification algorithm. In between the 1× and 2× resonance peaks, the lowest displacement of 14.92 μm is observed at 3816 rpm. Since this displacement is higher than that could be allowed while holding the concept of weight dominance good, no speeds in this speed range is used for identification. After the 2× resonance peak, the vibration displacement beyond 6232 rpm is below 12.2 μm. Thus two speed ranges are chosen for testing the algorithm, the lower speed range between 1563 rpm to 2060 rpm and higher speed range beyond 6232 rpm. Individual speeds selected in each speed range are presented in Table 5-2.

Table 5-2 Spin speeds used for identification

Speed range	Spin speeds (rpm)
Lower	1560, 1620, 1680, 1740, 1800, 1860, 1920, 1980 and 2040 (26-34 Hz)
Upper	6240, 6300, 6360, 6420, 6480, 6540, 6600, 6660 and 6720 (104 -112 Hz)

5.7 Results and Discussions

The frequency domain equations of motion developed for the purpose of identification requires various harmonic components of the displacement and AMB current signals, as inputs. The method to obtain this has been developed in the previous chapters. For use of the identification equation as outlined in Eqn. (5.18), the I_i and $\bar{\boldsymbol{\eta}}_i$ are be obtained from the full spectrum analysis detailed in Section 2.3.2 under Chapter 2. To simulate real measurement conditions, random noise

of 1%, 2% and 5% were added to the response. Results of the estimation in the above spin speed range and the effect of signal noise on estimation is presented in Table 5-3 and Table 5-4.

Table 5-3 Estimation results and signal noise sensitivity in speed range of 1560 -2040 rpm

Parameter	Assumed Values	Estimated value at various noise			
		0%	1%	2%	5%
Δk_{22}	3×10^5 (N/m)	299580	300900	302130	307260
	% error	-0.14	0.3	0.71	2.42
e_1	24 (μm)	24.00	23.91	24.17	24.28
	% error	0.00	-0.36	0.7	1.19
β_1	15º (deg.)	14.639	15.02	15.03	15.16
	% error	-0.1	0.16	0.25	1.1
e_2	58 (μm)	57.97	57.86	58.15	59.38
	% error	-0.04	-0.23	0.25	2.38
β_2	45º (deg.)	44.74	43.96	43.84	43.99
	% error	0.07	-0.29	-0.32	-0.28
k_s	105210 (N/m)	103350	103460	103210	103770
	% error	-1.77	-1.66	-1.9	-1.37
k_I	42.1 (N/A)	41.83	41.77	42.56	42.76
	% error	-0.65	-0.79	1.1	1.58
k_L^x	495.82 (MN/m)	497.87	497.15	496.57	496.51
	% error	0.41	0.27	0.15	0.13
k_L^y	950.13 (MN/m)	945.4	946.52	946.18	948.92
	% error	-0.49	-0.38	-0.41	-0.13
k_R^x	355.82 (MN/m)	357.52	357.18	357.35	357.46
	% error	0.47	0.38	0.43	0.46
k_R^y	805.82 (MN/m)	801.18	800.77	800.22	802.13
	% error	-0.57	-0.63	-0.69	-0.46

From Table 5-3 , it is observed that the identification is robust against signal noise. Identification of crack is made with a single parameter of Δk_{22}, which has been estimated well with clean signal and moderate signal noise. All support bearing stiffnesses have been identified with accuracy and the estimates are stable in presence of moderate signal noise. Error associated in estimation of the AMB force-displacement constant, k_s has been large as compared to other parameters, but

particularly inert to presence of signal noise, since the clean and noisy signals both yield almost the same result for this parameter. The identification of two disc unbalances show identical trend; while the unbalance magnitude (e_1 and e_2) estimates are affected by signal noise – estimates of unbalance orientation (β_1 and β_2) are stable in the presence of noise.

Table 5-4 Estimation results and signal noise sensitivity in speed range of 6240 -6720 rpm

Parameter	Assumed Values	Estimated value at various noise			
		0%	1%	2%	5%
Δk_{22}	3×10^5 (N/m)	299650	298600	304560	314310
	% error	-0.12	-0.47	1.52	4.77
e_1	24 (μm)	23.88	22.96	24.5	25.3
	% error	-0.47	-4.38	2.1	5.42
β_1	15º (deg.)	14.34	14.34	14.34	14.26
	% error	-4.35	-4.35	-4.38	-4.9
e_2	58 (μm)	57.01	55.5	55.25	59.54
	% error	-1.7	-4.3	-4.74	2.66
β_2	45º (deg.)	43.12	42.78	43.1	42.88
	% error	-4.18	-4.93	-4.22	-4.7
k_s	105210 (N/m)	106200	102990	109380	111020
	% error	0.94	-2.11	3.96	5.52
k_I	42.1 (N/A)	41.83	42.31	43.28	43.59
	% error	-0.64	0.49	2.81	3.55
k_L^x	495.82 (MN/m)	497.42	495.86	496.95	500.39
	% error	-0.32	0.01	0.23	0.92
k_L^y	950.13 (MN/m)	949.32	949.61	943	947.55
	% error	-0.08	-0.05	-0.75	-0.27
k_R^x	355.82 (MN/m)	357.61	355.82	357.23	360.92
	% error	0.5	0.00	0.39	1.43
k_R^y	805.82 (MN/m)	805.09	805.47	796.47	803.03
	% error	-0.09	-0.04	-1.16	-0.35

The observations in the higher speed range are somewhat diffrenet from the lower speed range in terms of the error of identification with clean signal. The error associated in estimation of phase of unbalance viz. β_1 and β_2 are low (-0.1 % and 0.07 % respectively) in the lower speed range of

estimation as compared to the higher speed range (-4.35 % and -4.18 % respectively). Effect of noise and estimation of other parameters are similar in both the speed ranges. The robustness of the identification procedure developed was tested by introduction of random *bias errors* of 1%, 2% and 5% to the most critical model components, viz. the mass matrix (**M**), the stiffness matrix (**K**) and the shaft static deflection (δ_x) and the effect of modelling error on results of estimation in the lower speed range is summarized in Table 5-5.

Table 5-5 Sensitivity of estimation to the modelling error in speed range of 1560 -2040 rpm

Parameter	Assumed Values	Estimated value at various bias error level			
		0%	1%	2%	5%
Δk_{22}	3×10^5 (N/m)	299580	299460	299670	299190
	% error	-0.14	-0.18	-0.11	-0.27
e_1	24 (μm)	24.00	24.00	23.99	24.17
	% error	0.00	0.03	-0.02	0.7
β_1	15º (deg.)	14.639	14.64	14.64	14.65
	% error	-0.1	-0.1	-0.1	-0.1
e_2	58 (μm)	57.97	58.01	57.97	57.87
	% error	-0.04	0.02	-0.06	-0.22
β_2	45º (deg.)	44.74	44.72	44.74	44.78
	% error	0.07	-0.07	-0.06	-0.06
k_s	105210 (N/m)	103350	103340	103350	103380
	% error	-1.77	-1.77	-1.76	-1.74
k_I	42.1 (N/A)	41.83	41.83	41.83	41.83
	% error	-0.65	-0.64	-0.65	-0.65
k_L^x	495.82 (MN/m)	497.87	497.87	497.85	497.77
	% error	0.41	0.41	0.4	0.39
k_L^y	950.13 (MN/m)	945.4	945.41	945.37	945.15
	% error	-0.49	-0.49	-0.5	-0.52
k_R^x	355.82 (MN/m)	357.52	357.5	357.53	357.44
	% error	0.47	0.47	0.48	0.45
k_R^y	805.82 (MN/m)	801.18	801.14	801.22	800.96
	% error	-0.57	-0.58	-0.57	-0.6

The reasons and origin of modelling errors has been dealt in previous chapters in detail, for instance in Section 4.7. It is observed from Table 5-5, that the estimates show only marginal variation due to the modeling error. The AMB force-current constant, k_s, have been estimated with error of 1.77 % with correct model parameters and registers almost similar deviation under the influence of bias error in the model parameters in all ranges. Residual unbalance parameters, viz. e_1, β_1 and e_2, β_2 are the least influenced and the deviation of estimates of crack stiffness (Δk_{22}), AMB force-current constant (k_I) and all the support bearing stiffness is less than 1%. The developed identification procedure is found robust against bias errors.

5.8 Concluding Remarks

In the present model, identification of crack and support bearing dynamic parameters in a flexible multi disc rotor with AMB support has been performed with help of the vibration displacement and AMB current signals. The identification algorithm developed in this chapter simultaneously estimates the AMB force-displacement and force-current constants along with the residual unbalances at different planes. The algorithm was tested with simulated response and found robust against the measurement noise and modelling errors. The estimation and identification of support dynamic parameters is considered a challenge in the practical rotors, a methodology to achieve this purpose has been presented in the present chapter, as a model based inverse problem.

The analysis in the present chapter deals the most generic situation expected in a rotor–AMB system with a crack, in terms of multiple discs and multiple AMB supports within the span of the rotor. The formulation is not limited for only end supports and could be incorporated to include multiple supports. The identification procedure has been developed to estimate unbalance on all the discs and stiffness constants of all the AMBs. This makes possible the multiplane balancing of

the rotor apart from the identification of crack in the rotor. For a demonstration of the procedure developed, identification problem in a numerical model with two discs has been presented, with sufficient accuracy in the estimation process.

The present chapter serves two purposes – first, to ensure that the signal processing procedures developed in Chapters 2 through 4 are applicable for complex rotor–AMB systems and the second, to establish an identification procedure for the support stiffness. Correct modelling, identification and even physical evaluation of support bearing stiffness is an active field of research and the present model accomplishes this by way of including the support stiffness in the model and identification, both. A summary of the various aspects of the identification process, model evolution, complexities addressed and results obtained with various models and assumptions of the rotor–AMB system, considered in Chapters 2 through 5, is presented in the next chapter. Scopes for future work based on insights gained from the present work are also discussed.

CHAPTER 6

Conclusions and Scope for Future Work

6.1 Summary of the present work

In the present study analytical work has been done to develop a model-based identification algorithm for detecting a transverse fatigue crack in a rotor-AMB system. Such systems pose special difficulty in identification problems due to attenuation of vibration signals due to the AMB action. The AMB control current has been used as additional information in the identification problem. The parameters estimated from the identification algorithm are the viscous damping, disc unbalances, additive stiffness due to the crack, support dynamic parameters and AMB stiffness parameters. The identification algorithm is developed based on the time and frequency domain EOMs of the cracked rotor system subjected to the crack and unbalance forcing, and the AMB support. The reduction in stiffness of the shaft cross-section due to the crack is used as the hypothesis for the identification algorithm. This forcing has multiple frequency components, which are harmonics of the rotor spin speed. While some of frequency components excite the rotor in the forward whirl, others excite the rotor in the reverse whirl; the complete spectrum of the frequency domain has been used in the analysis.

For the development of a frame work for the identification procedure, initially a model of cracked Jeffcott rotor with AMB support has been analysed. This fairly simple 2-DOF model serves the purpose of benchmarking various procedures, which would be used in the next models addressing greater complexities. The use of AMB current signals in conjunction with vibration displacements for the identification purpose is established. The extraction of full spectrum of the displacement

and current signals is attempted with help of a linear regression with the use of FFT. The need for phase correction in FFT based method has been identified and a novel multi–harmonic complex reference signal is envisioned. Incorporation of this reference signal rendered the FFT based method of determination of full spectrum more accurate and faster than the linear regression based method. The crack and AMB stiffness parameters could be identified along with the viscous damping and the disc unbalance. Since, the shaft displacement and AMB current history are the only measurable required in this model, the identification could be performed without adding any new component or sensor to the system, since the AMB implementation already has these two measurements performed on the continuous basis.

In the next model, the disc is considered offset from the central plane of the rotor. This configuration necessitates use of a 4-DOF model to include the rotational displacement in the analysis, arising out of the gyroscopic effect due to offset disc. Since, rotational displacements pose practical difficulty of accurate measurement, a dynamic reduction scheme is implemented to do away with rotational displacements in identification equations. The dynamic reduction scheme is generic in nature and would be used in subsequent models to eliminate rotational and some other DOFs from identification equations based on the FEM. The crack and AMB stiffness parameters, viscous damping and disc unbalance could be identified.

In the third model, the response is generated with a model developed with the FEM, hence expected to be more representative of the physical response from a rotor–AMB system. The rotor is supported on rigid bearings and AMB is used in auxiliary bearing configuration for a support within the rotor span. The procedures developed with the first and second models particularly for

the phase correction and dynamic reduction of DOFs, are utilised to estimate the crack and AMB stiffness parameters along with disc unbalances.

The last model is representative of a generic situation with the AMB support. A multi-disc rotor with a transverse crack, supported on flexible bearings is considered for the analysis. Multiple AMBs are assumed to provide support to the rotor within the span. At least one AMB would be needed but for multi-span rotor system at least one in each span would be required or AMBs can replace some of intermediate bearings. Analysis and identification is performed to estimate the crack and AMB stiffness parameters along with support dynamic parameters and unbalances on multiple planes. For the numerical example, two discs are assumed and all the listed parameters identified.

6.2 Major Conclusions and Recommendations from the Present Work

The present work adds to model based identification in rotor–AMB systems in the following counts

- The major contribution of the present work is in developing the concept of utilizing the AMB support as a diagnostic tool for rotor condition monitoring. In the present analysis the AMB forms the part of support system of the rotor.
- The AMB current can be used as one of the diagnostic information for the identification of rotor flaws. The other most prominent information is the vibration displacement. For practical application, the AMB current in real time can be obtained from the controller. The loss of vibration displacement signal due to active control can be made up with the additional information available in form of AMB control current.

- A new reference signal with multi-harmonic complex components is envisioned and tested for the correction of phase ambiguity arising in the FFT process due to random time instants of picking the signal.
- The phase correction algorithm is tested and effectiveness compared with harmonics obtained from the linear regression. This algorithm can be implemented in practical cases with minimum difficulty.
- In practical implementation a reference signal is obtained with a stationary proximity probe (or a photo electric probe) against a notch on the rotating shaft (or a reflecting tape fixed on the rotating shaft). This generates a periodic pulse referring to a particular position of the shaft. Practical complex signal would necessitate placement of two orthogonal proximity probes against the reference generator notch, which would generate x and y references viz. R_x and R_y (these would be periodic in nature). The FFT of $(R_x + \mathrm{j}R_y)$ will present a spectrum of the complex reference signal, from which the phase of frequencies of interest need to be picked up for the compensation purpose.
- The identification algorithm is new in the sense, it accords equal mathematical value to the AMB current signal and the shaft vibration signal. Attenuation of vibration signal due to AMB action is compensated by the AMB current signal.
- The shaft crack is modelled as a transverse switching crack. The early stage of fatigue cracks are reported to exhibit this behaviour. Thus the present methodology will be useful in early identification of cracks, in the event of its occurrence.
- The identification algorithms developed are generic in nature; they do not take into account the switching crack excitation function (SCEF) and the AMB control strategy, explicitly. The algorithm requires only the response of the vibration displacement and AMB current

for its implementation. Thus the algorithm can be extended to monitor crack and unbalance under different SCEF and AMB control strategies.

- The support dynamic parameters are modelled and identified. In practice, quantification of these is considered an important aspect of the rotor analysis.

6.3 Limitations and Applicability

The present work is analytical in nature. An identification algorithm has been developed for simple cracked rotor–AMB models with two translational and two rotational co-ordinates. However, effects of the disc moment of inertia, gyroscopic couple, and cross-coupling in flexibility and damping coefficients are considered. The dynamic reduction scheme for eliminating the rotational co-ordinates from the system EOMs is also implemented. The identification algorithm has been extended for complex finite element models using the developed mathematical methods.

The developed identification algorithms consider a switching crack. Since, this model of crack is applicable for initial stages of a rotor fatigue crack, the developed identification algorithms can be effectively used for early crack detection in rotor systems.

The identification algorithms are model-based and the mathematical models developed use a single crack parameter for the identification of crack. Only the additive stiffness due to crack is considered. The crack axial location and size parameters are not considered. So, these parameters cannot be directly obtained from identification algorithms in the present form.

The AMB present in this work is not meant to aggravate the vibration signals for ease of diagnosis, but it is a component of the support system itself. In this configuration the vibration signals get attenuated. In the identification step, shortfall due to attenuation of the vibration signals has been

made up for, by the AMB control current. With enhanced values of the AMB constants particularly k_s and k_i, the vibration displacecements may be very small (as seen in Figure 2-8) and pose practical difficulty in measurement. This shortcoming may be overcome with use of more sensitive displacement probes.

In the present work, location of the AMB support is decided by the application for which the AMB has been implemented in the rotor support system. This location of the AMB may not be the best location of the AMB support for identification purpose. This aspect of the problem needs further investigation.

The identification algorithms are developed for detecting crack, but unbalance is also taken into account by considering disc eccentricity and its phase. For the FEM based model, the algorithm can identify unbalances at multiple discs. For illustration, a two disc configuration has been numerically analysed. This could be effectively used for the multi−plane balancing of the physical rotor−AMB systems.

Full−spectrum signal processing is implemented to obtain the forward and reverse whirl frequency components from complex time responses. The complex DFT, half-spectrums or orbit plots can be used to obtain magnitude and phase of full−spectrum frequency components.

Though the identification algorithms use a switching crack model, they have the flexibility to consider any general opening/closing crack function. Also, the full-spectrum gives flexibility to consider any number of harmonics of frequency components of crack force, when the switching/breathing function is not known.

All the identification algorithms require measurements in two orthogonal directions. In reality some measurement locations on the shaft may not be accessible because of mountings over the shaft. Since the dynamic reduction scheme implemented in the work has the sole purpose to remove the unwanted DOFs from the identification equations, it could be effectively used to tackle the difficulty of measurements at certain locations.

6.4 Scope for Future Work

- The identification algorithms have been tested with the response generated by FEM based models. The work can be extended to validate the procedure and results of the analytical work with laboratory experimentation with the cracked rotor and the AMB support.

- Design of smart machines capable of sensing and correcting the operating faults autonomously has been envisoned and reported (Storozhev, 2009). The present work has potential of practical application on such machines for monitoring the rotor condition in real time. The present work can be extended to incorporate it in the design of smart machines.

- The crack model can be extended to consider crack cross-coupled flexibility coefficients, and the same can be estimated. Also, the newer crack excitation functions reported in literature can be used to model the crack effect.

- The mathematical model does not include parameters for the crack location. The algorithms can be extended for estimation of location parameters, with help of the crack location flag

λ_{cr}, conceptualised in this work. Also, the algorithms can be adapted for considering multiple cracks in the shaft.

- The scheme of dynamic reduction may be extended to limit the requirements for physical measurement of vibration displacements at only few locations.

- The experimental rotor on which the transverse crack has been seeded may contain bow due to loading it endures before the generation of crack. The identification algorithm in its present form identifies disc unbalance along with the crack parameter. This could be extended for the identification of shaft bow and mislignments as well.

- The identification algorithm could be tested for more characteristics such as: performance of the algorithms for cracks near supports and the minimum size of a crack that the algorithm can detect.

- The dynamics of the cracked rotor with AMB support under different control strategies has not been reported in literature. Comparison of different AMB control strategies and their effect on the accuracy of crack identification may be taken up.

Appendix A: Derivation of Stiffness Matrices by Inversion of Flexibility Matrices

The flexibility matrix of a cracked shaft is sum to the flexibilities due to intact shaft and flexibility due to crack. To obtain the stiffness matrices by inversion of the flexibility matrices, use of Miller (1981) lemma is made which helps in obtaining two stiffness matrices, which can be individually attributed to the intact shaft and the crack.

With reference to section 3.3.1, renaming the flexibility matrices as

$$\mathbf{A} = \begin{bmatrix} h_{22} & 0 & h_{23} & 0 \\ 0 & h_{22} & 0 & h_{23} \\ h_{32} & 0 & h_{33} & 0 \\ 0 & h_{32} & 0 & h_{33} \end{bmatrix} \quad \text{and} \quad \mathbf{B} = \begin{bmatrix} \Delta h_{22} & 0 & 0 & 0 \\ 0 & 0 & 0 & 0 \\ 0 & 0 & \Delta h_{44} & 0 \\ 0 & 0 & 0 & 0 \end{bmatrix} \tag{A.1}$$

From the Miller (1981) lemma , the inversion is as follows

$$\mathbf{(A+B)^{-1} = A^{-1} - (I + A^{-1}B)^{-1} A^{-1}BA^{-1}} \tag{A.2}$$

Here, $\mathbf{A^{-1}}$ is the stiffness of the intact shaft and $\mathbf{-(I + A^{-1}B)^{-1} A^{-1}BA^{-1}}$ is the contribution in stiffness due to presence of crack. Presence of crack weakens the shaft and so is indicated by the negative nature of the crack stiffness component. This inversion contains multiple matrix operations, which can be simplified by considering significant terms of the Taylor series expansion of the inversion function. The Taylor series expansion of this inversion is

$$\mathbf{(A+B)^{-1} = A^{-1} - A^{-1}BA^{-1} + A^{-1}BA^{-1}BA^{-1} - A^{-1}BA^{-1}BA^{-1}BA^{-1}} + \cdots \tag{A.3}$$

Here, the first term is the stiffness of the intact shaft and the remaining terms sum up to stiffness contribution due to crack. Retaining the first two significant terms of the above series, $\mathbf{A^{-1}}$ yields the stiffness of the intact shaft and $\mathbf{-A^{-1}BA^{-1}}$ yields the stiffness contribution due to crack. Thus,

$$\mathbf{A}^{-1} = \frac{1}{h_{22}h_{33} - h_{23}^2}\begin{bmatrix} h_{33} & 0 & -h_{23} & 0 \\ 0 & h_{33} & 0 & -h_{23} \\ -h_{32} & 0 & h_{22} & 0 \\ 0 & -h_{23} & 0 & h_{22} \end{bmatrix} \tag{A.4}$$

$$\mathbf{A}^{-1}\mathbf{B}\mathbf{A}^{-1} = \frac{1}{(h_{22}h_{33} - h_{23}^2)^2}\begin{bmatrix} \Delta h_{22}h^2{}_{33} + \Delta h_{44}h^2{}_{23} & 0 & -(\Delta h_{22}h_{23}h_{33} + \Delta h_{44}h_{22}h_{33}) & 0 \\ 0 & 0 & 0 & 0 \\ -(\Delta h_{22}h_{23}h_{33} + \Delta h_{44}h_{22}h_{33}) & 0 & \Delta h_{44}h^2{}_{22} + \Delta h_{22}h^2{}_{23} & 0 \\ 0 & 0 & 0 & 0 \end{bmatrix} \tag{A.5}$$

The negative entries in the matrix in Eqn. (A.5) appear due to early truncation of the series, which would tend to have negligible value in the complete series, so they can be replaced by zeros without loss of generality. This consideration alters Eqn. (A.5) to

$$\mathbf{A}^{-1}\mathbf{B}\mathbf{A}^{-1} = \frac{1}{(h_{22}h_{33} - h_{23}^2)^2}\begin{bmatrix} \Delta h_{22}h^2{}_{33} + \Delta h_{44}h^2{}_{23} & 0 & 0 & 0 \\ 0 & 0 & 0 & 0 \\ 0 & 0 & \Delta h_{44}h^2{}_{22} + \Delta h_{22}h^2{}_{23} & 0 \\ 0 & 0 & 0 & 0 \end{bmatrix} \tag{A.6}$$

Defining individual entries of this inverted matrix in terms of the flexibility terms as

$$H = h_{22}h_{33} - h_{23}^2, \quad k_{22} = \frac{h_{33}}{H}, \quad k_{33} = \frac{h_{22}}{H}, \quad k_{23} = k_{32} = -\frac{h_{23}}{H},$$

$$\Delta k_{22} = \frac{\Delta h_{22}h^2{}_{33} + \Delta h_{44}h^2{}_{23}}{H^2}, \quad \Delta k_{44} = \frac{\Delta h_{44}h^2{}_{22} + \Delta h_{22}h^2{}_{23}}{H^2} \tag{A.7}$$

Incorporation of definitions held in Eqn. (A.7), the final form of the inverted matrices are:

$$\mathbf{A}^{-1} = \begin{bmatrix} k_{22} & 0 & k_{23} & 0 \\ 0 & k_{22} & 0 & k_{23} \\ k_{32} & 0 & k_{33} & 0 \\ 0 & k_{32} & 0 & k_{33} \end{bmatrix} \quad \text{and} \quad \mathbf{A}^{-1}\mathbf{B}\mathbf{A}^{-1} = \begin{bmatrix} \Delta k_{22} & 0 & 0 & 0 \\ 0 & 0 & 0 & 0 \\ 0 & 0 & \Delta k_{44} & 0 \\ 0 & 0 & 0 & 0 \end{bmatrix} \tag{A.8}$$

Appendix B: Euler-Bernouli Beam Model

The FEM formulation in Chapters 4 and 5 are based on modelling the rotor as Euler-Bernouli beam. The various elemental matrices used in the formulation are detailed below.

B.1. Elemental mass matrix

$$\mathbf{M} = \frac{\rho A h}{420}\begin{bmatrix} 156 & 22h & 54 & -13h \\ 22h & 4h^2 & 13h & -3h^2 \\ 54 & 13h & 156 & -22h \\ -13h & -3h^2 & -22h & 4h^2 \end{bmatrix} \tag{B.1}$$

Here, ρ is the mass density of the finite element, A is the area of cross section of the element and h is the elemnt length.

Displacement vector $\boldsymbol{\eta} = \begin{bmatrix} u_x^i & \varphi_y^i & u_x^{i+1} & \varphi_y^{i+1} \end{bmatrix}^T$, where super-script i is the node number. Matrices and vectors in orthogonal planes are analogous.

B.2. Elemental Stiffness matrix

$$\mathbf{K} = \frac{EI}{h^3}\begin{bmatrix} 12 & 6h & -12 & 6h \\ 6h & 4h^2 & -6h & 2h^2 \\ -12 & -6h & 12 & -6h \\ 6h & 2h^2 & -6h & 4h^2 \end{bmatrix} \tag{B.2}$$

Here, E is the Youngs modulus of elasticity of the beam material and I is the area moment of inertia of the finite element.

B.3. Rigid disc model

Mass matrix

$$\mathbf{M}^d = \begin{bmatrix} m_d & 0 & 0 & 0 \\ 0 & m_d & 0 & 0 \\ 0 & 0 & I_d & 0 \\ 0 & 0 & 0 & I_d \end{bmatrix} \tag{B.3}$$

Gyroscopic matrix

$$\mathbf{G}^d = \begin{bmatrix} 0 & 0 & 0 & 0 \\ 0 & 0 & 0 & 0 \\ 0 & 0 & 0 & I_p \\ 0 & 0 & -I_p & 0 \end{bmatrix} \tag{B.4}$$

Displacement vector

$$\boldsymbol{\eta}^d = \begin{bmatrix} u_x & \varphi_y & u_y & \varphi_x \end{bmatrix}^T \tag{B.5}$$

As such present formulation of identification algorithm does not restrict the Timoshenko beam model usage and details of matrices are available in (Friswell et al., 2010).

Appendix C: Rayleigh Damping

Rayleigh damping or proportional damping is characterized by two proportionality constants viz. a_0 and a_1, such that the damping matrix caould be expressed in terms of known matices of mass and stiffness.

The relation between damping ratio, ζ, and natural frequency. ω_n, is expressed as

$$\zeta = \frac{a_0}{2\omega_n} + \frac{a_1\omega_n}{2} \tag{C.1}$$

where a_0 and a_1 are Rayleigh damping factors and this can be evaluated by the solution of a pair of simultaneous equations, if the damping ratios ζ_m and ζ_n associated with two specific known frequencies ω_m and ω_n respectively, writing equation (C.1) for each of these two cases and expressing them in the matrix form leads to

$$\begin{Bmatrix} \xi_m \\ \xi_n \end{Bmatrix} = \frac{1}{2}\begin{bmatrix} 1/\omega_m & \omega_m \\ 1/\omega_n & \omega_n \end{bmatrix}\begin{Bmatrix} a_0 \\ a_1 \end{Bmatrix} \tag{C.2}$$

From equation (B.2), a_0 and a_1 can be obtained as,

$$\begin{Bmatrix} a_0 \\ a_1 \end{Bmatrix} = \frac{2\omega_m\omega_n}{\omega_n^2 - \omega_m^2}\begin{bmatrix} \omega_n & -\omega_m \\ -1/\omega_n & 1/\omega_m \end{bmatrix}\begin{Bmatrix} \xi_m \\ \xi_n \end{Bmatrix} \tag{C.3}$$

where ω_m and ω_n are the system fundamental and highest natural frequencies of interest. Thus

$$\mathbf{C}^{(e)} = a_0\mathbf{M}^{(e)} + a_1\mathbf{K}^{(e)} \tag{C.4}$$

Appendix D: Fourier Transforms and Phase Ambiguity in FFT (or DFT)

Fourier analysis is a family of mathematical techniques, all based on decomposing signals into sinusoids. The aim is to obtain the amplitude and phase of the sinusoids at several frequencies, the addition of which can reproduce the original signal. The forward problem is termed as analysis and the reverse problem is termed as synthesis. Thus, analysis of time domain signal transforms it to frequency domain and the synthesis of thee frequency domain signal transforms it to time domain. Many a methods have been deviced and used udepending on the type of signal, the amount of data defining the signal, computational resources available and the accuracy required. For the digitized signals, following methods are available (Smith, 1998) :

1. Using simultaneous equations
2. Using correlation
3. Using FFT (or DFT) algorithm

Use of simultaneous equations is based on basic algebra of calculating N values of frequency domain, from N values of time domain data available. This requires development of N linearly independent equations. To do this, the first sample is taken from each sinusoid and added together. The sum must be equal to the first sample in the time domain signal, thus providing the first equation. Likewise, an equation can be written for each of the remaining points in the time domain signal, resulting in the required N equations, similar to Eqn. (2.33). The solution can then be found by using established methods for solving simultaneous equations. This method requires a tremendous number of calculations hence slow and expansive on computational resource. But this method provides a mathematical basis to decompose a signal into sinusoids. This method modified to estimate only 9 harmonics has been used in Section 2.3.1 for the present problem.

Use of correlation is based on search for the sinusoids of known nature in the analysis of the time domain signal. Each sample in the frequency domain is found by multiplying the time domain

signal by the sine or cosine wave being looked for, and adding the resulting points. In other words, it's correlating the input signal with each basis function. In order for this correlation algorithm to work, the basis functions must be completely uncorrelated with all of the others. Basis functions that are orthogonal are only useful in method of correlation. Many other orthognal basis functions exist, including: square waves, triangle waves, impulses, etc. Signals can be decomposed into these other orthognal basis functions using correlation, just as done here with sinusoids. Hence this method is more of a possibility and less of an application when the search is for decomposition into sinusoids. Due complexities envolved in the correlation metod, it is hardly used for in signal processing.

Use of FFT (or DFT) algorithm to obtain the frequency domain of the time domain signal is well documented, as detailed in the main text. It has been presented in section 2.3.2. The FFT is sensitive to the span of the time domain signal used for the transformation to frequency domain. An example is presented in the following paragraphs with help of a standard time domain wave form to enunciate the issue of phase ambiguity.

A complex signal composed of pure cosine and sine wave form is considered. For this example the signal is

$$s=5\cos(\omega t)+2j\sin(\omega t)+4\cos(2\omega t)+3j\sin(2\omega t)-\cos(3\omega t)+7j\sin(3\omega t)+7\cos(4\omega t)-2j\sin(4\omega t) \quad \text{(D.1)}$$

The plot of the real and imaginary components, the orbit plot and full spectrum FFT of the above signal $\omega = 4\pi$ rad/s is presented in Figure D-1.

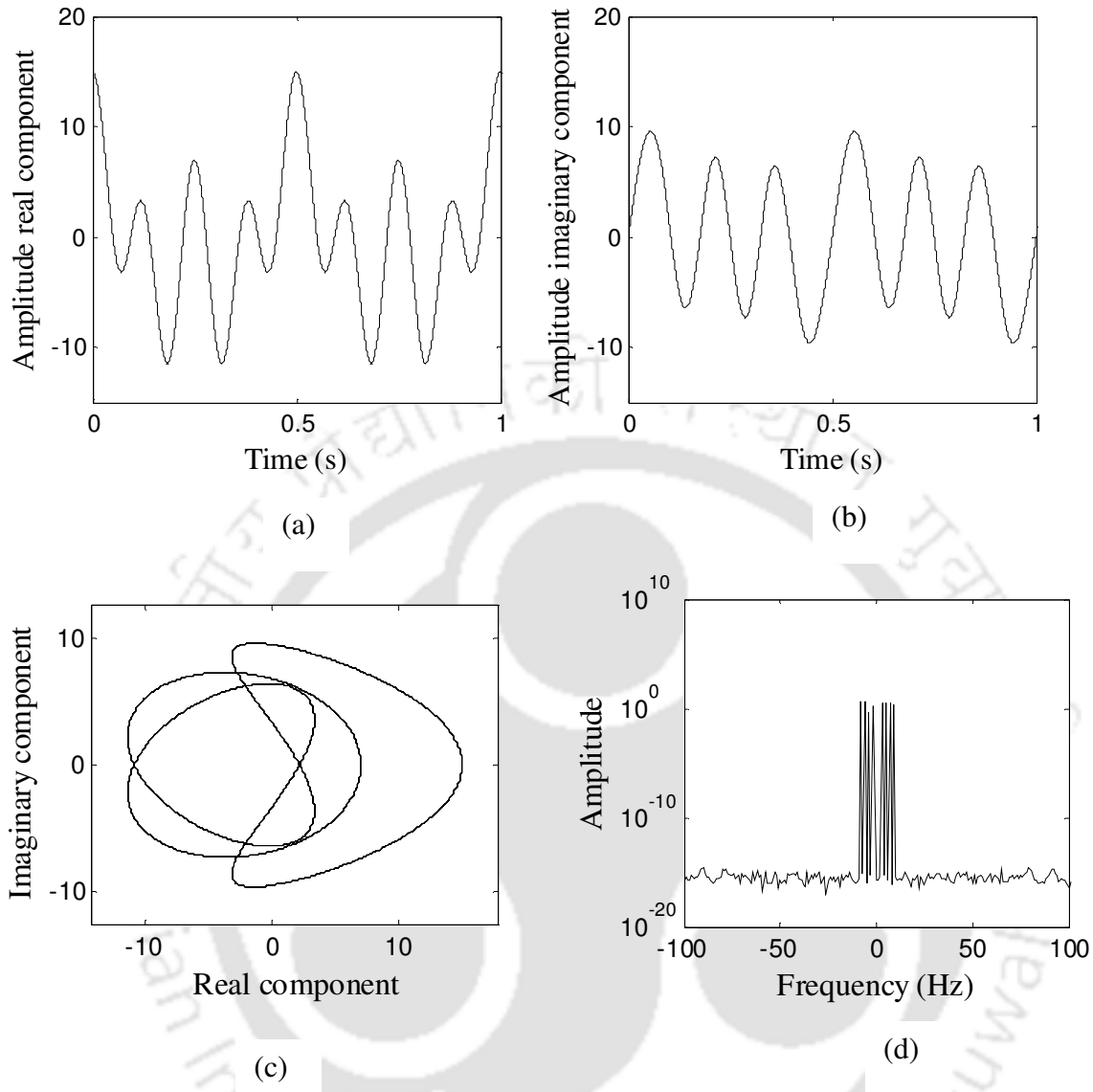

Figure D-1 Time plot of (a) real component (b) Imaginary component (c) orbit plot (d) full spectrum FFT

The amplitude and phase of the above signal picked in the span of 0 - 6π and a random span is obtained by array indexing the 1×, 2×, 3×, 4×, -1× -2×, 3× and -4× harmonics and presented in Table D- 1. The number of data points in the random span has been kept the same as in the span of 0 - 6π.

Table D- 1 Effect of span of the time domain signal on Amplitude and phase of harmonics

Singal span 0-6π			Random signal span		
Harmonic	Amplitude	Phase (deg.)	Harmonic	Amplitude	Phase (deg.)
1×	3.5	1.03×10^{-15}	1×	3.5	0.082
2×	3.5	3.12×10^{-15}	2×	3.5	0.144
3×	3	1.01×10^{-14}	3×	3	0.216
4×	2.5	1.22×10^{-14}	4×	2.5	0.288
-1×	1.5	-3.9×10^{-15}	-1×	1.5	-0.082
-2×	0.5	1.18×10^{-14}	-2×	0.5	-0.144
-3×	4	180	-3×	4	179.78
-4×	4.5	-1.43×10^{-14}	-4×	4.5	-0.288

Table D- 1 exposes some important observations about the FFT process. The amplitude part of the harmonics of the signal presented by Eqn. (D.1) can be obtained in closed form also and they are same as given out by the FFT. Irrespective of the span of the time domain signal passed on to FFT algorithm, the amplitudes are faithfully identified as seen in column 2 and column 5 of Table D- . Since a known waveform was considered in defining the complex signal, it is intuitive to expect the relative phase of the harmonics to be zero. This is truly represented in column 3, where the phase is shown zero within the computational limits. For the time domain signal picked at random span, the relative phase between the harmonics has shifted as seen in column 6. In case of different spans of the time domain signal, this phase shift is different. It differs also with change in the frequency of the signal. The observation is in line with the explanation available in literature, for instance, Smith (1998).

References

Adewusi, S. A. and Al-Bedoor, B. O. (2001) Wavelet analysis of vibration signals of an overhang rotor with a propagating transverse crack, *Journal of Sound and Vibration* ; 246(5), 777–793.

Aenis, M., Knopf, E. and Nordmann, R. (2002) Active magnetic bearings for the identification and fault diagnosis in turbomachinery, *Mechatronics*; 12(8), 1011-1021.

Al-Shudeifat, M. A. and Butcher, E. A. (2011) New breathing functions for the transverse breathing crack of the cracked rotor system: Approach for critical and subcritical harmonic analysis. *Journal of Sound and Vibration*; 330(3), 526-544.

ASTM D6595-00 (2011): "Standard Test Method for Determination of Wear Metals and Contaminants in Used Lubricating Oils or Used Hydraulic Fluids by Rotating Disc Electrode Atomic Emission Spectrometry".

Bachschmid, N., Pennacchi, P. and Tanzi, E. (2008) Some remarks on breathing mechanism, on non-linear effects and on slant and helicoidal cracks, *Mechanical Systems and Signal Processing*; 22 (4), 879–904.

Bachschmid N, Pennacchi P and Tanzi E (2010) In: *Cracked Rotors A Survey on Static and Dynamic Behaviour Including Modelling and Diagnosis*, Springer, Berlin – Heidelberg.

Basseville, M. (1999) On fault detectability and isolability. In European Control Conference (ECC), 1999 (pp. 385-390). IEEE.

Bayoumi, A., Goodman, N., Shah, R., Eisner, L., Grant, L. and Keller, J. (2008) Conditioned-Based Maintenance at USC - Part IV: Examination and Cost-Benefit Analysis of the CBM Process, *Proceedings of the American Helicopter Society Specialists' Meeting on Condition Based Maintenance*, 12-13 February, Huntsville, Alabama, USA.

Behzad, M., Ebrahimi, A., and Meghdari, A. (2008) A new continuous model for flexural vibration analysis of a cracked beam, Polish Maritime Research ; 2 (56), 32-39.

Bently, D. E. and Muszynska, A. (1986) Detection of Rotor Cracks, *Texas A&M University 15th Turbomachinery Symposium and Short Courses*, Corpus Christi, Texas, 129–139.

Besselink, B., Tabak, U., Lutowska, A., van de Wouw, N., Nijmeijer, H., Rixen, D.J., Hochstenbach, M.E. and Schilders, W.H.A. (2013) A comparison of model reduction techniques from structural dynamics, numerical mathematics and systems and control, *Journal of Sound and Vibration*; 332, 4403–4422.

Bordoloi D. J. and Tiwari R. (2013) Optimization of controller parameters of active magnetic bearings in rotorbearing systems, Advances in Vibration Engineering; 12(4): 319–327.

Cai, Z. (2011) *Vibration Diagnostics of Elastic Shafts with a Transverse Crack*, Thesis, Faculty of computing, health and science, Edith Cowan University.

Capecchi, D. and Vestroni, F. (1999) Monitoring of structural systems by using frequency data, *Earthquake Engineering and Structural Dynamics*; 28, 447–461.

Chasalevris, A. C. and Papadopoulos, C. A. (2013) Experimental detection of an early developed crack in rotor-bearing system using an AMB, *3rd International Conference of Engineering against Failure*; 26-28 June, Kos, Greece.

Chen, S., Hsu, M., Le, D. and Nguyen, V. (2013) ANFIS controller for an Active Magnetic Bearing system, *IEEE International Conference on Fuzzy Systems* , 1-8.

Childs, D. W., and Jordan, L. T. (1997) Clearance effects on spiral vibrations due to rubbing, Proceedings of the ASME- Design Engineering Technical Conference; DETC97/VIB-4058.

Christides S. and Barr A. D. S. (1984) One dimensional theory of cracked Bernoulli-Euler Beams, *International Journal of Mechanical Science*; 26(11), 639-648.

Chondros T. G., Dimarogonas A. D. and Yao J. (1998) A continuous cracked beam vibration theory, *Journal of Sound and Vibration*; 215(1), 17–34.

Chondros T. G., Dimarogonas A. D. and Yao J. (2001) Vibration of beam with a breathing crack , *Journal of Sound and Vibration*; 239(1), 57–67.

Church A. H., *Mechanical Vibrations* (1963) John Wiley and Sons Inc., New York.

Cooley, J.W. and Tukey, J.W. (1965) An algorithm for the machine calculation of complex Fourier series, Mathematics of computation; 19(90), 297-301.

Darpe, A. K., Gupta, K. and Chawla, A. (2003) Experimental investigations of the response of a cracked rotor to periodic axial excitation, *Journal of Sound and Vibration*; 260, 265-286.

Darpe, A. K., Gupta, K. and Chawla, A. (2004), Coupled bending, longitudinal and torsional vibrations of a cracked rotor, *Journal of Sound and Vibration*; 269(1-2), 33-60.

Darpe, A. K. (2007) Coupled vibrations of a rotor with slant crack, *Journal of Sound and Vibration*; 305(1-2), 172-193.

Dimarogonas A. D. (1995) Vibration of cracked structures: A state of the art review *Engineering Fracture Mechanics*; 55 (5): 831-857.

Dimarogonas, A. D. and Papodopoulos, C. A. (1983) Vibration of cracked shafts in bending, Journal of Sound and Vibration; 91, 583-593.

Dimentberg, F. M. (1961) *Flexural Vibrations of Rotating Shafts,* Butterworths, London, England.

Dharmaraju, N., Tiwari, R., and Talukdar, S. (2004) Identification of an open crack model in a beam based on force-response measurements, Computers & Structures; 82 (2-3), 167-179.

Dharmaraju, N., Tiwari, R. and Talukdar, S. (2005) Development of a novel hybrid reduction scheme for identification of an open crack model in a beam. Mechanical systems and signal processing; 19(3), 633-657.

Doebling, S. W., Farrar C. R., Prime, M. B. and Shevitz D. W. (1996) Damage identification and health monitoring of structural and mechanical systems from changes in their vibration characteristics: A literature review. *Los Alamos National Laboratory report*, LA-13070-MS, 1996.

Doebling S. W., Farrar C. R., Prime, M. B. and Shevitz D. W. (1998), A review of damage identification methods that examine changes in dynamic properties, *Shock and Vibration Digest*; 30, 91-105.

Downham, E. (1976) Vibration in rotating machinery: malfunction diagnosis- art and science, Proceedings of the Institution of Mechanical Engineers- Vibrations in Rotating Machinery; 1-6.

Ebrahimi, A., Heydari, M., and Behzad, M. (2014) A continuous vibration theory for rotors with an open edge crack, Journal of Sound and Vibration; 3522-3535.

Edwards, S., Lees, A. W. and Friswell M. I. (1998) Fault diagnosis of rotating machinery, *Shock and Vibration Digest*; 30(1), 4-13.

El Arem, S. and Maitournam, H. (2008) A cracked beam finite element for rotating shaft dynamics and stability analysis, *Journal of Mechanics of Materials and Structures*; 3 (5), 893-910.

Farrar C. R. and Doebling S. W. (1997) An overview of modal-based damage identification methods. *Proceedings of DAMAS Conference*; Sheffield, UK, 131-149.

Feldman M (2011) Hilbert transform in vibration analysis. *Mechanical Systems and Signal Processing* 25(3):735-802.

Friswell, M.I., Garvey, S.D. and Penny, J.E.T. (1995) Model reduction using dynamic and iterative IRS techniques, *Journal of Sound and Vibration*; 186, 311–323.

Friswell, M.I., Garvey, S.D. and Penny, J.E.T. (1998) The convergence of the iterated IRS method, *Journal of Sound and Vibration*; 211, 123–132.

Friswell, M. I. and Penny, J. E. T. (2002) Crack Modeling for Structural Health Monitoring, *Structural Health Monitoring*;1(2), 139-148.

Friswell, M. I. (2007) Damage identification using inverse methods, Philosophical Transactions of the Royal Society; 365 (1851), 393-410.

Friswell M.I., Penny J.E.T., Garvey S.D. and Lees A.W. (2010) Dynamics of Rotating Machines, Cambridge University Press, Cambridge.

Friswell M.I. and Mottershead J.E. (1995) Finite Element Model Updating in Structural Dynamics, Kluwer Academic Publishers, Dordrecht, the Netherlands.

Fu, C. (2015) The effect of switching cracks on the vibration of a continuous beam bridge subjected to moving vehicles *Journal of Sound and Vibration*; 339, 157-175.

Gasch, R. (1993) A survey of the dynamic behaviour of a simple rotating shaft with a transverse crack, *Journal of Sound and Vibration*; 160, 313-332.

Gasch, R. (2008) Dynamic behaviour of the Laval rotor with a transverse crack. *Mechanical Systems and Signal Processing*; 22(4), 790-804.

Genta G (2005) Dynamics of Rotating Systems, Springer Science + Business Media Inc., New York.

Goldman, P. and Muszynska, A. (1999), Application of full spectrum to rotating machinery diagnostics, *Orbit*; 17-21.

Gounaris, G., and Dimarogonas, A. (1988) A finite element of a cracked prismatic beam for structural analysis, Computers & Structures 1988; 28 (3), 309-313.

Grabowski, B. (1980) The vibrational behavior of a turbine rotor containing a transverse crack, Journal of Mechanical Design; 102 (1), 140-146.

Gudmundson, P. (1983) The dynamic behaviour of slender structures with cross-sectional cracks, *Journal of the Mechanics and Physics of Solids*; 31 (4), 329-345.

Guyan, R.J. (1965) Reduction of stiffness and mass matrices. AIAA journal; 3(2), 380-380.

Hasan, W. M. (1995) Crack detection from the variation of the eigenfrequencies of a beam on elastic foundation, *Engineering Fracture mechanic*s: 52(3), 409–421.

Henshell, R. D. and Ong, J. H. (1975) Automatic masters for eigenvalue economisation, *Earthquake Engineering and Structrual Dynamics*; 3, 375-383.

He, Z. J., Sheng, Y. D., and Qu, L. S. (1990) Rub failure signature analysis for large rotating machinery, Mechanical Systems and Signal Processing; 4 (5), 417-424.

Hill, J. W., and Baines, N. C. (1988) Applications of an expert system to rotating health monitoring, Proceedings of the Institution of Mechanical Engineers- Vibrations in Rotating Machinery; 449-454.

Humphris, R. R. (1992) A device for generating diagnostic information for rotating machinery using magnetic bearings, *Proceedings of MAG '92, Magnetic Bearings, Magnetic Drives, and Dry Gas Seals Conference and Exhibition*; 29-31 July, 123–135, Alexandria, Virginia, USA.

Irons, B. (1965) Structural eigenvalue problems-elimination of unwanted variables. AIAA journal, 3(5), pp.961-962.

Isermann, R. and Balle, P. (1997) Trends in the applications of Model-based fault detection and diagnosis of technical processes, Control Engineering Practice; 5, 709-719.

Ishida, Y., Hirokawa, K. and Hirose, M. (1995) Vibrations of a Cracked Rotor: 3/2-Order Super Sub-harmonic and One Half-Order Sub-harmonic Resonances, *American Society of Mechanical Engineers, Design Engineering Division*; 84(3), 605–612.

Ishida, Y. and Inoue, T. (2001) Detection of a rotor crack by a periodic excitation, *Proceedings of International Symposium on Stability Control of Rotating Machinery*; 17-19 August, South Lake Tahoe, California, USA, 1004–1011.

Iwatsubo, T. (1976) Error analysis of vibration of rotor/bearing system, Proceedings of the Institution of Mechanical Engineers- Vibrations in Rotating Machinery; 87-92.

Iwatsubo T., Arii S. and Oks A. (1992) Detection of a transverse crack in a rotor shaft by adding external force, *Proceedings of the International Conference on Vibrations in Rotating Machinery*, Paper no. C432/093, IMechE, 275–282.

Joh Y.D. and Lee C.W (1993) Excitation Methods and Modal Parameter Identification in Complex Modal Testing of Rotating Machinery, *International Journal of Analytical and Experimental Modal Analysis*; 8(3), 179–203

Jun, O. S., Eun, H. J., Earmme, Y. Y., and Lee, C. W. (1992) Modelling and vibration analysis of a simple rotor with a breathing crack, Journal of Sound and Vibration; 155, 273-290.

Kamel M. and Bauomy H. S. (2010) Nonlinear study of a rotor–AMB system under simultaneous primary-internal resonance, *Applied Mathematical Modelling*; 34(10), 2763-2777.

Karthikeyan, M., and Tiwari, R. (2010) Detection, localization, and sizing of a structural flaw in a beam based on forced response measurements – An experimental investigation, Mechanism and Machine Theory; 45, 584-600.

Kasarda M. E. F. (2000). An overview of active magnetic bearing technology and applications, *The shock and vibration digest*, *32*(2), 91-99

Kim, H.Y. and Lee, C.W. (2006) Design and control of active magnetic bearing system with Lorentz force-type axial actuator, Mechatronics; 16(1), 13-20

Lazzeri L., Cecconi S., Faravelli M., Scala, M. and Tolle, E. (1992) Second Harmonic Vibration Monitoring of a Cracked Shaft in a Turbo-Generator, Proceedings *of the American Power Conference* 1992; Chicago, Illinois, 54(2), 1337–1342.

Lalanne M and Ferraris G (1998) Rotor Dynamics Prediction in Engineering (Second edition) John Wiley and Sons, New York.

Lee, Y. S., and Chung, M. J. (2001) A study on crack detection using eigenfrequency test data, Computers and Structures ; 77, 327-342.

Lee C. W. and Han, Y. S. (1998) Use of directional Wigner distributions for identification of the instantaneous whirling orbit in rotating machinery, *7th International Symposium on Transport Phenomena and Dynamics of Rotating Machinery* 1998; 22-26.

Lee, C. W., and Joh, C. Y. (1994) Development of the use of directional frequency-response functions for the diagnosis of anisotropy and asymmetry in rotating machinery- Theory, Mechanical Systems and Signal Processing ; 8 (6), 665-678.

Leung, Y.T. (1978) An accurate method of dynamic condensation in structural analysis, *International Journal for Numerical Methods in Engineering*; 12, 1705–1715.

Liang R. Y., Hu J. L. and Choy F. (1992) Quantitative NDE technique for assessing damages in beam structures, *Journal of Engineering Mechanics (ASCE)*; 118(7), 1468–1487.

Mani G., Quinn D. D., Kasarda M. E. F., Inman D. J. and Kirk R. G. (2005) Health Monitoring of Rotating Machinery Through External Forcing, *International Symposium on Stability Control of Rotating Machinery* 2005, 19-23 September, Cleveland, Ohio, USA.

Mani G., Quinn D. D. and Kasarda M. E. F. (2006) Active Health Monitoring in a Rotating Cracked Shaft Using Active Magnetic Bearings as Force Actuators, *Journal of Sound and Vibration*; 294, 454-465.

Mendoza H. (2000) Evaluation of the effectiveness of an active magnetic damper (AMD) in damping sub-synchronous vibrations in a flexible rotor. Master's Thesis, Virginia Tech, Virginia.

Mevel, L., Hermans, L. and Van der Auweraer, H. (1999). Application of a subspace-based fault detection method to industrial structures. Mechanical Systems and Signal Processing;13(6), 823-838.

Mayes I. W. and Davies W.G.R. (1984) Analysis of the response of a multi-rotor-bearing system containing a transverse crack in a rotor, *Journal of Vibration, Acoustics, Stress, and Reliability in Design*; 106, 139–145.

Miller K. S. (1981) On the Inverse of the Sum of Matrices, *Mathematics Magazine* 54(2): 67-72.

Muszynska, A. (1995) Vibrational diagnostics of rotating machinery malfunctions, *International Journal of Rotating Machinery*; 1(3-4), 237-266.

Nelson, H. D., and Nataraj, C. (1986) The dynamics of a rotor system with a cracked shaft, ASME Journal of Vibration, Acoustics, Stress and Reliability in Design; 108, 189-196.

Nowicki A. N. (2004). Infrared Thermography Handbook – Volume 2: Applications, British Institute of Non-Destructive Testing, Northampton, Great Britain.

Nordmann R. and Aenis M. (2004) Fault Diagnosis in a Centrifugal Pump Using Active Magnetic Bearings, *International Journal of Rotating Machinery*; 10 (3), 183-191

O'callahan J.C. (1989) A Procedure for an improved reduced system (IRS) model, *Proceedings of Seventh International Modal Analysis Conference*, January 1989, Las Vegas, pp. 17–21.

Papadopoulos CA and Dimarogonas AD (1988) Stability of the cracked rotors in the coupled vibration mode *ASME Journal of Vibration, Acoustics, Stress, and Reliability in Design* 110 (3): 56-9.

Pandey A. K., Biswas M. and Samman M. M. (1991) Damage detection from changes in curvature mode shapes, *Journal of Sound and Vibration*; 145 (2), 321-332.

Parloo E., Guillaume P. and Van-Overmeire M. (2003) Damage assessment using mode shape sensitivities, *Mechanical Systems and Signal Processing*; 17, 499–518.

Patel T. H. and Darpe A. K. (2008) Vibration response of a cracked rotor in presence of rotor–stator rub, *Journal of Sound and Vibration*; 317(3-5), 841-865.

Patel T. H. and Darpe A. K. (2009) Vibration response of misaligned rotors. *Journal of Sound and Vibration*; 325(3), 609-628.

Patel T. H. and Darpe A. K. (2009) Application of full spectrum analysis for rotor fault diagnosis, *Proceedings of IUTAM Symposium on Emerging Trends in Rotor Dynamics* 2009; 23-26 March, New Delhi, India, 535-545.

Patton, R. J. (1997) Robustness in model-based fault diagnosis: The 1997 situation, Annual reviews in Control; 21, 103-123.

Paz, M. (1984) Dynamic condensation. AIAA journal; 22(5), 724-727.

Pennacchi, P., Bachschmid, N., and Vania, A. (2006) A model-based identification method of transverse cracks in rotating shafts suitable for industrial machines, Mechanical systems and signal processing; 20, 2112-2147.

Penny J. E. T. and Friswell M. I. (2003) The Dynamics of Rotating Machines with Cracks, *Materials Science Forum*, 311 – 318 .

Polajzer B (ed), *Magnetic Bearings, Theory and Applications* 2010, Rijeka, Croatia, Sciyo.

Quinn D. D. Mani, G. Kasarda, M. E. F., Bash, T., Inman D. J. and Kirk R. G. (2005) Damage Detection of a Rotating Cracked Shaft Using an Active Magnetic Bearing as a Force Actuator-Analysis and Experimental Verification, *IEEE/ASME Transactions on Mechatronics*; 10(6), 640-647.

Randall R. B. (2011) Vibration-based Condition Monitoring: Industrial, Aerospace and Automotive Applications, Wiley-Blackwell, Hoboken, New Jersey, USA

Rene Larsonneur (2009) Digital Control. In Maslen ER, Schweitzer G (editors) Magnetic Bearings – Theory, Design and Application to Rotating Machinery. Berlin: Springer-Verlag, pp.229-248.

Rizos, P. F., Aspragothas, N., and Dimarogonas, A. D. (1990) Identification of crack location and magnitude in a cantilever beam from the vibration modes, Journal of Sound and Vibration; 138 (3), 381-388.

Robichaud M. (2003) Reference Standards for Vibration Monitoring and Analysis, http://www.bretech.com/reference/reference.html, accessed 28/05/2015

Rytter, A. (1993) Vibration based inspection of civil engineering structures, Ph.D. Dissertation, Department of Building Technology and Structural Engineering ; Aalborg university, Denmark.

Saavedra P. N. and Cuitino L. A. (2002) Vibration Analysis of Rotor for Crack Identification, *Journal of Vibration and Control*; 8(1), 51–67.

Sabnavis G., Kirk R. G., Kasarda M. and Quinn D. (2004) Cracked shaft detection and diagnostics: a literature review, *The Shock and Vibration Digest*; 36(4), 287-296.

Salawu O. S. (1997) Detection of structural damage through changes in frequency: a Review, *Engineering Structures*; 19, 718-723.

Sanderson A. F. P. (1992) The Vibration Behavior of a Large Steam Tur- bine Generator During Crack Propagation Through the Generator Rotor, *International Conference on Vibrations in Rotating Machinery (ImechE)* 1992; Bath, UK, Paper No. C432/102, 263–273.

Sawicki J.T., Sen A.K. and Litak G. (2009), Multi-resolution wavelet analysis of the dynamics of a cracked rotor, *International Journal of Rotating Machinery* 2009; http://dx.doi.org/10.1155/2009/265198

Sawicki J. T., Friswell M. I., Kulesza Z., Wroblewski A. and Lekki J. D. (2011) Detecting cracked rotors using auxiliary harmonic excitation, *Journal of Sound and Vibration*; 330(7), 1365-1381.

Schweitzer, G. and Maslen, E. R., (eds) *Magnetic Bearings – Theory, Design and Application to Rotating Machinery* 2009, Berlin, Springer-Verlag.

Sekhar A. S. and Prabhu B. S. (1994) Vibration and stress fluctuation in cracked shafts, *Journal of Sound and Vibration*; 169(5), 655–667.

Sekhar A. S. and Prasad P. B. (1997) Dynamic analysis of a rotor system considering a slant crack in the shaft, *Journal of Sound and Vibration*; 208(3), 457–474.

Sekhar A. S. (1999) Vibration characteristics of a cracked rotor with two open cracks, *Journal of Sound and Vibration*; 223(4), 497–512.

Sekhar A. S. (2004a) Model-based identification of two cracks in a rotor system, *Mechanical Systems and Signal Processing*; 18 (4), 977-983.

Sekhar A. S. (2004b) Crack identification in a rotor system: a model-based approach, *Journal of Sound and Vibration*; 270, 887-902.

Sekhar A. S. (2004c) Detection and monitoring of crack in a coast-down rotor supported on fluid film bearings, *Tribology International*; 37(3), 279-287.

Shravankumar C. and Tiwari R. (2013) Identification of stiffness and periodic excitation forces of a transverse switching crack in a Laval rotor, *Fatigue & Fracture of Engineering Materials & Structures*; 36(3), 254-269.

Shravankumar C., Tiwari R. and Mahibalan A (2014) Experimental identification rotor fatigue crack forces, *Proceedings of 9th IFToMM International Conference on Rotor Dynamics*, September 22-25, 2014, Milan, Italy, pp 361-372

Singh, S. K., and Tiwari, R. (2010) Identification of a multi-crack in a shaft system using transverse frequency response functions, Mechanism and Machine Theory; 45 (12), 1813-1827.

Singh, S.K. and Tiwari, R. (2014) Detection and localisation of multiple cracks in a shaft system: An experimental investigation, Measurement; 53,182-193.

Sinha, J. K. (2007) Higher order spectra for crack and misalignment identification in the shaft of a rotating machine, Structural Health Monitoring; 6(4), 325-334.

Sinha J. K., Friswell M. I. and Edwards S. (2002) Simplified models for the location of cracks in beam structures using measured vibration data, *Journal of Sound and Vibration*; 251(1), 13-38.

Sinou J, Lees AW (2005). The Influence of Cracks in Rotating Shafts. Journal of Sound and Vibration; 285(4-5):1015-37

Smith, S. W. (1997) The Scientist and Engineer's Guide to Digital Signal Processing, California Technical Publishing, San Diego.

Southwick, D. (1993) Using Full spectrum plots, *Orbit*; 14(4), 12-16.

Stewart, R. M. (1976) Vibration analysis as an aid to the detection and diagnosis of faults in rotating machinery, Proceedings of the Institution of Mechanical Engineers- Vibrations in Rotating Machinery; 223-229.

Storozhev, D. L. (2009) "Smart Rotating Machines for Structural Health Mon- itoring," Master's thesis, Cleveland State University, Cleveland, OH.

Suarez L.E. (1992) Dynamic condensation method for structural eigenvalue analysis, *AIAA Journal*; 30, 1046–1054.

Tarantola A. (2005) *Inverse Problem Theory and Methods for Model Parameter Estimation*; the Society for Industrial and Applied Mathematics, City Science Centre, Philadelphia, USA.

Taylor, J. I. (1995) Back to the basics of rotating machinery vibration analysis, Sound and Vibration; 29 (2), 12-16.

Thomas, D. L. (1984) Vibration monitoring strategy for large turbogenerators, Proceedings of the Institution of Mechanical Engineers- Vibrations in Rotating Machinery ; 91-99.

Traxler A (2009) Losses in Magnetic Bearings, In Theory, Design, and Application to Rotating Machinery, Springer-Verlag Berlin Heidelberg 2009

Tuma J., Simek J., Skuta J. and Los J. (2010) Active vibration control of journal bearings with use of piezoactuators, *Mechanical Systems and Signal processing*; 36(2), 141-159.

Tuma J. and Bilos J. (2004) Full spectrum analysis in journal bearing diagnostics. In: proceedings of international Carpathian control conference, Velke Karlovice, Czech Republic, 28–30 May 2014.

Wauer J. (1990a) Modelling and formulation of equations of motion for cracked rotating shafts, *International Journal of Solids and Structures*; 26, 901-914.

Wauer J. (1990b), Dynamics of cracked rotors: A literature review, *Applied Mechanics Reviews*; 43(1), 13-18.

Werner F. (1993) The Ratio of 2X to 1X Vibration-A Shaft Crack Detection Myth, *Orbit*;14(3), 11.

Woodbury MA (1950) *Inverting modified matrices*, Memorandum Rept. 42, Statistical Research Group, Princeton University, Princeton, New Jersey.

Xia Y. and Lin R. M. (2004), A New iterative order reduction (IOR) method for eigensolutions of large structures, *International Journal for Numerical Methods in Engineering*; 59, 153–172.

Yamamoto T and Ishida Y (2001) Linear and Nonlinear Rotordynamics (Second edition) John Wiley and Sons, New York.

Zhang H., Schulz M. J., Ferguson F. and Pai P. F. (1999) Structural health monitoring using transmittance functions, *Mechanical Systems and Signal Processing*; 13(5),765-787.

Zhang C L, Li B, Yang Z B, et al. (2013) Crack location identification of rotating rotor systems using operating deflection shape data, *Science China Technical Sciences* 56: 1723-1732.

Zhao X, Patel T H and Zuo M J (2012) Multivariate EMD and full spectrum based condition monitoring for rotating machinery, *Mechanical Systems and Signal Processing* 27: 712-728.

Zhou T., Sun, Z. Xu, J., and Han, W. (2005) Experimental analysis of cracked rotor, Journal of Dynamic systems, Measurement, and Control; 127, 313-320.

Zhu C., Robb D. A. and Ewins D. J. (2003) The dynamics of a cracked rotor with an active magnetic bearing, *Journal of Sound and Vibration*; 265(3), 469–487.

Zou Y., Tong L. and Steven G. P. (2000) Vibration-based model-dependent damage (delamination) identification and health monitoring for composite structures – a review, *Journal of Sound and Vibration*; 230(2), 357-378.

Publications from the Present Work

Journals:

1. Singh S and Tiwari R, (2015) Model-based fatigue crack identification in rotors integrated with active magnetic bearings. *Journal of Vibration and Control*. DOI: 10.1177/1077546315587146.
2. Singh S and Tiwari R (2015) Model-Based Switching-Crack Identification in a Jeffcott Rotor with an Offset Disc Integrated with an Active Magnetic Bearing, *ASME Journal of Dynamic Systems, Measurement and Control*. DOI: 10.1115/1.4032292
3. Singh S and Tiwari R, 2016, Model Based Identification of Crack and Bearing Stiffnesses in Rotor Supported with an Auxiliary Active Magnetic Bearing (Ready for communication).

Conferences:

1. Singh S and Tiwari R (2014) Response Analysis of a Cracked Jeffcott Rotor Supported on Active Magnetic Bearings, National Symposium on Rotor Dynamics (*NSRD-2014*), During 12-14 Feb 2014, Dr Ambedkar Institute of Technology Bangalore, India
2. Singh S and Tiwari R, 2016, Finite Element Model Based Crack Force Identification in a Rotor System Integrated with Active Magnetic Bearings (Acepted for presentation at IMechE Conference on Vibration in Rotating Machinery, Manchester, 13-15 Sept. 2016).